
Electronic Thesis and Dissertation Repository

4-23-2018 11:00 AM

Novel Channel Estimation Techniques for Next Generation MIMO-OFDM Wireless Communication Systems: Design and Performance Analysis

Mohammed Zourob, *The University of Western Ontario*

Supervisor: Rao, Raveendra, *The University of Western Ontario*

Co-Supervisor: Al-Dweik, Arafat, *The University of Western Ontario*

A thesis submitted in partial fulfillment of the requirements for the Doctor of Philosophy degree in Electrical and Computer Engineering

© Mohammed Zourob 2018

Follow this and additional works at: <https://ir.lib.uwo.ca/etd>



Part of the [Systems and Communications Commons](#)

Recommended Citation

Zourob, Mohammed, "Novel Channel Estimation Techniques for Next Generation MIMO-OFDM Wireless Communication Systems: Design and Performance Analysis" (2018). *Electronic Thesis and Dissertation Repository*. 5306.

<https://ir.lib.uwo.ca/etd/5306>

This Dissertation/Thesis is brought to you for free and open access by Scholarship@Western. It has been accepted for inclusion in Electronic Thesis and Dissertation Repository by an authorized administrator of Scholarship@Western. For more information, please contact wlsadmin@uwo.ca.

Abstract

During the last decade, major evolutions were introduced for Multiple Input Multiple Output (MIMO) wireless communication systems. To reap the full benefits of MIMO systems, the Base Station (BS) and user equipments require accurate Channel State Information (CSI), which can be acquired using one of the two major approaches for Channel Estimation (CE): pilot-based or blind-based CE.

In this thesis, a pilot-based lower complexity channel estimator for Cell-Specific Reference Signals (C-RS) and User Equipment RS (UE-RS) in LTE-A Downlink (DL) system is proposed based on using a hybrid Wiener filter. The proposed system is a sub-optimum scheme that requires 8.8% and 74.5% of the number of computations required by the optimum system and other sub-optimum systems. Moreover, a less computationally complex CE scheme based on Fast Fourier Transform (FFT) is proposed. The presented pilot-based system is validated in end-to-end LTE-A system in terms of throughput, which confirms that the proposed system is suitable for practical implementation. Next, a new blind-based CE technique based on a hybrid OFDM symbol structure for SIMO and MIMO systems is presented. It is shown that the developed system, with enough receive antennas, performs as good as pilot-based system, with similar complexity and better spectral efficiency. Finally, new Resource Grid (RG) configurations that serve the blind-based CE scheme developed for MIMO-OFDM system are presented, with the aim to improve the Mean Squared Error (MSE) performance, while minimizing the number of required receive antennas. Results show that the proposed RG configurations provide superior MSE performance, from the perspective of the blind-based CE scheme under investigation, compared to the LTE-A RG configuration.

Throughout the thesis, performances of linear receivers is presented in terms of spectral efficiency as a function of Signal-to-Noise Ratio (SNR), and number of BS antennas. CE techniques are evaluated in terms of MSE as a function of SNR for different channel conditions. Analytical results wherever possible and, in general, simulation results are presented.

Keywords: MIMO, OFDM, Channel Estimation (CE), Least Squares, Mean Square Error, Wiener Filter, LTE-A, Blind-Based CE, Pilot-Based CE.

Dedication

To my father, Omar, and my mother, Ayda,

For their unconditional love and sacrifice, their dedication in my upbringing, and for pushing me to fight my way through hardships ...

To my beloved Aisha,

For her unyielding patience, her unwavering faith, her joyful laugh, and for being the sun of my world, because she always understood ...

To my mentor, MK, and my second mother, Amal,

For his ever encouraging 'harsh' and wise words, and her constant heart-warming prayers and smile...

Acknowledgements

All praise be to Allah for bestowing upon me His countless blessings.

Words cannot help me in describing my sincere appreciation and gratitude to my supervisor Dr. Raveendra K. Rao for giving me the opportunity of working under his guidance, for his time, unwavering support and imparting not only scientific knowledge, but also his life experience and wisdom, which have been a priceless inspiration for me. Only by his enthusiasm, analytical outlook and constructive criticism that this work can be presented here today. Also, I would like to thank my co-supervisor Dr. Arafat Al-Dweik for his continuous encouragement, kindness and support during my last year of Doctoral studies. Moreover, I would like to thank the examination committee members for their valuable remarks and considerable recommendations.

I would also like to show my sincere gratitude and deep thanks to my siblings and my dearest aunt, Sabah, for their support, encouragement, kindness and love. Also, I would like to thank my brothers-in-law Ibrahim MK, Mustafa MK and especially Ahmad Omar Daour for all the fun we had during our trips together to attend the different conferences.

I wish to thank my dear friends Dr. Mohamad Elfakhani and Rami Akeela for all their invaluable encouragement, motivation and support throughout the course of my Ph.D. I would like also to express my gratitude to my friend Salam Yaghi and to my colleagues Anas Saci and especially Muhammad Ajmal Khan, who provided me with valuable suggestions and help during the time of difficulties.

Last but not least, I am honoured and thankful to the Natural Sciences and Engineering Research Council of Canada (NSERC) for awarding me the Alexander Graham Bell Canada Graduate Scholarship towards my Doctoral studies.

Table of Contents

Abstract	i
Dedication	ii
Acknowledgements	iii
Table of Contents	iv
List of Tables	vii
List of Figures	viii
List of Abbreviations, Symbols, Nomenclature	xi
1 Introduction	1
1.1 Digital Wireless Communication System Overview	1
1.1.1 Communication Channel and Channel Estimation	4
1.2 Orthogonal Frequency Division Multiplexing	5
1.3 Multiple Input Multiple Output	6
1.4 Review of Channel Estimation Techniques	9
1.5 Problem Statement and Justification	13
1.6 Thesis Contributions	14
1.7 Thesis Organization	15
2 Hybrid Lower-Complexity Filters for Pilot-Based CE	17
2.1 Introduction	17
2.2 LTE-A OFDM DL System and Channel Model	18
2.3 Channel Estimation	22
2.3.1 Pilots Extraction	23
2.3.2 Pilots Equalization	24
2.3.3 Noise Reduction	24

2.3.3.1	Equal Weight Averaging	25
2.3.3.2	Wiener Filtering	27
2.3.4	Interpolation	29
2.3.4.1	Linear Spline Interpolation	29
2.3.4.2	Cubic Spline Interpolation	30
2.3.4.3	Wiener Interpolation	31
2.3.4.4	2×1 -D FFT/IFFT Filtering and Interpolation	32
2.4	Results and Discussion	32
2.4.1	CE Results Before Interpolation	33
2.4.2	CE Results After Interpolation	36
2.4.2.1	2×1 -D FFT/IFFT Filtering and Interpolation	42
2.4.2.2	Complexity Analysis	44
2.4.3	Throughput Conformance Testing in LTE-A System	45
2.5	Conclusion	47
3	OSBCE for SIMO-OFDM Systems	48
3.1	Introduction	48
3.2	OSBCE System Model Overview	49
3.3	SIMO-OFDM $1 \times N_{R_x}$ OSBCE System Models	55
3.3.1	Review of Multiple Antenna Linear Receivers	56
3.3.2	SIMO 1-D F.OSBCE - Across Frequency	61
3.3.2.1	Results and Discussion - $\kappa \in \{1, 6\}$	63
3.3.3	SIMO 1-D T.OSBCE - Across Time	67
3.3.3.1	Results and Discussion - $\iota \in \{1, 7\}$	72
3.3.4	SIMO 2-D T/F.OSBCE - Across Time & Frequency	75
3.3.4.1	Results and Discussion - $(\kappa, \iota) \in \{(1, 1), (3, 4)\}$	77
3.4	Conclusion	80
4	OSBCE for MIMO-OFDM Systems	82
4.1	Introduction	82
4.2	MIMO-OFDM $N_{T_x} \times N_{R_x}$ OSBCE System Models	82
4.2.1	MIMO 1-D F.OSBCE - Across Frequency	83
4.2.1.1	Mode 1	83
4.2.1.2	Mode 1 M	87
4.2.1.3	Results and Discussion - Mode 1 vs. Mode 1 M	90
4.2.1.4	Mode 2	93
4.2.1.5	Results and Discussion - Mode 1 M vs. Mode 2	94

4.2.2	MIMO 1-D T.OSBCE - Across Time	97
4.2.2.1	Mode 1	97
4.2.2.2	Mode 2	100
4.2.2.3	Results and Discussion - Mode 1 vs. Mode 2	101
4.2.3	MIMO 2-D T/F.OSBCE - Across Time & Frequency	104
4.2.3.1	Mode 1	104
4.2.3.2	Mode 2	107
4.2.3.3	Results and Discussion - Mode 1 vs. Mode 2	108
4.3	Conclusion	110
5	New Pilot Distributions for MIMO OSBCE	111
5.1	Introduction	111
5.2	Proposed Pilot Distributions	112
5.2.1	Proposed Distribution for MIMO 1-D F.OSBCE	112
5.2.1.1	Results and Discussion - Proposed vs. Mode 2	113
5.2.2	Proposed Distribution for MIMO 1-D T.OSBCE	116
5.2.2.1	Results and Discussion - Proposed vs. Mode 2	117
5.2.3	Proposed Distribution for MIMO 2-D T/F.OSBCE	120
5.2.3.1	Results and Discussion - Proposed vs. Mode 2	121
5.3	Conclusion	123
6	Conclusion	124
6.1	Introduction	124
6.2	Summary of Contributions	124
6.3	Recommendations for Future Work	126
	Bibliography	129
	Curriculum Vitae	137

List of Tables

2.1	Channel delay profiles used in simulation	21
2.2	Mathematical equations for C-RS pilot indices	23
2.3	Comparison of noise reduction techniques complexity for C-RS Port-0 - EPA 5	45
2.4	TM1 - Single antenna (Port-0)	46
2.5	TM2 - Transmit diversity	46
2.6	TM3: Open loop codebook based precoding	46
2.7	TM4: Closed loop codebook based spatial multiplexing	46
2.8	TM6: Single layer closed loop codebook based spatial multiplexing	46
3.1	Correlation Coefficient ρ for common channel models($N = 256$)	52
4.1	MIMO 1-D F.OSBCE Mode 1 coding scheme	84
4.2	MIMO 1-D F.OSBCE Mode 1 M coding scheme	87
4.3	MIMO 1-D T.OSBCE Mode 1 coding scheme	97
4.4	MIMO 2-D T/F.OSBCE Mode 1 coding scheme	104

List of Figures

1.1	Block diagram of general DWCS	2
1.2	Block diagram of binary modulator	3
1.3	Block diagram of general OFDM modulator and demodulator	6
1.4	Time-frequency resource grid of LTE-A example	10
2.1	Mapping of C-RS in LTE-A – Normal CP	19
2.2	Frame Structure in LTE-A FDD	20
2.3	Block diagram of SISO OFDM modulator and demodulator	21
2.4	Channel Estimation in LTE-A OFDM	23
2.5	Examples of EWA	28
2.6	MSE vs. SNR for EPA 5 & EVA 70 before interp.	34
2.7	MSE vs Maximum Doppler Frequency for ETU 300 at SNR = 30 dB	35
2.8	MSE vs. SNR for ETU 300 (NCP & ECP) before interp.	36
2.9	MSE vs. SNR with interp. - EWA - EPA 5 & EVA 70	37
2.10	MSE vs. SNR with interp. - EWA - ETU 300 (NCP & ECP)	38
2.11	MSE vs. SNR with interp. - 1-D Wiener - EPA 5 & EVA 70	38
2.12	MSE vs. SNR with interp. - 1-D Wiener - ETU 300 (NCP & ECP)	39
2.13	MSE vs. SNR with interp. - 2-D and 2×1 -D Wiener - EPA 5 & EVA 70	40
2.14	MSE vs. SNR with interp. - 2-D and 2×1 -D Wiener - ETU 300 (NCP & ECP)	40
2.15	MSE vs. SNR for EPA 5 & EVA 70 after interp. - All schemes	41
2.16	MSE vs. SNR for ETU 300 (NCP & ECP) after interp. - All schemes	42
2.17	MSE vs. SNR with 2×1 -D FFT/IFFT interp. - EPA 5 & EVA 70	43
2.18	MSE vs. SNR with 2×1 -D FFT/IFFT interp. - ETU 300 (NCP & ECP)	43
2.19	CE with different interpolators example	44
3.1	Time/Frequency grid in LTE-A	51
3.2	Block diagram of the proposed OFDM modulator	53
3.3	Block diagram of the proposed OFDM demodulator	53
3.4	Proposed SISO F.OSBCE grid in LTE-A	54
3.5	SNR gain vs. N_{R_x}	58

3.6	BER vs. SNR using MRC and EGC	59
3.7	$1 \times N_{R_x}$ Frequency OSBCE system - $\kappa \in \{1, 6\}$	61
3.8	$1 \times N_{R_x}$ F. OSBCE - \hat{A}_k BER & SER vs. SNR. $\kappa \in \{1, 6\}$	64
3.9	$1 \times N_{R_x}$ F. OSBCE - MSE vs. SNR for different N_{R_x} . $\kappa \in \{1, 6\}$	64
3.10	$1 \times N_{R_x}$ F. OSBCE - MSE vs. SNR for different channels. $\kappa \in \{1, 6\}$	65
3.11	$1 \times N_{R_x}$ F. OSBCE - MSE vs. SNR for different M_A, M_P . $\kappa \in \{1, 6\}$	65
3.12	$1 \times N_{R_x}$ F. OSBCE - Example of $\rho(\kappa)$ vs. κ for different channels	66
3.13	$1 \times N_{R_x}$ Time OSBCE system - $\iota \in \{1, 7\}$	70
3.14	$1 \times N_{R_x}$ T. OSBCE - \hat{A}_ℓ BER & SER vs. SNR. $\iota \in \{1, 7\}$	72
3.15	$1 \times N_{R_x}$ T. OSBCE - MSE vs. SNR for different N_{R_x} . $\iota \in \{1, 7\}$	73
3.16	$1 \times N_{R_x}$ T. OSBCE - MSE vs. SNR for different channels. $\iota \in \{1, 7\}$	73
3.17	$1 \times N_{R_x}$ T. OSBCE - MSE vs. SNR for different M_A, M_P . $\iota \in \{1, 7\}$	74
3.18	$1 \times N_{R_x}$ T. OSBCE - Example of $\rho(\iota)$ vs. ι for different speeds	75
3.19	$1 \times N_{R_x}$ Time/Frequency OSBCE system - $(\kappa, \iota) \in \{(1, 1), (3, 4)\}$	76
3.20	$1 \times N_{R_x}$ T/F. OSBCE - $\hat{A}_{k,\ell}$ BER & SER vs. SNR. $(\kappa, \iota) \in \{(1, 1), (3, 4)\}$	78
3.21	$1 \times N_{R_x}$ T/F. OSBCE - MSE vs. SNR for different N_{R_x} . $(\kappa, \iota) \in \{(1, 1), (3, 4)\}$	78
3.22	$1 \times N_{R_x}$ T/F. OSBCE - $ \rho(\kappa, \iota) $. TUX channel. $V = 200$ Km/hr	79
3.23	$1 \times N_{R_x}$ T/F. OSBCE - $\arg \{\rho(\kappa, \iota)\}$. TUX channel. $V = 200$ Km/hr	80
4.1	$2 \times N_{R_x}$ Frequency OSBCE system - Mode 1	84
4.2	$E \{\Delta_\kappa \Delta_\kappa^*\}$ vs κ for different channels	85
4.3	$2 \times N_{R_x}$ Frequency OSBCE system - Mode 1 M	88
4.4	$2 \times N_{R_x}$ F. OSBCE - \hat{A}_k & $\hat{A}_{k+\kappa}$ BER & SER vs. SNR - Modes 1 M & 1	90
4.5	$2 \times N_{R_x}$ F. OSBCE - MSE vs. SNR for different N_{R_x} - Modes 1 M & 1	91
4.6	$2 \times N_{R_x}$ F. OSBCE - MSE vs. SNR for different channels - Modes 1 M & 1	91
4.7	$2 \times N_{R_x}$ F. OSBCE - MSE vs. SNR for different M_A, M_P - Modes 1 M & 1	92
4.8	$2 \times N_{R_x}$ Frequency OSBCE system - Mode 2	93
4.9	$2 \times N_{R_x}$ F. OSBCE - \hat{A}_k BER & SER vs. SNR - Modes 1 M & 2	94
4.10	$2 \times N_{R_x}$ F. OSBCE - MSE vs. SNR for different N_{R_x} - Modes 1 M & 2	95
4.11	$2 \times N_{R_x}$ F. OSBCE - MSE vs. SNR for different channels - Modes 1 M & 2	96
4.12	$2 \times N_{R_x}$ F. OSBCE - MSE vs. SNR for different M_A, M_P - Modes 1 M & 2	96
4.13	$2 \times N_{R_x}$ Time OSBCE system - Mode 1	98
4.14	$2 \times N_{R_x}$ Time OSBCE system - Mode 2	100
4.15	$2 \times N_{R_x}$ T. OSBCE - \hat{A}_ℓ BER & SER vs. SNR - Modes 1 & 2	101
4.16	$2 \times N_{R_x}$ T. OSBCE - MSE vs. SNR for different N_{R_x} - Modes 1 & 2	102
4.17	$2 \times N_{R_x}$ T. OSBCE - MSE vs. SNR for different speeds - Modes 1 & 2	103

4.18	$2 \times N_{R_x}$	T. OSBCE - MSE vs. SNR for different M_A, M_P - Modes 1 & 2 . . .	103
4.19	$2 \times N_{R_x}$	Time-Frequency OSBCE system - Mode 1	104
4.20	$2 \times N_{R_x}$	Time-Frequency OSBCE system - Mode 2	107
4.21	$2 \times N_{R_x}$	T/F. OSBCE - $\hat{A}_{k,\ell}$ BER & SER vs. SNR - Modes 1 & 2	108
4.22	$2 \times N_{R_x}$	T/F. OSBCE - MSE vs. SNR for different N_{R_x} - Modes 1 & 2 . . .	109
5.1	$2 \times N_{R_x}$	Frequency OSBCE system - proposed	112
5.2	$2 \times N_{R_x}$	F. OSBCE - \hat{A}_k BER & SER vs. SNR - Proposed & Mode 2	113
5.3	$2 \times N_{R_x}$	F. OSBCE - MSE vs. SNR for different N_{R_x} - Proposed & Mode 2 .	114
5.4	$2 \times N_{R_x}$	F. OSBCE - MSE vs. SNR for different channels - Proposed & Modes	2114
5.5	$2 \times N_{R_x}$	F. OSBCE - MSE vs. SNR for different M_A, M_P - Proposed & Mode	2115
5.6	$2 \times N_{R_x}$	Time OSBCE system - proposed	116
5.7	$2 \times N_{R_x}$	T. OSBCE - \hat{A}_ℓ BER & SER vs. SNR - Proposed & Mode 2	118
5.8	$2 \times N_{R_x}$	T. OSBCE - MSE vs. SNR for different N_{R_x} - Proposed & Mode 2 .	118
5.9	$2 \times N_{R_x}$	T. OSBCE - MSE vs. SNR for different speeds - Proposed & Mode 2	119
5.10	$2 \times N_{R_x}$	T. OSBCE - MSE vs. SNR for different M_A, M_P - Proposed & Mode	2120
5.11	$2 \times N_{R_x}$	Time/Frequency OSBCE system - proposed	121
5.12	$2 \times N_{R_x}$	T/F. OSBCE - $\hat{A}_{k,\ell}$ BER & SER vs. SNR - Proposed & Mode 2 . .	121
5.13	$2 \times N_{R_x}$	T/F. OSBCE - MSE vs. SNR for different N_{R_x} - Proposed & Mode 2	122
6.1		Suggested future pilot-based hybrid system	127
6.2		Suggested iterative OSBCE system	128

List of Abbreviations

3GPP	3rd Generation Partnership Project
5G	Fifth-Generation
ADC	Analog to Digital Convertor
AWGN	Additive White Gaussian Noise
BER	Bit Error Rate
BS	Base Station
C-RS	Cell-specific Reference Signals
CE	Channel Estimation
CFO	Carrier Frequency Offset
CFR	Channel Frequency Response
CIR	Channel Impulse Response
CM	Complex Multiplication
CMM	Constant Modulus
CP	Cyclic Prefix
CSI	Channel State Information
DAC	Digital to Analog Converter
DD	Decision Directed
DFT	Discrete Fourier Transform

DL	Downlink
DVB-T2	Second-Generation Digital Video Broadcasting-Terrestrial
DWCS	Digital Wireless Communication System
ECP	Extended Cyclic Prefix
EGC	Equal Gain Combining
EPA	Extended Pedestrian A model
ETU	Extended Typical Urban model
EVA	Extended Vehicular A model
EWA	Equal Weight Averaging
FDD	Frequency Division Duplex
FFT	Fast Fourier Transform
ICI	Inter Carrier Interference
IDFT	Inverse Discrete Fourier Transform
IFFT	Inverse Fast Fourier Transform
ISI	Inter Symbol Interference
LMMSE	Linear Minimum Mean Square Error
LSE or LS	Least Square Estimation
LTE-A	Long Term Evolution-Advanced
MA-FIR	Moving Average-Finite Impulse Response
MASK	M -ary Amplitude Shift Keying
MIMO	Multiple Input Multiple Output
MLD	Maximum Likelihood Detection
MPSK	M -ary Phase Shift Keying
MRC	Maximum Ratio Combining

MRT	Maximum Ratio Transmission
MSE	Mean Squared Error
MU-MIMO	Multi User-Multiple-Input-Multiple-Output
NCP	Normal Cyclic Prefix
OFDM	Orthogonal Frequency Division Multiplexing
OSBCE	One Shot Blind Channel Estimator
PAPR	Peak Average Power Ratio
PDF	Probability Density Function
QAM	Quadrature Amplitude Modulation
QoS	Quality of Service
RB	Resource Block
RC	Reference Channels
RE	Resource Elements
RF	Radio Frequency
RG	Resource Grid
RM	Real Multiplication
RMS	Root Mean Square
SER	Symbol Error Rate
SIMO	Single Input Multiple Output
SISO	Single Input Single Output
SNR	Signal to Noise Ratio
STBC	Space Time Block Codes
TDD	Time Division Duplex
TM	Transmission Modes

UE	User Equipment
UE-RS	User Equipment-specific Reference Signals
UL	Uplink
WiMAX	Worldwide Interoperability for Microwave Access
WLAN	Wireless Local Area Networks
WSSUS	Wide Sense Stationary Uncorrelated Scattering
ZF	Zero Forcing

Chapter 1

Introduction

In this Chapter, an overview of the functional block diagram of a Digital Wireless Communication System (DWCS) is presented with emphasis on the communication channel and Channel Estimation (CE) blocks. Moreover, Orthogonal Frequency Division Multiplexing (OFDM) and Multiple Input Multiple Output (MIMO) are introduced as key technologies towards the realization of the Fifth-Generation (5G) DWCS with focus on their advantages, and the role of CE in their operation. CE classification, techniques, and state-of-the-art research are discussed. All in all the emphasis in this Chapter is mainly on the literature review, problem statements, their justifications, approaches for their solutions, and organization of the thesis.

1.1 Digital Wireless Communication System Overview

Digital communication is one of the most rapidly growing industries in the world, and its products cover a wide array of applications and they are exerting a direct impact on our daily lives. The communication process involves implicitly the transmission of information from one point to another through a succession of processes. The first step is the generation of a message signal, either analog (voice, music or picture) or digital (computer data). The second step is to describe that message signal with a certain measure of precision by using a set of electrical, aural or visual symbols. These symbols are encoded in a form that is suitable for transmission over the available physical medium. The encoded symbols are transmitted to a specific destination using a transmission device. The encoded symbols are received on the other side using a receiver device. Then, the encoded symbols are decoded to produce an estimate of the original symbols. Thus, the message signal is re-created with a definable degradation in quality due to signal fading, system imperfections and the different types of noise (thermal noise, Additive White Gaussian Noise (AWGN), etc). A typical digital

communication system is shown in Figure 1.1.

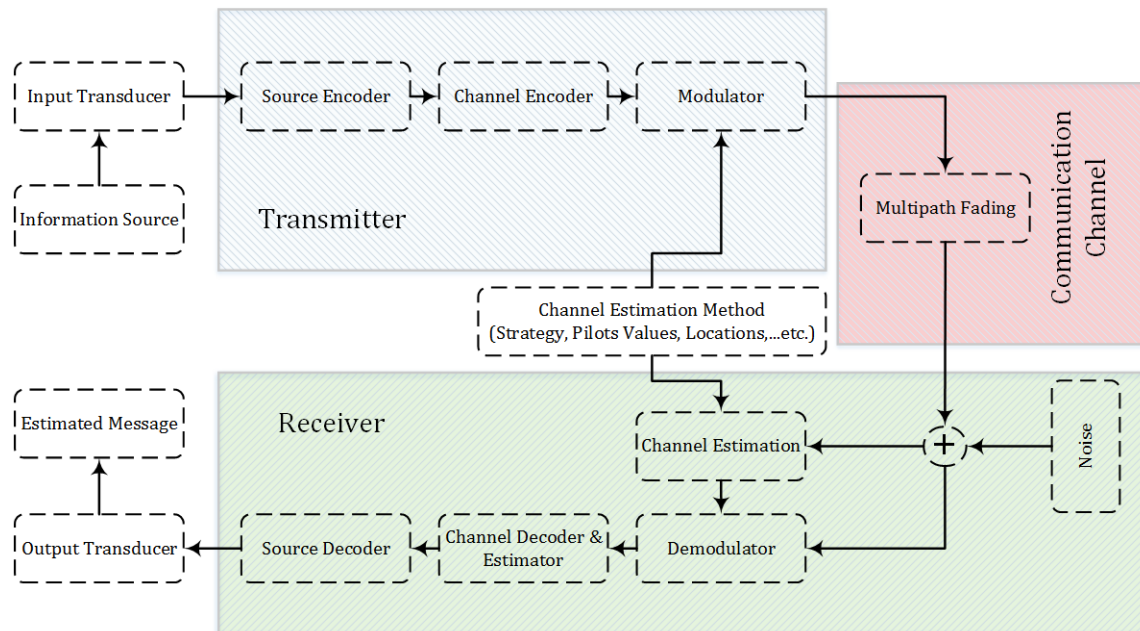


Figure 1.1: Block diagram of general DWCS

Information source may be either analog (audio or video) or digital (computer output) signal. In a Digital communication system, messages produced by a source are always converted to a sequence of binary digits (010110...). If the source output is analog, analog to digital conversion (sampling, quantization and encoding) is employed using Analog to Digital Converter (ADC).

The second stage is the source encoder. Ideally, we would like to represent the source output by as few binary digits as possible. Thus, the objective of the source encoder is to provide an efficient representation of the source output. The process of efficiently converting the source output into a sequence of binary digits is called Source Encoding or Data Compression. Examples of source encoding are Huffman Coding and Lempel-Ziv Coding [1], which use information theoretic concepts to remove redundancies present in the source output.

The third stage is the channel encoder block. The purpose of the channel encoder is to introduce, in a controlled manner, some redundancy in the binary sequence at its input; primarily to combat the effects of noise and interference over the channel. The added redundancy improves the fidelity of the received signal and increases the signal's immunity to noise. It provides the message with error detection and correction capabilities. Examples of channel encoding are single-parity check codes, convolutional coding and cyclic redundancy

check codes. Typically, channel encoding involves taking k -information bits at a time as input and in response producing a unique n -bit sequence, called the code word, as output. The amount of redundancy introduced by the channel encoder in this manner is measured by the ratio n/k . The code rate is the ratio k/n .

The fourth stage is the Modulator. Modulation is a fundamental process in any communication system and especially so in a radio system. In DWCS, the modulator's function is the translation between digital data and the electrical signal required at the input to the Radio Frequency (RF) section. The modulator can be considered as a signal sub-system that maps input data, usually binary 0 and 1, on to a modulated RF carrier for later processing, transmission and amplification by the RF section. First, the modulator maps the binary information sequence into a set of values suitable for the modulation scheme that will be used at the RF transmission stage. Second, each value in the set is assigned to its corresponding RF signal that will be used over the channel. Suppose that the coded information sequence will be transmitted one bit at a time at some uniform rate R bits/sec. The coded bits will be assigned to two values, $+1$ or -1 , then each value is assigned to two signals, $S_1(t)$ or $S_2(t)$ as illustrated in Figure 1.2, which shows a block diagram of a binary modulator.

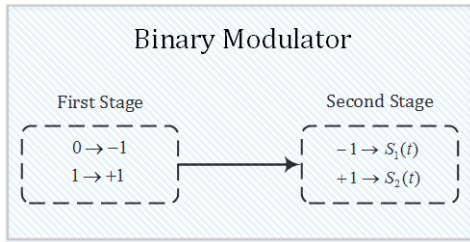


Figure 1.2: Block diagram of binary modulator

In binary modulation, two values, $+1$ or -1 , are used to map to $S_1(t)$ or $S_2(t)$. Alternatively, the modulator may transmit n coded information bits at a time by using $M = 2^n$ values, where each one of the 2^n possible n -bit sequences has its own distinct waveform $S_i(t), i = 1, 2, \dots, M$. M is called the modulation order and the modulation scheme is called M -ary modulation. Various types of waveforms can be used at the RF stage, such as phase shift keying and frequency shift keying. Thus, the modulator is characterized by the modulation order and the type of waveforms used in the process along with other modulation parameters specific to each scheme. The modulation stage decides the bandwidth occupied by the transmitted signal. Furthermore, modulation controls the robustness of the communication system to channel impairments, due both to the RF sub-systems (such as phase distortion and amplifier nonlinearity) and the RF channel (such as additive noise, multipath

fading and dispersion). Thus, a suitable choice of modulation scheme is important for the efficient operation of DWCS.

The source encoder, channel encoder and Channel State Information (CSI) aware-modulator form the integral parts of the transmitter. The reverse of all these processes is taken care of on the destination side by the receiver, which will typically contain a demodulator, channel decoder and source decoder. When an analog output is desired, the output of the source decoder is fed to the Digital to Analog Converter (DAC) to reconstruct the estimated message. Because of channel conditions and distortions, the message at the destination output is an approximation to the original source message.

1.1.1 Communication Channel and Channel Estimation

The communication channel represents the physical medium that is used to send the signal from the transmitter to the receiver such as telephone/wire-line channels, fiber-optic channels, underwater channels and wireless/free space channels. The essential feature of the wireless channel is that the transmitted signal is corrupted in a random manner by a variety of mechanisms, namely AWGN and multipath fading.

The adverse effects of the wireless communication channel are due to the channel's physical properties that are governed by the environment (obstacles, moving objects, ..., etc) between the transmitter and receiver. There are always reflections, diffraction as well as signal scattering. The overall result of these interactions are many distorted signal copies arriving at the receiver from multipaths with different attenuations, delays and phase shifts, resulting in either a constructive or destructive interaction between the copies. The phenomenon when signal power significantly diminishes due to destructive interference is known as fading. Deep fading channel is the term used to describe the channel when strong destructive inference occurs, which may eventually cause temporary communication interruption attributed to the severe drop in the Signal to Noise Ratio (SNR) associated with the channel.

Basically, wireless communication channels is associated with two types of fading effects: large and small-scale fading [2]. Large-scale fading describes the average path loss or signal power attenuation due to motion over large areas. Small-scale fading describes the dramatic variations in phase and amplitude of a transmitted signal due to the slight spatial separation variations between transmitter and receiver. A Small-scale fading with various multiple reflective paths and no line of sight component is referred to as Rayleigh fading. Therefore, a Rayleigh Probability Density Function (PDF) can statistically describe the received signal envelope. On the other hand, if line of sight propagation component is present, the envelope of the small scale fading is statistically described by a Rician PDF [2]. Those PDFs describe

the nature of the rapid changes of the wireless channel across frequency, whether it is a flat or a frequency selective channel. Another property of a wireless channel is the Doppler shift, which is a result of the movement of any object contributing to the channel's physical environment, as well as the relative motion between receiver and transmitter. The Doppler shift describes the nature of the wireless channel across time, whether it is a slow or a fast fading channel.

In order for the receiver to coherently detect the transmitted signal, accurate CSI is required at the receiver end, which is regarded as a major challenge to the optimum performance of DWCS. In the case CSI is not available at the receiver, only non-coherent detection methods could be used such as differential demodulation, which comes at the expense of about 3-4 dB loss in SNR compared with coherent detection methods [3]. Therefore, the development of CE schemes has gained a lot of attention in order to acquire accurate CSI at low complexity, to enable coherent detection and eliminate the huge loss associated with the usage of non-coherent detection. In general, CE is an arranged process between receiver and transmitter, as shown in Figure 1.1, where an agreed upon signaling instances, values, and techniques are incorporated at the modulator stage of the transmitter. This provides the receiver with means to learn the CSI and use them to successfully demodulate the received signal.

Each one of the blocks shown in Figure 1.1 is a research field on its own, and our focus in this thesis is on the CE block of DWCS. In the next Section, an overview of OFDM, currently deployed in 4G and a strong modulation candidate for the upcoming 5G [4], is introduced as CE will be studied in the context of OFDM.

1.2 Orthogonal Frequency Division Multiplexing

OFDM is a multicarrier modulation technique that received great attention from the academia and industry over the past decade. The motive behind such interest, is the special characteristics that OFDM has, such as resistance against multipath propagation, spectral efficiency, low-complexity equalization and efficient employment using the Fast Fourier Transform (FFT) and Inverse FFT (IFFT) pair [5]. OFDM systems convert a frequency selective channel into a group of flat fading channels, which can be equalized by simply employing a one-tap equalizer [6]. Therefore, equalizer design can be greatly simplified by using OFDM, while enabling rather high data rates. However, the performance of OFDM systems is affected by both frame synchronizer and channel estimator, for which several methods have been proposed for timing synchronization [7–11].

OFDM is currently implemented by several commercial standards, such as Long Term

Evolution-Advanced (LTE-A) [12], the Second-Generation Digital Video Broadcasting-Terrestrial (DVB-T2) [13], Worldwide Interoperability for Microwave Access (WiMAX) [14] and Wireless Local Area Networks (WLAN) IEEE 802.11 [15]. Therefore, OFDM is one of the technologies that will surely be carried over to the upcoming 5G wireless communications standard [4], due to its numerous advantages.

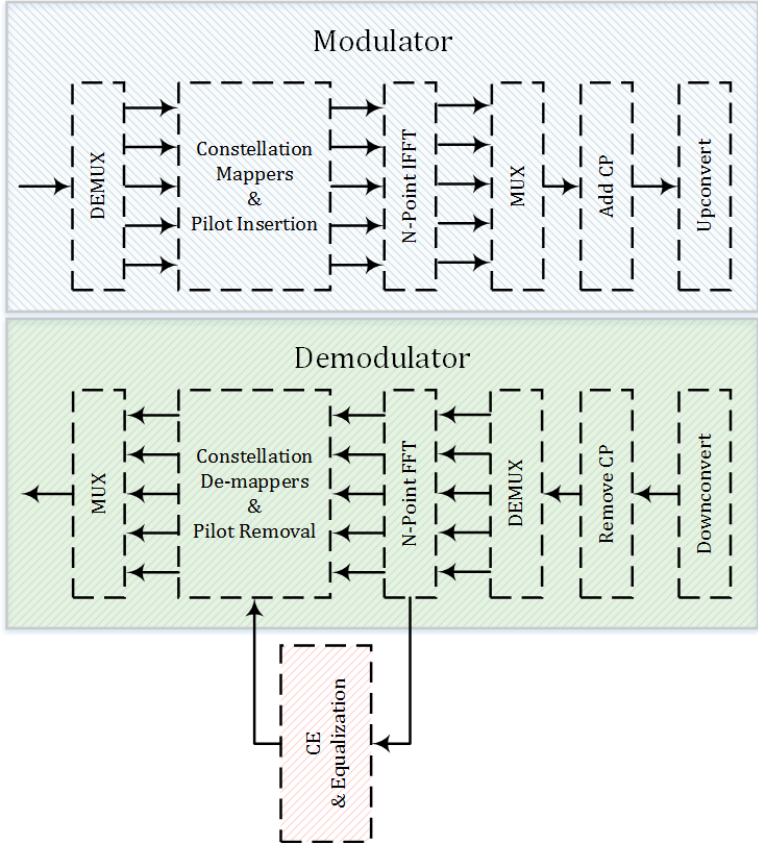


Figure 1.3: Block diagram of general OFDM modulator and demodulator

Figure 1.3 shows a block diagram of the general OFDM modulator and demodulator, which will be further elaborated in Chapter 2. In the next Section, Massive MIMO, which is considered as a vital technology in the deployment of 5G, is introduced in order to demonstrate the role of CE in the performance of future DWCS.

1.3 Multiple Input Multiple Output

During the last decade, mobile and fixed data traffic has grown exponentially. This is due to the rapid growth of smartphones, tablets, laptops, and many other wireless data demanding equipments. Moreover, it is anticipated that the demand for wireless data traffic will further

increase [16]. During 2017, Cisco measured the global mobile data traffic at 17 exabytes per month and they are expecting it to grow to 49 exabytes per month by 2021, which is about a 3-fold increase over 2017. In addition, the number of mobile devices and connections were measured at 8.6 billion devices and is also expected to increase to 11.6 billion by 2021. Thus, new technologies are required to accommodate this demand. The key factor to consider in wireless data traffic is throughput, which is defined as,

$$\text{Throughput (bits/sec)} = \text{Spectral Efficiency (bits/sec/Hz)} \times \text{Bandwidth (Hz)}.$$

Clearly, some new technologies that can enhance the spectral efficiency or increase the bandwidth or both should be employed in order to improve the throughput. Since bandwidth is a fixed resource, research has focused on techniques which can increase the spectral efficiency. Using multiple antennas at the receiver or transmitter or both is a recognized method to improve the spectral efficiency. The major fundamental challenge for reliable wireless communication is signal attenuation by shadowing, due to large obstacles between transmitter and receiver, and by fading, due to multipath propagation. Transmission with MIMO is a famous diversity scheme known to improve the reliability of DWCS. Moreover, a multiplexing gain can be achieved by using MIMO to send multiple signals out, which drastically enhances the communication capacity. Therefore, MIMO systems have received major attention during the past decades, and are utilized in numerous current wireless standards (e.g., LTE-Advanced, 802.16m), and are considered for future DWCS.

The focus to employ spatial multiplexing gain has been shifted from MIMO to Multi User-MIMO (MU-MIMO), where a MIMO Base Station (BS) serves multiple users simultaneously. Since MU-MIMO systems have the ability to achieve spatial multiplexing gain even with single antenna users [17], User Equipments (UEs) with low-cost and small physical size requirements can be designed. Moreover, MU-MIMO systems are able to realize all MIMO systems benefits. In addition, it overcomes most of the MIMO propagation limitations, such as ill-behaved channels through using scheduling techniques. Furthermore, the problem of line of sight propagation in MIMO systems, which causes major performance degradation, does not effect MU-MIMO systems. Hence, there has been significant interest in MU-MIMO [17–22].

The tradeoff between implementation complexity and system performance is always present. MU-MIMO benefits come at the cost of multiuser interference and complex user scheduling, while requiring fast and accurate CE schemes. On the other hand, increasing the number of BS antennas increases the degrees of freedom in the system. Thus, in the same time/frequency resource, more users are able to communicate simultaneously, and that

results in a huge sum throughput. The downside of large antenna arrays is that regular signal processing schemes, such as Maximum Likelihood Detection (MLD), become excessively complex because of the high dimensionality of the received signal.

Marzetta demonstrated in [23] that simple linear processing becomes nearly optimal when using a huge number of antennas at the BS relative to the number of active users. More specifically, as the number of antennas at the BS grows large, the effects of uncorrelated noise, fast fading and intra-cell interference tend to disappear, even with simple Maximum Ratio Transmission (MRT) in the Downlink (DL), from BS to users, or Maximum Ratio Combining (MRC) in the Uplink (UL), from users to BS. MU-MIMO systems, serving tens or more of users concurrently in the same time/frequency resource with a hundred or more antennas at the BS, are identified as very large MU-MIMO or Massive MIMO. The main advantages of Massive MIMO systems are high communication reliability, huge energy and spectral efficiency, and simple signal processing. Furthermore, a massive BS antenna array does not have to be physically large. For example, consider 128 antennas contained in a cylindrical array, arranged in four circles with 16 dual-polarized antennas per circle. The distance between adjacent antennas at 2.6 GHz would be about 6 cm, which is half a wavelength. Thus, such an array would occupy a physical size of only 28cm×29cm [24]. Moreover, it is expected that each antenna in Massive MIMO would be contained in an inexpensive unit with low-power amplifier and simple processing.

The aforementioned benefits of Massive MIMO can be fully realized only if perfect CSI are available at the BS and users. Nevertheless, in practice, CSI has to be acquired. The BS obtains CSI through UL training to pre-code the signals in the DL to resist channel effects, and to detect signals transmitted from the users in the UL. Moreover, for each user to coherently detect transmitted signals from the BS, they may require partial knowledge of CSI, which can be obtained through DL training. It was shown in [25] that each user's transmission power can be reduced by the number of BS antennas in the case of perfect CSI, and can be reduced by the square root of the number of BS antennas in the case of imperfect CSI, while using simple linear receivers, which demonstrates the effect of CE accuracy on the achievable rates by the system.

One of the requirements for Massive MIMO is to be backward compatible [26], meaning that techniques developed for current MIMO-OFDM systems would be utilized in future DWCS. Hence, the work in this thesis targets current MIMO-OFDM systems. In the next Section, an overview of the relevant developments in the area of CE techniques, classification, evaluation criteria, and state-of-the-art research is provided.

1.4 Review of Channel Estimation Techniques

A receiver has to accomplish two important tasks before information symbols could be extracted from the received signal: obtain CSI, and use them for channel equalization. In the literature, most CE methods are categorized based on their computational complexity, required observation window, spectral efficiency and estimation accuracy. A practical and efficient estimator is one that minimizes complexity and observation window size, while exploiting spectral efficiency and accuracy. Nevertheless, realizing all such contradicting goals into one single scheme is generally not possible. Therefore, the system design is a trade-off between these objectives based on Quality of Service (QoS) requirements and the available system resources. For most real-world applications, a practical trade-off can be realized by using training symbols, denoted as pilot or reference symbols, where specific subcarriers at the transmitter side are modulated using known symbols, and later used at the receiver side for CSI estimations and CE purposes [27–34].

Pilot designs and interpolation techniques have been widely studied in the literature. Two types of pilot designs have been adopted, namely, comb pilots and block pilots [35], while other 2-D pilot designs were discussed in [28]. Comb pilots-based CE and time/frequency plane scattered pilots generally achieve better performance than block type pilot design in tracking the variations of fast fading channels in time. In general, pilot-based CE algorithms in OFDM systems are based on Least Square Estimation (LSE or LS) to acquire Channel Frequency Responses (CFR). LSE is relatively simple, since it does not consider relevant channel information, and hence, is easily affected by noise [36]. Therefore, filtering techniques are used to enhance the estimation by reducing the noise effect on the CFRs. Noise reduction filters are classified into two categories based on their incorporation of channel’s statistical information in their design. There is simple, yet, powerful moving average filters and the more complex Linear Minimum Mean Square Error (LMMSE)-based filters such as 2-D Wiener filter, which was first derived in [37]. The major difference between the two is that LMMSE-based filters are more computationally complex compared to moving average filters. In the literature, there has been attempts at finding lower complexity LMMSE-based filtering techniques at the expense of processing latency, since they are iterative-based [38–40]. Generally, optimal 2-D Wiener filtering is followed by optimal interpolation using 2-D Wiener interpolation to find the CFRs for the rest of the time/frequency plane. Hence, robust channel statistics independent interpolators with comparable performance to that of 2-D Wiener interpolator are also needed, in order to further reduce the complexity of the whole CE system.

Linear interpolation, second-order polynomial interpolation, spline, lowpass interpolation

and transform domain interpolation for comb pilots were studied in [32, 35], and parametric estimation and least-square-fitting were presented in [41] and [42], respectively. In [43], the authors presented the performance analysis and design of a linear interpolator followed by a 2-D Moving Average-Finite Impulse Response (MA-FIR) filter for a rectangular pilot grid design. In [28], a diamond shape lowpass filter was proposed that is implemented in the transform domain using 2-D Discrete Fourier Transform (DFT)/Inverse DFT (IDFT), which has high computational complexity. It is worth noting that when a nonlinear interpolator is used, the pre-interpolation channel estimates at pilots positions are replaced by post-interpolations estimates obtained from the fitting polynomial [42].

Figure 1.4 shows comb-type pilots distribution in a time/frequency plane in LTE-A [12], where the pilots constitute 4.8% of the total time/frequency resource, which represents a reduction in spectral efficiency. For some other systems, such as IEEE 802.11n, pilots occupy 7.1% of the total time/frequency resource, which means reducing the spectral efficiency even more. Additionally, if channel coefficients over successive OFDM symbols are uncorrelated, as it is the case with burst transmission systems, pilots are then required in every OFDM symbol, which means greater reduction in spectral efficiency. Hence, many algorithms have been developed to obtain the CSI blindly, without the use of any pilots, by extensively processing the received data symbols [44–54] to estimate CSI. Consequently, such algorithms enhance the spectral efficiency at the cost of higher computational complexity.

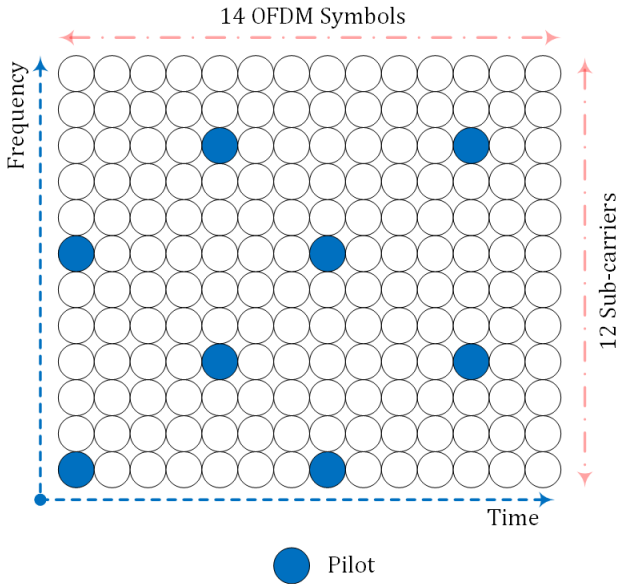


Figure 1.4: Time-frequency resource grid of LTE-A example

In the literature, blind CE is a major research area in wireless communication [28–34, 44–55]. The key idea behind the design of numerous blind estimators is the usage of a Constant

Modulus (CMM) constellation, such as M -ary Phase Shift Keying (MPSK), to modulate all subcarriers [45–48], and no pilots are required in such schemes. However, such blind techniques prevent the usage of spectrally efficient modulation techniques, such as Quadrature Amplitude Modulation (QAM), hence, indirectly reducing the system’s spectral efficiency. Hence, a more accurate description of such CE schemes would be conditionally-blind, to differentiate them from fully and semi-blind schemes. In fully blind systems, there are no restrictions on the modulation order or type, and no pilots are needed. In semi-blind schemes, CE is performed using both, the data symbols and pilots [53–55]. In [56], a novel conditionally-blind One Shot Blind Channel Estimator (OSBCE) was introduced for Single Input Single Output (SISO) OFDM systems. The system is based on modifying the conventional OFDM symbol structure, by placing MPSK data symbols instead of pilot subcarriers, and modulating adjacent subcarriers using M -ary Amplitude Shift Keying (MASK). Since no phase is associated with the MASK symbol, it can be considered as an imperfect CFR with respect to the MPSK symbol. Therefore, the MPSK symbol can be immediately decoded, and used to estimate the CFR. Since the proposed OSBCE in [56] restricts the modulation type for only a small number of the subcarriers, it is spectrally efficient. Moreover, the authors showed that the proposed OSBCE outperforms the subspace estimator [57] for the entire SNR test range, with drastically smaller observation window.

Another important performance measure used to compare different CE techniques is computational complexity. In general, blind-based CE schemes have higher computational complexity than pilot-based CE schemes [32, 50]. This is due to the extreme computational complexity resulting from extensively searching over the solution space [49], or due to the iterative nature of such techniques [50–52]. [49] presents a blind-based CE system, which has comparable complexity to pilot-based CE at high SNRs, however, in practical scenarios, such condition is usually not the case.

Moreover, the observation window size is another critical criteria in CE systems design, and it specifies the number of OFDM symbols needed to acquire the CSI estimates. CE techniques that demand large observation window are based on the assumption that the channel is invariable over the observation period [45, 46, 48, 50], which is an acceptable assumption for slow flat fading channels. However, this is not essentially the case for frequency selective fast fading channels. Usually, CE techniques that require an observation window of one OFDM symbol perform better than estimators with several OFDM symbols observation window [49]. Such CE schemes are referred to as one-shot estimators.

The accuracy of CE schemes is usually assessed using Mean Squared Error (MSE). Theoretically, MSE should be appropriately low to minimize the reduction in Bit Error Rate (BER) resulting from CE errors [58]. Since pilot-based CE schemes have satisfactory effect

on the BER by offering reliable CFR estimates, their MSE performance is regularly used in the literature as a benchmark for comparison [27, 47, 58].

The previous review is focused on SISO-OFDM systems. The major difference between SISO-OFDM and MIMO-OFDM in terms of CE is the fact that the received signal is a superposition of signals from several transmit antennas. Therefore, SISO-OFDM CE techniques cannot be directly applied in MIMO-OFDM [59]. There are two major strategies for CE in MIMO-OFDM [43]. The first strategy, which is widely used in MIMO-OFDM based wireless systems [60], is to send pilots from only one transmit antenna during a signaling period while the other transmit antennas are nulled or turned off [61–63]. As a result, the receive signal at pilot locations is reduced to a single transmitting antenna case, and the CFR for each transmit antenna can be estimated using the SISO-OFDM techniques. In [64], the authors investigate optimum pilot design for MIMO-OFDM, which achieves optimum MSE performance. Since the pilot design in [64] uses nulling, the method is also proposed for SISO-OFDM in [65]. The nulling strategy is powerful, yet, it has some drawbacks, such as reducing the spectral efficiency and increasing the Peak Average Power Ratio (PAPR) [66] by reducing the signal’s total Root Mean Square (RMS) value.

The other strategy for CE in MIMO-OFDM does not null any of the transmit antennas, and pilots are simultaneously transmitted from all antennas. In this case, pilot sequences are designed and coded to insure that they are separable at the receiver side. Generally, such methods involve lots of computational complexity due to the matrix inversion involved [59, 67]. If the channel is assumed to be quasi-static across two successive OFDM symbols, complexity can be reduced by using Space Time Block Coded (STBC) pilots. In [68] and [69], pilots from multiple transmit antennas are designed based on Alamouti’s scheme [70]. Other sequences can also be used for the same purpose [60, 71, 72]. As a result, CFR estimation can be performed at the receiver without matrix inversion. Nevertheless, this method is limited by the requirement for the channel to be fixed over several successive OFDM symbols that are equal in number to the the number of transmit antennas. Otherwise, the system performance is significantly degraded. In addition to the reduced complexity, optimum MSE performance [59] is achieved due to the orthogonal design of the pilot symbols.

In practice, the leading standards such as LTE-A [12], WiMAX [14] and DVB-T2 [13] are using pilot-based CE, which indicates that compromising the spectral efficiency is preferred in the pursuit of the other advantages. Consequently, it is necessary to investigate pilot-based CE schemes to obtain sub-optimal channel estimates compared to the optimal 2-D Wiener system, at a reduced computational complexity level, while maintaining a minimum MSE threshold for a desired QoS. Since LTE-A systems, which mainly use pilot-based CE with nulling [60], are the focus of this work, the LTE-A MIMO-OFDM system is regarded

as a SISO-OFDM system.

1.5 Problem Statement and Justification

Although pilot-based system reduces spectral efficiency, it does fulfill most of the other CE requirements such as: estimation accuracy, complexity and observation window size. Previous related works in the literature use the Wiener filter for both noise filtering and interpolation, which is the optimum filter and interpolator design [36, 73–76]. Nevertheless, the associated complexity of using 2-D Wiener filter for both estimation and interpolation is still high [77]. Therefore, the first objective of the thesis is to investigate less complex versions of 2-D Wiener filtering implementation that can be applied to the current 4G LTE, and can be carried forward to 5G. Thus, a new lower complexity implementation scheme is presented, which uses 2×1 -D Wiener instead of 2-D Wiener to filter the noisy CFR LS estimates at pilots locations only, and then use cubic spline interpolation for data symbols locations. Performance evaluation and complexity analysis in estimating LTE-A Cell-specific Reference Signals (C-RS) and UE-specific Reference Signals (UE-RS) are reported and compared to different variations of Wiener and moving average filters, with different interpolation techniques. In addition, to eliminate the need to store pilot locations using look-up tables, we analyze pilot locations and provide equations that give C-RS locations based on the related parameters.

In addition, the second objective is to test the proposed CE scheme in full LTE-A system to measure throughput performance for some LTE-A test cases, which were specified by the 3rd Generation Partnership Project (3GPP) [60], to validate the proposed scheme's performance in real-life application.

Moreover, the usage of 2-D DFT/IDFT in pilot-based CE incurs high computational complexity [28]. Therefore, the third objective of this work is to investigate the implementation of a less computationally complex filter and interpolator that uses 2×1 -D FFT/IFFT, instead of 2-D DFT/IDFT, in LTE-A OFDM CE. 1-D FFT is deployed to find the noisy Channel Impulse Response (CIR) from the LS estimated CFRs, filter the CIR based on the number of channel taps, then find the CFRs at data symbols locations by zero-padding and using 1-D IFFT. Performance and complexity comparisons with other techniques, especially with 2-D DFT/IDFT, are reported.

Since none of the blind-based techniques reported in the literature, to the best of our knowledge, succeeds in resolving the contradicting CE design objectives perfectly, blind CE remains one of the extensively addressed topics in wireless communication. Although the work in [56] showed that the proposed OSBCE can be efficiently and effectively utilized

in practical systems such as LTE-A standard, it did not take into consideration the Single Input Multiple Output (SIMO) and MIMO cases, which are being deployed in the current 4G, and are strong candidates for future DWCS. Therefore, the fourth objective of the thesis is to develop the novel OSBCE technique for SIMO and MIMO systems, describe the system model and report the performance and potential of this new OSBCE for the different SIMO and MIMO variations.

Moreover, the OSBCE technique for MIMO-OFDM will first be developed for an LTE-A resource grid configuration, which is not optimal in terms of MSE performance from the OSBCE operation point of view. Therefore, the fifth objective would be to propose resource grid configurations, which enhances the MSE performance of the OSBCE for MIMO-OFDM.

1.6 Thesis Contributions

The major contributions of the thesis are summarized below:

- MSE mathematical expressions for LS estimation, Equal Weight Averaging (EWA), currently used by manufacturers such as Samsung, and Wiener filters are derived and presented.
- A pilot-based lower complexity channel estimator for C-RS and UE-RS in LTE-A DL system is proposed based on using a hybrid Wiener filter, where 2×1 -D Wiener, instead of 2-D Wiener, is used to filter the noisy CFR LS estimates at pilot locations only and is followed by cubic spline, instead of 2-D Wiener, interpolation for data symbol locations. Moreover, equations that describe C-RS locations for pilots insertion and extraction are given, which eliminates the need for look-up tables. Analytical results wherever possible and, in general, simulation results are presented.
- Validate throughput performance using the proposed pilot-based system in full end-to-end LTE-A system, and report the throughput measurements for successful LTE-A test cases with different Transmission Modes (TM), and different Reference Channels (RC) at a number of SNR points that were all specified by 3GPP [12].
- 2×1 -D FFT/IFFT for filtering and interpolation, in place of 2-D DFT/IDFT, is proposed as a less computationally complex overall system to de-noise the CIR in time domain and interpolate the CFRs at data locations by oversampling. Performance and complexity comparisons with other techniques, especially with 2-D DFT/IDFT, are reported.

- Develop the new OSBCE scheme for SIMO and MIMO systems, and evaluate the performance for different system and channel configurations in terms of MSE, and symbol and bit error rates using computer simulations. In general, numerical results are presented and discussed for the different implementations of SIMO-OFDM and MIMO-OFDM.
- Propose new resource grid configurations that enhances the MSE performance of the developed OSBCE for MIMO-OFDM, and compare its performance to the equivalent OSBCE variation for MIMO-OFDM in different channel conditions. Different configurations of OSBCE are presented, namely across frequency, time and time/frequency.

1.7 Thesis Organization

In Chapter 2, the problem of lower-complexity pilot-based CE techniques is addressed. LTE-A OFDM DL system, and MSE mathematical explicit expressions for LS estimation, EWA, and Wiener filters are presented and derived, respectively. In addition, equations that describe C-RS locations for pilots insertion and extraction are given. A hybrid lower-complexity Wiener filter for pilot-based CE for C-RS and UE-RS in LTE-A DL system is proposed, and tested under various channel conditions. Simulations in real-life LTE-A scenarios are carried out to confirm that the proposed CE sub-optimum scheme produces reliable CFR estimates at a much lower complexity. The optimal noise filter is shown to be composite of both EWA and Wiener filtering, where the lower bound is a function of both SNR and the channel statistics. Moreover, 2×1 -D FFT/IFFT filtering and interpolation system is proposed for CE, instead of 2-D DFT/IDFT, and performance and complexity comparisons are provided. Numerical results are reported, and discussions of the performance of the sub-optimum filter and 2×1 -D FFT/IFFT in LTE-A are given.

In Chapter 3, a novel spectrally efficient OSBCE, first introduced to SISO-OFDM in [56], is developed for SIMO-OFDM system. The approach is illustrated using various examples in both dimensions (time and frequency), and performance is verified in various channel conditions in terms of Symbol Error Rate (SER) and MSE using computer simulations, with the benchmark set by the pilot system [43]. Discussions of numerical results are given with focus on the effect of the increased number of antennas on the performance of the OSBCE, and the effect of the separation distance between MPSK and MASK symbols.

In Chapter 4, different OSBCE configurations are developed for MIMO-OFDM systems using LTE-A pilots configuration, where two different schemes are introduced, namely Mode 1 and Mode 2. In Mode 1, MASK symbols are coded and transmitted multiple times across

the resource grid as a form of transmit diversity. This facilitates the extraction of the associated MASK symbol per transmit antenna, which is needed for the OSBCE operation. When MPSK symbols are transmitted from one transmit antenna, other antennas will be nulled. In Mode 2, no coding is required, and the RE locations where MPSK and MASK symbols are transmitted from one antenna, are nulled at all other transmitting antennas. Discussions of numerical results are presented by comparing the MSE performance between the different modes of OSBCE for MIMO and the pilot-based MSE performance as the number of receive antennas increases.

In Chapter 5, new RG configurations, instead of the LTE-A configurations from Chapter 4, that enhances the MSE performance of the OSBCE for MIMO-OFDM are proposed. The criteria for the new configurations is to minimize the separation distance within the resource grid between the MASK and MPSK symbols of the OSBCE system. The proposed grid configurations transmit the MPSK and MASK symbols next to each other across frequency, time, or time and frequency, in order to improve the MSE performance. Discussion of numerical results are given with comparison to the equivalent OSBCE variation for MIMO-OFDM using LTE-A grid.

The thesis is concluded in Chapter 6 by summarizing the work carried out, contributions made and conclusions from the results obtained. Also, we outline areas for further research in the light of the needs of modern reliable DWCS and the work done in the thesis.

Chapter 2

Hybrid Lower-Complexity Filtering Schemes for Pilot-Based Channel Estimation¹

2.1 Introduction

The objective of this Chapter is to propose and examine new pilot-based lower complexity CE schemes. The optimum pilot-based CE system is dependent on 2-D Wiener filtering and interpolation, which has high computational complexity. Hence, lower complexity filters and interpolators are needed for future DWCS, and it is also necessary to test the proposed

¹Related Publications:

1. M. Zourob and R. Rao, "2×1-D Fast Fourier Transform Interpolation for LTE-A OFDM Pilot-Based Channel Estimation," 2017 International Conference on Electrical and Computing Technologies and Applications (ICECTA), Nov. 21-23, 2017, pp. 1-5. (**Best Student Paper Award - Second Place**)
2. M. Zourob and R. Rao, "Hybrid Lower-Complexity Wiener Filter for Pilot-Based Channel Estimation for C-RS in LTE-A DL System," Mobile Networks and Applications Journal (MONET by Springer), 2017, pp. 1-19.
3. M. Zourob and R. Rao, "Lower-Complexity Wiener Filtering for UE-RS Channel Estimation in LTE DL System," 2017 International Symposium on Wireless Systems and Networks (ISWSN), Nov. 19-22, 2017, pp. 1-5.
4. M. Zourob and R. Rao, "A Low-Complexity C-RS-Aided Channel Estimation Scheme for LTE Downlink System," 2017 International Conference on Smart Grid and Internet of Things (SGIoT), Jul. 11-13, 2017, pp. 1-10.
5. M. Zourob and R. Rao, "Reduced-Complexity Implementation Scheme for OFDM Channel Estimation," 2017 IEEE 30th Canadian Conference on Electrical and Computer Engineering (CCECE), May. 1-3, 2017, pp. 1-4.

systems in practical scenarios such as LTE-A. Therefore, the Chapter starts by introducing the LTE-A OFDM DL system model, with focus on two types of pilot signals: C-RS and UE-RS. Next, equations that describe C-RS locations for pilots insertion and extraction are given, in order to minimize storage requirements for look-up tables. Afterwards, MSE mathematical explicit expressions for LS estimation, EWA, and Wiener filters are derived and presented. Thereafter, some common interpolators are presented, and the 2×1 -D FFT/IFFT is proposed, as a less computationally complex alternative, for CE instead of 2-D DFT/IDFT. Next, a hybrid pilot-based CE system is proposed, based on using 2×1 -D Wiener filter for noise filtering at pilot locations only, and cubic spline interpolation for data symbol locations. In general, numerical analysis of MSE performance and complexity comparison are provided. Finally, simulations in real-life LTE-A scenarios are carried out to confirm the feasibility of the proposed CE scheme, before the Chapter is concluded.

2.2 LTE-A OFDM DL System and Channel Model

Data is transmitted between one BS and one UE in the form of packets called radio frames. 3GPP LTE-A supports two radio frame structures; one is applicable to both full duplex and half duplex Frequency Division Duplex (FDD) system, which is shown in Figure 2.2. The other is applicable to Time Division Duplex (TDD). Each radio frame consists of 10 sub-frames and spanning 10 milliseconds in time. Each sub-frame occupies 1 millisecond in time and consists of two time slots. The OFDM time/frequency plane is called a Resource Grid (RG). Each 12 sub-carriers and 14 OFDM symbols are labeled as a single Resource Block (RB) and contains $12 \times 14 = 168$ Resource Elements (RE).

Different reference signals, or pilots, are transmitted in LTE-A system for different purposes. C-RS are one type of pilots and they are transmitted in all DL subframes on antenna ports 0,1,2 and 3. Antenna ports do not correspond to physical antennas, but rather are logical entities distinguished by their reference signal sequences. C-RS are used by UE for channel estimation, cell selection, cell re-selection and handover. Figure 2.1 shows C-RS distribution for ports 0, 1, 2, and 3. The white-colored REs are used for data transmission, and the colored REs are occupied by C-RS from different ports. The grey-colored REs denote unused REs, because locations of REs used for C-RS transmission on any antenna port shall not be used for transmission by other antenna ports and are set to zero. Thus, the received RE at any of the C-RS locations from port q , $q \in \{0, 1, 2, 3\}$, would represent the pilot transmitted by one port only. Therefore, at C-RS locations, the system can be considered as a SISO system.

The other type of reference signals considered in this Chapter are UE-RS. UE-RS are

transmitted on DL antenna ports 5 and 7-14 and they are used to derive the channel estimates to demodulate the data, and enable beamforming for data transmissions to specific UEs. Moreover, UE-RS are used for pre-coding wherein the UE-RS are also pre-coded in the same manner as the data. UE-RS are transmitted within the resource blocks allocated only to a specific UE. There are different pilot distributions based on the antenna port number [60]. UE-RS, although different from C-RS, but have the same basic properties in terms of modulation type and order. Therefore, for simplification, discussion will focus on C-RS, however the analysis and results are also applicable to UE-RS. We will be using ‘‘C-RS’’ and ‘‘pilots’’ interchangeably from here on and we will consider the number of ports to be equal to the number of transmitters throughout the Chapter.

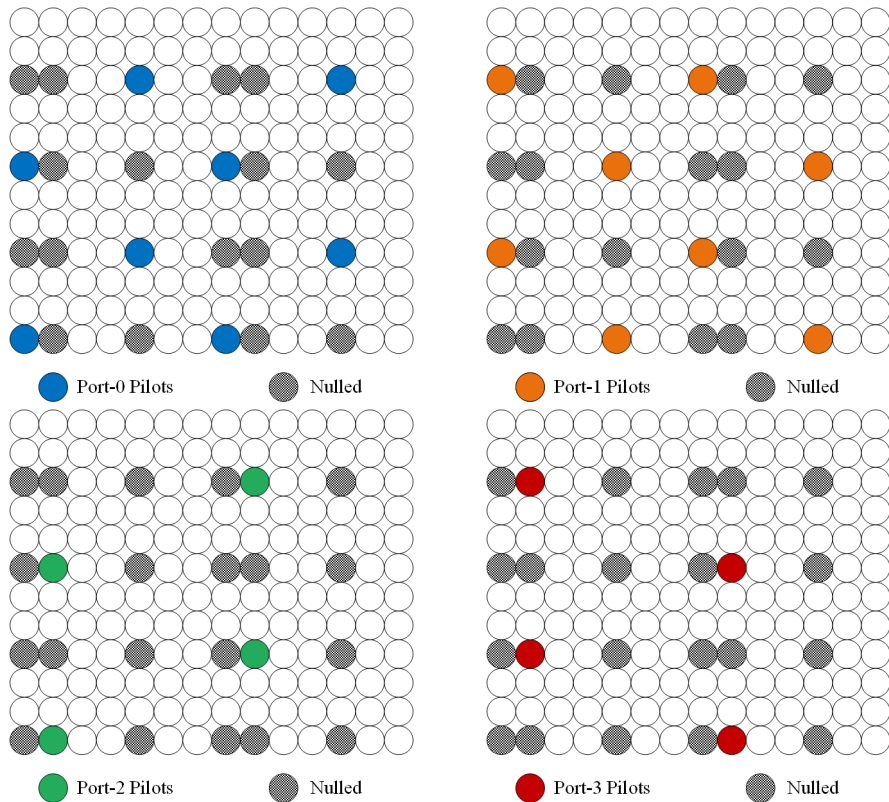


Figure 2.1: Mapping of C-RS in LTE-A – Normal CP

Consider an $N_T \times N_R$ LTE-A OFDM system, where N_T and N_R describe the number of transmit and receive antennas, respectively, with N sub-carriers modulated by a sequence of N complex data symbols at each transmit antenna $\mathbf{a}^s = [A_0^s, A_1^s, \dots, A_{N-1}^s]^T$ where $s \in \{1, 2, \dots, N_T\}$. The data symbols in \mathbf{a}^s are selected uniformly from a general constellation such as MPSK with modulation order M_P . It is worth noting that the average symbol power is set to $1/N_T$ to normalize the total transmit power from both antennas to unity. In pilot-based practical OFDM systems [12], $k_{N_P}^s$ of the subcarriers at $\ell_{N_P}^s$ OFDM symbols

are reserved for pilot symbols, which are used for channel estimation and synchronization purposes. $P^s = (k_P^s, \ell_P^s)$, where $k_P^s = \{k_1^s, k_2^s, \dots, k_{N_P}^s\}$ and $\ell_P^s = \{\ell_1^s, \ell_2^s, \dots, \ell_{N_P}^s\}$, are the set of indices for pilot-carrying REs within transmitter's s RG.

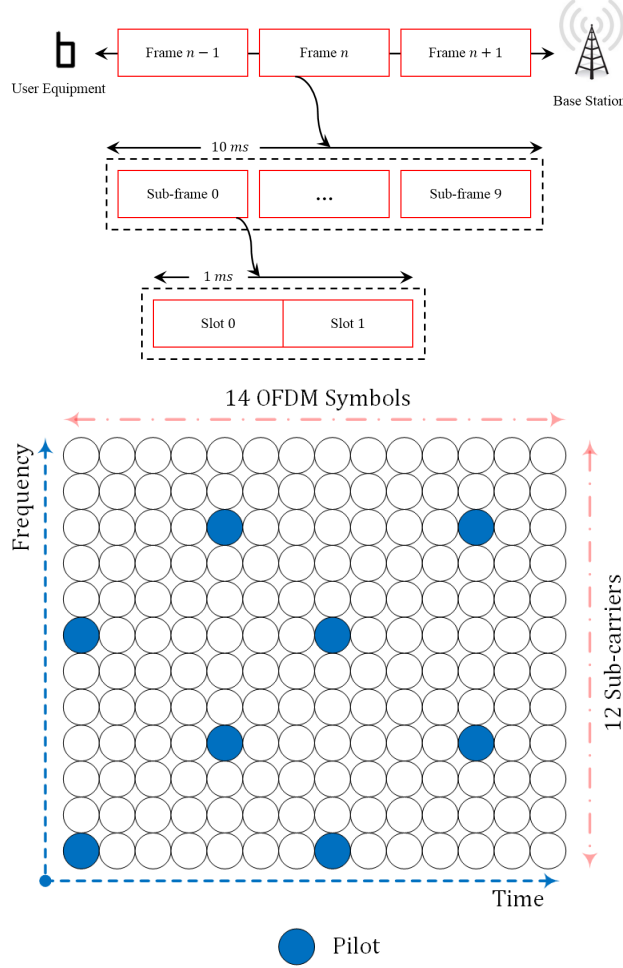


Figure 2.2: Frame Structure in LTE-A FDD

The modulation process at each transmit antenna can be implemented efficiently using N -point IFFT. The output of the IFFT process during the ℓ^{th} OFDM symbol is given by $\mathbf{x}(\ell) = \mathbf{F}^H \mathbf{a}(\ell)$; where \mathbf{F} is the normalized $N \times N$ FFT matrix, and hence, \mathbf{F}^H is the IFFT matrix. The elements of \mathbf{F}^H are defined as $F_{\hat{k}, k} = (1/\sqrt{N})e^{j2\pi\hat{k}k/N}$ where \hat{k} and k denote the row and column indices $\hat{k}, k \in \{0, 1, \dots, N-1\}$, respectively. To eliminate Inter Symbol Interference (ISI) between consecutive OFDM symbols and maintain the subcarriers' orthogonality in frequency selective multipath fading channels, a Cyclic Prefix (CP) of length N_{CP} samples no less than the channel maximum delay spread (L_h) is formed by copying the last N_{CP} samples of \mathbf{x} and appending them in front of the IFFT output to compose the OFDM symbol with a total length $N_t = N + N_{CP}$ samples and a duration of T_t seconds.

Then, the complex baseband OFDM symbol during the ℓ^{th} signaling period $\tilde{\mathbf{x}}$ is upsampled, filtered and up-converted to a radio frequency centered at f_c before transmission through each transmit antenna.

Table 2.1: Channel delay profiles used in simulation

Delay Profile	Doppler Spread (Hz)	Max. Excess Tap Delays (ns)
EPA	5	410
EVA	70	2510
ETU	300	5000

At the receiver front-end, the N_R received signals are down-converted to baseband and sampled at a rate $T_s = T_t/N_t$. In this work, we assume that the channel between each pair of transmit and receive antennas is composed of $L_h + 1$ independent multipath components each of which has a gain $h_m \sim \mathcal{CN}(0, 2\sigma_{h_m}^2)$ and delay $m \times T_s$, where $m \in \{0, 1, \dots, L_h\}$. In this Chapter, channel taps are set to represent different channel delay profiles that are outlined by 3GPP [60] and are shown in Table 2.1. Figure 2.3 shows a block diagram of the pilot-based SISO OFDM modulator and demodulator. The modulator and demodulator blocks of an OFDM system are available at each transmit and receive antennas, respectively, in a MIMO OFDM system.

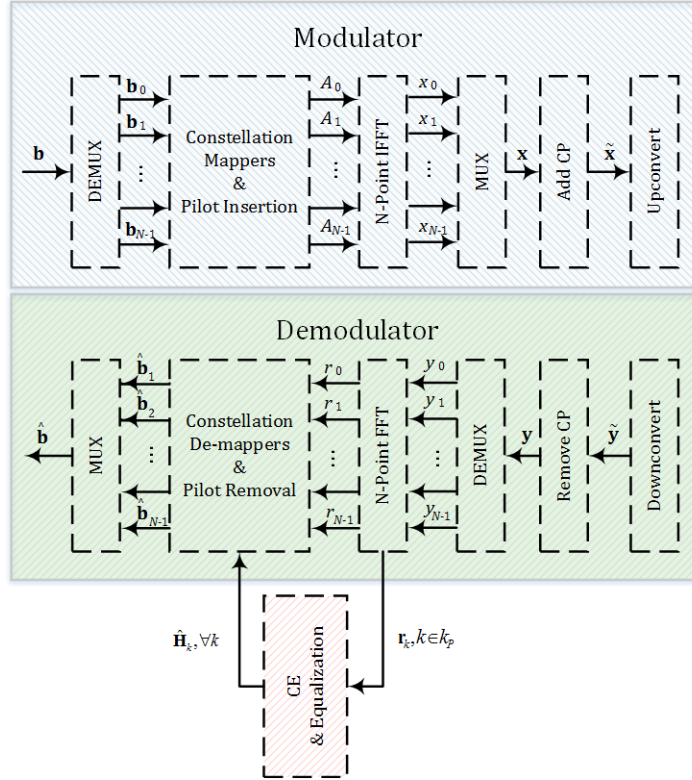


Figure 2.3: Block diagram of SISO OFDM modulator and demodulator

Then, the received signal for the ℓ^{th} OFDM symbol after discarding the first N_{CP} CP samples, and computing the FFT can be expressed as,

$$\mathbf{r}^v(\ell) = \sum_{s=1}^{N_T} \mathbf{H}^{s,v}(\ell) \mathbf{a}^s(\ell) + \mathbf{n}^v(\ell) \quad (2.1)$$

where $v \in \{1, 2, \dots, N_R\}$, $\mathbf{r}^v(\ell) = [r_{0,\ell}^v, r_{1,\ell}^v, \dots, r_{k,\ell}^v, \dots, r_{N-1,\ell}^v]^T$, $\mathbf{r}^v(\ell) \in \mathbb{C}^{N \times 1}$, $\mathbf{n}^v(\ell)$ denotes AWGN vector at receiver v , whose samples are independent and identically distributed (i.i.d.) $\eta_{k,\ell}^v \sim \mathcal{CN}(0, 2\sigma_\eta^2)$, and $\mathbf{H}^{s,v}(\ell)$ denotes the CFR between transmitter s and receiver v , which is defined as

$$\mathbf{H}^{s,v}(\ell) = \text{diag} \{ |H_{0,\ell}^{s,v}, H_{1,\ell}^{s,v}, \dots, H_{k,\ell}^{s,v}, \dots, H_{N-1,\ell}^{s,v}| \} \quad (2.2)$$

where

$$H_{k,\ell}^{s,v} = \sum_{m=0}^{L_h} h_m e^{-j2\pi mk/N}. \quad (2.3)$$

We can rewrite (2.1) to represent the REs at subcarrier k as follows

$$r_{k,\ell}^v = \sum_{s=1}^{N_T} H_{k,\ell}^{s,v} A_{k,\ell}^s + \eta_{k,\ell}^v. \quad (2.4)$$

Thus, the received REs at locations (k_P^s, ℓ_P^s) at receiver v are

$$r_{k_P^s, \ell_P^s}^v = H_{k_P^s, \ell_P^s}^{s,v} A_{k_P^s, \ell_P^s}^s + \eta_{k_P^s, \ell_P^s}^v \quad (2.5)$$

where $s \in \{1, 2, \dots, N_T\}$ and $A_{k_P^s, \ell_P^s}^s$ describes the pilots at transmitter's s RG at locations described by (k_P^s, ℓ_P^s) .

2.3 Channel Estimation

CE in pilot-based LTE-A OFDM systems can be broken into four major steps that are shown in Figure 2.4. Based on the availability of channel statistical information and system complexity, different noise reduction schemes and interpolation techniques can be implemented. C-RS CFRs are first extracted from the RGs and equalized using LS estimation. Afterwards, different schemes are applied to the LS estimates to reduce the noise effect and produce better estimates. Since the first three steps are all done at pilot-carrying REs only, we need to interpolate for the other REs using one of the many interpolation techniques.

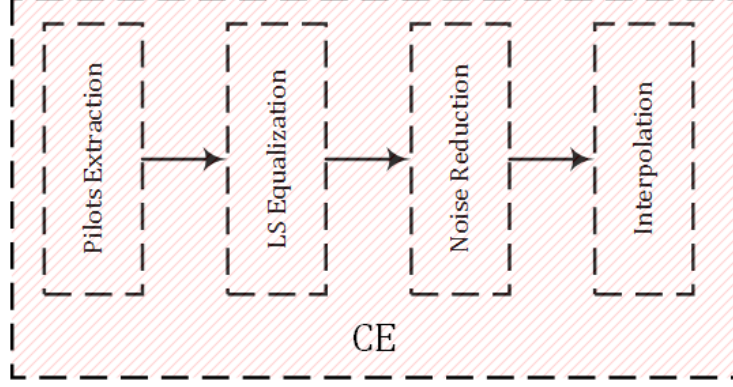


Figure 2.4: Channel Estimation in LTE-A OFDM

2.3.1 Pilots Extraction

First, C-RS symbols need to be extracted from the received RG at each receiver. By thoroughly analyzing the pilot symbols distribution scheme proposed in [60], we arrived at mathematical equations that describe C-RS pilots locations for each antenna port or transmit antenna for both Normal CP (NCP) and Extended CP (ECP) cases, which are shown in Table 2.2.

Table 2.2: Mathematical equations for C-RS pilot indices

Port 0, $s = 1$ $(k_P^s, \ell_P^s) = [6i + (3t + v_{shift}) \bmod 6, (3 + N_{CP})t + (6 + N_{CP})[n_s \bmod 2]]$
Port 1, $s = 2$ $(k_P^s, \ell_P^s) = [6i + (3[(t + 1) \bmod 2] + v_{shift}) \bmod 6, (3 + N_{CP})t + (6 + N_{CP})[n_s \bmod 2]]$
Port 2, $s = 3$ $(k_P^s, \ell_P^s) = [6i + (3[n_s \bmod 2] + v_{shift}) \bmod 6, 1 + [N_{CP}[n_s \bmod 2]] + 6[n_s \bmod 2]]$
Port 3, $s = 4$ $(k_P^s, \ell_P^s) = [6i + (3 + 3[n_s \bmod 2] + v_{shift}) \bmod 6, 1 + [N_{CP}[n_s \bmod 2]] + 6[n_s \bmod 2]]$
$v_{shift} = N_{ID}^{Cell} \bmod 6, N_{CP} = \begin{cases} 1, & \text{For Normal Cyclic Prefix (NCP)} \\ 0, & \text{For Extended Cyclic Prefix (ECP)} \end{cases}$ $i = 0, \dots, 2 \times N_{RB}^{max, DL} - 1, t = 0, 1, n_s = \{1, 2\}$

N_{ID}^{Cell} is a number that identifies the cell in the network, v_{shift} is the cell-specific frequency shift, $N_{RB}^{max, DL}$ is the maximum number of DL RBs, and n_s is the time slot number. To verify the distributions shown in Figure 2.1, set $N_{ID}^{Cell} = 0$. The difference between NCP and ECP will be covered in detail in section 2.4, and pilot distributions with ECP can be found in [60].

2.3.2 Pilots Equalization

Now, LS estimation is used to equalize the CFRs at pilot locations sent from different transmitters at all receive antennas. C-RS locations and values are known to both receiver and transmitter. Using LS estimation to solve for $H_{k_P^s, \ell_P^s}^{s,v}$ for all transmitter and receiver pairs (s, v) , $s \in \{1, 2, \dots, N_T\}$, $v \in \{1, 2, \dots, N_R\}$ from (2.5), we get

$$\hat{H}_{k_P^s, \ell_P^s}^{s,v} = \frac{\gamma_{k_P^s, \ell_P^s}^v}{A_{k_P^s, \ell_P^s}^s} = H_{k_P^s, \ell_P^s}^{s,v} + \hat{\eta}_{k_P^s, \ell_P^s}^v. \quad (2.6)$$

$\hat{H}_{k_P^s, \ell_P^s}^{s,v}$ represents LS estimated CFRs between transmitter s and receiver v RG at locations (k_P^s, ℓ_P^s) and $\hat{\eta}_{k_P^s, \ell_P^s}^v = \eta_{k_P^s, \ell_P^s}^v / A_{k_P^s, \ell_P^s}^s$. The filter coefficient in the LS case is expressed as

$$w_{k_P^s, \ell_P^s}^{s,v} = \frac{1}{A_{k_P^s, \ell_P^s}^s}, \quad k_P^s = \{k_1^s, k_2^s, \dots, k_{N_P}^s\}, \quad \ell_P^s = \{\ell_1^s, \ell_2^s, \dots, \ell_{N_P}^s\}. \quad (2.7)$$

Thus, the MSE is defined as

$$\text{MSE}_{ls} = E \left\{ \left| H_{k_P^s, \ell_P^s}^{s,v} - \hat{H}_{k_P^s, \ell_P^s}^{s,v} \right|^2 \right\} \quad (2.8)$$

$$= E \left\{ \left| -H_{k_P^s, \ell_P^s}^{s,v} - \hat{\eta}_{k_P^s, \ell_P^s}^v + H_{k_P^s, \ell_P^s}^{s,v} \right|^2 \right\} \quad (2.9)$$

$$= E \left\{ \left| \hat{\eta}_{k_P^s, \ell_P^s}^v \right|^2 \right\} \quad (2.10)$$

$$= E \left\{ \left| \frac{\eta_{k_P^s, \ell_P^s}^v}{A_{k_P^s, \ell_P^s}^s} \right|^2 \right\} \quad (2.11)$$

$$= 1/\gamma^{s,v} \quad (2.12)$$

where $E \{.\}$ denotes the expectation, and $\gamma^{s,v}$ is the SNR between transmitter s and receiver v .

2.3.3 Noise Reduction

After arriving at the LS estimated CFRs, the estimation performance is generally not good enough because of the presence of $\hat{\eta}_{k_P^s, \ell_P^s}^v$. Thus, further processing is needed to enhance the CFRs estimates. Two major techniques are presented based on complexity and availability of channel statistics: EWA and Wiener Filtering. Time domain interpolation using 2×1 -D FFT/IFFT instead of 2-D DFT/IDFT is proposed, but since it involves de-noising the LSE and interpolation, it will be completely covered under the interpolation section.

2.3.3.1 Equal Weight Averaging

EWA is considered a simple, yet, powerful tool to reduce the noise effect, especially at low SNRs, after LS estimation without the need for channel statistical information. In EWA, LS estimates are treated as deterministic but unknown. So, LS estimation is followed by EWA at each (k_P^s, ℓ_P^s) location, which simply averages all $\hat{H}_{k_P^s, \ell_P^s}^{s,v}$ that falls in the RG within a window bounded by $k_P^s - \frac{F}{2} \leq k_P^s \leq k_P^s + \frac{F}{2}$ and $\ell_P^s - \frac{T}{2} \leq \ell_P^s \leq \ell_P^s + \frac{T}{2}$. EWA is then performed according to the following

$$\overline{H}_{k_P^s, \ell_P^s}^{s,v} = \frac{1}{Z} \sum_{\hat{k}_P^s = k_P^s - \frac{F}{2}}^{k_P^s + \frac{F}{2}} \sum_{\hat{\ell}_P^s = \ell_P^s - \frac{T}{2}}^{\ell_P^s + \frac{T}{2}} \hat{H}_{\hat{k}_P^s, \hat{\ell}_P^s}^{s,v} \quad (2.13)$$

where Z is the number of LS estimated CFRs around $\hat{H}_{k_P^s, \ell_P^s}^{s,v}$ within the window bounded by $k_P^s - \frac{F}{2} \leq k_P^s \leq k_P^s + \frac{F}{2}$ and $\ell_P^s - \frac{T}{2} \leq \ell_P^s \leq \ell_P^s + \frac{T}{2}$. EWA is a discrete, linear, and generally shift variant filter with an odd number of taps. Thus we can write (2.13) as follows

$$\overline{H}_{k_P^s, \ell_P^s}^{s,v} = \sum_{\{\hat{k}_P^s, \hat{\ell}_P^s\}} w(k_P^s, \ell_P^s; \hat{k}_P^s, \hat{\ell}_P^s) \hat{H}_{\hat{k}_P^s, \hat{\ell}_P^s}^{s,v} \quad (2.14)$$

$$= \sum_{\{\hat{k}_P^s, \hat{\ell}_P^s\}} w(k_P^s, \ell_P^s; \hat{k}_P^s, \hat{\ell}_P^s) \left(H_{\hat{k}_P^s, \hat{\ell}_P^s}^{s,v} + \hat{\eta}_{\hat{k}_P^s, \hat{\ell}_P^s}^v \right) \quad (2.15)$$

where $\hat{k}_P^s, \hat{\ell}_P^s$ are bounded as specified previously, and $w(k_P^s, \ell_P^s; \hat{k}_P^s, \hat{\ell}_P^s)$ is the shift-variant impulse response of the EWA filter, where the number of filter coefficients is Z . We can write (2.15) in matrix form as

$$\overline{H}_{k_P^s, \ell_P^s}^{s,v} = \mathbf{w}_P^{s,v} \hat{\mathbf{H}}_{T/F}^{s,v} \quad (2.16)$$

where

$$\mathbf{w}_P^{s,v} = \frac{1}{Z} \times [1_1, 1_2, \dots, 1_Z]. \quad (2.17)$$

$\mathbf{w}_P^{s,v}$ is the $1 \times Z$ -taps filter coefficients vector and $\hat{\mathbf{H}}_{T/F}^{s,v}$ is the $Z \times 1$ LS estimated CFRs vector at pilot locations bounded by $k_P^s - \frac{F}{2} \leq k_P^s \leq k_P^s + \frac{F}{2}$ and $\ell_P^s - \frac{T}{2} \leq \ell_P^s \leq \ell_P^s + \frac{T}{2}$. Thus, the MSE is defined as

$$\begin{aligned} \text{MSE}_{ewa} &= E \left\{ \left| H_{k_P^s, \ell_P^s}^{s,v} - \overline{H}_{k_P^s, \ell_P^s}^{s,v} \right|^2 \right\} \\ &= E \left\{ \left(H_{k_P^s, \ell_P^s}^{s,v} - \overline{H}_{k_P^s, \ell_P^s}^{s,v} \right) \left(H_{k_P^s, \ell_P^s}^{s,v} - \overline{H}_{k_P^s, \ell_P^s}^{s,v} \right)^H \right\} \\ &= E \left\{ H_{k_P^s, \ell_P^s}^{s,v} \left(H_{k_P^s, \ell_P^s}^{s,v} \right)^H \right\} - E \left\{ \mathbf{w}_P^{s,v} \hat{\mathbf{H}}_{T/F}^{s,v} \left(H_{k_P^s, \ell_P^s}^{s,v} \right)^H \right\} \end{aligned}$$

$$- E \left\{ H_{k_P^s, \ell_P^s}^{s,v} \left(\mathbf{w}_P^{s,v} \hat{\mathbf{H}}_{T/F}^{s,v} \right)^H \right\} + E \left\{ \mathbf{w}_P^{s,v} \hat{\mathbf{H}}_{T/F}^{s,v} \left(\mathbf{w}_P^{s,v} \hat{\mathbf{H}}_{T/F}^{s,v} \right)^H \right\} \quad (2.18)$$

where $(\cdot)^H$ is the Hermitian transpose. Knowing that $\mathcal{R}_{xx} = E \{xx^H\}$ is the autocorrelation coefficient for a RV x , and $\mathcal{R}_{yx} = \mathcal{R}_{xy}^H = E \{yx^H\}$ is the crosscorrelation coefficient between two RVs y and x , (2.18) becomes

$$\begin{aligned} \text{MSE}_{ewa} &= \mathcal{R}_{(HH)_{k_P^s, \ell_P^s}^{s,v}} - \mathbf{w}_P^{s,v} \mathbf{R}_{(H\hat{\mathbf{H}})_{T/F}^{s,v}}^H \\ &\quad - \mathbf{R}_{(H\hat{\mathbf{H}})_{T/F}^{s,v}} \left(\mathbf{w}_P^{s,v} \right)^H + E \left\{ \mathbf{w}_P^{s,v} \hat{\mathbf{H}}_{T/F}^{s,v} \left(\hat{\mathbf{H}}_{T/F}^{s,v} \right)^H \left(\mathbf{w}_P^{s,v} \right)^H \right\} \\ &= \mathcal{R}_{(HH)_{k_P^s, \ell_P^s}^{s,v}} - \frac{1}{Z} \sum_Z \mathcal{R}_{(H\hat{\mathbf{H}}_{T/F}^{s,v})_{k_P^s, \ell_P^s}^{s,v}}^H \\ &\quad - \frac{1}{Z} \sum_Z \mathcal{R}_{(H\hat{\mathbf{H}}_{T/F}^{s,v})_{k_P^s, \ell_P^s}^{s,v}} + \mathbf{w}_P^{s,v} E \left\{ \hat{\mathbf{H}}_{T/F}^{s,v} \left(\hat{\mathbf{H}}_{T/F}^{s,v} \right)^H \right\} \left(\mathbf{w}_P^{s,v} \right)^H \\ &= \sum_{m=0}^{L_h} 2\sigma_{h_m}^2 - \frac{2}{Z} \sum_Z \text{Re} \left\{ \mathcal{R}_{(H\hat{\mathbf{H}}_{T/F}^{s,v})_{k_P^s, \ell_P^s}^{s,v}} \right\} + \mathbf{w}_P^{s,v} \mathbf{R}_{(\hat{\mathbf{H}}\hat{\mathbf{H}})_{T/F}^{s,v}} \left(\mathbf{w}_P^{s,v} \right)^H \\ &= \sum_{m=0}^{L_h} 2\sigma_{h_m}^2 - \frac{2}{Z} \sum_Z \text{Re} \left\{ \mathcal{R}_{(H\hat{\mathbf{H}}_{T/F}^{s,v})_{k_P^s, \ell_P^s}^{s,v}} \right\} + \frac{1}{Z^2} \left(\sum_Z \sum_Z \mathcal{R}_{(\hat{\mathbf{H}}\hat{\mathbf{H}})_{k_P^s, \ell_P^s}^{s,v}} \right) \end{aligned} \quad (2.19)$$

where $\text{Re} \{ \cdot \}$ denotes the real part, $\mathbf{R}_{(H\hat{\mathbf{H}})_{T/F}^{s,v}}$ is the $1 \times Z$ crosscorrelation vector between $H_{k_P^s, \ell_P^s}^{s,v}$ and $\hat{\mathbf{H}}_{T/F}^{s,v}$, and $\mathbf{R}_{(\hat{\mathbf{H}}\hat{\mathbf{H}})_{T/F}^{s,v}}$ is the $Z \times Z$ channel autocorrelation matrix. We assume that the noise and the fading are statistically independent. Assuming the Wide Sense Stationary Uncorrelated Scattering (WSSUS) model for $H_{k_P^s, \ell_P^s}^{s,v}$ with two-dimensional autocorrelation function; $\mathcal{R}^{s,v}(f, t)$, and that noise and fading are statistically independent, then the elements of $\mathbf{R}_{(\hat{\mathbf{H}}\hat{\mathbf{H}})_{T/F}^{s,v}}$ and $\mathbf{R}_{(H\hat{\mathbf{H}})_{T/F}^{s,v}}$ are expressed as, respectively

$$\mathcal{R}^{s,v}(\dot{k}_P^s - \dot{k}_P^s, \dot{\ell}_P^s - \dot{\ell}_P^s) + \left(\frac{1}{\gamma^{s,v}} \right) \delta^{s,v}(\dot{k}_P^s - \dot{k}_P^s, \dot{\ell}_P^s - \dot{\ell}_P^s) \quad (2.20)$$

$$\mathcal{R}^{s,v}(\dot{k}_P^s - \dot{k}_P^s, \dot{\ell}_P^s - \dot{\ell}_P^s). \quad (2.21)$$

For WSSUS channels [36], the scattering function and the two-dimensional autocorrelation function factorizes to

$$\mathcal{R}^{s,v}(\Delta f, \Delta t) = \mathcal{R}^{s,v}(f, 0) \mathcal{R}^{s,v}(0, t) = \mathcal{R}_H^{s,v}(f) \mathcal{R}_c^{s,v}(t). \quad (2.22)$$

$\mathcal{R}_c^{s,v}(t)$ is given as the inverse Fourier transform of the Doppler spectrum. For the Jakes spectrum with $f_{d,max}$ as the maximum Doppler frequency, it is given by

$$\mathcal{R}_c^{s,v}(t) = J_0(2\pi f_{d,max}t). \quad (2.23)$$

$\mathcal{R}_H^{s,v}(f)$ is given as the Fourier transform of the delay power spectrum. For a rectangular delay power spectrum between 0 and τ_{max} as the maximum tap delay, it is given by

$$\mathcal{R}_H^{s,v}(f) = e^{-j\pi f\tau_{max}} \text{sinc}(f\tau_{max}). \quad (2.24)$$

If we substitute (2.20) into (2.19), it is noted that as SNR increases, MSE_{ewa} will hit an error floor that is a function of the number of taps, Z , and the channel statistical information. Figure 2.5 shows an example of different EWA schemes. Note that EWA is applied for each antenna port separately; meaning that the averaging window spans pilots from one antenna port at a time. We will use $N_{freq} \cdot F \times N_{time} \cdot T$ notation to specify the EWA averaging window size.

2.3.3.2 Wiener Filtering

Estimation performance can be greatly improved by exploiting the channel's statistical information, which is the case in Wiener filtering. The LS estimates are considered as random variables and a linear filter based on the MMSE theory is used for noise reduction, namely Wiener filter. We are trying to find the CFRs $H_{k_P^s, \ell_P^s}^{s,v}$ from the noisy channel measurements $\hat{H}_{k_P^s, \ell_P^s}^{s,v}$ with properly chosen estimator coefficients. This linear estimator can be expressed as

$$\check{H}_{k_P^s, \ell_P^s}^{s,v} = \sum_{\{\check{k}_P^s, \check{\ell}_P^s\}} b(k_P^s, \ell_P^s; \check{k}_P^s, \check{\ell}_P^s) \hat{H}_{\check{k}_P^s, \check{\ell}_P^s}^{s,v}. \quad (2.25)$$

To simplify the formalism, we assume that a CFR, $H_{k_P^s, \ell_P^s}^{s,v}$, must be estimated from a finite number of \mathcal{M} measurements, $\hat{H}_{k_P^s, \ell_P^s}^{s,v}$. The sample and \mathcal{M} measurements are taken only at pilots locations. We may then write the estimated sample, $\check{H}_{k_P^s, \ell_P^s}^{s,v}$, at pilots locations only as

$$\check{H}_{k_P^s, \ell_P^s}^{s,v} = \mathbf{b}_P^{s,v} \hat{\mathbf{H}}_P^{s,v} \quad (2.26)$$

where

$$\mathbf{b}_P^{s,v} = \begin{bmatrix} b_{11}^{s,v} & b_{12}^{s,v} & \cdots & \cdots & b_{1\mathcal{M}}^{s,v} \end{bmatrix}. \quad (2.27)$$

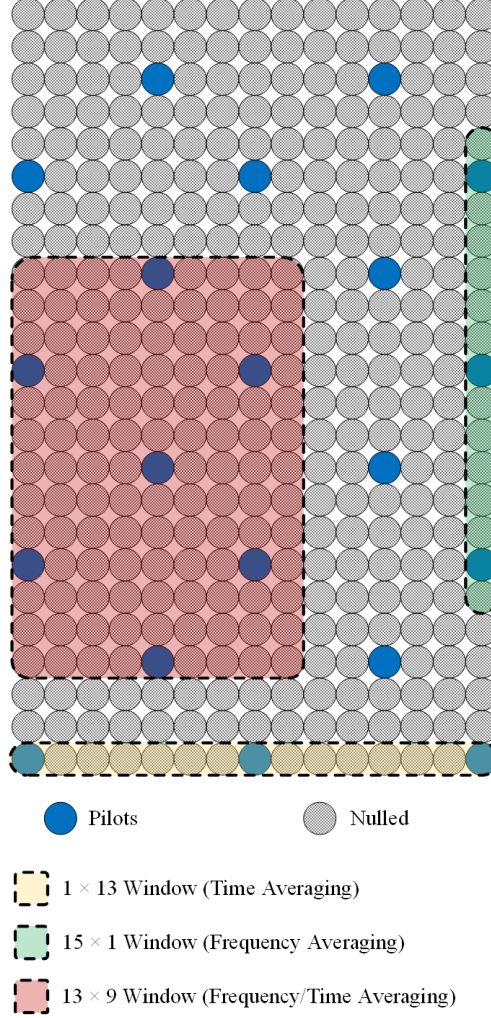


Figure 2.5: Examples of EWA

The criteria for designing the Wiener filter coefficients $\mathbf{b}_P^{s,v}$ is to minimize the following

$$E \left\{ \left| e_{k_P^s, \ell_P^s}^{s,v} \right|^2 \right\} = E \left\{ \left| H_{k_P^s, \ell_P^s}^{s,v} - \check{H}_{k_P^s, \ell_P^s}^{s,v} \right|^2 \right\}. \quad (2.28)$$

Based on the MMSE theory, we arrive at the Wiener-Hopf equation that describes the values of $\mathbf{b}_P^{s,v}$ as

$$\mathbf{b}_P^{s,v} = \mathbf{R}_{(H\hat{\mathbf{H}})_{\mathcal{M}}}^{s,v} \left(\mathbf{R}_{(\hat{\mathbf{H}}\hat{\mathbf{H}})_{\mathcal{M}}}^{s,v} \right)^{-1} \quad (2.29)$$

where $\mathbf{R}_{(H\hat{\mathbf{H}})_{\mathcal{M}}}^{s,v}$ is the crosscorrelation vector of size $1 \times \mathcal{M}$ between $H_{k_P^s, \ell_P^s}^{s,v}$ and $\hat{\mathbf{H}}_P^{s,v}$, and $\left(\mathbf{R}_{(\hat{\mathbf{H}}\hat{\mathbf{H}})_{\mathcal{M}}}^{s,v} \right)^{-1}$ is the inverse of the channel autocorrelation matrix of size $\mathcal{M} \times \mathcal{M}$. If the crosscorrelation and autocorrelation functions are known, the MSE_w is obtained and de-

scribed as

$$\text{MSE}_w = \sum_{m=0}^{L_h} 2\sigma_{h_m}^2 - \mathbf{R}_{(H\hat{\mathbf{H}})_{\mathcal{M}}^{s,v}} \left(\mathbf{R}_{(\hat{\mathbf{H}}\hat{\mathbf{H}})_{\mathcal{M}}^{s,v}} \right)^{-1} \left(\mathbf{R}_{(H\hat{\mathbf{H}})_{\mathcal{M}}^{s,v}} \right)^H. \quad (2.30)$$

Different variations of Wiener filtering can be used such as: 1-D frequency Wiener, 1-D time Wiener, 2×1-D Wiener and 2-D Wiener. It was indicated in [78] that the cascade of two 1-D Wiener filters achieves performance similar to that of the 2-D Wiener filter with negligible degradation and reduced implementation complexity. The order can be shown to be arbitrary due to linearity of the estimation and due to the fact that the rectangular constellation is the Cartesian product of two one-dimensional ones. We will use $N_{freq} \times F \times N_{time} \times T$ notation to specify the number of taps being used by Wiener filter.

2.3.4 Interpolation

Once the noise has been reduced or removed from the CFRs estimates, it is possible to use interpolation to estimate the missing values from the channel estimation grid. For the purpose of this work, two of the widely used interpolation techniques namely spline interpolation and Wiener interpolation are presented. Moreover, time domain interpolation is proposed using 2×1-FFT/IFFT instead of the computationally complex 2-D DFT/IDFT.

2.3.4.1 Linear Spline Interpolation

Given a tabulated function $f_k = f(x_k), k = 0, 1, \dots, N$, a spline is a polynomial between each pair of tabulated points, but one whose coefficients are determined “slightly” non-locally. The non-locality is intended to make sure that there will be global smoothness in the interpolated function up to some order of derivative. We start first by presenting the linear spline interpolation.

If we have two consecutive points $(x_k, y_k), (x_{k+1}, y_{k+1})$ where $y_k = f_k = f(x_k)$, Linear interpolation in the interval $[k, k + 1]$ gives the interpolation formula

$$f = C f_k + D f_{k+1} \quad (2.31)$$

where

$$C = \frac{x_{k+1} - x}{x_{k+1} - x_k}, \quad D = 1 - C. \quad (2.32)$$

Linear interpolation is simple and performs well for low-variant functions. Nevertheless, because the interpolation function represents a straight line, it fails at tracing the curvatures of the function. The accuracy can be improved by using more interpolating points. However, a major issue is that the first derivatives of the interpolating function are discontinuous at

the interpolated points. The order of complexity for ζ number of points using linear spline interpolation is $O(\zeta)$.

2.3.4.2 Cubic Spline Interpolation

The objective in cubic spline interpolation is to arrive at an interpolation formula that is continuous in both the first and second derivatives, both within the intervals and at the interpolating points. This will result in a smoother interpolating function. In general, if the function to be approximated is smooth, then cubic splines will do better than linear spline interpolation.

Continuing on from the subsection 2.3.4.1, assume that in addition to the tabulated values of f_i , we also have tabulated values for the function's second derivatives, that is, a set of numbers f_i'' . Then within each interval $[k, k + 1]$, we can add to the right-hand side of (2.31) a cubic polynomial whose second derivative changes linearly from a value f_k'' on the left of a value f_{k+1}'' on the right. Doing so, we arrive at the desired continuous second derivative. If the cubic polynomial is constructed to have zero values at x_k and x_{k+1} , then adding it in will not spoil the agreement with the tabulated functional values f_k and f_{k+1} at the end points x_k and x_{k+1} . A little side calculation shows that there is only one way to arrange this construction, namely replacing (2.31) by

$$f = C f_k + D f_{k+1} + E f_k'' + F f_{k+1}'' \quad (2.33)$$

where C and D are defined as before and

$$E = \frac{1}{6} (C^3 - C) (x_{k+1} - x_k)^2, \quad F = \frac{1}{6} (D^3 - D) (x_{k+1} - x_k)^2. \quad (2.34)$$

It can be seen that the number of multiplications needed per one cubic spline interpolated point is 3 multiplication operations. Note that since C and D are linearly dependent on x , E and F (through C and D) have cubic x -dependence. We can readily check that f'' is in fact the second derivative of the new interpolating polynomial. We take derivatives of (2.33) with respect to x , using the definitions of A, B, C and D to compute dC/dx , dD/dx , dE/dx and dF/dx . The result is

$$\frac{df}{dx} = \frac{f_{k+1} - f_k}{x_{k+1} - x_k} - \frac{3C^2 - 1}{6} (x_{k+1} - x_k) f_k'' + \frac{3D^2 - 1}{6} (x_{k+1} - x_k) f_{k+1}''. \quad (2.35)$$

For the first derivative, and

$$\frac{d^2 f}{dx^2} = C f_k'' + D f_{k+1}''. \quad (2.36)$$

For the second derivative. Since $C = 1$ at x_k and $C = 0$ at x_{k+1} , and $D = 0$ at x_k and $D = 1$ at x_{k+1} , (2.36) shows that f'' is just the tabulated second derivative, and also that the second derivative will be continuous across the boundary between two intervals, say (x_{k-1}, x_k) and (x_k, x_{k+1}) .

We supposed the f''_k s to be known, when actually they are not. However, we have not yet applied the constraint that the first derivative, computed from (2.35), be continuous across the boundary between two intervals. The key idea of a cubic spline is to require this continuity and to use it to get equations for the second derivatives f''_k .

The required equations are obtained by setting (2.35) evaluated for $x = x_k$ in the interval (x_{k-1}, x_k) equal to the same equation evaluated for $x = x_k$ in the interval (x_k, x_{k+1}) . With some rearrangement, this give (for $k = 1, 2, \dots, N - 1$)

$$\frac{x_k - x_{k-1}}{6} f''_{k-1} + \frac{x_{k+1} - x_{k-1}}{3} f''_k + \frac{x_{k+1} - x_k}{6} f''_{k+1} = \frac{f_{k+1} - f_k}{x_{k+1} - x_k} - \frac{f_k - f_{k-1}}{x_k - x_{k-1}}. \quad (2.37)$$

These are $N - 1$ linear equations in the $N + 1$ unknowns f''_i , $i = 0, 1, \dots, N$. Thus, there is a two-parameter family of possible solutions. To arrive at a unique solution, one needs to specify further conditions, typically taken as boundary conditions at x_0 and x_N . The most common way of doing this is to set both f''_0 and f''_N equal to zero, which results in the so-called natural cubic spline, which has zero second derivatives on both boundaries. Now that we have the solution for f''_k , $k = 0, 1, \dots, N$, we can substitute back into (2.31) to give the cubic interpolation formula in each interval (x_k, x_{k+1}) . The order of complexity for ζ number of points using cubic spline interpolation is $O(3^2\zeta)$.

To minimize notations, we will refer to linear spline interpolation as “linear” interpolation, and cubic spline interpolation as “spline” interpolation.

2.3.4.3 Wiener Interpolation

In subsection 2.3.3.2, the formulation assumed that we are estimating CFRs at pilot locations only, $H_{k_P^s, \ell_P^s}^{s,v}$, from a finite number of \mathcal{M} measurements at pilot locations as well, $\hat{H}_{k_P^s, \ell_P^s}^{s,v}$. The difference between Wiener filtering and Wiener interpolation is that now the estimation is done for all data locations in the RG, $H_{k, \ell}^{s,v}$, using estimates at pilot locations. The finite \mathcal{M} measurements can be either the Wiener filtered estimates, $\check{H}_{k_P^s, \ell_P^s}^{s,v}$, or the LS equalized estimates, $\hat{H}_{k_P^s, \ell_P^s}^{s,v}$. Thus, Wiener interpolation following Wiener filtering is written as

$$\check{H}_{k, \ell}^{s,v} = \sum_{\{k_P^s, \ell_P^s\}} b(k^s, \ell^s; k_P^s, \ell_P^s) \check{H}_{k_P^s, \ell_P^s}^{s,v} \quad (2.38)$$

where k and ℓ are the indices for all non-pilot RE locations.

2.3.4.4 2×1 -D FFT/IFFT Filtering and Interpolation

Although the proposed technique in this subsection is listed under interpolation techniques, it does involve de-noising of the CFRs at pilot locations in the middle of the process of interpolating for data locations. The proposed technique involves transforming the CFRs into the time domain using FFT to find the noisy CIR. Then, based on statistical measurements, the number of taps of the channel, L_h , is obtained, and is used to low-pass the noisy CIR, and only keep the first L_h taps. Thereafter, a fixed number of zeros is inserted to the end of the CIR, followed by IFFT of the modified CIR sequence and scaling. It is essentially a process of upsampling using zero padding in the transform domain. It is worth mentioning that this type of filter/interpolator is a reasonable compromise between EWA and Wiener filtering, as the process is essentially averaging using a channel statistics dependent low-pass filter. The complexity associated with 1-D DFT is of the order $O(\zeta^2)$ for ζ points and is reduced by using 1-D FFT to $O(\zeta \log_2 \zeta)$. In the case of 2-D DFT for a $\zeta_1 \times \zeta_2$ matrix, the complexity is $O(\zeta_2 \zeta_1^2) + O(\zeta_1 \zeta_2^2)$, which is also reduced to $O(\zeta_2 \zeta_1 \log_2 \zeta_1) + O(\zeta_1 \zeta_2 \log_2 \zeta_2)$ using 2-D FFT.

Assume a RG of size $k \times \ell$. First, channel estimates at pilot locations are rearranged into an $k_{N_P} \times \ell_{N_P}$ matrix $\mathbf{H}_P^{s,v}$. Next, 1-D k_{N_P} -point FFT is applied along the frequency direction for each individual ℓ_{N_P} symbol. Afterwards, the ℓ_{N_P} FFT sequences, each of length k_{N_P} , are passed through a low pass filter keeping only the first L_h samples, and then each one of the ℓ_{N_P} FFT sequences is padded with enough zeros to account for all data carrying subcarriers, $k_{N_D} = k - k_{N_P}$. Now the inverse k -point IFFT for all ℓ_{N_P} symbols is performed to get the $k \times \ell_{N_P}$ matrix. The same procedure along the time dimension is applied without low-pass filtering, to find the estimates at all $\ell_{N_D} = \ell - \ell_{N_P}$ OFDM symbols, and obtain the estimated CFR matrix $k \times \ell$.

2.4 Results and Discussion

Simulations were carried out to compare the different types of noise reduction schemes with different interpolation techniques in different channel conditions. Table 2.1 shows the specifications for the multipath delay profiles for the simulated channels and they are: Extended Typical Urban model (ETU), Extended Vehicular A model (EVA) and Extended Pedestrian A model (EPA) [60]. Simulation results will be divided into three sections to report the different results and their associated discussions.

2.4.1 CE Results Before Interpolation

The simulated system is a 2×2 LTE-A-OFDM antenna system. The system has 100 RBs, 1200 sub-carriers, $\Delta_f = 15$ KHz/subcarrier and every time slot occupies 500μ seconds. In the case of NCP, 7 OFDM symbols occupy the time slot, where each symbol has a length of $\cong 66.7\mu$ seconds with a CP length of $\cong 5.2\mu$ seconds for the first symbol and $\cong 4.7\mu$ seconds for the other 6 symbols. In the case of ECP, 6 OFDM symbols occupy the time slot, where each symbol has a length of $\cong 66.7\mu$ seconds with a CP length of $\cong 16.67\mu$ seconds per symbol. Notice that with ECP, one OFDM symbol has been sacrificed to increase the CP length to protect the data from ISI resulting from frequency selective channels, such as ETU. We are considering the channel statistical models provided by (2.23) and (2.24) in our simulations. For each delay profile, we have tested different variations of EWA and Wiener filter. We are comparing the LS estimates, 2-D Wiener ($8F \times 4T$ taps), 2×1 -D Wiener ($8F \times 4T$ taps), 1-D Wiener-16 ($16F$ taps), 1-D Wiener-8 ($8F$ taps), EWA-13 ($13F \times 27T$), EWA-53 ($53F \times 27T$) and EWA-91 ($91F \times 27T$). The EWA windows were selected to represent light (EWA-13), medium (EWA-53) and extreme (EWA-91) averaging cases for the different SNR values and different channel delay profiles. The time-direction window size in EWA is set to 27 to span two full sub-frames. We have omitted the plots of frequency averaging and time averaging of EWA, as the results were quite poor, due to the simplicity of such schemes. Complexity study will be performed in subsection 2.4.2. Simulation results for each channel delay profile are presented separately.

Figure 2.6 shows the MSE simulation results for CFRs before interpolation for EPA 5 channel delay profile. The LS estimates simulation result matches the mathematical analysis reported in subsection 2.3.2. It is noticed that EWA-91 and EWA-53 perform worse as SNR increases, which is to be expected. From (2.19), it can be noticed that for low SNR values, a bigger EWA window is required to mitigate the noise effect, which is distorting the channel statistical information as well. Up till $\text{SNR} = -6$ dB, EWA-91 performs better than EWA-53 and EWA-13. However, as SNR increases, the number of EWA taps, Z , becomes the major noise contributor to the channel statistical information, and with bigger number of averaging taps, the estimates are smeared by harsher averaging. This results in worse performance compared to LS estimates for both EWA-91 and EWA-53, for which both hit error floors that are described by (2.19) as $\text{SNR} \rightarrow \infty$. EWA-13 starts performing better than EWA-91 and EWA-53 after $\text{SNR} \cong 10$ dB. It can be seen that EWA-13's performance starts to get worse towards the end of the graph and will eventually hit its respective error floor.

All the different variations of Wiener shown in Figure 2.6 provide different, yet, consistent results across the SNR range, with 2-D Wiener providing the best noise reduction among all the other variations. Based on the MIMO detector and the acceptable MSE threshold for

successful detection, one can select the appropriate Wiener variation. As expected, there is a slight degradation in the performance of 2×1 -D Wiener when compared to 2-D Wiener. However, as SNR gets higher, 2×1 -D Wiener approaches the performance of 2-D Wiener. At $\text{MSE} = 10^{-2}$, 1-D Wiener-8 and 1-D Wiener-16 performances suffer by almost ~ 5 dB and ~ 4 dB, respectively, when compared to 2×1 -D Wiener.

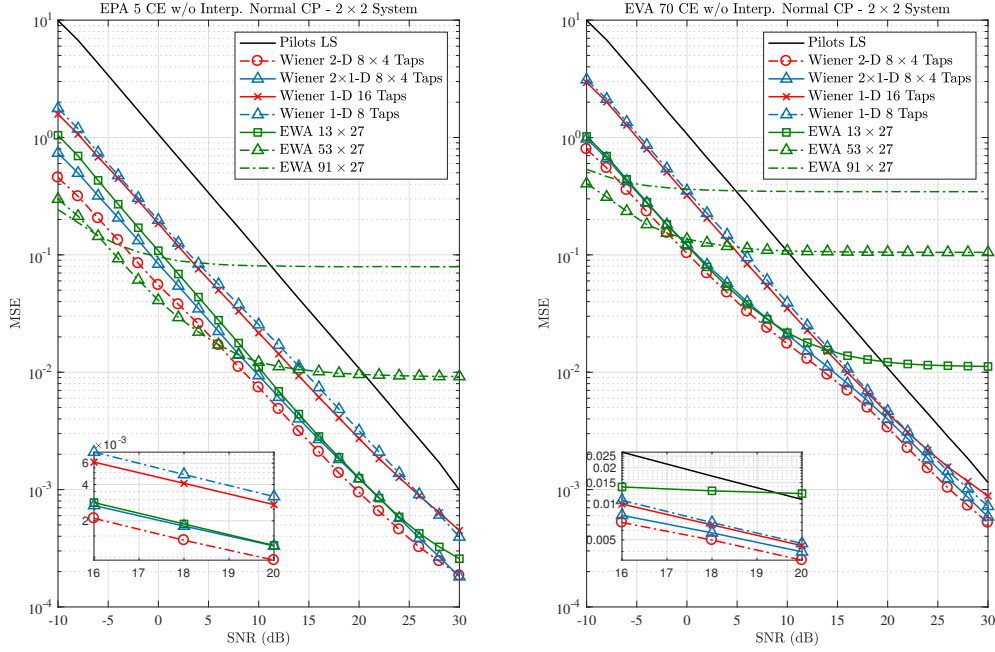


Figure 2.6: MSE vs. SNR for EPA 5 & EVA 70 before interp.

Figure 2.6 shows the MSE simulation results for CFRs before interpolation for EVA 70 channel delay profile. EWA-91 performs poorly across the whole SNR region, while EWA-53 provides the best performance up till $\text{SNR} \cong -2$ dB. After that, EWA-13 outperforms EWA-53 until it hits its MSE error floor of $\cong 10^{-2}$. The LSE simulation result almost matches the mathematical analysis reported in subsection 2.3.2. This is due to Inter Carrier Interference (ICI) and ISI. ICI is an impairment well known to degrade performance of OFDM systems. In this case, it arises from higher Doppler spreads due to channel time-variations and users mobility. ICI effect will be clearer in the case of ETU 300. Generally, when ICI is present, (2.6) becomes

$$\hat{H}_{k_P^s, \ell_P^s}^{s,v} = \frac{r_{k_P^s, \ell_P^s}^v}{A_{k_P^s, \ell_P^s}^s} = H_{k_P^s, \ell_P^s}^{s,v} + \Psi_{k_P^s, \ell_P^s}^{s,v}(\epsilon) + \hat{\eta}_{k_P^s, \ell_P^s}^v \quad (2.39)$$

where $\Psi_{k_P^s, \ell_P^s}^{s,v}(\epsilon)$ is the ICI term as a function of the normalized Carrier Frequency Offset

(CFO), ϵ , due to Doppler shift. Hence, the MSE for LS estimation will have an error floor at high SNR decided by the term $\Psi_{k_P^s, \ell_P^s}^{s,v}(\epsilon)$, which is attributed to the time-varying nature of the channel. ICI will be covered extensively in subsection 3.3.3. Figure 2.7 shows the MSE at SNR = 30 dB vs maximum Doppler frequency ($f_{d,max}$), with a zoomed-in version in the figure's corner, for the different techniques considered in this Chapter, and it shows how MSE gets worse as $f_{d,max}$ increases. Better results are obtained using ECP, which mitigates ISI, however, the ICI effect is still present and degrades the overall performance.

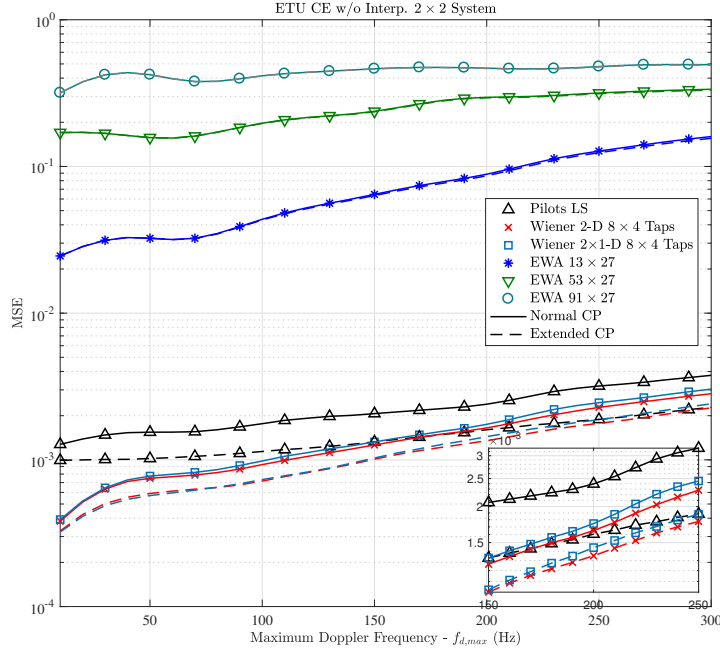


Figure 2.7: MSE vs Maximum Doppler Frequency for ETU 300 at SNR = 30 dB

Moreover, the different variations of Wiener show better results than EWA variations after SNR $\cong 0$ dB, with 2-D Wiener providing the best noise reduction. 1-D Wiener variations approach the performance of the 2-D and 2×1 -D Wiener as SNR increases, but still performs better than LSE. This is due to ICI, which is not completely remedied by Wiener filtering.

Figure 2.8 shows the MSE for CFRs before interpolation in ETU 300 with NCP and ECP. Since ETU 300 suffers from both ISI and ICI, the LS estimated CFRs deviate from the mathematical analysis reported in subsection 2.3.2 after SNR $\cong 10$ dB. Moreover, the length of the NCP is not enough in the case of ETU to mitigate ISI as shown in Figure 2.8. Therefore, the performance improves slightly with ECP, but still suffers from ICI as shown in Figure 2.8. This is due to higher Doppler shift, which becomes the major source of distortion once SNR increases. This will cause both the LS estimates and Wiener filtered

estimates to hit their own respective error floors.

In ETU 300, all EWA variations perform best at the low SNR region up till SNR \cong 1 dB, before hitting their respective error floors based on the number of averaging taps, Z . The different variations of Wiener show better results than EWA, since it adapts to channel variations using the channel statistical information and SNR value, with 2-D Wiener outperforming the other variations, and 2×1 -D Wiener providing very similar performance results, rendering it as a sub-optimal version of 2-D Wiener. The performance of the 1-D Wiener variations approach those of 2-D Wiener as SNR increases.

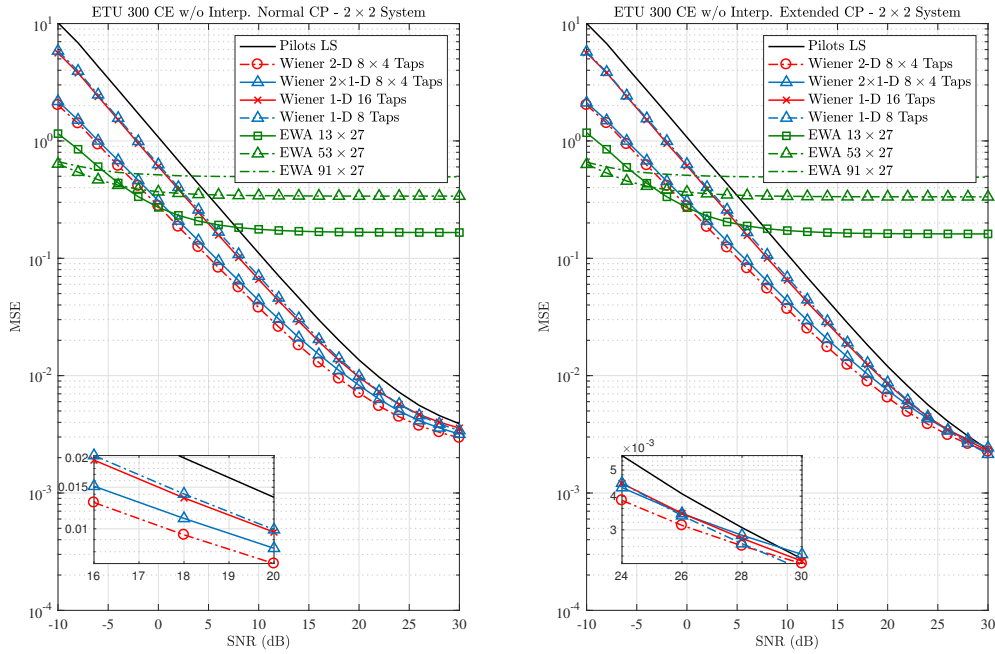


Figure 2.8: MSE vs. SNR for ETU 300 (NCP & ECP) before interp.

2.4.2 CE Results After Interpolation

In general, CFR interpolated estimates are as good as the CFR estimates before interpolation. If CFR estimates are properly filtered before interpolation, then further improvement would be obtained after interpolation. However, if an error persists and causes the CFR estimates before interpolation to hit an error floor, that error will also propagate through interpolation. In this subsection, we present the performance simulation results for each one of the following schemes separately: the proposed scheme, 2×1 -D Wiener filtering with spline interpolation, EWA variations with spline and linear interpolation, 1-D, 2×1 -D and 2-D Wiener filter variations MSE with Wiener, spline and linear interpolations. Comparisons are

carried out using the different channel delay profiles.

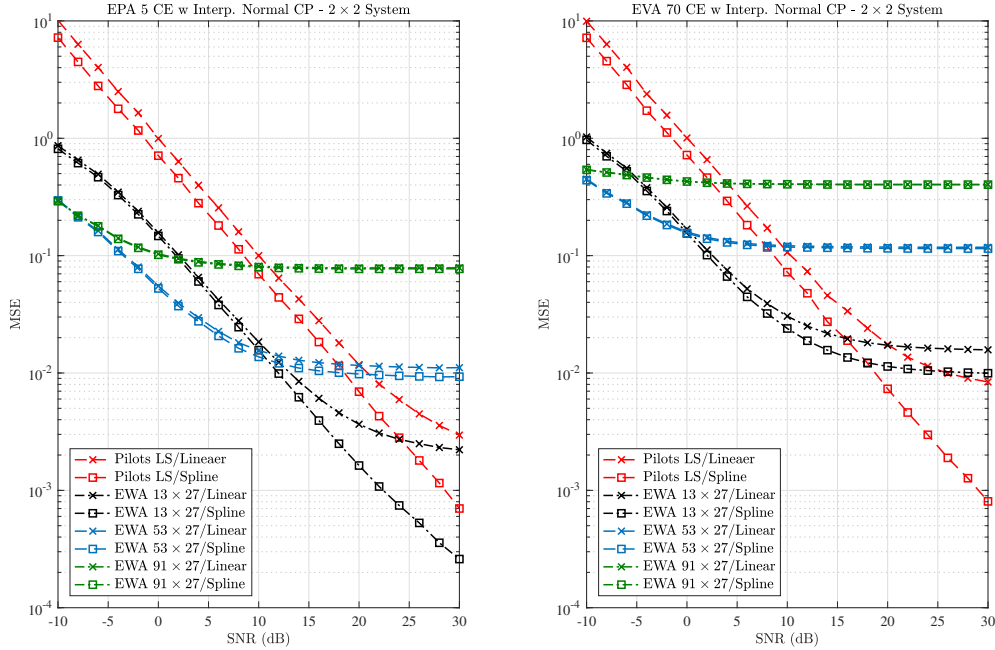


Figure 2.9: MSE vs. SNR with interp. - EWA - EPA 5 & EVA 70

Figures 2.9 and 2.10 show the MSE simulation results for estimated CFRs using different EWA variations after interpolation using two main techniques, namely linear and spline, for the three channel delay profiles in use. By comparing LS/Spline and LS/Linear, it is noticed that spline interpolation performs better than linear interpolation. Moreover, it can be noticed that performance for the different EWA/Spline variations outperform EWA/Linear variations as SNR increases. However, as channel variations increase, moving from EPA to EVA to ETU, both EWA/Linear and EWA/Spline converge to their respective error floors at various SNR points depending on the channel delay profile. This is due to the fact that the different EWA variations has their own respective error floors, which will still propagate through the interpolated values. The performance gap between linear and spline interpolation disappears as the number of EWA taps increases.

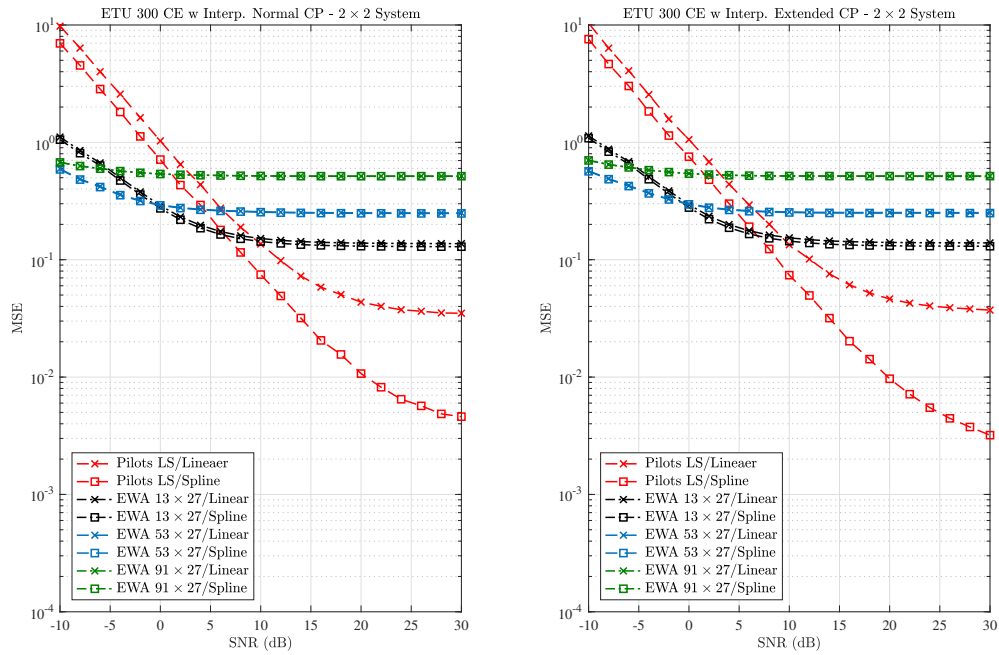


Figure 2.10: MSE vs. SNR with interp. - EWA - ETU 300 (NCP & ECP)

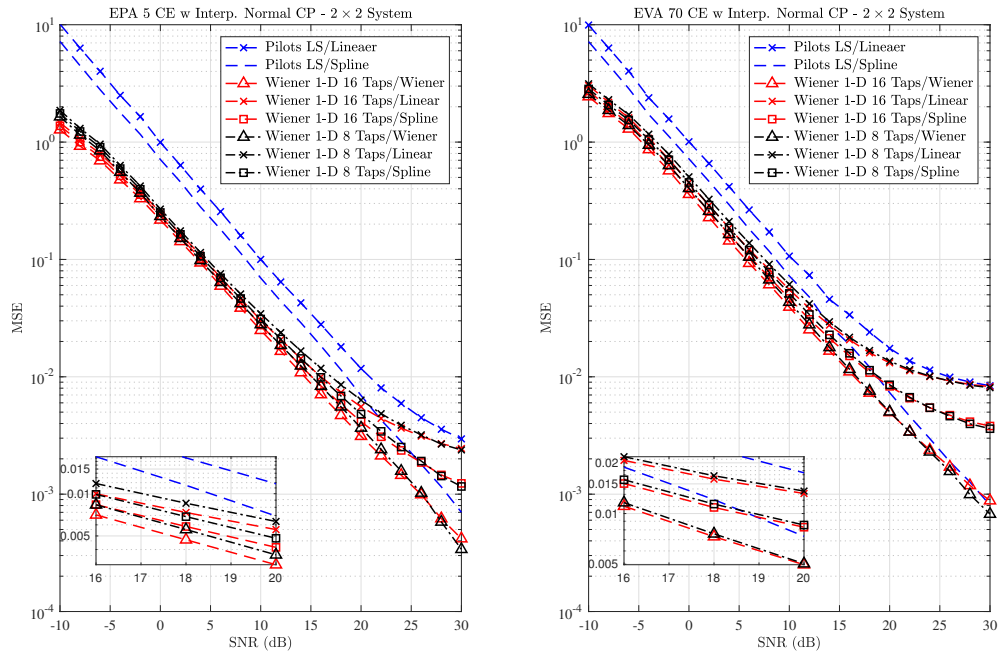


Figure 2.11: MSE vs. SNR with interp. - 1-D Wiener - EPA 5 & EVA 70

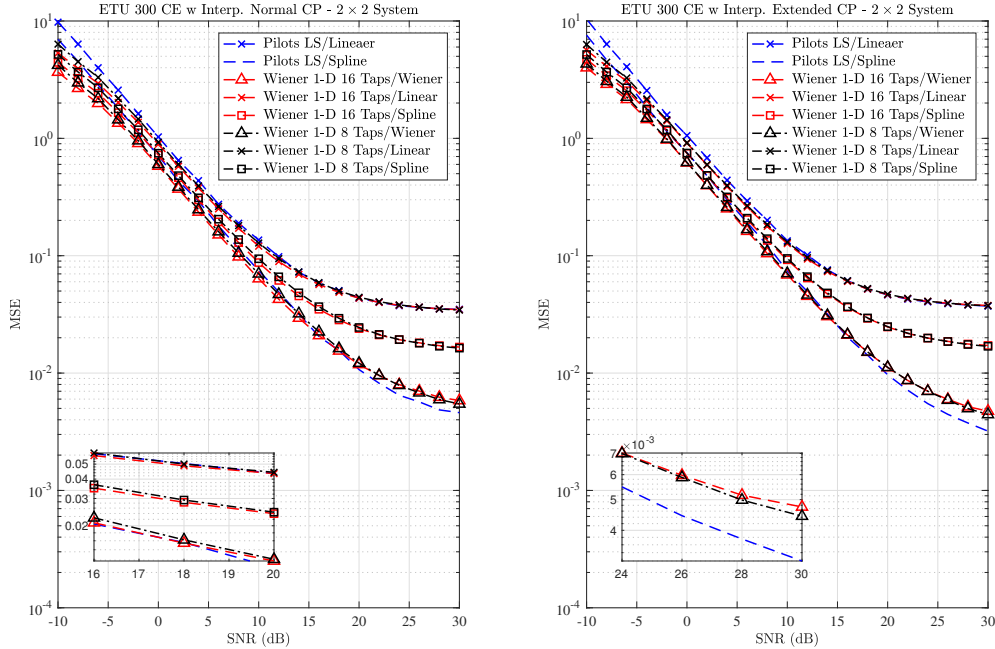


Figure 2.12: MSE vs. SNR with interp. - 1-D Wiener - ETU 300 (NCP & ECP)

Figures 2.11 and 2.12 show the MSE simulation results for estimated CFRs comparing 1-D Wiener-8 and 1-D Wiener-16 after interpolation using three main techniques, namely linear, spline and Wiener, for the three channel delay profiles in use. It can be noticed that 1-D Wiener/Wiener provides the best performance among the other interpolation variations. Moreover, 1-D Wiener/Spline outperforms 1-D Wiener/Linear with the performance gap between them increasing as SNR increases. However, as channel variations increase, all different interpolation techniques starts converging to their respective error floors at various SNR points depending on the channel delay profile due to ICI.

Figures 2.13 and 2.14 show the MSE simulation results for estimated CFRs comparing 2-D Wiener and 2×1 -D Wiener after interpolation using three main techniques, namely linear, spline and Wiener, for the three channel delay profiles in use. Similar to the case of 1-D Wiener, it is noticed that 2-D and 2×1 -D Wiener/Wiener provides the best performance among the other interpolation variations. 2-D and 2×1 -D Wiener/Spline outperforms 2-D and 2×1 -D Wiener/Linear as SNR increases, and generally speaking, 2×1 -D Wiener eventually matches 2-D Wiener at higher SNR values.

Again, as channel variations increase, moving from EPA to EVA to ETU, all different interpolation techniques starts converging to their respective error floors at various SNR points depending on the channel delay profile. This happens with Wiener interpolation as well, because its performance is only as good as the performance of the LS CFR estimates

before interpolation. Again, this is due to the higher ICI before interpolation.

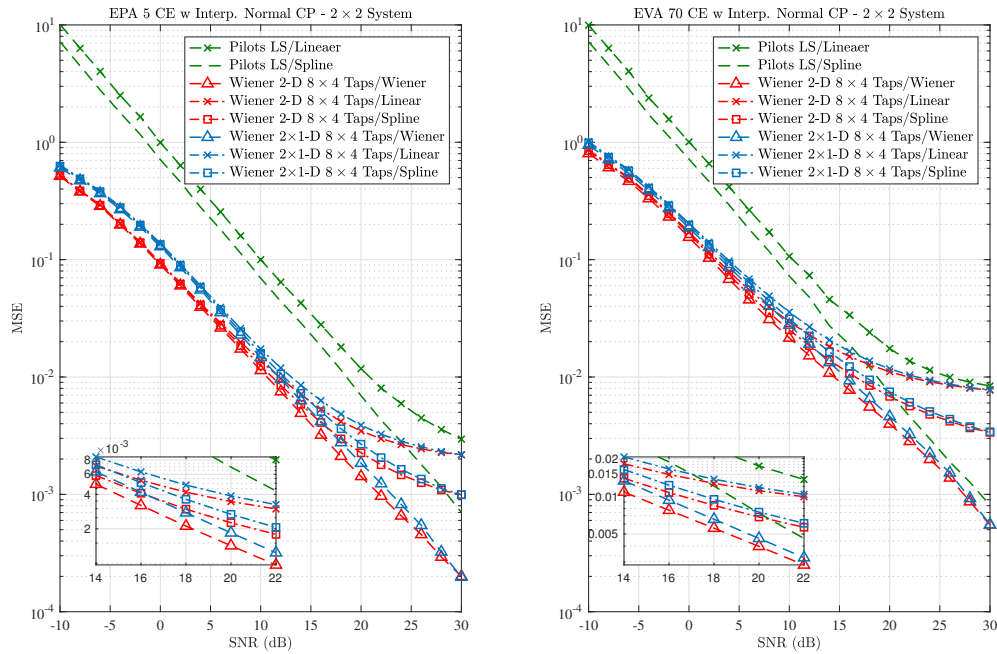


Figure 2.13: MSE vs. SNR with interp. - 2-D and 2×1 -D Wiener - EPA 5 & EVA 70

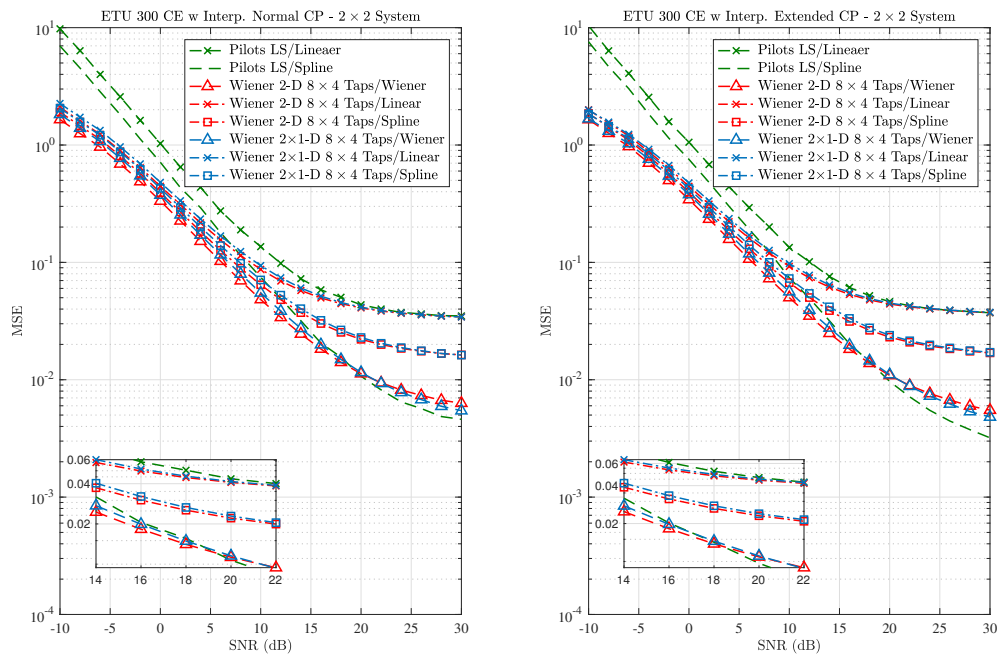


Figure 2.14: MSE vs. SNR with interp. - 2-D and 2×1 -D Wiener - ETU 300 (NCP & ECP)

One important observation for ETU 300 is that after $\text{SNR} \cong 20$ dB, the LS/Spline outperforms 2-D Wiener/Wiener before it hits its associated error floor. This indicates that Wiener interpolation for the ICI affected 2-D Wiener filtered estimates gives poorer performance compared to LS/Spline system, which is also affected by ICI.

Figures 2.15 and 2.16 summarize important simulation results in channel delay profiles EPA 5, EVA 70 and ETU 300, respectively. Our proposed scheme, 2×1 -D Wiener/Spline, provides very similar results to 2-D Wiener/Spline and suffers a bit when compared to the computationally exhaustive 2-D Wiener/Wiener.

From Figure 2.15, the proposed scheme in EPA 5 suffers by almost ~ 0.5 dB at $\text{MSE} = 10^{-2}$. For EVA 70 channel delay profile, which is shown in Figure 2.15, the proposed scheme suffers by almost ~ 3 dB at $\text{MSE} = 10^{-2}$. As for ETU 300 that is shown in Figure 2.16, the proposed scheme hits an error floor of $\text{MSE} = 1.8 \times 10^{-2}$ compared to the MSE error floor of 2-D Wiener/Wiener of $\sim 0.5 \times 10^{-2}$. Results show that performance gap between the proposed scheme and 2-D Wiener/Wiener increases as channel variations increase.

Therefore, the optimal method for CFR estimation would be a combination of both EWA/Spline, 2-D Wiener/Wiener and 2×1 -D Wiener/Spline, where the lower bound is a function of both SNR and the channel statistics. Thus, based on the acceptable MSE threshold for successful detection by the MIMO detector in use, SNR value and channel delay profile, one can select the appropriate filtering and interpolation to be used.

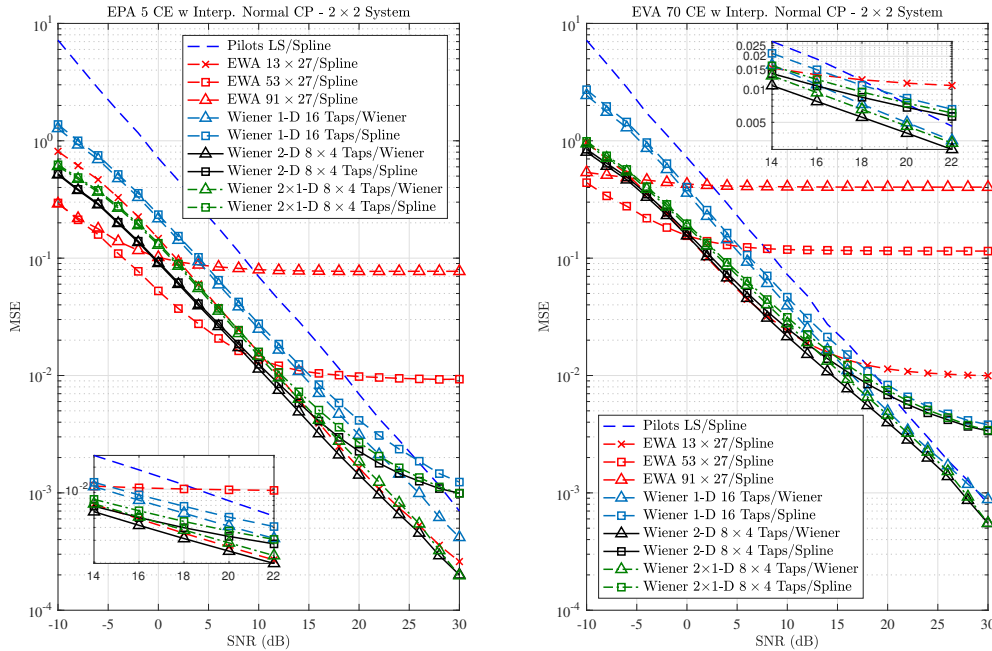


Figure 2.15: MSE vs. SNR for EPA 5 & EVA 70 after interp. - All schemes

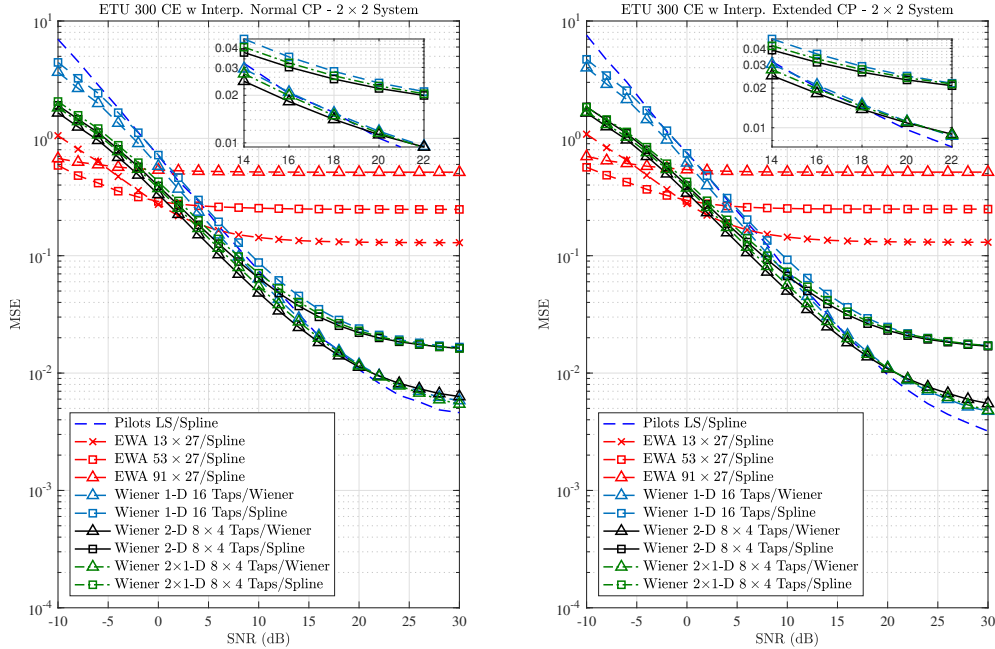


Figure 2.16: MSE vs. SNR for ETU 300 (NCP & ECP) after interp. - All schemes

In the next subsection, simulation results for the proposed time domain filtering and interpolation using 2×1 -D FFT/IFFT instead of 2-D DFT/IDFT are presented and compared to proposed hybrid CE and EWA variations.

2.4.2.1 2×1 -D FFT/IFFT Filtering and Interpolation

For all channel delay profiles shown in Figures 2.17 and 2.18, the proposed scheme, time domain filtering using 2×1 -D FFT/IFFT provides comparable performance to LS and other variations of Wiener up till a certain SNR point depending on the channel conditions. Since time domain filtering is essentially averaging the CFRs in time domain, it is compared to the different EWA variations. EWA-13 outperforms the proposed method in EPA5 and EVA 70 across most of the SNR values. This is due to the huge oscillations at the boundaries of the interpolated data, which is shown in Figure 2.19 at the left-most and right-most interpolated points. In ETU 300, the proposed method outperforms all EWA variations. While EWA requires fine tuning the number of taps in different channels, time domain filtering is governed by the maximum number of CIR taps. Unlike EWA, time domain filtering is capable of using part of the channel statistics to reduce the noise effect on the estimated CFRs. In addition, since the de-noising involved performing FFT to obtain the CIRs, simply oversampling and performing IFFT would produce the CFRs at the non-pilot data locations.

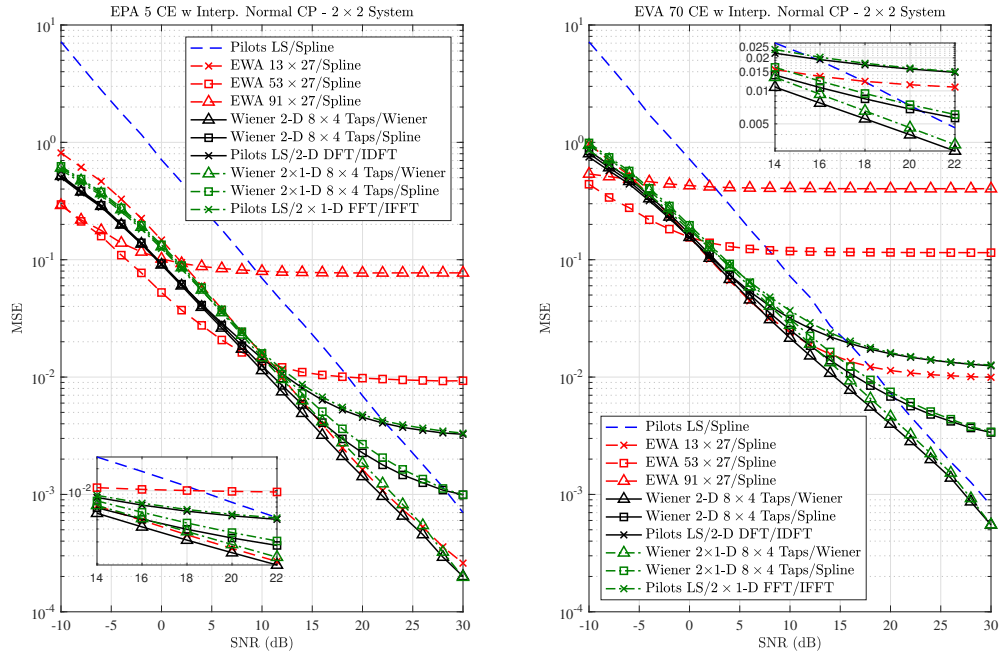


Figure 2.17: MSE vs. SNR with 2×1 -D FFT/IFFT interp. - EPA 5 & EVA 70

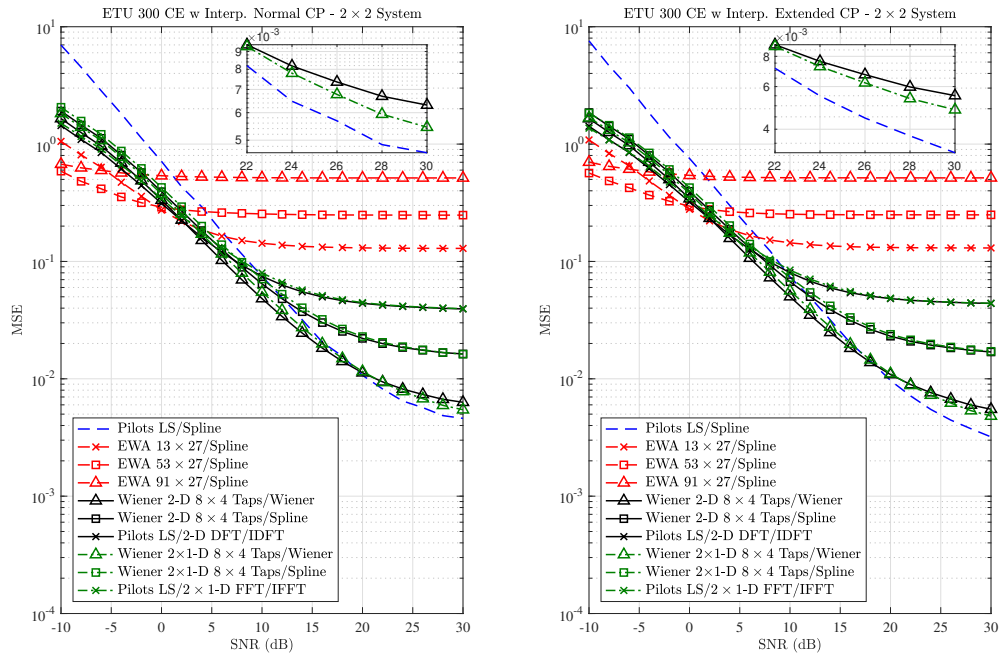


Figure 2.18: MSE vs. SNR with 2×1 -D FFT/IFFT interp. - ETU 300 (NCP & ECP)

Moreover, the proposed implementation scheme performs as good as the 2-D DFT/IDFT,

but with less computational complexity. The drawback of this method is the less desirable performance compared to other different versions of Wiener. Also, since large number of observed data is needed to obtain good interpolation performance, 2×1 -D FFT/IFFT method incurs large latency, is not real time, and requires large data storage.

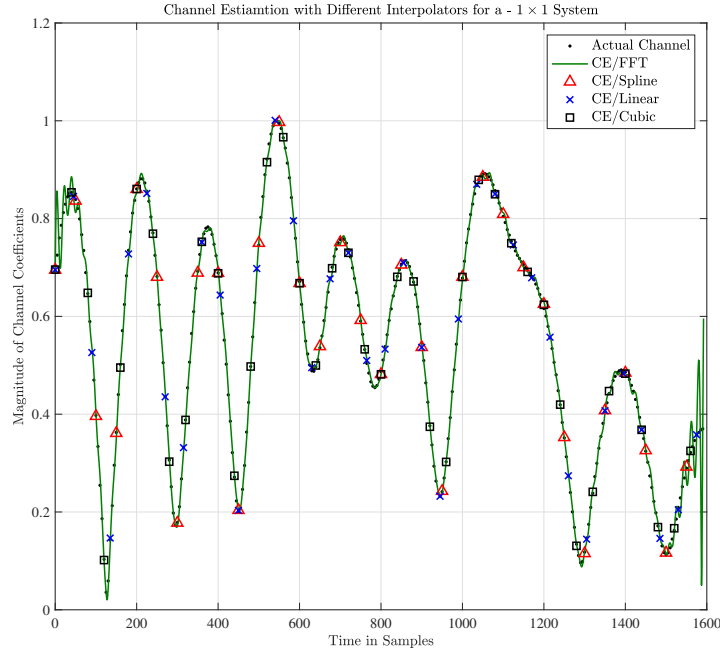


Figure 2.19: CE with different interpolators example

2.4.2.2 Complexity Analysis

Table 2.3 presents the complexity analysis for interpolated CFR estimates for a 1×1 system with a frequency time plane spanning 1200 sub-carriers and 14 OFDM symbols in EPA 5 at $\text{SNR} = 20$ dB. Increasing the number of transmitters or receivers does not make a difference in complexity analysis since there is no cross talk between transmitters at pilot locations, rendering the system as a SISO at pilot locations. Since we are using Wiener filters with $8F \times 4T$ taps, we set the parameters for the EWA windows to span similar number of pilots. We are using the number of multiplications needed at the filtering stage as a metric of the complexity level. On DSP processors, each Complex Multiplication (CM) operation translates to four Real Multiplication (RM) operations. Using EWA filter constitutes real operations in filtering and using Wiener filter constitutes complex operations in filtering. spline interpolation operations are considered as real operations.

Although 2-D Wiener/Wiener outperforms all other schemes in terms of MSE at $\text{SNR} = 20$ dB, this is achieved is at the cost of a relatively higher number of computations as shown

Table 2.3: Comparison of noise reduction techniques complexity for C-RS Port-0 - EPA 5

Algorithm - Filter/Interpolation	Est. # of Operations. Filtering & Interpolation	Total in RM	MSE at SNR = 20 dB
EWA 53×27 /Spline	$200 \times 4 \times 32$ RM & $1200 \times 14 \times 9$ RM	176,800	1.0×10^{-2}
2-D Wiener/Wiener	$200 \times 4 \times 32$ CM & $(1200 \times 14 - 200 \times 4) \times 32$ CM	2,150,400	1.5×10^{-3}
2-D Wiener/Spline	$200 \times 4 \times 32$ CM & $1200 \times 14 \times 9$ RM	253,600	2.3×10^{-3}
2×1 -D Wiener/Spline	$200 \times 4 \times 12$ CM & $1200 \times 14 \times 9$ RM	189,600	2.8×10^{-3}
1-D Wiener-16/Spline	$200 \times 4 \times 16$ CM & $1200 \times 14 \times 9$ RM	202,400	4.0×10^{-3}
Time domain filtering 2×1 -D FFT/IFFT	$200 \times \log_2 200 \times 4$ CM & $1200(4 \times \log_2 1200 + 4 \times$ $\log_2 4 + 14 \times \log_2 14)$ CM	515,112	4.5×10^{-3}
Time domain filtering 2-D DFT/IDFT	$200^2 \times 4 + 200 \times 4^2$ CM & $1200^2 \times 14 + 1200 \times 14^2$ CM	20,558,400	4.5×10^{-3}

in Table 2.3. The proposed scheme, 2×1 -D Wiener/Spline, requires 8.8% and 74.5% the number of computations needed by 2-D Wiener/Wiener and 2-D Wiener/Spline, respectively, while still maintaining relatively similar MSE up till a certain SNR value depending on the channel delay profile. Moreover, the proposed implementation of time domain filtering using 2×1 -D FFT/IFFT requires just 2.5% the number of computations of 2-D DFT/IDFT, while providing similar performance.

In addition to the higher complexity of Wiener filtering compared to EWA, Wiener requires a considerable higher memory to store the $\mathbf{b}_p^{s,v}$ coefficients for different combinations of delay profiles and SNR values. This is needed in order to avoid calculating the filter coefficients on the fly, which introduces great computational complexity because of the inversion process associated with the autocorrelation matrices.

2.4.3 Throughput Conformance Testing in LTE-A System

We have run simulations for full LTE-A system to measure throughput performance for some LTE-A test cases with different TMs, and different RCs at a number of SNR points that were all specified by 3GPP [60]. This was done in order to validate the usage of the proposed CE scheme, namely 2×1 -D Wiener/Spline. The simulation generates one sub-frame at a time and a populated RG is generated and OFDM modulated to get the transmit waveform. The transmitted waveform goes through one of noisy fading channels specified in Table 2.1.

At the receiver side, CE, equalization, demodulation and decoding are all performed and the throughput performance is determined. The results reported in Tables 2.4, 2.5, 2.6, 2.7 and 2.8, where A and B represent the minimum fraction of maximum throughput and the proposed system throughput, respectively, proves that the proposed system can be used in actual practical LTE-A systems.

Table 2.4: TM1 - Single antenna (Port-0)

RC	Channel	MIMO	SNR (dB)	Modulation	A (%)	B (%)
R.1	ETU 70	1×2	-1.9	16-QAM	30	37.6
R.3	EVA 5	1×2	6.7	16-QAM	70	78.8
R.3	ETU 70	1×2	1.4	16-QAM	30	35.1
R.3	ETU 300	1×2	9.4	16-QAM	70	71.1
R.7	EVA 5	1×2	17.7	64-QAM	70	100
R.7	ETU 70	1×2	19	64-QAM	70	95.7

Table 2.5: TM2 - Transmit diversity

RC	Channel	MIMO	SNR (dB)	Modulation	A (%)	B (%)
R.11	EVA 5	2×2	6.8	16-QAM	70	86.2
R.12	EVA 5	2×2	5.9	16-QAM	70	70.7

Table 2.6: TM3: Open loop codebook based precoding

RC	Channel	MIMO	SNR (dB)	Modulation	A (%)	B (%)
R.11	EVA 70	2×2	13	16-QAM	70	74.8
R.12	EVA 70	2×2	12.7	16-QAM	70	71.5
R.35	EVA 200	2×2	20.2	64-QAM	70	79.9
R.14	EVA 70	4×2	14.3	16-QAM	70	88.5

Table 2.7: TM4: Closed loop codebook based spatial multiplexing

RC	Channel	MIMO	SNR (dB)	Modulation	A (%)	B (%)
R.35	EPA 5	2×2	18.9	64-QAM	70	77.3

Table 2.8: TM6: Single layer closed loop codebook based spatial multiplexing

RC	Channel	MIMO	SNR (dB)	Modulation	A (%)	B (%)
R.10	EVA 5	2×2	-2.5	QPSK	70	70.2

2.5 Conclusion

In this Chapter, a new pilot-based lower complexity CE scheme for C-RS and UE-RS in LTE-A DL system was introduced. The proposed scheme uses 2×1 -D Wiener filter to filter the noisy CFR LS estimates at pilot locations only instead of 2-D Wiener filter. Next, cubic spline interpolation is used for data symbol locations instead of 2-D Wiener interpolation. Results indicated that the optimal method for noise filtering would be a combination of both averaging and Wiener filtering, where the lower bound is a function of both SNR and the channel statistics. The performance of the proposed scheme was evaluated in terms of MSE using simulations under various channel conditions. Numerical results showed that the proposed scheme is sub-optimum in the sense that it provides performance that almost matches the 2-D Wiener filter and interpolation, up till certain channel conditions and noise levels, at a much reduced computational complexity. Complexity analysis showed that the proposed scheme requires 8.8% of the number of computations needed by 2-D Wiener filtering with Wiener interpolation. Moreover, accurate description for C-RS pilot locations were given using mathematical equations. Despite the proposed time domain filtering using 2×1 -D FFT/IFFT having less complexity than 2-D DFT/IDFT, its MSE performance is still worse than 2×1 -D Wiener/Spline in different channel conditions. This is due to the huge oscillations produced at the boundaries of the interpolated data. Results indicate that one need to select the appropriate filtering and interpolation combination based on the acceptable MSE threshold for successful detection provided by the system detector in use, SNR value and channel delay profile. Thus, the optimal method for noise reduction after equalization. Finally, simulations in real-life LTE-A proved that the proposed CE system, 2×1 -D Wiener/Spline, achieves the throughput threshold for numerous test cases of the different transmission modes in LTE-A.

Chapter 3

One-Shot Blind Channel Estimation for SIMO-OFDM Systems¹

3.1 Introduction

Since the pilot-based system in Chapter 2 depends on non-data carrying pilot symbols, the spectral efficiency of the pilot-based system is reduced. Moreover, if the channel is ill-behaved, more pilots will be needed to track the channel variations. Hence, it is important to investigate CE algorithms that do not use pilots, which enhances the spectral efficiency especially for future DWCS, which will be required to provide much higher data rates than what is provided now. Therefore, in this Chapter, a novel blind CE technique for SIMO-OFDM DWCS is presented. The system is based on replacing pilots from pilot-based systems by a pair of MASK and MPSK symbols [56]. Hence, first, the system model overview and the OSBCE scheme is presented. Next, OSBCE is proposed for SIMO systems with different variations based on the channel conditions and system requirements. Since numerous implementation schemes are proposed in this Chapter, numerical results and discussions are presented throughout the Chapter after introducing each new variation. The developed systems are compared to the benchmark pilot-based system, to verify that the developed OSBCE can achieve reliable CFRs, with improved spectral efficiency, and with similar complexity. Discussions of numerical results are given with focus MSE performance enhancement as a result of increasing N_{R_x} . Finally, the Chapter is concluded with a summary of results.

¹Related Publications:

1. M. Zourob, A. Al-Dweik and R. Rao, "Different Implementation Schemes for One-Shot Blind Channel Estimation in SIMO-OFDM Systems," 2018 IEEE Conference on Standards for Communications and Networking (IEEE CSCN), to be submitted.

3.2 OSBCE System Model Overview

Consider an N -subcarriers OFDM system modulated by a sequence of N complex data symbols $\mathbf{a} = [A_0, A_1, \dots, A_{N-1}]^T$. Data symbols are selected from a general constellation uniformly such as MPSK, QAM or MASK, with modulation orders M_P, M_Q and M_A , respectively. In pilot-based practical OFDM systems [12], N_P of the subcarriers are reserved for pilot symbols, which can be used for channel estimation and synchronization purposes. For the purpose of this section, we define three sets of indices for the subcarriers, namely, the set of pilots' indices $k_P = \{k_1, k_2, \dots, k_{N_P}\}$, the set of subcarriers' indices adjacent to the pilots are defined as $\vec{k}_P = \{\vec{k}_1, \vec{k}_2, \dots, \vec{k}_{N_P}\}$, where $\vec{k}_i = k_i + \kappa$, $\kappa = 1$, and the set of indices of the remaining data symbols-carrying subcarriers is denoted as k . It is worth noting that the three sets are disjoint, $k_P \cap \vec{k}_P \cap k = \emptyset$.

An N -point IFFT is used to efficiently implement the modulation process. The output of the IFFT process during the ℓ^{th} OFDM block is given by $\mathbf{x}(\ell) = \mathbf{F}^H \mathbf{a}(\ell)$, where \mathbf{F}^H is the normalized $N \times N$ IFFT matrix, and hence, \mathbf{F} is the FFT matrix. The elements of \mathbf{F}^H are defined as $F_{\vec{k}, k} = (1/\sqrt{N})e^{j2\pi\vec{k}k/N}$ where \vec{k} and k denote the row and column indices $\vec{k}, k \in \{0, 1, \dots, N-1\}$, respectively. Since this work deals with an observation window of size 1, we drop the block index notation ℓ in the remaining parts unless it is necessary to include it. A CP is added to maintain the subcarriers' orthogonality in frequency-selective multipath fading channels and eliminate ISI between consecutive OFDM symbols. The added CP of length N_{CP} samples, which is no less than the channel maximum delay spread (L_h), is formed by copying the last N_{CP} samples of \mathbf{x} and appending them in front of the IFFT output to compose the OFDM symbol with a total length $N_t = N + N_{CP}$ samples and a duration of T_t seconds, which can be expressed as,

$$\tilde{\mathbf{x}} = [x_{N-N_{CP}}, \dots, x_{N-1}, x_0, x_1, \dots, x_{N-1}]. \quad (3.1)$$

Then, the complex baseband OFDM symbol during the ℓ^{th} signaling period with the added CP, $\tilde{\mathbf{x}}$, is upsampled, filtered and up-converted to a radio frequency centered at f_c before transmission through the antenna.

At the receiver front-end, the received signal is sampled at a rate $T_s = T_t/N_t$ after down-converting it to baseband. It is assumed that the channel has $L_h + 1$ independent complex multipath components each of which has a gain $h_v \sim \mathcal{CN}(0, 2\sigma_{h_v}^2)$ and delay $v \times T_s$, where $v \in \{0, 1, \dots, L_h\}$. The channel taps are assumed to be time-invariant over one OFDM symbol, but may change over two consecutive symbols, which represents to a quasi-static multipath channel [9]. Then, the received signal after discarding the first N_{CP} CP samples,

and computing the FFT can be expressed as,

$$\begin{aligned} r_k &= H_k A_k + \eta_k \\ \mathbf{r} &= \mathbf{H}\mathbf{a} + \mathbf{n} \end{aligned} \quad (3.2)$$

where $\mathbf{r} \in \mathbb{C}^{N \times 1}$, \mathbf{n} denotes AWGN vector, whose samples are independent and identically distributed (i.i.d.) $\eta_k \sim \mathcal{CN}(0, 2\sigma_\eta^2)$, and \mathbf{H} denotes the CFR, which is defined as,

$$\begin{aligned} \mathbf{H} &= \mathbf{F}^H \mathbf{h} \\ &= \text{diag} \{[H_0, H_1, \dots, H_{N-1}]\} \end{aligned} \quad (3.3)$$

$$H_k = \sum_{v=0}^{L_h} h_v e^{-j2\pi vk/N}. \quad (3.4)$$

It is worth noting that the diagonal elements of \mathbf{H} are highly correlated, particularly the adjacent elements where the correlation coefficient $\rho \triangleq E \{H_k H_k^*\}$ is defined as

$$\rho = E \left\{ \sum_{\hat{v}=0}^{L_h} \sum_{v=0}^{L_h} h_{\hat{v}} h_v^* e^{j2\pi \frac{-(\hat{v}-v)k+\hat{v}}{N}} \right\}. \quad (3.5)$$

Given that h_v and $h_{\hat{v}}$ are mutually independent $\forall v \neq \hat{v}$, then $E \{|h_{\hat{v}}|^2\} = 2\sigma_{h_{\hat{v}}}^2$ and $E \{h_{\hat{v}} h_v^*\} |_{\hat{v} \neq v} = 0$. Thus

$$\rho = \sum_{\hat{v}=0}^{L_h} \sigma_{h_{\hat{v}}}^2 e^{j2\pi \frac{\hat{v}}{N}}. \quad (3.6)$$

Afterwards, the elements of the output of the FFT are fed to a single-tap equalizer such as MMSE or Zero Forcing (ZF), followed by an MLD. ZF equalizer is considered for the following discussion. Thus, the estimated k^{th} symbol can be expressed as

$$\hat{A}_k = \arg \min_{A_k^{(i)}, i \in \mathbb{M}_Q} \left| \frac{\hat{H}_k^*}{|\hat{H}_k|^2} r_k - A_k^{(i)} \right|^2, \quad k \notin k_P \quad (3.7)$$

where $A_k^{(i)}$ are the possible values of the data symbols, \mathbb{M}_Q is the modulation subspace, and \hat{H}_k is the estimated CFR at the k^{th} subcarrier. It is worthwhile to mention that single-tap frequency-domain MMSE and ZF detectors provide approximately similar performance in quasi-static SISO systems [79, 80]. Nevertheless, ZF is considered, since the MMSE detector has higher computational complexity.

The data symbols in OFDM-based systems, such as LTE-A, are distributed in a time/freq-

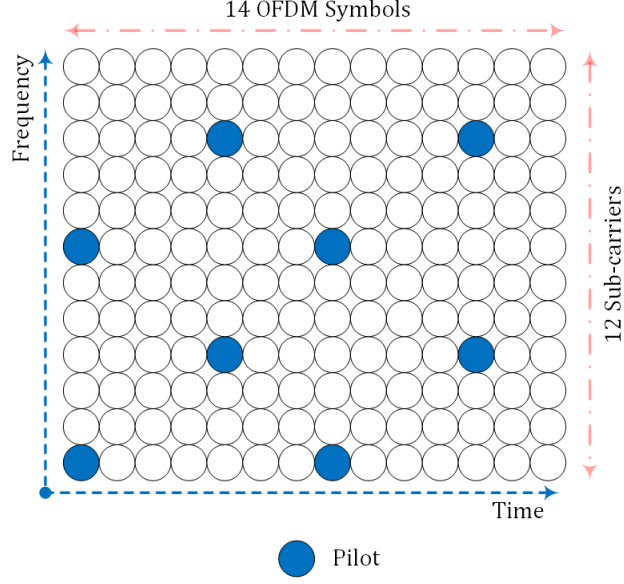


Figure 3.1: Time/Frequency grid in LTE-A

uency plane as shown in Figure 3.1, and CE for such structure is typically performed over two steps after pilots are extracted, and with no noise reduction techniques under consideration. First, initial CFRs are obtained at pilot symbols positions using LS estimation,

$$\hat{H}_k = \frac{r_k}{A_k}, \quad k \in k_P \quad (3.8)$$

where A_k , the actual pilot symbols values, are assumed to be known by the receiver. Since $r_k = H_k A_k + \eta_k$, the CFR estimates can be expressed as

$$\hat{H}_k = H_k + \hat{\eta}_k \quad (3.9)$$

where $H_k \sim \mathcal{CN}(0, 2\sigma_H^2)$ and $\hat{\eta}_k \sim \mathcal{CN}\left(0, \frac{2\sigma_\eta^2}{|A_k|^2}\right)$.

Once the initial CFR $\hat{H}_k \forall k \in k_P$ is obtained, noise reduction techniques that were thoroughly covered in Chapter 2 can be utilized to further improve the quality of the estimates. By exploiting the frequency and time correlation of the channel, 2×1 -D Wiener filtering at pilot locations can be used, followed by cubic spline interpolation for the remaining REs in the RG. However, in order to investigate the basic performance of the proposed OSBCE with the pilot-based system that is used as the benchmark [43], noise reduction and interpolation schemes from Chapter 2 are not going to be included in this Chapter.

In the special case where A_k belongs to a CMM constellation, only the phase of the CFR

Table 3.1: Correlation Coefficient ρ for common channel models($N = 256$)

Channel model	Channel Profile	$ \rho $	$\arg\{\rho\}$
cost207RAx4	Rural Area (RAx), 4 taps	0.99998	0.00169
cost207TUx6	Typical Urban (TUx), 6 taps	0.99475	0.05616
cost207TUx12	Typical Urban (TUx), 12 taps	0.99556	0.07981
cost207BUx6	Bad Urban (BUx), 6 taps	0.97447	0.19145

is needed for coherent MLD, which can be expressed as

$$\hat{A}_k = \arg \min_{A_k^{(i)}, i \in \mathbb{M}_P} \left| e^{-j\hat{\theta}_k} r_k - A_k^{(i)} \right|^2 \quad (3.10)$$

where $\hat{\theta}_k \triangleq \arg\{\hat{H}_k\}$ is the estimated version of $\theta_k \triangleq \arg\{H_k\}$. Table 3.1 indicates that for most practical channels, $|\rho| \approx 1$ and $\arg\{\rho\} \approx 0$, where ρ is the correlation coefficient, and that indicates that $H_k \approx H_{\vec{k}}$ [56]. Hence, the output of the FFT at subcarriers k and \vec{k} , where $\vec{k} = k + \kappa$, $\kappa = 1$, can be expressed as

$$r_k = H_k A_k + \eta_k \quad (3.11)$$

and

$$\begin{aligned} r_{k+\kappa} &= H_{k+\kappa} A_{k+\kappa} + \eta_{k+\kappa} \\ r_{k+\kappa} &\approx H_k A_{k+\kappa} + \eta_{k+\kappa}. \end{aligned} \quad (3.12)$$

Equation (3.12) can be further simplified to $r_{k+\kappa} \approx H_k A_{k+\kappa}$ by dropping AWGN at high SNRs. Hence, by wisely selecting the modulation types for the data symbols A_k and $A_{k+\kappa}$, the information symbol A_k can be blindly recovered without explicit knowledge of H_k . To achieve this goal, assume A_k is modulated using MPSK and $A_{k+\kappa}$ is modulated using unipolar MASK, $A_{k+\kappa} \in \mathbb{R}^+$, where \mathbb{R}^+ is the set of real positive numbers excluding zero. Therefore, MLD of A_k needs only knowledge of $\hat{\theta}_k$, which can be estimated by noting that $\arg\{r_{k+\kappa}\} = \arg\{H_{k+\kappa} A_{k+\kappa} + \eta_{k+\kappa}\} \triangleq \hat{\theta}_{k+\kappa} \approx \theta_k$. It is considered a preliminary estimate since it includes the AWGN component and depends on the correlation with the adjacent subcarrier. Hence, the preliminary estimate of the phase of the CFR $\hat{\theta}_{k+\kappa}$ can be used to preliminary estimate the symbol A_k , where

$$\hat{A}_k = \arg \min_{A_k^{(i)}, i \in \mathbb{M}_P} \left| e^{-j\hat{\theta}_{k+\kappa}} r_k - A_k^{(i)} \right|^2. \quad (3.13)$$

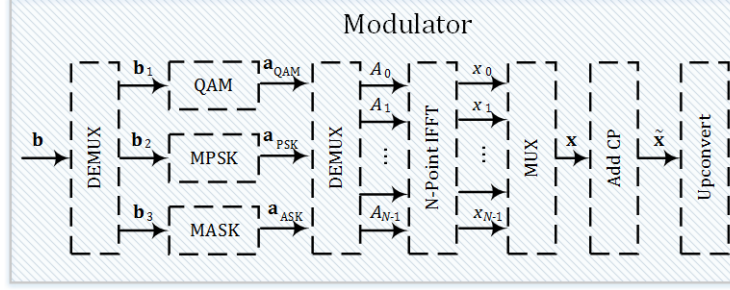


Figure 3.2: Block diagram of the proposed OFDM modulator

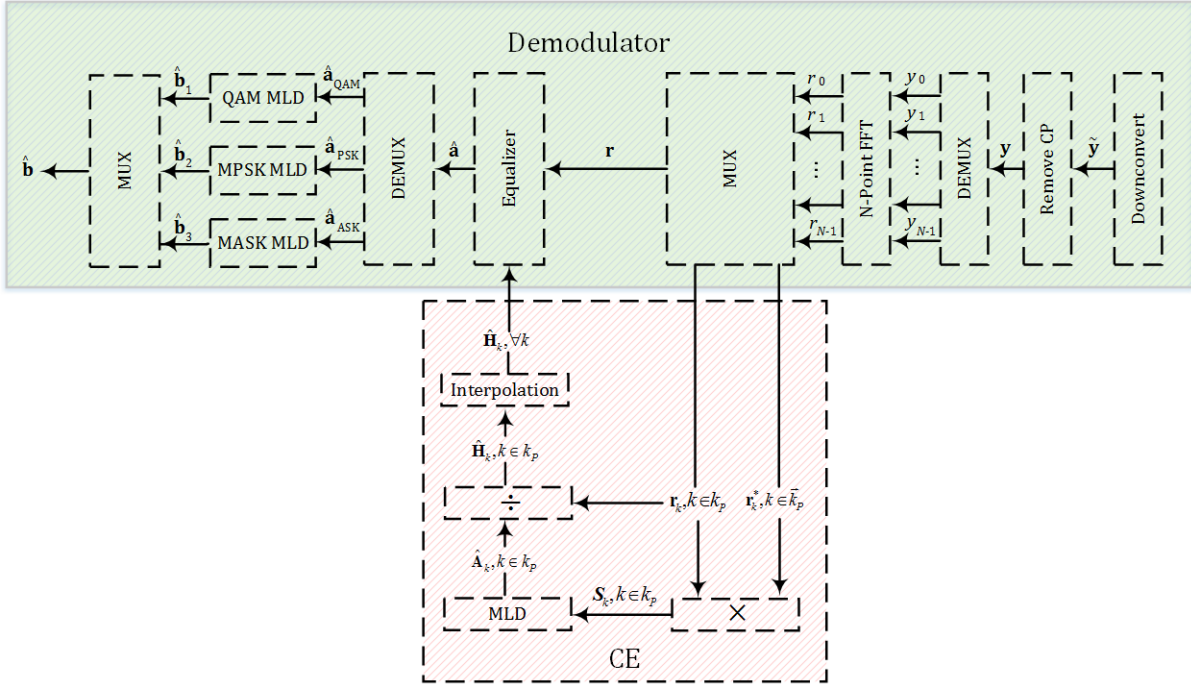


Figure 3.3: Block diagram of the proposed OFDM demodulator

Moreover, since $A_{k+\kappa} \in \mathbb{R}^+$ and A_k has CMM, the MLD in (3.13) can also be realized as,

$$\hat{A}_k = \arg \min_{A_k^{(i)}, i \in \mathbb{M}_P} \left| r_k r_{k+1}^* - A_k^{(i)} \right|^2. \quad (3.14)$$

Once \hat{A}_k is obtained, \hat{H}_k can be computed in a Decision Directed (DD) manner as expressed in (3.8),

$$\hat{H}_k = \frac{r_k}{\hat{A}_k}, \quad k \in k_P. \quad (3.15)$$

Thus, the OSBCE scheme can be employed by replacing pilot symbols with data symbols that have CMM, and using MASK to modulate the adjacent subcarriers, $A_{k+\kappa} \in \mathbb{R}^+$. Finally,

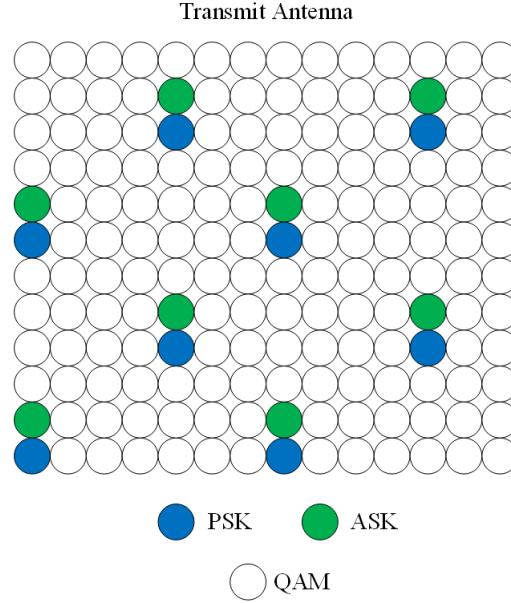


Figure 3.4: Proposed SISO F.OSBCE grid in LTE-A

interpolation is used to find \hat{H}_k , $k \notin k_P$ at non-pilot locations using \hat{H}_k , $k \in k_P$ at MPSK pilot locations using any of the techniques that were presented in Chapter 2, or any technique that is originally used in conjunction with pilot-based systems [32, 41, 42]. Transmitter and receiver block diagrams for the OSBCE scheme under consideration are shown in Figures 3.2 and 3.3, respectively [56]. At the transmitter, the information bits are passed through a channel encoder with the output split into three parallel streams, and each stream is modulated using the corresponding modulation scheme. The streams are combined to form the OFDM blocks/symbols, and the rest is similar to a conventional OFDM system.

Figure 3.4 shows the OSBCE system RG. It is noticed that the OSBCE transmitter is generally similar to other practical OFDM-based systems such as LTE-A, however, the pilot subcarriers within an OFDM block are replaced with MPSK data symbols while the adjacent subcarriers are modulated using MASK. It is worthwhile to mention that pilot symbols in LTE-A are originally QPSK modulated and, most importantly, do not carry any data-specific information. Moreover, since the adjacent symbols to the pilots can be QPSK, 16 or 64 QAM modulated, channel information cannot be directly acquired from the modulation techniques. Hence, MASK is used to obtain an estimate of the channel phase directly from the received symbols. Consequently, that allows for coherent detection of the MPSK symbols at pilots locations. The MASK average power of the modulated symbols $A_{k+\kappa}$ can be normalized to unity according to $\mathcal{P}_s = \frac{1}{M_A} \sum_{i=0}^{M_A-1} \left(A_{k+\kappa}^{(i)} \right)^2 = 1$. If equally

spaced amplitudes are assumed [44], where $\delta \triangleq A_{k+\kappa}^{(i+1)} - A_{k+\kappa}^{(i)}$, $A_{k+\kappa}^{(i)}$ can be written as

$$A_{k+\kappa}^{(i)} = (i + 1) \times \delta, i \in \{0, 1, \dots, M_A - 1\} \quad (3.16)$$

where,

$$\delta = \sqrt{\frac{6}{(2M_A + 1)(M_A + 1)}}. \quad (3.17)$$

The modulation type and order for all other subcarriers other than the pilots' and their adjacent subcarriers can be chosen randomly. Though the OSBCE is employed for LTE-A scenario in this thesis, it can be utilized in other OFDM-based systems by changing the frequency spacing Δ_f and the time spacing Δ_t based on the respective system specifications.

It is noticed from the description of the aforementioned system that the computational complexity of the OSBCE is comparable to that of LS estimation using pilots. If re-detection of the pilot MPSK symbols is applied after the estimation of $\hat{\mathbf{H}}$, the only added complexity, compared to pilot systems, will result from N_P complex multiplications and N_P MLD detections for the MPSK symbols. Hence, the OSBCE complexity is similar to pilot-based CE and is generally low.

3.3 SIMO-OFDM $1 \times N_{R_x}$ OSBCE System Models

Using multiple antennas at the receiver is one form of space diversity, called receiver diversity. It is considered a special case of $N_{T_x} \times N_{R_x}$ MIMO systems with $m = 1, n \in \{1, 2, \dots, N_{R_x}\}$. To simply explain the advantage of using multiple receive antennas, assume a 1×1 SISO system, with an outage probability proportional $1/\chi$ due to the random multipath channel coefficient between the single transmit antenna and the single receive antenna. Outage occurs if the signal drops below the noise power level. If N_{R_x} antennas were to be installed at the receiver, there will be N_{R_x} random coefficients. The probability that all random multipath channel coefficients cause the transmitted signal power to fall below the noise power would be proportional to $(1/\chi)^{N_{R_x}}$. This means that by using N_{R_x} receive antennas, the probability that the transmitted signal is lost at all N_{R_x} receive antennas would be much lower. One of the aims of using space diversity is to achieve array gain, which is a result of coherent combining of multiple branches. Array gain can be simply called power gain and it is defined as the average effective combined SNR divided by the average branch SNR. In receiver diversity, array gain is achieved even if there is no fading.

In order to obtain the array/SNR gain, the different signals replicas at the receiver need to be combined. In general, the replicas from the N_{R_x} receive antennas are linearly

combined using the complex weighted sum of each branch after the phase of each received path is aligned. This means that the signals from each branch are coherently combined. Several methods are used to combine the branches such as MRC and Equal Gain Combining (EGC). The difference between each scheme is the type of tradeoff between performance and complexity. For the purpose of our work, we briefly explain MRC and EGC.

3.3.1 Review of Multiple Antenna Linear Receivers

Maximum Ratio Combining

If the channel is assumed to be a 1-tap Rayleigh channel with $h \sim \mathcal{CN}(0, 2\sigma_h^2)$ and the channel is time-invariant during one signaling period, there will be no need to use OFDM with a slow flat fading. Hence, the channel would be simply multiplied by the transmitted signal. Also, the modulation in use is assumed to be BPSK. Thus, the received signal at the n^{th} antenna, where $n \in \{1, 2, \dots, N_{R_x}\}$, the associated instantaneous SNR, and the associated average SNR are given as

$$r_n = h_n A + \eta_n \quad (3.18)$$

$$\gamma_n = \frac{|h_n A|^2}{E\{|\eta_n|^2\}} = \frac{E_b |h_n|^2}{\mathcal{N}_o} \quad (3.19)$$

$$\begin{aligned} \bar{\gamma}_n = E\{\gamma_n\} &= E\left\{\frac{E_b |h_n|^2}{\mathcal{N}_o}\right\} \\ &= \frac{E_b}{\mathcal{N}_o} E\{|h_n|^2\} \\ &= \frac{E_b 2\sigma_h^2}{\mathcal{N}_o} \end{aligned} \quad (3.20)$$

where $\eta \sim \mathcal{CN}(0, 2\sigma_\eta^2)$ is AWGN noise with total noise power $\mathcal{N}_o = 2\sigma_\eta^2$, $E\{|h_n|^2\} = E\{h_n h_n^*\} = 2\sigma_h^2$ is the variance of h_n with mean equal to 0, and E_b is the energy per bit. Since MRC's design criteria is to maximize the combiner's SNR, Cauchy-Schwarz inequality dictates that the n^{th} equalization coefficient, w_n , be linearly proportional to h_n [25]. In some sense, this is effectively the matched filter for the fading signal, which is known to be optimal in the single antenna case.

Hence, equalization in MRC is performed by multiplying the n^{th} received signal by the complex conjugate of the a priori known channel coefficients $w_{mrc,n} = h_n = |h_n| e^{j\theta_n}$. To

decode for A , the N equalized signals are summed as follows,

$$\begin{aligned}\tilde{r}_{mrc} &= \sum_{n=1}^{N_{R_x}} r_n w_{mrc,n}^* = \sum_{n=1}^{N_{R_x}} (w_{mrc,n}^* h_n A + \tilde{\eta}_{mrc,n}) \\ &= A \sum_{n=1}^{N_{R_x}} |h_n|^2 + \sum_{n=1}^{N_{R_x}} \tilde{\eta}_{mrc,n}\end{aligned}\quad (3.21)$$

where $\tilde{\eta}_{mrc,n} = \eta_n w_{mrc,n}^*$. Knowing that,

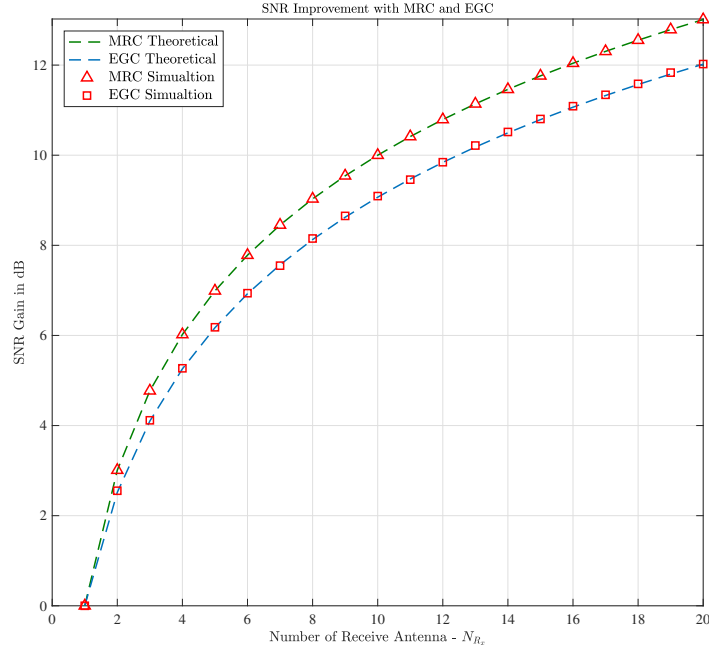
$$\begin{aligned}E \left\{ \left(\sum_{n=1}^{N_{R_x}} \eta_n h_n^* \right) \left(\sum_{\hat{n}=1}^{N_{R_x}} \eta_{\hat{n}} h_{\hat{n}}^* \right)^* \right\} &= \begin{cases} \sum_{n=1}^{N_{R_x}} \sum_{\hat{n}=1}^{N_{R_x}} (E \{ \eta_n \eta_{\hat{n}}^* \} E \{ h_n h_{\hat{n}}^* \}) & n \neq \hat{n} \\ \sum_{n=1}^{N_{R_x}} (E \{ \eta_n \eta_n^* \} E \{ h_n h_n^* \}) & n = n \end{cases} \\ &= \begin{cases} 0 & n \neq \hat{n} \\ \sum_{n=1}^{N_{R_x}} (E \{ |\eta_n|^2 \} E \{ |h_n|^2 \}) & n = n \end{cases} \\ &= \begin{cases} 0 & n \neq \hat{n} \\ 2N_{R_x} \sigma_h^2 \mathcal{N}_o & n = n \end{cases}\end{aligned}\quad (3.22)$$

the combiner's instantaneous SNR will be

$$\gamma_{mrc} = \frac{\left(\left| A \sum_{n=1}^{N_{R_x}} |h_n|^2 \right| \right)^2}{E \left\{ \left| \sum_{n=1}^{N_{R_x}} \tilde{\eta}_{mrc,n} \right|^2 \right\}} = \frac{E_b \left| \sum_{n=1}^{N_{R_x}} |h_n|^2 \right|^2}{2N_{R_x} \sigma_h^2 \mathcal{N}_o}.\quad (3.23)$$

Hence, the average SNR is given as

$$\begin{aligned}\bar{\gamma}_{mrc} &= E \{ \gamma_{mrc} \} = E \left\{ \frac{E_b \left| \sum_{n=1}^{N_{R_x}} |h_n|^2 \right|^2}{2N_{R_x} \sigma_h^2 \mathcal{N}_o} \right\} \\ &= \frac{E_b}{2N_{R_x} \sigma_h^2 \mathcal{N}_o} E \left\{ \left| \sum_{n=1}^{N_{R_x}} |h_n|^2 \right|^2 \right\} \\ &= \frac{E_b}{2N_{R_x} \sigma_h^2 \mathcal{N}_o} E \left\{ \left| \sum_{n=1}^{N_{R_x}} |h_n|^2 \right| \left| \sum_{n=1}^{N_{R_x}} |h_n|^2 \right| \right\} \\ &= \frac{E_b}{2N_{R_x} \sigma_h^2 \mathcal{N}_o} \left(\left| \sum_{n=1}^{N_{R_x}} E \{ |h_n|^2 \} \right| \left| \sum_{n=1}^{N_{R_x}} E \{ |h_n|^2 \} \right| \right) \\ &= \frac{E_b}{2N_{R_x} \sigma_h^2 \mathcal{N}_o} (2N_{R_x} \sigma_h^2) (2N_{R_x} \sigma_h^2)\end{aligned}$$


 Figure 3.5: SNR gain vs. N_{R_x}

$$= N_{R_x} \frac{2\sigma_h^2 E_b}{\mathcal{N}_o} = N_{R_x} \bar{\gamma}_n. \quad (3.24)$$

Therefore, the output SNR of the MRC is the sum of all SNRs from all branches, and on average, the SNR improves by N_{R_x} , which is the array gain. However, the technique requires the weights to vary with the fading signals, meaning that CE is required.

Equal Gain Combining

On the other hand, EGC avoids this problem by setting unit gain at each branch, and performing co-phasing to the received signal at each branch. Therefore, Equalization is performed by multiplying the n^{th} received signal by the complex conjugate of the apriori known phase of $h_n = |h_n| e^{j\theta_n}$. Thus, the equalizer weight for the n^{th} branch would be $w_{egc,n} = e^{j\theta_n}$. To decode for A , the N_{R_x} phase-compensated signals are summed as follows,

$$\begin{aligned} \tilde{r}_{egc} &= \sum_{n=1}^{N_{R_x}} r_n w_{egc,n}^* \\ &= \sum_{n=1}^{N_{R_x}} (|h_n| A + \tilde{\eta}_{egc,n}) \end{aligned}$$

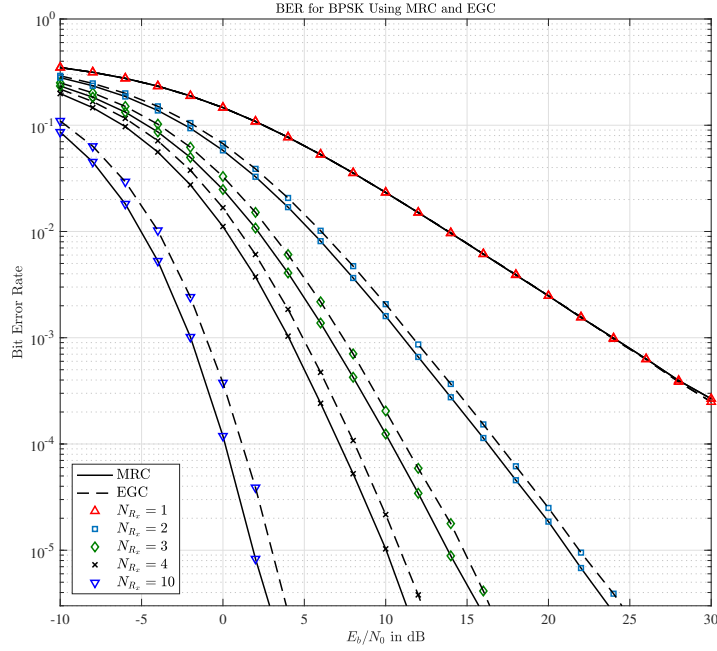


Figure 3.6: BER vs. SNR using MRC and EGC

$$= \sum_{n=1}^{N_{R_x}} |h_n| A + \sum_{n=1}^{N_{R_x}} \tilde{\eta}_{egc,n} \quad (3.25)$$

where $\tilde{\eta}_{egc,n} = \eta w_{egc,n}^*$. Knowing that

$$E \left\{ \left(\sum_{n=1}^{N_{R_x}} \eta_n e^{-j\theta_n} \right) \left(\sum_{\hat{n}=1}^{N_{R_x}} \eta_{\hat{n}} e^{-j\theta_{\hat{n}}} \right)^* \right\} = \begin{cases} \sum_{n=1}^{N_{R_x}} \sum_{\hat{n}=1}^{N_{R_x}} (E \{ \eta_n \eta_{\hat{n}}^* \} E \{ e^{j\theta_{\hat{n}}} e^{-j\theta_n} \}) & n \neq \hat{n} \\ \sum_{n=1}^{N_{R_x}} (E \{ \eta_n \eta_n^* \} E \{ e^{j\theta_n} e^{-j\theta_n} \}) & n = n \end{cases} \\ = \begin{cases} 0 & n \neq \hat{n} \\ N_{R_x} \mathcal{N}_o & n = n \end{cases}, \quad (3.26)$$

the combiner's instantaneous SNR will be

$$\gamma_{egc} = \frac{\left| \sum_{n=1}^{N_{R_x}} |h_n| A \right|^2}{E \left\{ \left| \sum_{n=1}^{N_{R_x}} \tilde{\eta}_{egc,n} \right|^2 \right\}} \\ = \frac{E_b \left| \sum_{n=1}^{N_{R_x}} |h_n| \right|^2}{N_{R_x} \mathcal{N}_o}. \quad (3.27)$$

Knowing that

$$\begin{aligned}
 E \left\{ \left| \sum_{n=1}^{N_{R_x}} |h_n| \right|^2 \right\} &= \begin{cases} E \left\{ \sum_{n=1}^{N_{R_x}} \sum_{\hat{n}=1}^{N_{R_x}} |h_n| |h_{\hat{n}}| \right\} & \hat{n} \neq n \\ E \left\{ \sum_{n=1}^{N_{R_x}} |h_n|^2 \right\} & n = n \end{cases} \\
 &= \begin{cases} \sum_{n=1}^{N_{R_x}} \left(E \{ |h_n| \} \sum_{\hat{n}=1}^{N_{R_x}} E \{ |h_{\hat{n}}| \} \right) & \hat{n} \neq n \\ \sum_{n=1}^{N_{R_x}} E \{ |h_n|^2 \} & n = n \end{cases} \\
 &= \begin{cases} \sum_{n=1}^{N_{R_x}} \left(E \{ |h_n| \} [(N_{R_x} - 1) \sqrt{\frac{\pi}{2}} \sigma_h] \right) & n \neq \hat{n} \\ 2N_{R_x} \sigma_h^2 & n = n \end{cases} \\
 &= \begin{cases} N_{R_x} \sqrt{\frac{\pi}{2}} \sigma_h [(N_{R_x} - 1) \sqrt{\frac{\pi}{2}} \sigma_h] & n \neq \hat{n} \\ 2N_{R_x} \sigma_h^2 & n = n \end{cases} \\
 &= \begin{cases} N_{R_x} (N_{R_x} - 1) \frac{\pi}{2} \sigma_h^2 & n \neq \hat{n} \\ 2N_{R_x} \sigma_h^2 & n = n \end{cases} \tag{3.28}
 \end{aligned}$$

where $E \{ |h_n| \} = \sqrt{\frac{\pi}{2}} \sigma_h$ is the mean for the envelop, $|h_n|$, of the Rayleigh distributed channel h_n , the average SNR will be

$$\begin{aligned}
 \bar{\gamma}_{egc} &= E \{ \gamma_{egc} \} \\
 &= E \left\{ \frac{E_b \left| \sum_{n=1}^{N_{R_x}} |h_n| \right|^2}{N_{R_x} \mathcal{N}_o} \right\} \\
 &= \frac{E_b}{N_{R_x} \mathcal{N}_o} E \left\{ \left| \sum_{n=1}^{N_{R_x}} |h_n| \right|^2 \right\} \\
 &= \frac{E_b}{N_{R_x} \mathcal{N}_o} \left[2N_{R_x} \sigma_h^2 + N_{R_x} (N_{R_x} - 1) \frac{\pi}{2} \sigma_h^2 \right] \\
 &= \frac{2\sigma_h^2 E_b}{\mathcal{N}_o} \left[1 + (N_{R_x} - 1) \frac{\pi}{4} \right] \\
 &= \bar{\gamma}_n \left[1 + (N_{R_x} - 1) \frac{\pi}{4} \right]. \tag{3.29}
 \end{aligned}$$

The goal of the previous analysis is to demonstrate that, despite having significantly simpler implementation, EGC results in improved SNR that is comparable to that of the optimal MRC [1]. The EGC array gain is $1 + (N_{R_x} - 1) \frac{\pi}{4}$. The SNR of both combiners increases linearly with N_{R_x} as shown in Figure 3.5. Moreover, it is worth noting that the maximum rate of improvement happens at $N_{R_x} = 2$, and the rate of improvement decreases

as the number of antennas increase. No closed form solution for the BER of EGC with N_{R_x} antennas has been found, but several works in the literature have investigated the BER performance in different fading channels [81]. Figure 3.6 shows how the BER improves when the number of receive antennas increase using MRC and EGC.

For MPSK modulation schemes, equalization by the phase of the channel coefficients is sufficient, which is the idea behind the blind OSBCE method introduced in this chapter. Therefore, EGC is considered for the rest of the discussion. In the following sections, OSBCE across frequency, time and time/frequency are presented. The system model setup and defined variables from Section 3.2 are carried over to the different SIMO cases.

3.3.2 SIMO 1-D F.OSBCE - Across Frequency

The pilots are distributed across one dimension (frequency) within one OFDM symbol, which means this system model is not susceptible to high Doppler frequencies due to high mobility, but, is effected by the selectivity of the channel. Assume an RG of 12 subcarriers and 14 OFDM symbols as shown in Figure 3.7. The indexing starts from 0 to 11 and 0 to 13 for k (vertical axis, subcarriers) and ℓ (horizontal axis, OFDM symbols), respectively. This is a special case of the $mT_x \times nR_x$ MIMO system, namely SIMO, where $m = 1, n \in \{1, 2, \dots, N_{R_x}\}$. Since this work deals with an observation window of size 1, the block index notation ℓ is dropped in the remaining parts unless it is necessary to include it.

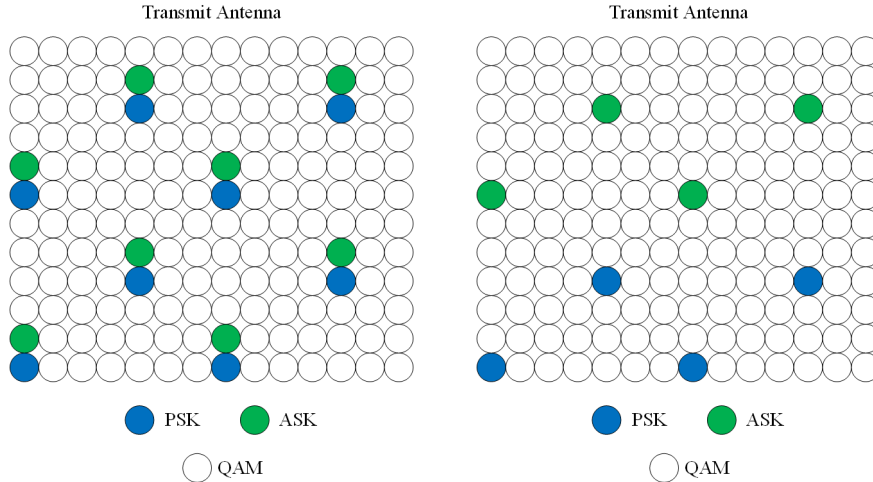


Figure 3.7: $1 \times N_{R_x}$ Frequency OSBCE system - $\kappa \in \{1, 6\}$

The MPSK and MASK symbols are transmitted at subcarriers k and $k + \kappa$, respectively. After dropping the N_{CP} CP samples, the received post-FFT samples from the transmit antenna at time index ℓ and subcarriers $k, k + \kappa$ for receive antenna n , where κ is the

subcarrier spacing between the MASK and MPSK symbols,

$$r_k^{(n)} = A_k H_k^{(n)} + \eta_k^{(n)} \quad (3.30)$$

$$r_{k+\kappa}^{(n)} = A_{k+\kappa} H_{k+\kappa}^{(n)} + \eta_{k+\kappa}^{(n)}. \quad (3.31)$$

The pattern is repeated for different κ as shown in Figure 3.7 . Now, we can decode for A_k as follows,

$$\begin{aligned} \mathcal{S}_k^{(n)} &= r_k^{(n)} / r_{k+\kappa}^{(n)} \\ &= \frac{H_k^{(n)} A_k + \eta_k^{(n)}}{H_{k+\kappa}^{(n)} A_{k+\kappa} + \eta_{k+\kappa}^{(n)}} \\ &= \frac{H_k^{(n)} A_k + \eta_k^{(n)}}{\left| H_{k+\kappa}^{(n)} A_{k+\kappa} + \eta_{k+\kappa}^{(n)} \right| e^{j\hat{\theta}_{k+\kappa}^{(n)}}} \\ &= \frac{A_k \left| H_k^{(n)} \right| e^{j(\theta_k^{(n)} - \hat{\theta}_{k+\kappa}^{(n)})} + \left| \eta_k^{(n)} \right| e^{j(\arg(\eta_k^{(n)}) - \hat{\theta}_{k+\kappa}^{(n)})}}{\left| H_{k+\kappa}^{(n)} A_{k+\kappa} + \eta_{k+\kappa}^{(n)} \right|} \\ &= \frac{1}{\left| r_{k+\kappa}^{(n)} \right|} \left(\left| H_k^{(n)} \right| e^{j\vartheta_k^{(n)}} A_k + \check{\eta}_k^{(n)} \right) \end{aligned} \quad (3.32)$$

where $\vartheta_k^{(n)} = \theta_k^{(n)} - \hat{\theta}_{k+\kappa}^{(n)}$ and $\check{\eta}_k^{(n)} = \left| \eta_k^{(n)} \right| e^{j(\arg(\eta_k^{(n)}) - \hat{\theta}_{k+\kappa}^{(n)})}$. The n^{th} receiver branch can now detect the transmitted symbol A_k from the phase of $\mathcal{S}_k^{(n)}$, since it has been equalized by an imperfect CFR, namely $r_{k+\kappa}^{(n)}$. However, since there are N_{R_x} receive antennas, EGC is employed to enhance the SNR of the detected symbol. EGC is applied by adding all the co-phased $\mathcal{S}_k^{(n)}$, $n \in \{1, 2, \dots, N_{R_x}\}$, from the different receive antennas as follows,

$$\sum_{n=1}^{N_{R_x}} \mathcal{S}_k^{(n)} = A_k \sum_{n=1}^{N_{R_x}} \frac{\left| H_k^{(n)} \right| e^{j\vartheta_k^{(n)}}}{\left| r_{k+\kappa}^{(n)} \right|} + \sum_{n=1}^{N_{R_x}} \frac{\check{\eta}_k^{(n)}}{\left| r_{k+\kappa}^{(n)} \right|}. \quad (3.33)$$

The combiner's MLD detection for the MPSK symbol would only need the phase of $\sum_{n=1}^{N_{R_x}} \mathcal{S}_k^{(n)}$. Since $\left| H_k^{(n)} \right|$ and $\left| r_{k+\kappa}^{(n)} \right|$ are scalar entities, they have no effect on the MLD, while $\vartheta_k^{(n)}$ and $\check{\eta}_k^{(n)}$ are the two sources of phase error that would effect the detection process. From the discussion of EGC, it was demonstrated that noise effect in general is reduced by collecting the signal from multiple receivers. Moreover, it is worth mentioning that κ inherently affects $\vartheta_k^{(n)} = \theta_k^{(n)} - \hat{\theta}_{k+\kappa}^{(n)}$. As κ increases, the correlation between the associated CFRs decreases and $E \left\{ H_k^{(n)} \left(H_{k+\kappa}^{(n)} \right)^* \right\} \approx e^{j \times 0}$ no longer holds, thus, producing more phase

error in the MLD detection. Using MLD, the initial estimate for \hat{A}_k is expressed as,

$$\hat{A}_k = \arg \min_{A_k^{(i)}, i \in \mathbb{M}_P} \left| \sum_{n=1}^{N_{Rx}} \mathcal{S}_k^{(n)} - A_k^{(i)} \right|^2. \quad (3.34)$$

Using \hat{A}_k , $\hat{H}_k^{(n)}$ at each branch can be found using LSE as follows,

$$\begin{aligned} \hat{H}_k^{(n)} &= \frac{r_k^{(n)}}{\hat{A}_k} \\ &= \frac{A_k H_k^{(n)} + \eta_k}{\hat{A}_k} \\ &\approx H_k^{(n)} + \hat{\eta}_k \end{aligned} \quad (3.35)$$

where $\hat{\eta}_k^{(n)} = \left| \eta_k^{(n)} \right| e^{j(\arg\{\eta_k^{(n)}\} - \arg\{\hat{A}_k\})}$. The source of improvement in this system is the added accuracy in the initial detection of the MPSK symbol, which would lead to better estimation of $H_k^{(n)}$.

3.3.2.1 Results and Discussion - $\kappa \in \{1, 6\}$

The initial estimate \hat{A}_k SER and BER vs. SNR for a TUx channel environment are presented in Figure 3.8 with $\kappa = 1$ and $\kappa = 6$, in order to show the effect of separating distance in terms of REs between MPSK and MASK on the OSBCE performance. In Figure 3.8, the pilot system curve represents the error rate of the MPSK symbols when equalized using perfect CSI. The SER with $\kappa = 1$ and 2 receive antennas outperforms the SER with $\kappa = 6$ and 4 antennas, due to the fact that the distance in terms of REs, κ , between MPSK and MASK is reduced from 6 to 1. In mathematical terms, it means that the phase error, $\vartheta_k^{(n)} = \theta_k^{(n)} - \hat{\theta}_{k+\kappa}^{(n)}$, would be higher and cause more detection errors for A_k , which is later used to estimate $H_k^{(n)}$. In addition, this means that $\vartheta_k^{(n)}$ is a function of κ . Moreover, with 2 receive antennas and $\kappa = 1$, the \hat{A}_k SER becomes lower than the \hat{A}_k SER using perfect CSI. The \hat{A}_k SER gets lower as SNR increases, however, for the blindly estimated \hat{A}_k , it hits an error floor produced by $\vartheta_k^{(n)}$. Moreover, the improvement rate gets lower as the number of receive antennas increase, as was noted in the EGC subsection.

Figure 3.9 shows the impact of increasing the number of receive antennas for $\kappa \in \{1, 6\}$ in a TUx channel environment. With $\kappa = 1$, simply using 2 receive antennas would improve the detection of A_k to the point where the MSE of CFRs estimated using OSBCE matches that of the pilot-based system. As κ increases, more receive antennas are needed to match the pilot-based system performance. With $\kappa = 6$, 4 receive antennas are not enough to

match the pilot-based system performance, and more receive antennas are required.

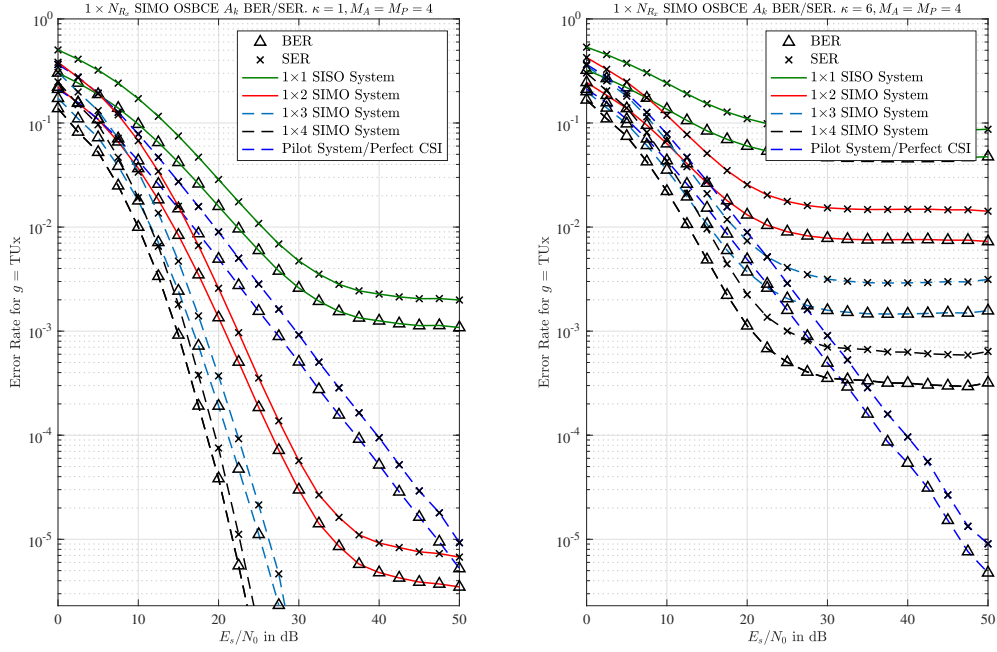


Figure 3.8: $1 \times N_{R_x}$ F. OSBCE - \hat{A}_k BER & SER vs. SNR. $\kappa \in \{1, 6\}$

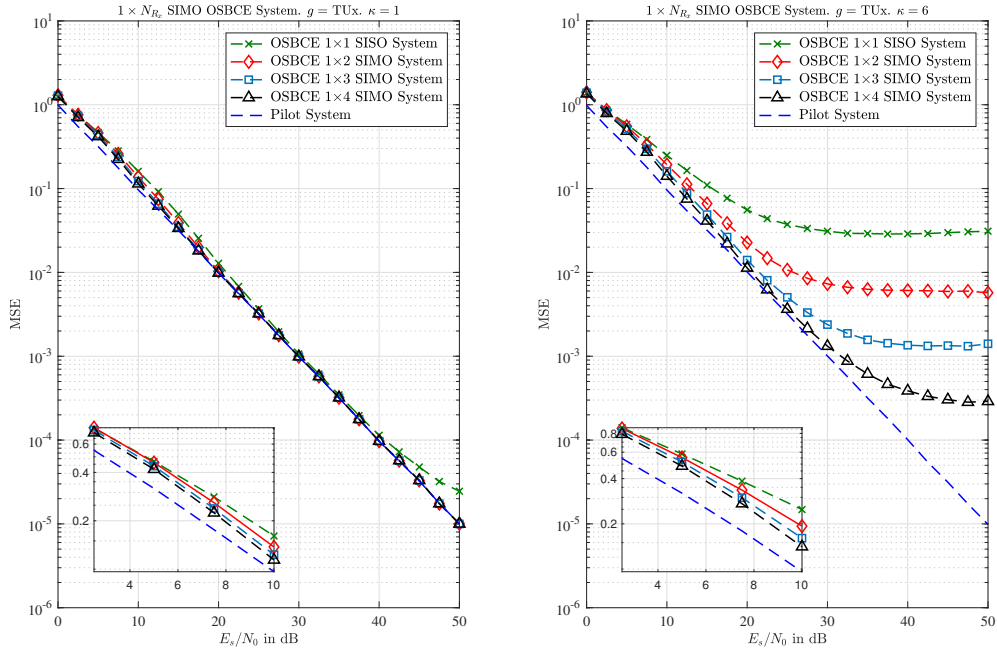


Figure 3.9: $1 \times N_{R_x}$ F. OSBCE - MSE vs. SNR for different N_{R_x} . $\kappa \in \{1, 6\}$

CHAPTER 3. OSBCE FOR SIMO-OFDM SYSTEMS

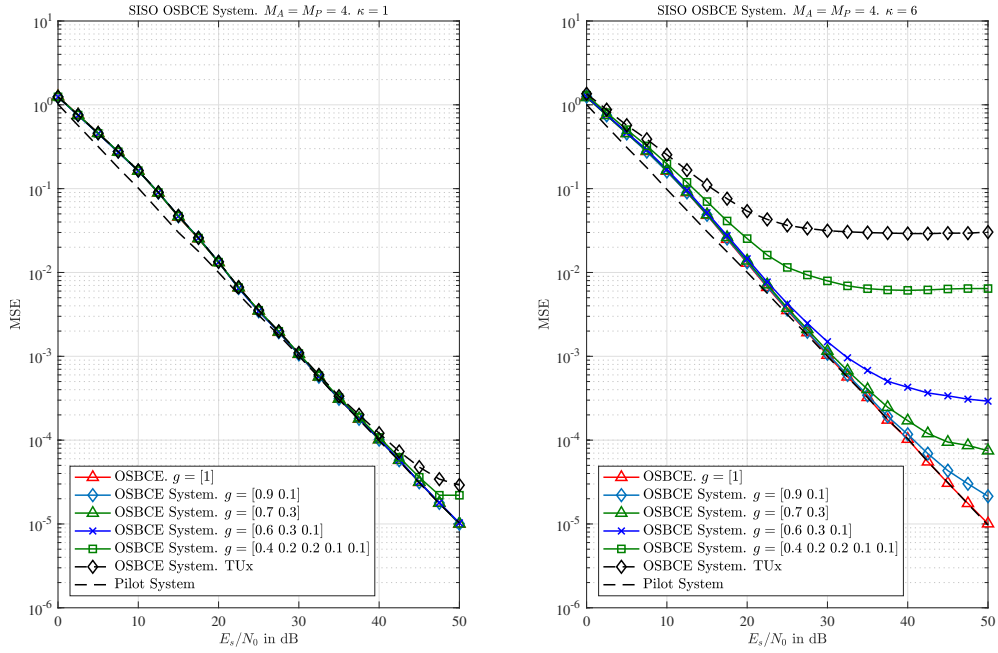


Figure 3.10: $1 \times N_{R_x}$ F. OSBCE - MSE vs. SNR for different channels. $\kappa \in \{1, 6\}$

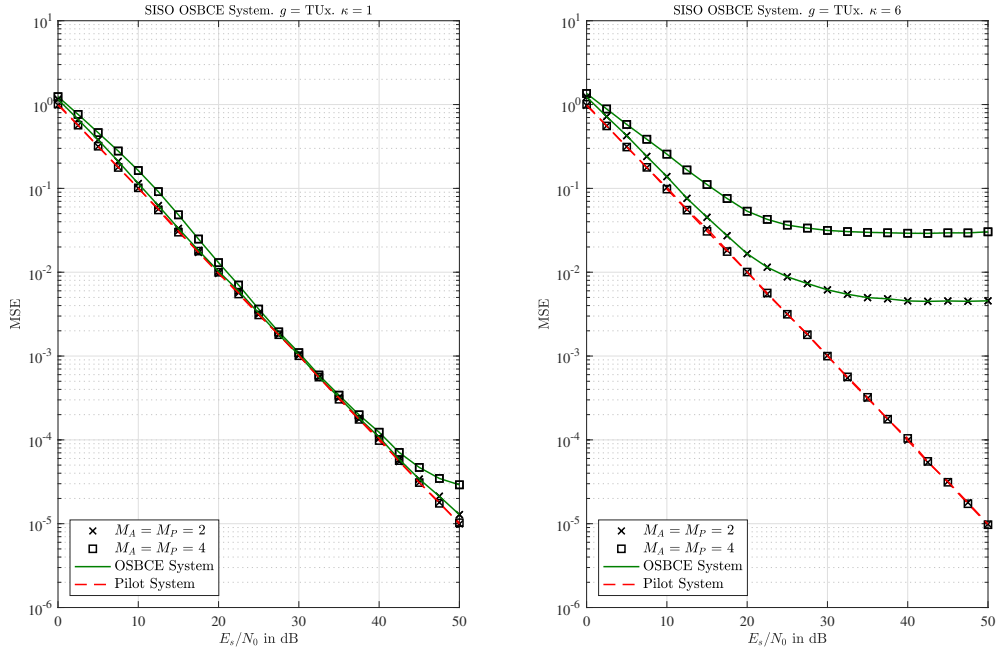


Figure 3.11: $1 \times N_{R_x}$ F. OSBCE - MSE vs. SNR for different M_A, M_P . $\kappa \in \{1, 6\}$

Figure 3.10 shows the MSE vs. SNR for $\kappa \in \{1, 6\}$ with different channel gains. With

$\kappa = 1$, the MSE performance of the OSBCE in a TUx channel environment starts deviating from the pilot-based system after $\text{SNR} \simeq 40$ dB. On the other hand, with $\kappa = 6$, the MSE performance is significantly degraded compared to the $\kappa = 1$ case. In general, the closer the MASK and MPSK symbols in terms of κ , the better the OSBCE performance.

Figure 3.11 shows the impact of increasing the modulation order across the whole system for $\kappa \in \{1, 6\}$ in a TUx channel environment. As the modulation order increase, the MSE performance gets worse, which is a result of a worse SER performance of A_k . This is expected since increasing M_A will introduce more amplitudes with small values, which is similar to equalizing using less reliable channel estimates. Moreover, as M_P increases, smaller margins of phase noise can cause detection errors in A_k . The performance degradation when increasing the modulation order is controlled by κ . For $\kappa = 1$, the MSE OSBCE performance stays close to that of the pilot-based system, while with $\kappa = 6$, performance gets significantly worse.

Figure 3.12 shows $\rho(\kappa)$ between H_k and $H_{k+\kappa}$, as a function of κ . As κ increase, the correlation between H_k and $H_{k+\kappa}$ decreases and the rate at which κ affects $\rho(\kappa)$ depends on the channel's number of taps. In other words, it depends on the power spectrum function for H_k .

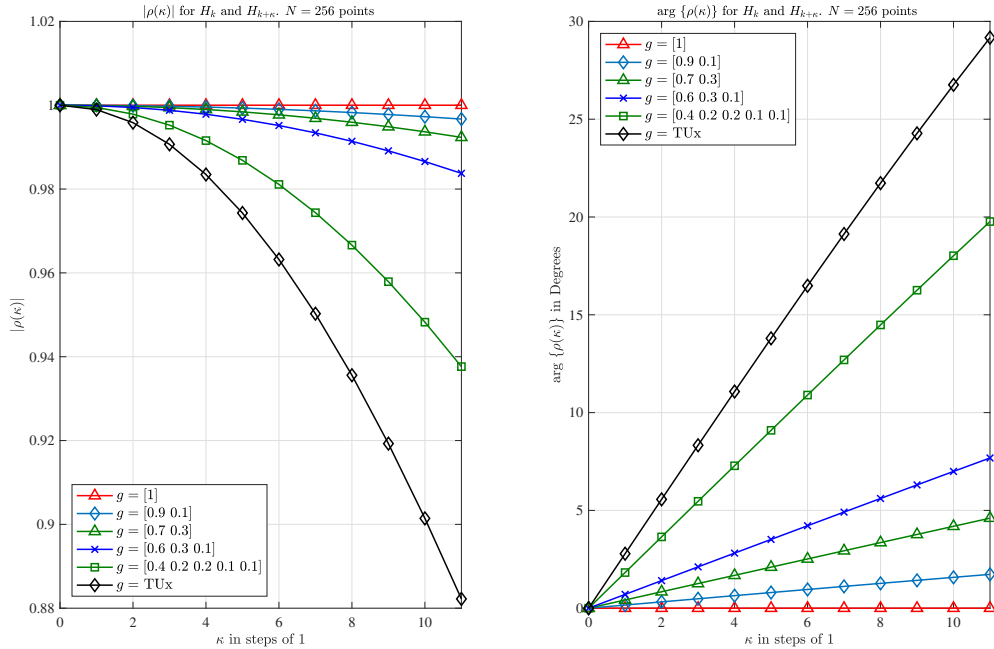


Figure 3.12: $1 \times N_{R_x}$ F. OSBCE - Example of $\rho(\kappa)$ vs. κ for different channels

It is worth mentioning that the pilot system performance is consistent with different

channel gains and different modulation orders, however, it does not benefit from increasing the number of receive antennas with respect to CE. Increasing the number of receive antennas would simply mean that there are more CFRs to estimate at the receiver side. Thus, perfect CSI does not benefit from increasing N_{R_x} .

3.3.3 SIMO 1-D T.OSBCE - Across Time

Since the analysis in section 3.2 focused on the selectivity of the channel across frequency, the definition did not reflect the changes across different OFDM symbols. Therefore, the Doppler effect should be included in the channel definition for CE across time, since it will constitute an error source as will be demonstrated later. It is worth mentioning that while CFO may result from frequency mismatch in the transmitter and the receiver oscillators; or from the Doppler effect as the transmitter or the receiver is moving, the focus of this work is the Doppler effect due to motion. Thus, it is assumed perfect frequency synchronization between transmitter and receiver. Hence, the Doppler frequency/shift is defined as

$$f_d = \mathcal{V} \left(\frac{5}{18} \right) \left(\frac{f_c}{c} \right) \cos(\delta) \quad (3.36)$$

where f_d is the Doppler shift, \mathcal{V} is the radial velocity of the target in Km/hrs, δ is the signal's angle of arrival, f_c is the carrier frequency and c is the speed of light. Doppler spread is defined as the difference between the maximum and minimum values of f_d . To simplify the problem, assume minimum f_d occurs at $\cos(\delta) = 0$ and maximum f_d occurs at $\cos(\delta) = 1$. It is assumed that the channel has $L_h + 1$ independent complex multipath components each of which has a gain $h_v \sim \mathcal{CN}(0, 2\sigma_{h_v}^2)$ and delay $v \times T_s$, where $v \in \{0, 1, \dots, L_h\}$. The channel taps are assumed to be time-invariant over one OFDM symbol, but may change over two consecutive symbols, which represents a quasi-static multipath channel [9]. Then, the received signal after discarding the first N_{CP} CP samples would be,

$$\mathbf{y}(\ell) = e^{j2\pi\epsilon\ell\frac{N+N_{CP}}{N}} \mathbf{C}(\epsilon)\mathbb{H}(\ell)\mathbf{x}(\ell) + \mathbf{z}(\ell) \quad (3.37)$$

where ϵ is the normalized CFO which can be modeled as a uniformly RV $(-\epsilon_{max}, \epsilon_{max})$, which is given as

$$|\epsilon_{max}| = \frac{f_{d,max}}{\Delta_f} = \frac{N}{2K(N + N_{CP})} \quad (3.38)$$

where K is the number of phase shift rotations for a given constellation. $\mathbf{C}(\epsilon)$ is an $N \times N$ diagonal matrix that represents the accumulated phase shift to the time domain samples

caused by the CFR, which is expressed as,

$$\mathbf{C}(\epsilon) = \text{diag} \left(\left[e^{j\frac{2\pi\epsilon}{N} \times 0}, e^{j\frac{2\pi\epsilon}{N} \times 1}, \dots, e^{j\frac{2\pi\epsilon}{N} \times (N-1)} \right]^T \right). \quad (3.39)$$

The CIR matrix \mathbb{H} is an $N \times N$ Toeplitz matrix with h_0 on the principle diagonal and h_1, h_2, \dots, h_{L_h} on the minor diagonals. The noise vector $\mathbf{z}(\ell)$ is modeled as AWGN process where $z_n \sim \mathcal{CN}(0, 2\sigma_z^2)$. After some simple mathematical manipulations, the received symbol in (3.37) can be expressed as,

$$y_n(\ell) = \frac{1}{\sqrt{N}} e^{j2\pi\epsilon\ell \frac{N+N_{CP}}{N}} \sum_{i=0}^{N-1} A_i(\ell) H_i(\ell) e^{j2\pi n \frac{\epsilon+i}{N}} + z_n(\ell). \quad (3.40)$$

Afterwards, the receiver removes the first N_{CP} CP samples, and performs N-FFT of \mathbf{y} to obtain the received samples,

$$\mathbf{r}(\ell) = \mathbf{F}\mathbf{y}(\ell).$$

The received element at the k^{th} subcarrier is expressed as,

$$\begin{aligned} r_k(\ell) &= \frac{1}{\sqrt{N}} \sum_{n'=1}^{N-1} y_{n'}(\ell) e^{-j2\pi \frac{n'k}{N}}, \quad k \in \{0, 1, \dots, N-1\} \\ &= \frac{e^{j2\pi\epsilon\ell \frac{N+N_{CP}}{N}}}{N} \sum_{i=0}^{N-1} \frac{\sin(\pi\epsilon)}{N \sin\left(\pi \frac{(\epsilon+i-k)}{N}\right)} A_i(\ell) H_i(\ell) e^{j\pi \frac{(N-1)(\epsilon+i-k)}{N}} + \eta_k(\ell) \end{aligned} \quad (3.41)$$

where $\eta_k(\ell)$ is the FFT of $z_n(\ell)$ and can be modeled as Gaussian RV $\sim \mathcal{CN}(0, 2\sigma_\eta^2)$. After separating the desired term at the k^{th} subcarrier from the other subcarriers, (3.41) is expressed as,

$$\begin{aligned} r_k(\ell) &= e^{j\pi\epsilon \left(\frac{2\ell(N+N_{CP})+(N-1)}{N} \right)} \times \frac{\sin(\pi\epsilon)}{N \sin\left(\pi \frac{\epsilon}{N}\right)} A_k(\ell) H_k(\ell) + \\ &e^{j2\pi\epsilon\ell \frac{N+N_{CP}}{N}} \sum_{i \neq k}^{N-1} \frac{\sin(\pi\epsilon)}{N \sin\left(\pi \frac{(\epsilon+i-k)}{N}\right)} A_i(\ell) H_i(\ell) e^{j\pi \frac{(N-1)(\epsilon+i-k)}{N}} + \eta_k(\ell). \end{aligned} \quad (3.42)$$

The first term in (3.42) represents the desired signal, while the second term is the ICI, which causes the loss of the orthogonality among the subcarriers. Notice that the $e^{j\pi\epsilon \left(\frac{2\ell(N+N_{CP})+(N-1)}{N} \right)}$ part from the first term, describes the CFR change from one OFDM symbol to the other at the k^{th} subcarrier. To simplify notation for the upcoming discussions, (3.42) is

expressed as,

$$r_k(\ell) = \varphi(\ell, \epsilon) A_k(\ell) H_k(\ell) + \Psi_k(\ell, \epsilon) + \eta_k(\ell). \quad (3.43)$$

Since $\sin\left(\frac{\pi\epsilon}{N}\right) \approx \frac{\pi\epsilon}{N}$ for $N \gg \pi\epsilon$, and $\lim_{a \rightarrow 0} \frac{\sin(a)}{a} = 1$, the following is true,

$$\begin{aligned} \lim_{\epsilon \rightarrow 0} \varphi(\ell, \epsilon) &= \lim_{\epsilon \rightarrow 0} e^{j\pi\epsilon \left(\frac{2\ell(N+N_{CP})+(N-1)}{N} \right)} \times \frac{\sin(\pi\epsilon)}{N \sin\left(\pi \frac{\epsilon}{N}\right)} \\ &= \lim_{\epsilon \rightarrow 0} e^{j\pi\epsilon \left(\frac{2\ell(N+N_{CP})+(N-1)}{N} \right)} \times \frac{\sin(\pi\epsilon)}{\pi\epsilon} \\ &= 1. \end{aligned} \quad (3.44)$$

Moreover,

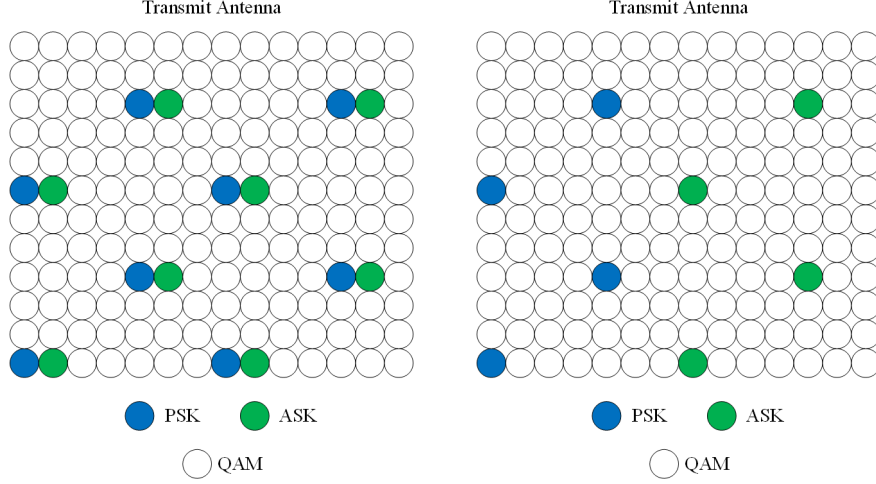
$$\begin{aligned} \lim_{\epsilon \rightarrow 0} \Psi_k(\ell, \epsilon) &= \lim_{\epsilon \rightarrow 0} e^{j2\pi\epsilon\ell \frac{N+N_{CP}}{N}} \sum_{i \neq k}^{N-1} \frac{\sin(\pi\epsilon)}{N \sin\left(\pi \frac{(\epsilon+i-k)}{N}\right)} A_i(\ell) H_i(\ell) e^{j\pi \frac{(N-1)(\epsilon+i-k)}{N}} \\ &= 0. \end{aligned} \quad (3.45)$$

Now, in this OSBCE configuration, the pilots are distributed across one dimension (time) within one subcarrier frequency, which means this system model is not susceptible to frequency selective channels, but, is effected by the Doppler frequency of the channel. The pilot distribution for this OSBCE system is shown in Figure 3.13. Again, This is a special case of the $mT_x \times nR_x$ MIMO system, namely SIMO, where $m = 1, n \in \{1, 2, \dots, N_{R_X}\}$. Notation is rearranged to include the OFDM symbol number in subscript, and it is assumed that ϵ does not change within ι symbols duration. For ease of notation and because of the assumption that ϵ is constant during ι OFDM symbols, the ϵ is dropped from $\varphi_\ell(\epsilon)$ and $\Psi_{k,\ell}(\epsilon)$. Moreover, the subcarrier notation k is dropped, and will be included only if necessary.

The MPSK and MASK symbols are transmitted at OFDM blocks ℓ and $\ell + \iota$, respectively. It is assumed that ϵ is constant during ι OFDM blocks, meaning that the relative speed between transmitter and receiver is constant during ι symbols. Hence, the received FFT samples from the transmit antenna at subcarrier k and OFDM symbols $\ell, \ell + \iota$ for receive antenna n , where ι is the OFDM symbols spacing between the ASK and PSK symbols,

$$r_\ell^{(n)} = \varphi_\ell A_\ell H_\ell^{(n)} + \Psi_\ell^{(n)} + \eta_\ell^{(n)} \quad (3.46)$$

$$r_{\ell+\iota}^{(n)} = \varphi_{\ell+\iota} A_{\ell+\iota} H_{\ell+\iota}^{(n)} + \Psi_{\ell+\iota}^{(n)} + \eta_{\ell+\iota}^{(n)}. \quad (3.47)$$


 Figure 3.13: $1 \times N_{R_x}$ Time OSBCE system - $\iota \in \{1, 7\}$

It is worth mentioning that this OSBCE system model focuses on estimating $\varphi_\ell H_\ell^{(n)}$ as a whole and considers it to be the actual CFR. Notice that φ_ℓ is the term that describes the change due to Doppler at the k^{th} subcarrier CFR. The pattern is repeated for different ι as shown in Figure 3.13. Now, we can decode for A_ℓ as follows

$$\begin{aligned}
 \mathcal{S}_\ell^{(n)} &= r_\ell^{(n)} / r_{\ell+\iota}^{(n)} \\
 &= \frac{\varphi_\ell A_\ell H_\ell^{(n)} + \Psi_\ell^{(n)} + \eta_\ell^{(n)}}{\varphi_{\ell+\iota} A_{\ell+\iota} H_\ell^{(n)} + \Psi_{\ell+\iota}^{(n)} + \eta_{\ell+\iota}^{(n)}} \\
 &= \frac{\varphi_\ell A_\ell H_\ell^{(n)} + \Psi_\ell^{(n)} + \eta_\ell^{(n)}}{|r_{\ell+\iota}^{(n)}| e^{j(\hat{\theta}_{\ell+\iota}^{(n)})}} \\
 &= \frac{A_\ell |\varphi_\ell H_\ell^{(n)}| e^{j(\theta_\ell^{(n)} - \hat{\theta}_{\ell+\iota}^{(n)})} + \check{\Psi}_\ell^{(n)} + \check{\eta}_\ell^{(n)}}{|r_{\ell+\iota}^{(n)}|} \\
 &= \frac{1}{|r_{\ell+\iota}^{(n)}|} \left(A_\ell |\varphi_\ell H_\ell^{(n)}| e^{j\vartheta_\ell^{(n)}} + \check{\Psi}_\ell^{(n)} + \check{\eta}_\ell^{(n)} \right) \tag{3.48}
 \end{aligned}$$

where $\vartheta_\ell^{(n)} = \theta_\ell^{(n)} - \hat{\theta}_{\ell+\iota}^{(n)}$, $\check{\Psi}_\ell^{(n)} = |\Psi_\ell^{(n)}| e^{j(\arg\{\Psi_\ell^{(n)}\} - \hat{\theta}_{\ell+\iota}^{(n)})}$, $\check{\eta}_\ell^{(n)} = |\eta_\ell^{(n)}| e^{j(\arg\{\eta_\ell^{(n)}\} - \hat{\theta}_{\ell+\iota}^{(n)})}$. $\vartheta_\ell^{(n)}$ in the T.OSBCE is a function of ι . The n^{th} receiver branch can now detect the transmitted symbol A_ℓ from the phase of $\mathcal{S}_\ell^{(n)}$, since it has been equalized by an imperfect CFR, namely $r_{\ell+\iota}^{(n)}$. However, since there are multiple receive antennas, EGC is employed to enhance the SNR of the detected symbol. EGC is applied by adding all the co-phased $\mathcal{S}_\ell^{(n)}$, $n \in$

$\{1, 2, \dots, N_{R_x}\}$, from the different receive antennas as follows,

$$\sum_{n=1}^{N_{R_x}} \mathcal{S}_\ell^{(n)} = A_\ell \sum_{n=1}^{N_{R_x}} \frac{|H_\ell^{(n)} \varphi_\ell| e^{j\vartheta_\ell^{(n)}}}{|r_{\ell+\iota}^{(n)}|} + \sum_{n=1}^{N_{R_x}} \frac{\check{\Psi}_\ell^{(n)} + \check{\eta}_\ell^{(n)}}{|r_{\ell+\iota}^{(n)}|}. \quad (3.49)$$

The combiner's MLD detection for the MPSK symbol would only need the phase of $\sum_{n=1}^{N_{R_x}} \mathcal{S}_\ell^{(n)}$. Since $|H_\ell^{(n)} \varphi_\ell|$ and $|r_{\ell+\iota}^{(n)}|$ are scalar entities, they have no effect on the phase of A_ℓ , while $\vartheta_\ell^{(n)}$, $\check{\Psi}_\ell^{(n)}$ and $\check{\eta}_\ell^{(n)}$ are the sources of phase error that would effect the detection process. From the discussion of EGC, it was demonstrated that noise effect in general is reduced by collecting the signal from multiple receivers. Moreover, it is worth mentioning that ι and ϵ inherently affect $\vartheta_\ell^{(n)} = \theta_\ell^{(n)} - \hat{\theta}_{\ell+\iota}^{(n)}$. For $\iota = 1$, $\iota \in \mathbb{R}^+$, $\vartheta_\ell^{(n)} \approx 0$ since $\theta_\ell^{(n)} \approx \hat{\theta}_{\ell+\iota}^{(n)}$. Moreover, as ι increases while $\epsilon \neq 0$, so does the phase error produced by $\vartheta_\ell^{(n)}$. Also, as $\epsilon \rightarrow 0$, the $\arg\{\varphi_\ell\} = \arg\{\check{\Psi}_\ell^{(n)}\} = 0$ and the opposite is true. Meaning that as the relative speed between transmitter and receiver increases, the Doppler frequency, ϵ , $\arg\{\varphi_\ell\}$, and $\arg\{\check{\Psi}_\ell^{(n)}\}$ would increase and cause phase distortions. Using MLD, \hat{A}_ℓ is expressed as,

$$\hat{A}_\ell = \arg \min_{A_\ell^{(i)}, i \in \mathbb{M}_P} \left| \sum_{n=1}^{N_{R_x}} \mathcal{S}_\ell^{(n)} - A_\ell^{(i)} \right|^2. \quad (3.50)$$

Using \hat{A}_ℓ , $\hat{H}_\ell^{(n)}$ at each branch can be found using LSE as follows,

$$\hat{H}_\ell^{(n)} = \frac{r_\ell^{(n)}}{\hat{A}_\ell} = \frac{\varphi_\ell A_\ell H_\ell^{(n)} + \Psi_\ell^{(n)} + \eta_\ell^{(n)}}{\hat{A}_\ell} \approx \varphi_\ell(\epsilon) H_\ell^{(n)} + \hat{\Psi}_\ell^{(n)} + \hat{\eta}_\ell^{(n)} \quad (3.51)$$

where $\hat{\eta}_\ell^{(n)} = |\eta_\ell^{(n)}| e^{j(\arg\{\eta_\ell^{(n)}\} - \arg\{\hat{A}_\ell\})}$, and $\hat{\Psi}_\ell^{(n)} = |\Psi_\ell^{(n)}| e^{j(\arg\{\Psi_\ell^{(n)}\} - \arg\{\hat{A}_\ell\})}$. In SIMO OSBCE across frequency, enough N_{CP} CP samples were used to eliminate ISI between consecutive OFDM symbols. The added CP of length N_{CP} samples is no less than the channel maximum delay spread (L_h). In order to stay consistent, it is assumed that ICI cancellation/estimation is used. Thus, (3.51) becomes,

$$\hat{H}_\ell^{(n)} = \frac{r_\ell^{(n)}}{\hat{A}_\ell} = \frac{\varphi_\ell A_\ell H_\ell^{(n)} + \eta_\ell^{(n)}}{\hat{A}_\ell} \approx \varphi_\ell H_\ell^{(n)} + \hat{\eta}_\ell^{(n)}. \quad (3.52)$$

Similar to the SIMO F.OSBCE, the obtained enhancement is the added accuracy in the initial detection of the MPSK symbol, which would result in better CFR estimates $\varphi_\ell H_\ell^{(n)}$.

3.3.3.1 Results and Discussion - $\iota \in \{1, 7\}$

The impact of increasing the number of receive antennas on the initial estimate \hat{A}_ℓ in terms of SER and BER is shown in Figure 3.14 with $\iota = 1$ and $\iota = 7$. The speed of the moving object in Figure 3.14 is 200 Km/hr, which translates to a maximum Doppler frequency of 351.9 Hz for $f_c = 1.9$ GHz. The SER with $\iota = 1$ and 2 receive antennas outperforms the SER with $\iota = 7$ and 5 antennas, due to the fact that the distance in terms of OFDM blocks, ι , between MPSK and MASK is reduced from 7 to 1. In mathematical terms, it means that the phase error, $\vartheta_\ell^{(n)} = \theta_\ell^{(n)} - \hat{\theta}_{\iota+\iota}^{(n)}$, would be higher and cause more detection errors for \hat{A}_ℓ , which is later used to estimate $\varphi_\ell H_\ell^{(n)}$. Moreover, with 2 receive antennas and $\iota = 1$, the \hat{A}_ℓ SER is slightly worse than the \hat{A}_ℓ SER using perfect CSI, and can be further improved if the number of receive antennas increases. As expected, blindly estimated \hat{A}_ℓ SER decreases as SNR increases until it hits an error floor produced by $\vartheta_\ell^{(n)}$. Also, the rate of enhancement resulting from increasing N_{R_x} gets lower as the number of receive antennas increases.

Figure 3.15 shows how increasing the number of receive antennas for $\iota \in \{1, 7\}$ affects the CFRs MSE. With $\iota = 1$ and $N_{R_x} = 2$, the detection of A_ℓ improves to the point where the MSE of OSBCE estimated CFRs matches that of the pilot-based system. As ι increases, more receive antennas are needed to match the pilot-based system performance. With $\iota = 7$, more than 20 receive antennas are needed to perfectly match the pilot-based system performance.

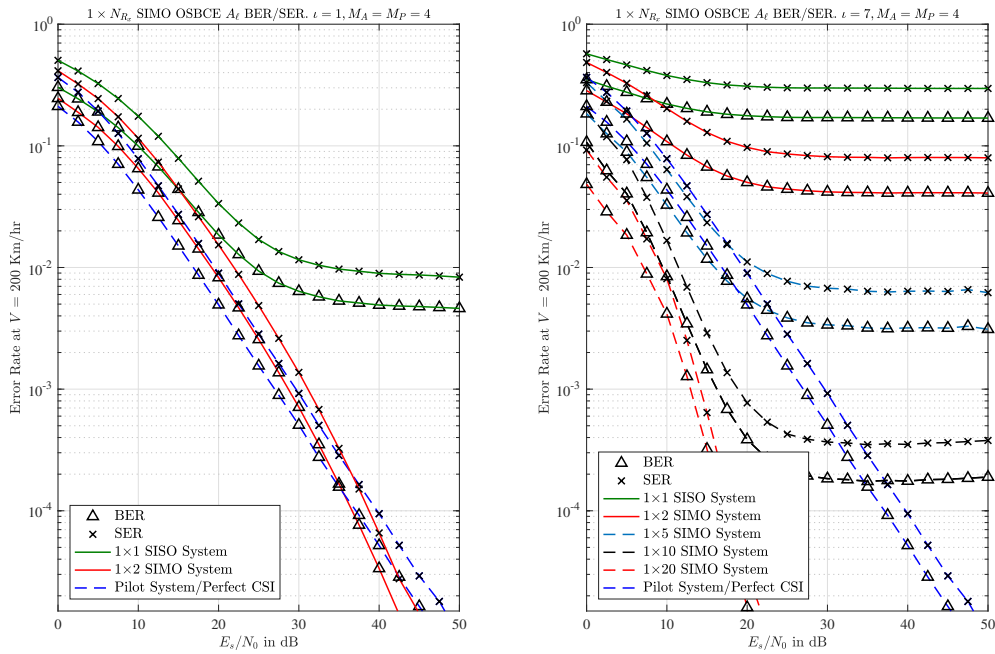


Figure 3.14: $1 \times N_{R_x}$ T. OSBCE - \hat{A}_ℓ BER & SER vs. SNR. $\iota \in \{1, 7\}$

CHAPTER 3. OSBCE FOR SIMO-OFDM SYSTEMS

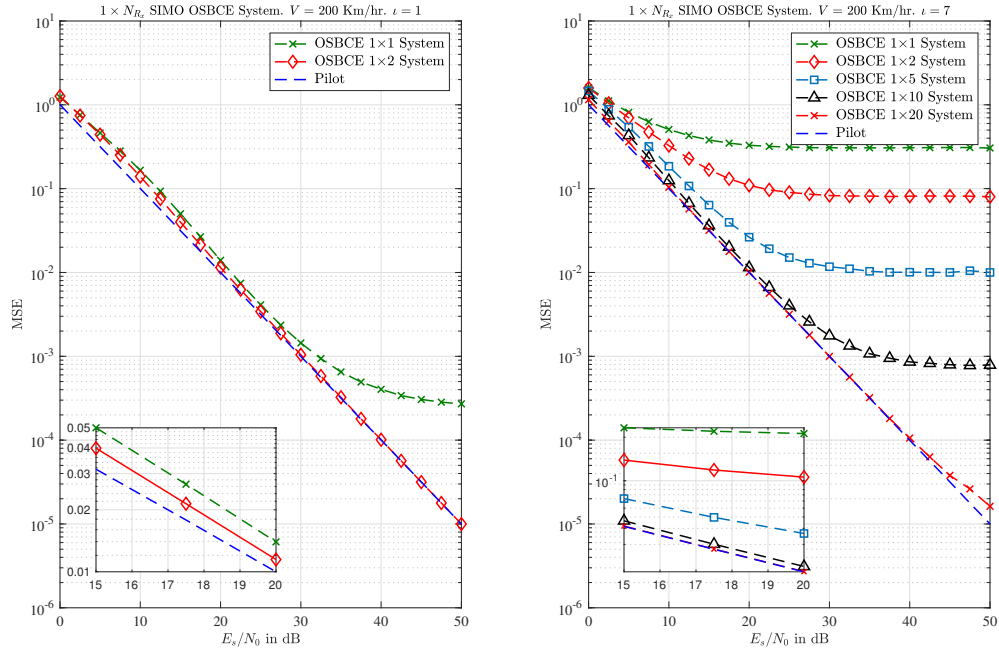


Figure 3.15: $1 \times N_{R_x}$ T. OSBCE - MSE vs. SNR for different N_{R_x} . $l \in \{1, 7\}$

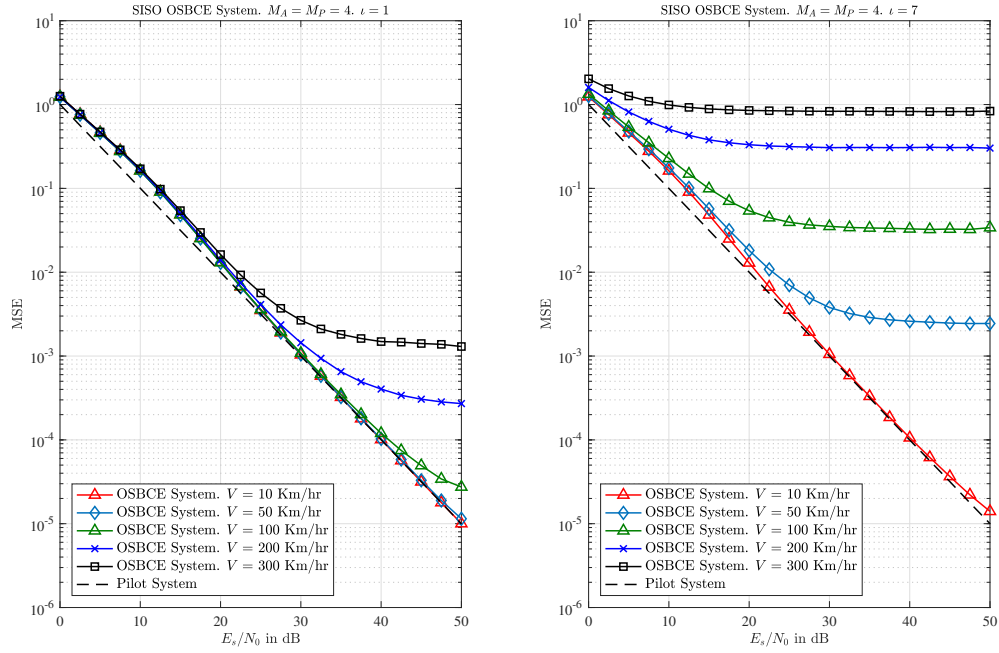


Figure 3.16: $1 \times N_{R_x}$ T. OSBCE - MSE vs. SNR for different channels. $l \in \{1, 7\}$

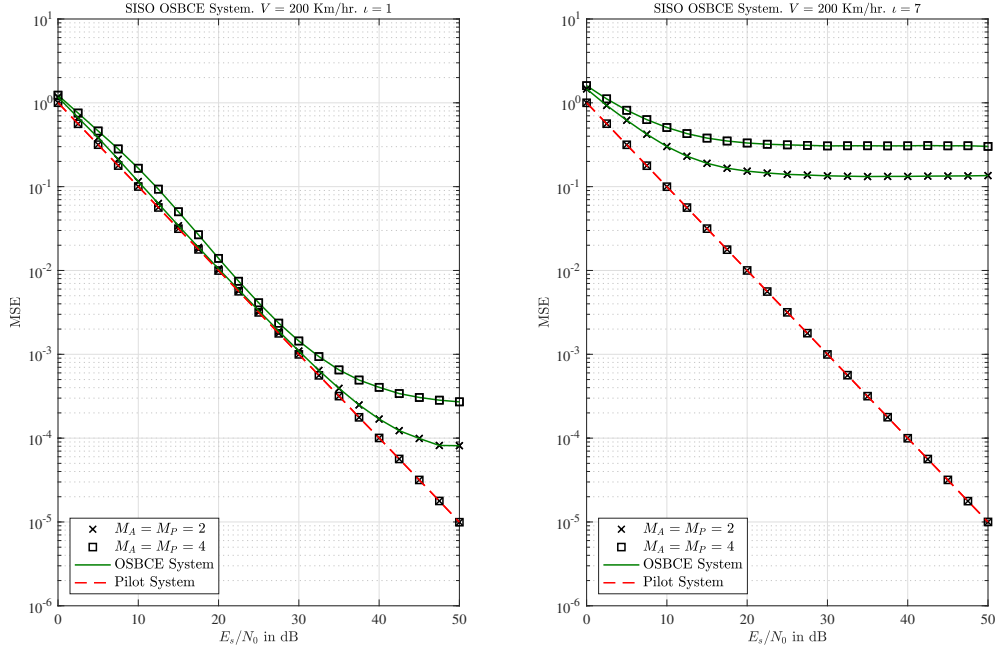


Figure 3.17: $1 \times N_{R_x}$ T. OSBCE - MSE vs. SNR for different M_A , M_P . $l \in \{1, 7\}$

Figure 3.16 shows the impact of the receiver's relative speed on the OSBCE MSE for $l \in \{1, 7\}$. With $l = 1$, the MSE performance of the OSBCE for a relative speed of 200 Km/hr starts deviating from the pilot-based system performance after $\text{SNR} \simeq 30$ dB. The Doppler frequency in this case is 351.9 Hz for $f_c = 1.9$ GHz. In such case, performance would match the pilot-based performance by simply using 2 receive antennas. On the other hand, with $l = 7$, the MSE performance is significantly degraded compared to the $l = 1$ case. Again, the previous results show that the closer the MASK and MPSK symbols in terms of subcarrier spacing, the better the OSBCE performance.

Figure 3.17 shows how the modulation order impacts the OSBCE system for $l \in \{1, 7\}$ at a relative motion speed of 200 Km/hr. In general, as the modulation order increases, the MSE performance gets worse, which is a result of a worse SER performance of A_ℓ . The rate of performance degradation as modulation order increases is a function of l . For $l = 1$, the MSE OSBCE performance with binary modulation is comparable to pilot-based system till $\text{SNR} \simeq 35$, while with $l = 6$, performance is significantly worse.

Figure 3.18 shows the cross-correlation coefficient between $\varphi_\ell H_\ell$ and $\varphi_{\ell+l} H_\ell$, $\rho(l)$, as a function of l . As l increase, the correlation between $\varphi_\ell H_\ell$ and $\varphi_{\ell+l} H_\ell$ decreases and the rate at which l affects $\rho(l)$ depends on the channel variations with respect to time. Moreover, even if $\rho(l) = -1$ between $\varphi_\ell H_\ell$ and $\varphi_{\ell+l} H_\ell$, the negative sign would mean a phase rotation by a 180 degrees. In that case, if the transmitted symbol was A_ℓ , it would be detected as

$-A_\ell$. Also, it is worth noting here that the effect of 1 step of ι on the correlation in general is greater than the effect of 1 step of κ on the correlation.

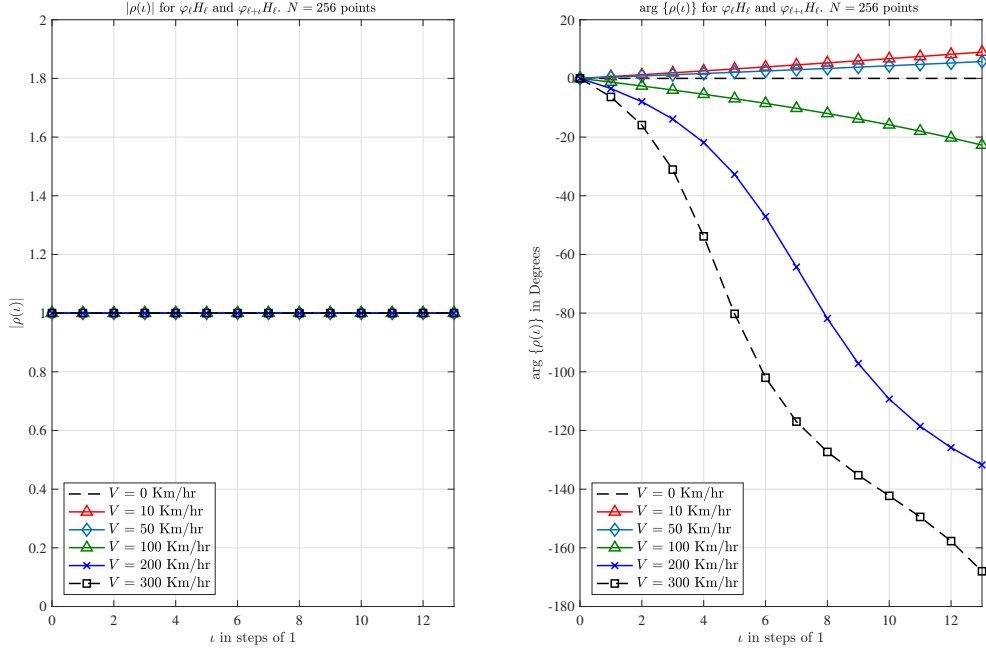


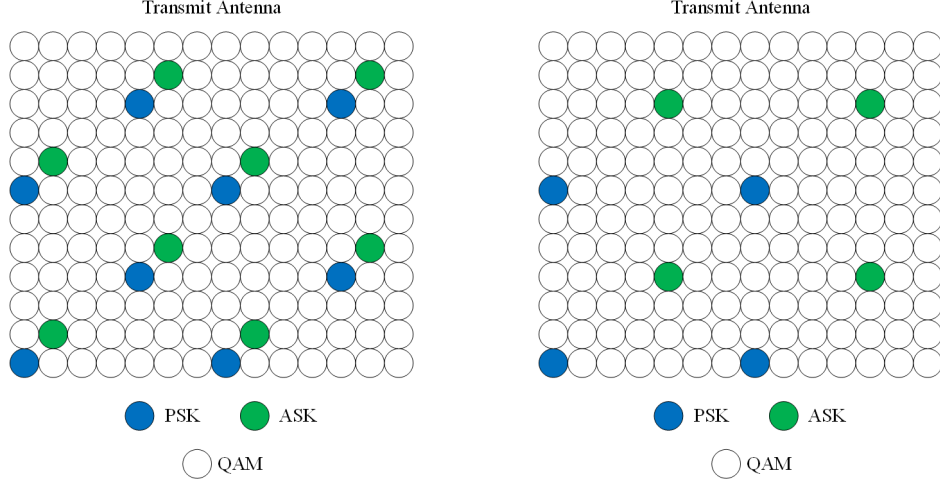
Figure 3.18: $1 \times N_{R_x}$ T. OSBCE - Example of $\rho(\iota)$ vs. ι for different speeds

3.3.4 SIMO 2-D T/F.OSBCE - Across Time & Frequency

In this configuration, the OSBCE system is designed to work across the two dimensions, time and frequency. The aim is to investigate how OSBCE performs when distortions to the correlation between CFRs happens in both time and frequency. The pilot distribution for this OSBCE system is shown in Figure 3.19. Again, This is a special case of the $mT_x \times nR_x$ MIMO system, namely SIMO, where $m = 1, n \in \{1, 2, \dots, N_{R_x}\}$. Similar notations as in subsections 3.3.2 and 3.3.3 are used. Moreover, it is assumed that ISI and ICI are eliminated before the CE step. Enough N_{CP} CP samples are used for ISI mitigation, and ICI estimation or guard bands are used for ICI mitigation, and ϵ does not change within ι symbols duration. The MPSK and MASK symbols are transmitted at locations (k, ℓ) and $(k + \kappa, \ell + \iota)$, respectively. It is assumed that ϵ is constant during ι OFDM blocks. Hence, the received post-FFT samples at MPSK and MASK locations at receive antenna n , respectively, are

$$r_{k,\ell}^{(n)} = \varphi_\ell A_{k,\ell} H_{k,\ell}^{(n)} + \eta_{k,\ell}^{(n)} \quad (3.53)$$

$$r_{k+\kappa,\ell+\iota}^{(n)} = \varphi_{\ell+\iota} A_{k+\kappa,\ell+\iota} H_{k+\kappa,\ell+\iota}^{(n)} + \eta_{k+\kappa,\ell+\iota}^{(n)}. \quad (3.54)$$


 Figure 3.19: $1 \times N_{R_x}$ Time/Frequency OSBCE system - $(\kappa, \iota) \in \{(1, 1), (3, 4)\}$

The actual CFR to be estimated is represented as $\varphi_\ell H_{k,\ell}^{(n)}$. The pattern is repeated for different (κ, ι) as shown in Figure 3.19. Now, $A_{k,\ell}$ is detected as follows

$$\begin{aligned}
 \mathcal{S}_{k,\ell}^{(n)} &= r_{k,\ell}^{(n)} / r_{k+\kappa,\ell+\iota}^{(n)} \\
 &= \frac{\varphi_\ell A_{k,\ell} H_{k,\ell}^{(n)} + \eta_{k,\ell}^{(n)}}{\varphi_{\ell+\iota} A_{k+\kappa,\ell+\iota} H_{k+\kappa,\ell+\iota}^{(n)} + \eta_{k+\kappa,\ell+\iota}^{(n)}} \\
 &= \frac{\varphi_\ell A_{k,\ell} H_{k,\ell}^{(n)} + \eta_{k,\ell}^{(n)}}{\left| r_{k+\kappa,\ell+\iota}^{(n)} \right| e^{j(\hat{\theta}_{k+\kappa,\ell+\iota}^{(n)})}} \\
 &= \frac{A_{k,\ell} \left| \varphi_\ell H_{k,\ell}^{(n)} \right| e^{j(\theta_{k,\ell}^{(n)} - \hat{\theta}_{k+\kappa,\ell+\iota}^{(n)})} + \check{\eta}_{k,\ell}^{(n)}}{\left| r_{k+\kappa,\ell+\iota}^{(n)} \right|} \\
 &= \frac{1}{\left| r_{k+\kappa,\ell+\iota}^{(n)} \right|} \left(A_{k,\ell} \left| \varphi_\ell H_{k,\ell}^{(n)} \right| e^{j\vartheta_{k,\ell}^{(n)}} + \check{\eta}_{k,\ell}^{(n)} \right) \tag{3.55}
 \end{aligned}$$

where $\vartheta_{k,\ell}^{(n)} = \theta_{k,\ell}^{(n)} - \hat{\theta}_{k+\kappa,\ell+\iota}^{(n)}$, $\check{\eta}_{k,\ell}^{(n)} = \left| \eta_{k,\ell}^{(n)} \right| e^{j(\arg\{\eta_{k,\ell}^{(n)}\} - \hat{\theta}_{k+\kappa,\ell+\iota}^{(n)})}$. In comparison to the previous OSBCE systems, $\vartheta_{k,\ell}^{(n)}$ here is a function of both κ and ι . As demonstrated previously, EGC is applied by adding all the co-phased $\mathcal{S}_{k,\ell}^{(n)}$, $n \in \{1, 2, \dots, N_{R_x}\}$, from the different receive antennas as follows,

$$\sum_{n=1}^{N_{R_x}} \mathcal{S}_{k,\ell}^{(n)} = A_{k,\ell} \sum_{n=1}^{N_{R_x}} \frac{\left| H_{k,\ell}^{(n)} \varphi_\ell \right| e^{j\vartheta_{k,\ell}^{(n)}}}{\left| r_{k+\kappa,\ell+\iota}^{(n)} \right|} + \sum_{n=1}^{N_{R_x}} \frac{\check{\eta}_{k,\ell}^{(n)}}{\left| r_{k+\kappa,\ell+\iota}^{(n)} \right|}. \tag{3.56}$$

For the MPSK symbol detection, only the phase of $\sum_{n=1}^{N_{R_x}} \mathcal{S}_{k,\ell}^{(n)}$ is required. $\left| H_{k,\ell}^{(n)} \varphi_\ell \right|$ and $\left| r_{k+\kappa,\ell+\iota}^{(n)} \right|$ are scalar entities and does not affect the phase of $A_{k,\ell}$. For this configuration of OSBCE, $\vartheta_{k,\ell}^{(n)}$, and $\hat{\eta}_{k,\ell}^{(n)}$ are phase distortion sources that would affect the detection process. EGC would reduce the effect of such distortions by processing the signal from multiple receivers. Moreover, it is worth mentioning that κ , ι , and ϵ inherently affect $\vartheta_{k,\ell}^{(n)} = \theta_{k,\ell}^{(n)} - \hat{\theta}_{k+\kappa,\ell+\iota}^{(n)}$. For $(\kappa, \iota) = (1, 1)$, $\kappa \in \mathbb{R}^+$ and $\iota \in \mathbb{R}^+$, $\vartheta_{k,\ell}^{(n)} \approx 0$ since $\theta_{k,\ell}^{(n)} \approx \hat{\theta}_{k+\kappa,\ell+\iota}^{(n)}$. Moreover, if either κ or ι increases while $\epsilon \neq 0$, so does the phase distortion from $\vartheta_{k,\ell}^{(n)}$. Also, as the relative speed between receiver and transmitter increase, the Doppler frequency, ϵ , and $\arg \{ \varphi_\ell \}$ would increase. Using MLD, the initial estimate for $\hat{A}_{k,\ell}$ is expressed as,

$$\hat{A}_{k,\ell} = \arg \min_{A_{k,\ell}^{(i)}, i \in \mathbb{M}_P} \left| \sum_{n=1}^{N_{R_x}} \mathcal{S}_{k,\ell}^{(n)} - A_{k,\ell}^{(i)} \right|^2. \quad (3.57)$$

Using $\hat{A}_{k,\ell}$, each branch can find its associated CFR, $\hat{H}_{k,\ell}^{(n)}$, using LSE as follows,

$$\begin{aligned} \hat{H}_{k,\ell}^{(n)} &= \frac{r_{k,\ell}^{(n)}}{\hat{A}_{k,\ell}} = \frac{\varphi_\ell A_{k,\ell} H_{k,\ell}^{(n)} + \eta_{k,\ell}^{(n)}}{\hat{A}_{k,\ell}} \\ &\approx \varphi_\ell H_{k,\ell}^{(n)} + \hat{\eta}_{k,\ell}^{(n)} \end{aligned} \quad (3.58)$$

where $\hat{\eta}_{k,\ell}^{(n)} = \left| \eta_{k,\ell}^{(n)} \right| e^{j(\arg \{ \eta_{k,\ell}^{(n)} \} - \arg \{ \hat{A}_{k,\ell} \})}$. Similar to the previous SIMO OSBCE systems, the added accuracy in blindly detecting $\hat{A}_{k,\ell}$ eventually results in better CFR estimates $\varphi_\ell H_{k,\ell}^{(n)}$.

3.3.4.1 Results and Discussion - $(\kappa, \iota) \in \{(1, 1), (3, 4)\}$

The impact of increasing the number of receive antennas on the initial estimate \hat{A}_k in terms of SER and BER is shown in Figure 3.20 with $(\kappa, \iota) = (1, 1)$ and $(\kappa, \iota) = (3, 4)$. The environment is assumed to be a TUx channel and the speed of the moving object in Figure 3.20 is 50 Km/hr, which translates to a maximum Doppler frequency of 88 Hz for $f_c = 1.9$ GHz. As expected, the error floor with $(\kappa, \iota) = (1, 1)$ and 2 receive antennas is lower than the error floor with $(\kappa, \iota) = (3, 4)$ and 10 antennas, due to the fact that the Euclidean distance between MPSK and MASK is reduced from 5 to $\sqrt{2}$. In mathematical terms, it means that due to higher phase error, $\vartheta_{k,\ell}^{(n)} = \theta_{k,\ell}^{(n)} - \hat{\theta}_{k+\kappa,\ell+\iota}^{(n)}$, detection errors for $\hat{A}_{k,\ell}$ are higher, which is later reflected in the estimates of $H_{k,\ell}^{(n)}$. Moreover, with 10 receive antennas and $(\kappa, \iota) = (1, 1)$, the $\hat{A}_{k,\ell}$ SER is better than the $\hat{A}_{k,\ell}$ SER using perfect CSI. As expected, blindly estimated $\hat{A}_{k,\ell}$ SER decreases as SNR increases until it hits an error floor produced by $\vartheta_{k,\ell}^{(n)}$. Again, the enhancement rate from increasing N_{R_x} gets lower as N_{R_x} increases.

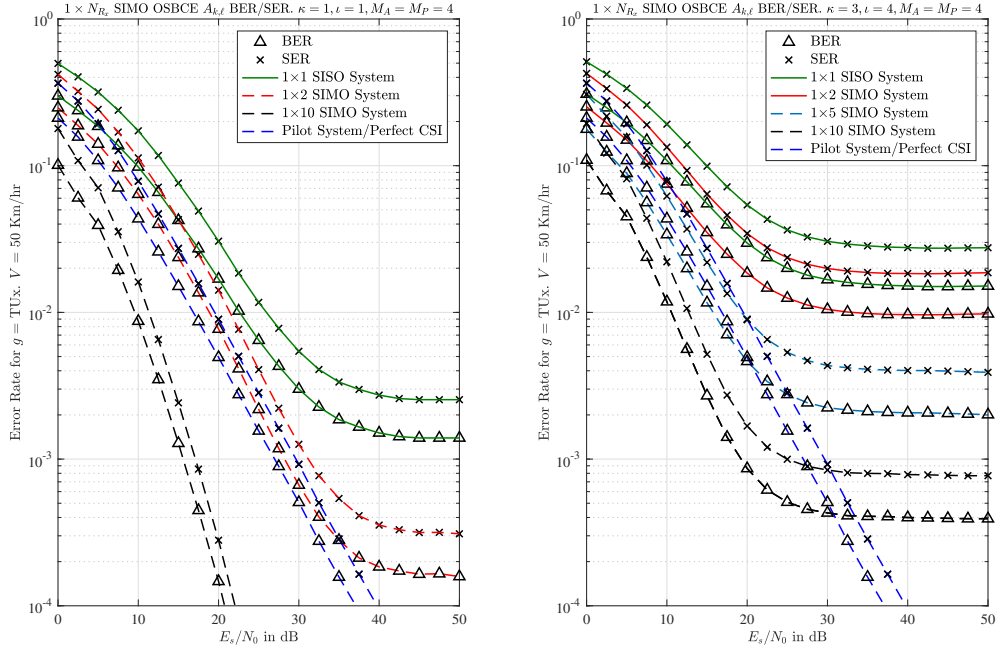


Figure 3.20: $1 \times N_{R_x}$ T/F. OSBCE - $\hat{A}_{k,\ell}$ BER & SER vs. SNR. $(\kappa, \ell) \in \{(1, 1), (3, 4)\}$

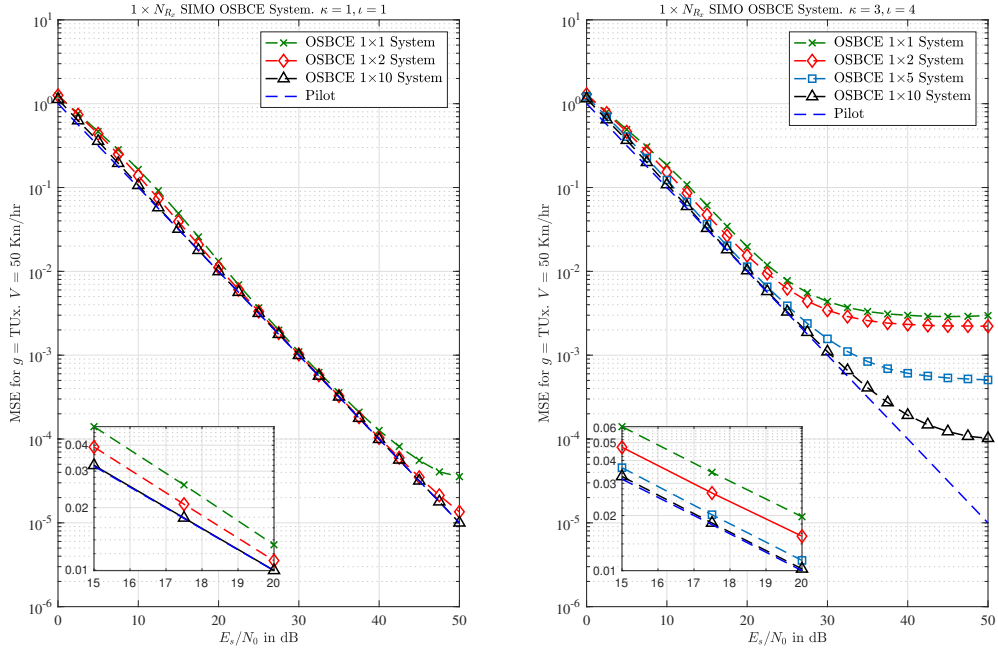


Figure 3.21: $1 \times N_{R_x}$ T/F. OSBCE - MSE vs. SNR for different N_{R_x} . $(\kappa, \ell) \in \{(1, 1), (3, 4)\}$

Figure 3.21 shows how increasing the number of receive antennas for $(\kappa, \ell) \in \{(1, 1), (3, 4)\}$

cases affects the CFRs MSE. With $(\kappa, \iota) = (1, 1)$ and $N_{R_x} = 2$, the detection of $A_{k,\ell}$ is enhanced to the point where the MSE of OSBCE estimated CFRs almost matches that of the pilot-based system. As the Euclidean distance increases, more receive antennas are needed to match the pilot-based system performance. With $(\kappa, \iota) = (3, 4)$, the MSE with 10 receive antennas still deviates from the pilot-based MSE at $\text{SNR} \simeq 30$, which means higher N_{R_x} are required.

From Figures 3.9, 3.15, and 3.21, it is noticed that the improvement rate due to higher N_{R_x} is slower with SIMO 2-D OSBCE than the 2 variations of SIMO 1-D OSBCE. Generally speaking, for a frequency selective fast fading channel, a higher number of receive antennas are needed for 2-D OSBCE than 1-D OSBCE. This is due to the fact that 2-D OSBCE system has to deal with phase distortions from two dimensions, frequency and time. Thus, generally speaking, SIMO 2-D OSBCE will have poorer performance than SIMO 1-D OSBCE.

Figures 3.22 and 3.23 show the magnitude and angle, respectively, of $\rho(\kappa, \iota)$ between $\varphi_\ell H_{k,\ell}$ and $\varphi_{\ell+\iota} H_{k+\kappa,\ell}$, as a function of κ and ι . It is evident from Figure 3.22 that the rate at which $|\rho(\kappa, \iota)|$ decreases with each ι -step is higher than the degradation rate resulting from each κ -step. For high values of ι , as κ increase $|\rho(\kappa, \iota)|$ starts increasing, however, the $\arg\{\rho(\kappa, \iota)\}$ is negative and increasing, which means that the phase will be shifted. Thus, the MLD detection of the transmitted MPSK symbol $A_{k,\ell}$ would suffer.

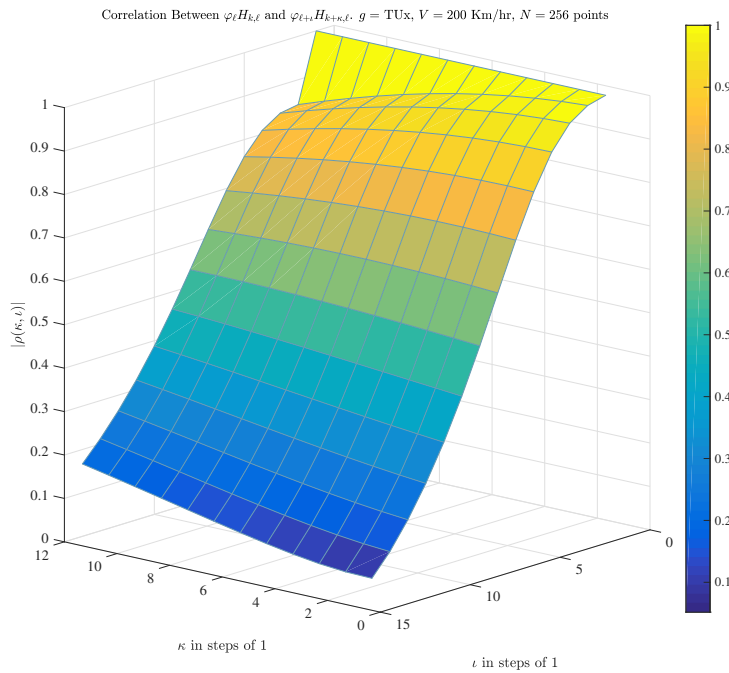


Figure 3.22: $1 \times N_{R_x}$ T/F. OSBCE - $|\rho(\kappa, \iota)|$. TUx channel. $V = 200$ Km/hr

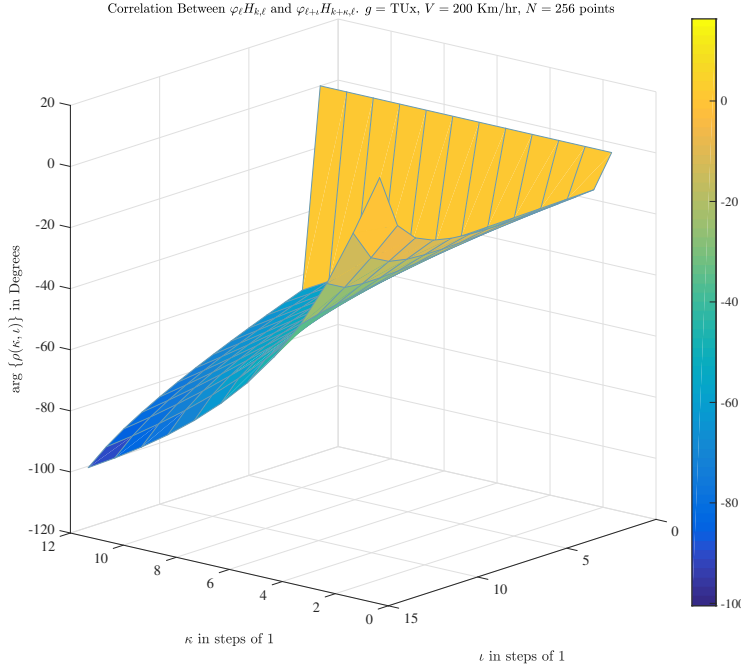


Figure 3.23: $1 \times N_{R_x}$ T/F. OSBCE - $\arg \{\rho(\kappa, \iota)\}$. TUx channel. $V = 200$ Km/hr

Although 2-D OSBCE generally requires higher number of N_{R_x} than 1-D OSBCE systems, it is preferable because it provides information about the channel behavior over both dimensions and can eventually be reduced to one of the 1-D OSBCEs. If 2-D OSBCE matches the performance of one of the other 1-D OSBCEs, it means that there are no significant variations in the channel across the other dimension, since it did not contribute any phase distortion. In addition, this means that it would not be required to interpolate across the static dimension, and can simply repeat the CFR coefficients along that static dimension as long as the 2-D OSBCE performance matches the 1-D OSBCE performance across the other dimension. For example, assume 2 MPSKs and 1 MASK were sent at (k, ℓ) , $(k + \kappa, \ell)$, and $(k + \kappa, \ell + \iota)$, respectively. If $E \{H_{k,\ell} H_{k+\kappa,\ell}^*\} \simeq E \{H_{k,\ell} (\varphi_{\ell+\iota} H_{k+\kappa,\ell})^*\}$, then no significant variations are happening across the different OFDM symbols. Hence, 1-D OSBCE across frequency is used to obtain the CFRs across frequency, perform interpolation, and then repeat the CFRs for the other OFDM symbols as long as $E \{H_{k,\ell} H_{k+\kappa,\ell}^*\} \simeq E \{H_{k,\ell} (\varphi_{\ell+\iota} H_{k+\kappa,\ell})^*\}$. Generally, this means that less interpolation-related computations are needed as well.

3.4 Conclusion

In this Chapter, a new blind CE technique for SIMO-OFDM systems is proposed based on a hybrid OFDM symbol structure, where MPSK symbols are transmitted at conventional

OFDM pilot REs, and MASK symbols are transmitted at REs that are generally separated from MPSK locations by $d_{\kappa,\iota} = \sqrt{\kappa^2 + \iota^2}$, where κ and ι are the frequency and time dimension separation distances, respectively, in terms of REs. Assuming channel variations are minimal within $\kappa\Delta_f$ Hz and $\iota\Delta_t$ seconds, then the MASK symbol is equivalent to an imperfect CFR with respect to the MPSK symbol. Therefore, the MPSK symbol can be immediately decoded, and then used in obtaining the CFR at the MPSK location. The OSBCE was presented in LTE-A system with 1 transmit antenna, in order to show that the system can be practically incorporated to current systems. It was shown that as the number of receive antennas increases, the MSE of the OSBCE-estimated CFRs approaches that of the pilot-based system. Because of the nature of pilot-based systems, its MSE does not benefit from increasing the number of receive antennas.

The proposed estimator, generally speaking, requires a minimum $d_{\kappa,\iota} = 1$ for the F.OSBCE and T.OSBCE variations, and a minimum $d_{\kappa,\iota} = \sqrt{2}$ for the T/F.OSBCE variations to estimate the CFR. This means that the minimum possible observation windows for F.OSBCE, T.OSBCE, and T/F.OSBCE are 1 OFDM symbol, 1 subcarrier, and 1 OFDM/1 subcarrier, respectively. This means that the OSBCE for SIMO-OFDM systems is suitable for mobile channels, where the channel frequently varies in either frequency, time or both domains. With the pilot-based system set as a benchmark [43], computer simulations were used to verify the analytical results wherever possible, and confirm that the OSBCE is capable of producing reliable channel estimates as compared to pilot-based systems, with similar complexity, but with improved spectral efficiency. Discussions of numerical results were provided with focus on the effect of the increased number of antennas on the performance of the OSBCE.

Chapter 4

One-Shot Blind Channel Estimation for MIMO-OFDM Systems¹

4.1 Introduction

The OSBCE system in Chapter 3 only considered the case with single transmit antenna and multiple receive antennas, which is generally suitable for UE transmitting to the BS. However, LTE-A has different transmission modes in which multiple transmit antennas are used, such as transmitting from the BS to UEs. In that case, the received symbols at one RE at one receive antenna would be a collective of all transmitted symbols from different transmit antennas. Hence, the MPSK and MASK symbols of the OSBCE system will be mixed with other symbols. Therefore, in this Chapter, the blind CE technique from Chapter 3 is developed for MIMO-OFDM DWCS, and investigated with different system requirements and channel conditions, hence, multiple implantation schemes are proposed in this Chapter. Numerical results and discussions are presented throughout the Chapter after presenting each system variation. Finally, the Chapter is concluded with a summary of results.

4.2 MIMO-OFDM $N_{T_x} \times N_{R_x}$ OSBCE System Models

The clear distinction between MIMO and SIMO, is that multiple transmit symbols are transmitted from N_{T_x} antennas at the same time at the same subcarrier. Hence, the ℓ^{th}

¹Related Publications:

1. M. Zourob, A. Al-Dweik and R. Rao, "One-Shot Blind Channel Estimation for MIMO-OFDM Systems Over Fast and Frequency-Selective Fading Channels," IEEE Transactions on Vehicular Technology (TVT by IEEE), under preparation.

received symbol at the k^{th} subcarrier at the n^{th} receive antenna, $n \in \{1, 2, \dots, N_{R_x}\}$ would be the collective of all multipath faded ℓ^{th} transmitted symbols at the k^{th} subcarrier from the N_{T_x} antenna plus the additive white noise. Usually, some form of coding or orthogonality is embedded in coordination between the different transmitters, to make sure that the received symbols can be easily separated at the receiver side. However, those methods usually incur high computational complexity, and does not guarantee accurate recovery of transmitted pilot symbols for CE. Therefore, in practical systems such as LTE-A, a single transmitter is assigned specific locations in the RG where it transmits its associated pilot symbols, while the other transmitters are nulled [60]. This is done to make sure that receive antennas at specific locations in the RG only receive the pilot symbols from one specific transmitter. Therefore, similar to Chapter 2, the LTE-A distribution is used to investigate the application of OSBCE for MIMO-OFDM systems.

In the following sections, different variations of OSBCE across frequency, time and time/frequency are presented. The same system model setup and defined variables for the SIMO cases are carried over to the different MIMO cases. Because of the way LTE-A pilots are distributed and for ease of demonstration, the discussion is limited to $mT_x \times nR_x$ MIMO systems, where $m = 2, n \in \{1, 2, \dots, N_{R_x}\}$, but the system is general for N_{T_x} , given the appropriate coding scheme is used to ensure that the MPSK or MASK symbols per transmit antenna are separable at the receiver.

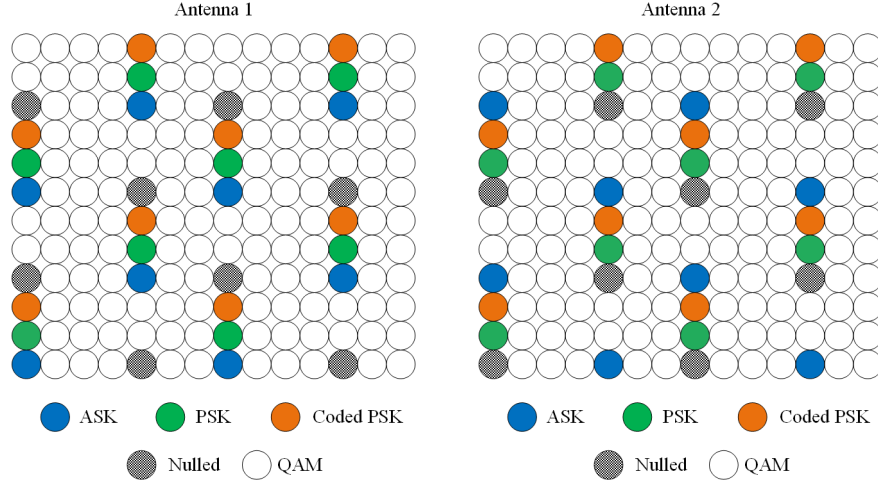
4.2.1 MIMO 1-D F.OSBCE - Across Frequency

4.2.1.1 Mode 1

In this OSBCE variation, the pilots are distributed across one dimension (frequency) within one OFDM symbol, where MASK symbols are sent at original pilot locations from Antenna 1, while the Antenna 2 is nulled. Therefore, only the MASK symbol from Antenna 1 would be received at the specific OFDM symbols at specific subcarriers with no interference from other transmit antennas. Thus, the phase of the received MASK would act as an imperfect channel estimate to be used for equalizing the MPSK symbols, similar to the SIMO cases. Next, MPSK symbols are sent at the adjacent subcarrier at Antenna 1, meaning that $\kappa = 1$ as shown in Figure 4.1, however, the transmitted symbol from Antenna 2 would interfere with the MPSK symbol sent from Antenna 1. Therefore, some form of coding is needed to make sure the received symbols from the two antennas at the adjacent locations to pilots' locations are separable. Therefore, the coding scheme in Table 4.1 is proposed to facilitate the implementation of different variations of OSBCE in MIMO systems. Since this work deals with an observation window of size 1, the block index notation ℓ is dropped in the remaining

	Transmit Antenna 1	Transmit Antenna 2
Nullled	$A_{k+3\kappa}^{(1)}$	$A_k^{(2)}$
MASK	$A_k^{(1)}$	$A_{k+3\kappa}^{(2)}$
MPSK	$A_{k+\kappa}^{(1)}$	$A_{k+\kappa}^{(2)}$
Coded MPSK	$A_{k+2\kappa}^{(1)} = -A_{k+\kappa}^{(1)}$	$A_{k+2\kappa}^{(2)} = A_{k+\kappa}^{(2)}$

Table 4.1: MIMO 1-D F.OSBCE Mode 1 coding scheme


 Figure 4.1: $2 \times N_{R_x}$ Frequency OSBCE system - Mode 1

parts unless it is necessary to include it. For consistency, in all subsequent systems with the label “Mode 1”, the energy for the MPSK and coded MPSK symbols are 1/2 the energy of the MPSK symbols in systems labeled as “Mode 2”.

It is assumed that ISI is eliminated before the CE step using enough N_{CP} CP samples. Following the transmission scheme shown in Table 4.1, the received post-FFT symbols at the ℓ^{th} OFDM and subcarriers $k, k + \kappa, k + 2\kappa, k + 3\kappa$ for receive antenna n are,

$$r_k^{(n)} = A_k^{(1)} H_k^{(1,n)} + \eta_k^{(n)} \quad (4.1)$$

$$r_{k+\kappa}^{(n)} = \frac{1}{2} \left(A_{k+\kappa}^{(1)} H_{k+\kappa}^{(1,n)} + A_{k+\kappa}^{(2)} H_{k+\kappa}^{(2,n)} \right) + \eta_{k+\kappa}^{(n)} \quad (4.2)$$

$$r_{k+2\kappa}^{(n)} = \frac{1}{2} \left(-A_{k+\kappa}^{(1)} H_{k+2\kappa}^{(1,n)} + A_{k+\kappa}^{(2)} H_{k+2\kappa}^{(2,n)} \right) + \eta_{k+2\kappa}^{(n)} \quad (4.3)$$

$$r_{k+3\kappa}^{(n)} = A_{k+3\kappa}^{(2)} H_{k+3\kappa}^{(2,n)} + \eta_{k+3\kappa}^{(n)}. \quad (4.4)$$

Due to nulling, $r_k^{(n)}$ and $r_{k+3\kappa}^{(n)}$ can be considered as imperfect channel estimates to be used for equalization. Next, the MPSK symbols from each antenna need to be separated. It is worth nothing here that the CFRs, $H_k^{(m,n)}$, are $\sim \mathcal{CN} \left(0, \sum_{v=0}^{L_h} 2\sigma_{h_v}^2 \right)$, for a channel with $L_h + 1$ independent complex multipath components each of which has a gain $h_v \sim \mathcal{CN} (0, 2\sigma_{h_v}^2)$ and

delay $v \times T_s$, where $v \in \{0, 1, \dots, L_h\}$. In OSBCE, it is assumed that $E \left\{ H_k^{(m,n)} \left(H_{k+\kappa}^{(m,n)} \right)^* \right\} = e^{j \times 0}$, where $\kappa = 1$. Thus, $H_{k+\kappa}^{(m,n)} = \left(H_k^{(m,n)} + \Delta_\kappa^{(m,n)} \right) \approx H_k^{(m,n)}$, where

$$\begin{aligned} \Delta_\kappa^{(m,n)} &= \sum_{v=0}^{L_h} h_v \left[e^{-j2\pi v(k+\kappa)/N} - e^{-j2\pi vk/N} \right] \\ &= \sum_{v=0}^{L_h} h_v e^{-j2\pi vk/N} \left[e^{-j2\pi v\kappa/N} - 1 \right]. \end{aligned} \quad (4.5)$$

$\Delta_\kappa^{(m,n)}$ is a RV describing the complex difference between CFRs of subcarriers separated by κ , with values $\Delta_\kappa^{(m,n)} \sim \mathcal{CN} \left(0, \left[2 \sum_{v=0}^{L_h} 2\sigma_{h_v}^2 (1 - \text{Re} \{ \rho(\kappa) \}) \right] \right)$. If $\kappa = 0$, then the variance of $\Delta_\kappa^{(m,n)} = 0$. Figure 4.2 shows the impact of κ on the variance of $\Delta_\kappa^{(m,n)}$ for different channels, and proves that variance of $\Delta_\kappa^{(m,n)}$ is a function of channel's frequency auto-correlation.

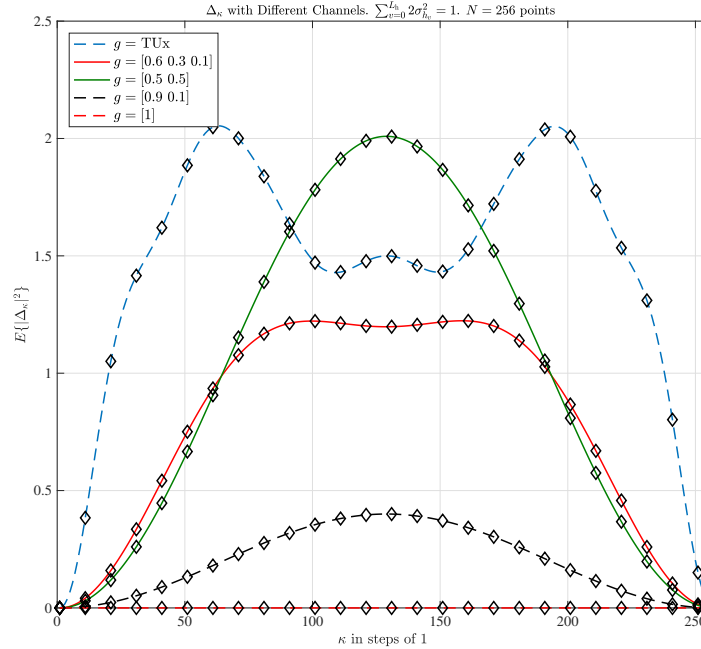


Figure 4.2: $E \{ \Delta_\kappa \Delta_\kappa^* \}$ vs κ for different channels

Hence, MPSK are separated as follows,

$$\begin{aligned} A_{k+\kappa}^{(1,n)} &= r_{k+\kappa}^{(n)} - r_{k+2\kappa}^{(n)} \\ &= A_{k+\kappa}^{(1)} \left(H_{k+\kappa}^{(1,n)} + \frac{\Delta_\kappa^{(1,n)}}{2} \right) - \frac{A_{k+\kappa}^{(2)} \Delta_\kappa^{(2,n)}}{2} + \check{\eta}_{k+\kappa}^{(n)} \end{aligned} \quad (4.6)$$

$$\begin{aligned}
 A_{k+\kappa}^{(2,n)} &= r_{k+\kappa}^{(n)} + r_{k+2\kappa}^{(n)} \\
 &= A_{k+\kappa}^{(2)} \left(H_{k+2\kappa}^{(2,n)} - \frac{\Delta_{\kappa}^{(2,n)}}{2} \right) - \frac{A_{k+\kappa}^{(1)} \Delta_{\kappa}^{(1,n)}}{2} + \tilde{\eta}_{k+\kappa}^{(n)}
 \end{aligned} \tag{4.7}$$

where $\tilde{\eta}_{k+\kappa}^{(n)}$ and $\hat{\eta}_{k+\kappa}^{(n)}$ are two white noise RVs $\sim \mathcal{CN}(0, 2(2\sigma_{\eta}^2))$. Now, it will be possible to decode for $A_{k+\kappa}^{(1)}$ and $A_{k+\kappa}^{(2)}$ using $r_k^{(n)}$ and $r_{k+3\kappa}^{(n)}$, respectively. The pattern is repeated as shown in Figure 4.1. The procedure per transmitter is similar and the following is a demonstration with respect to transmitter 1. Now, $A_{k+\kappa}^{(1)}$ is detected as follows,

$$\begin{aligned}
 \mathcal{S}_{k+\kappa}^{(1,n)} &= A_{k+\kappa}^{(1,n)} / r_k^{(n)} \\
 &= \frac{A_{k+\kappa}^{(1)} \left(H_{k+\kappa}^{(1,n)} + \frac{\Delta_{\kappa}^{(1,n)}}{2} \right) - \frac{A_{k+\kappa}^{(2)} \Delta_{\kappa}^{(2,n)}}{2} + \tilde{\eta}_{k+\kappa}^{(n)}}{A_k^{(1)} H_k^{(1,n)} + \eta_k^{(n)}} \\
 &= \frac{A_{k+\kappa}^{(1)} \left(H_{k+\kappa}^{(1,n)} + \frac{\Delta_{\kappa}^{(1,n)}}{2} \right) - \frac{A_{k+\kappa}^{(2)} \Delta_{\kappa}^{(2,n)}}{2} + \tilde{\eta}_{k+\kappa}^{(n)}}{\left| A_k^{(1)} H_k^{(1,n)} + \eta_k^{(n)} \right| e^{j\hat{\theta}_k^{(1,n)}}} \\
 &= \frac{A_{k+\kappa}^{(1)} \left| H_{k+\kappa}^{(1,n)} + \frac{\Delta_{\kappa}^{(1,n)}}{2} \right| e^{j(\hat{\theta}_{k+\kappa}^{(1,n)} - \hat{\theta}_k^{(1,n)})} + \left| \tilde{\eta}_{k+\kappa}^{(n)} \right| e^{j(\arg(\tilde{\eta}_{k+\kappa}^{(n)}) - \hat{\theta}_k^{(1,n)})}}{\left| H_{k+\kappa}^{(n)} A_{k+\kappa} + \eta_{k+\kappa}^{(n)} \right|} \\
 &= \frac{1}{\left| r_k^{(n)} \right|} \left(\left| H_{k+\kappa}^{(1,n)} + \frac{\Delta_{\kappa}^{(1,n)}}{2} \right| e^{j\vartheta_k^{(1,n)}} A_{k+\kappa}^{(1)} + \tilde{\eta}_{k+\kappa}^{(n)} \right)
 \end{aligned} \tag{4.8}$$

where $\vartheta_k^{(m,n)} = \hat{\theta}_{k+\kappa}^{(m,n)} - \hat{\theta}_k^{(m,n)}$, $\hat{\theta}_{k+\kappa}^{(m,n)} \approx \theta_{k+\kappa}^{(m,n)}$, $\tilde{\eta}_{k+\kappa}^{(n)} = \left| \tilde{\eta}_{k+\kappa}^{(n)} \right| e^{j(\arg(\tilde{\eta}_{k+\kappa}^{(n)}) - \hat{\theta}_k^{(1,n)})}$. Next, EGC is employed to combine all the co-phased $\mathcal{S}_{k+\kappa}^{(1,n)}$, $n \in \{1, 2, \dots, N_{R_x}\}$, from the different receive antennas as follows,

$$\sum_{n=1}^{N_{R_x}} \mathcal{S}_{k+\kappa}^{(1,n)} = A_{k+\kappa}^{(1)} \sum_{n=1}^{N_{R_x}} \frac{\left| H_{k+\kappa}^{(1,n)} + \frac{\Delta_{\kappa}^{(1,n)}}{2} \right| e^{j\vartheta_k^{(1,n)}}}{\left| r_k^{(n)} \right|} + \sum_{n=1}^{N_{R_x}} \frac{\tilde{\eta}_{k+\kappa}^{(n)}}{\left| r_k^{(n)} \right|}. \tag{4.9}$$

As mentioned previously, the MPSK symbol is detected using the phase of the combined equalized waveforms, hence, only the phase of $\sum_{n=1}^{N_{R_x}} \mathcal{S}_{k+\kappa}^{(1,n)}$ is required for detection. $\vartheta_k^{(m,n)}$ and $\tilde{\eta}_{k+\kappa}^{(n)}$ are the two sources of phase error that would effect the detection process. In this subsection, $\vartheta_k^{(m,n)}$ is redefined as $\vartheta_k^{(m,n)} = \hat{\theta}_{k+\kappa}^{(m,n)} - \hat{\theta}_k^{(m,n)}$. Due to EGC, the noise effect in general is reduced by collecting the signal from multiple receivers. Moreover, κ inherently affects $\vartheta_k^{(m,n)} = \hat{\theta}_{k+\kappa}^{(m,n)} - \hat{\theta}_k^{(m,n)}$. As κ increases, the correlation between the associated CFRs decreases and $E \left\{ H_k^{(n)} \left(H_{k+\kappa}^{(n)} \right)^* \right\} \approx e^{j \times 0}$ no longer holds, thus, producing more phase error

in the MLD detection. Using MLD, the initial estimate, $\hat{A}_{k+\kappa}^{(1)}$, is expressed as,

$$\hat{A}_{k+\kappa}^{(1)} = \arg \min_{(A_{k+\kappa}^{(1)})^{(i)}, i \in \mathbb{M}_P} \left| \sum_{n=1}^{N_{R_x}} \mathcal{S}_{k+\kappa}^{(1,n)} - (A_{k+\kappa}^{(1)})^{(i)} \right|^2. \quad (4.10)$$

Using $\hat{A}_{k+\kappa}^{(1)}$, $\hat{H}_{k+\kappa}^{(1,n)}$ at each n^{th} branch can be found using LSE as follows,

$$\hat{H}_{k+\kappa}^{(1,n)} = \frac{A_{k+\kappa}^{(1,n)}}{\hat{A}_{k+\kappa}^{(1)}} = \frac{A_{k+\kappa}^{(1)} \left(H_{k+\kappa}^{(1,n)} + \frac{\Delta_{k+\kappa}^{(1,n)}}{2} \right) - \frac{A_{k+\kappa}^{(2)} \Delta_{k+\kappa}^{(2,n)}}{2} + \tilde{\eta}_{k+\kappa}^{(n)}}{\hat{A}_{k+\kappa}^{(1)}} \quad (4.11)$$

$$\text{At high SNR} \approx H_{k+\kappa}^{(1,n)} + \frac{\Delta_{k+\kappa}^{(1,n)}}{2} - \frac{A_{k+\kappa}^{(2)} \Delta_{k+\kappa}^{(2,n)}}{2\hat{A}_{k+\kappa}^{(1)}} + \ddot{\eta}_{k+\kappa}^{(n)} \quad (4.12)$$

where $\ddot{\eta}_{k+\kappa}^{(n)} = \left| \tilde{\eta}_{k+\kappa}^{(n)} \right| e^{j(\arg\{\tilde{\eta}_{k+\kappa}^{(n)}\} - \arg\{\hat{A}_{k+\kappa}^{(1)}\})}$. The first term corresponds to the CFR estimate.

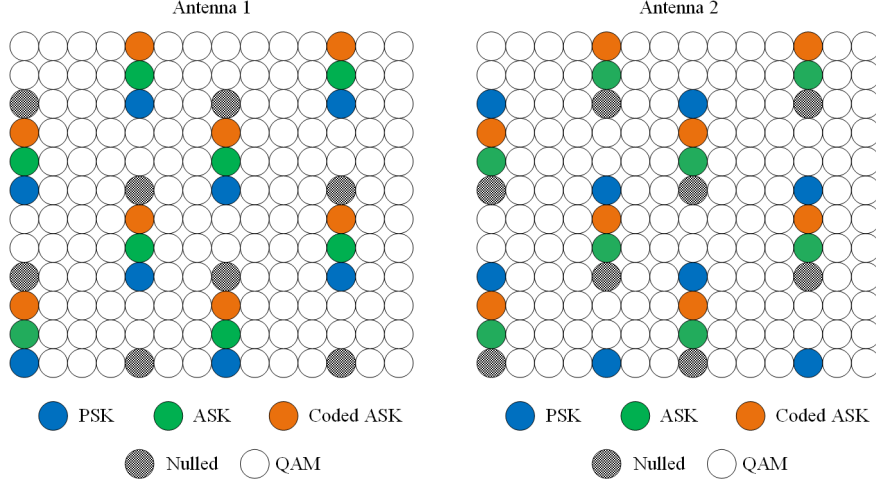
As the number of receiving antennas N_{R_x} increases, the SER for $\hat{A}_{k+\kappa}^{(m)}$ improves drastically, to the point where $\hat{A}_{k+\kappa}^{(m)} = A_{k+\kappa}^{(m)}$ and the first term of (4.11) becomes the perfect CFR. For low SNR, increasing the number of receive antennas would result in some system enhancement. However, the second and third terms of (4.11) constitutes distortion that persists at each receiving antenna and mainly depends on the channel statistics. The problem is that those terms do not reap the benefits of increasing the number of receive antennas. Hence, it is expected that an error floor would persist no matter how many receive antennas are used. Similarly, we can decode for $A_{k+\kappa}^{(2)}$ using $A_{k+\kappa}^{(2,n)}$ and $r_{k+3\kappa}^{(n)}$.

4.2.1.2 Mode 1 M

In this section, a modified MIMO OSBCE across frequency is presented to remedy the distortion problem presented in subsection 4.2.1.1. The modification is based on replacing the positions of MASK with MPSK and vice versa, and apply the coding to the MASK symbols as shown in Table 4.2.

	Transmit Antenna 1	Transmit Antenna 2
Nullled	$A_{k+3\kappa}^{(1)}$	$A_k^{(2)}$
MPSK	$A_k^{(1)}$	$A_{k+3\kappa}^{(2)}$
MASK	$A_{k+\kappa}^{(1)}$	$A_{k+\kappa}^{(2)}$
Coded MASK	$A_{k+2\kappa}^{(1)} = -A_{k+\kappa}^{(1)}$	$A_{k+2\kappa}^{(2)} = A_{k+\kappa}^{(2)}$

Table 4.2: MIMO 1-D F.OSBCE Mode 1 M coding scheme


 Figure 4.3: $2 \times N_{R_x}$ Frequency OSBCE system - Mode 1 M

By using the scheme shown in Table 4.2, and following the procedure in subsection 4.2.1.1, the received post-FFT symbols at the ℓ^{th} OFDM and subcarriers $k, k + \kappa, k + 2\kappa, k + 3\kappa$ for receive antenna n are,

$$r_k^{(n)} = A_k^{(1)} H_k^{(1,n)} + \eta_k^{(n)} \quad (4.13)$$

$$r_{k+\kappa}^{(n)} = \frac{1}{2} \left(A_{k+\kappa}^{(1)} H_{k+\kappa}^{(1,n)} + A_{k+\kappa}^{(2)} H_{k+\kappa}^{(2,n)} \right) + \eta_{k+\kappa}^{(n)} \quad (4.14)$$

$$r_{k+2\kappa}^{(n)} = \frac{1}{2} \left(-A_{k+\kappa}^{(1)} H_{k+2\kappa}^{(1,n)} + A_{k+\kappa}^{(2)} H_{k+2\kappa}^{(2,n)} \right) + \eta_{k+2\kappa}^{(n)} \quad (4.15)$$

$$r_{k+3\kappa}^{(n)} = A_{k+3\kappa}^{(2)} H_{k+3\kappa}^{(2,n)} + \eta_{k+3\kappa}^{(n)}. \quad (4.16)$$

Notice here that the MPSK symbols are received without any cross-talk from another symbol. However, now the MASK symbols from each antenna need to be separated. Using the same notation and variable definitions as in subsection 4.2.1.1, MASKs from the different transmit antennas are separated as follows,

$$\begin{aligned} A_{k+\kappa}^{(1,n)} &= r_{k+\kappa}^{(n)} - r_{k+2\kappa}^{(n)} \\ &= A_{k+\kappa}^{(1)} \left(H_{k+\kappa}^{(1,n)} + \frac{\Delta_{\kappa}^{(1,n)}}{2} \right) - \frac{A_{k+\kappa}^{(2)} \Delta_{\kappa}^{(2,n)}}{2} + \tilde{\eta}_{k+\kappa}^{(n)} \end{aligned} \quad (4.17)$$

$$\begin{aligned} A_{k+\kappa}^{(2,n)} &= r_{k+\kappa}^{(n)} + r_{k+2\kappa}^{(n)} \\ &= A_{k+\kappa}^{(2)} \left(H_{k+2\kappa}^{(2,n)} - \frac{\Delta_{\kappa}^{(2,n)}}{2} \right) - \frac{A_{k+\kappa}^{(1)} \Delta_{\kappa}^{(1,n)}}{2} + \hat{\eta}_{k+\kappa}^{(n)}. \end{aligned} \quad (4.18)$$

Now, $A_k^{(1)}$ is detected as follows,

$$\begin{aligned}
 \mathcal{S}_k^{(1,n)} &= r_k^{(n)} / \Lambda_{k+\kappa}^{(1,n)} \\
 &= \frac{A_k^{(1)} H_k^{(1,n)} + \eta_k^{(n)}}{A_{k+\kappa}^{(1)} \left(H_{k+\kappa}^{(1,n)} + \frac{\Delta_{k+\kappa}^{(1,n)}}{2} \right) - \frac{A_{k+\kappa}^{(2)} \Delta_{k+\kappa}^{(2,n)}}{2} + \tilde{\eta}_{k+\kappa}^{(n)}} \\
 &= \frac{A_k^{(1)} H_k^{(1,n)} + \eta_k^{(n)}}{\left| A_{k+\kappa}^{(1)} \left(H_{k+\kappa}^{(1,n)} + \frac{\Delta_{k+\kappa}^{(1,n)}}{2} \right) - \frac{A_{k+\kappa}^{(2)} \Delta_{k+\kappa}^{(2,n)}}{2} + \tilde{\eta}_{k+\kappa}^{(n)} \right| e^{j\hat{\theta}_{k+\kappa}^{(1,n)}}} \\
 &= \frac{A_k^{(1)} \left| H_k^{(1,n)} \right| e^{j(\theta_k^{(1,n)} - \hat{\theta}_{k+\kappa}^{(1,n)})} + \left| \eta_k^{(n)} \right| e^{j(\arg(\eta_k^{(n)}) - \hat{\theta}_{k+\kappa}^{(1,n)})}}{\left| A_{k+\kappa}^{(1)} \left(H_{k+\kappa}^{(1,n)} + \frac{\Delta_{k+\kappa}^{(1,n)}}{2} \right) - \frac{A_{k+\kappa}^{(2)} \Delta_{k+\kappa}^{(2,n)}}{2} + \tilde{\eta}_{k+\kappa}^{(n)} \right|} \\
 &= \frac{1}{\left| \Lambda_{k+\kappa}^{(1,n)} \right|} \left(\left| H_k^{(1,n)} \right| e^{j\vartheta_k^{(1,n)}} A_k^{(1)} + \tilde{\eta}_k^{(n)} \right) \tag{4.19}
 \end{aligned}$$

where $\vartheta_k^{(m,n)} = \theta_k^{(m,n)} - \hat{\theta}_{k+\kappa}^{(m,n)}$, $\tilde{\eta}_k^{(n)} = \left| \eta_k^{(n)} \right| e^{j(\arg(\eta_k^{(n)}) - \hat{\theta}_{k+\kappa}^{(1,n)})}$. Next, EGC is employed combine all the co-phased $\mathcal{S}_k^{(1,n)}$, $n \in \{1, 2, \dots, N_{R_x}\}$, from the different receive antennas as follows,

$$\sum_{n=1}^{N_{R_x}} \mathcal{S}_k^{(1,n)} = A_k^{(1)} \sum_{n=1}^{N_{R_x}} \frac{\left| H_k^{(1,n)} \right| e^{j\vartheta_k^{(1,n)}}}{\left| \Lambda_{k+\kappa}^{(1,n)} \right|} + \sum_{n=1}^{N_{R_x}} \frac{\tilde{\eta}_k^{(n)}}{\left| \Lambda_{k+\kappa}^{(1,n)} \right|}. \tag{4.20}$$

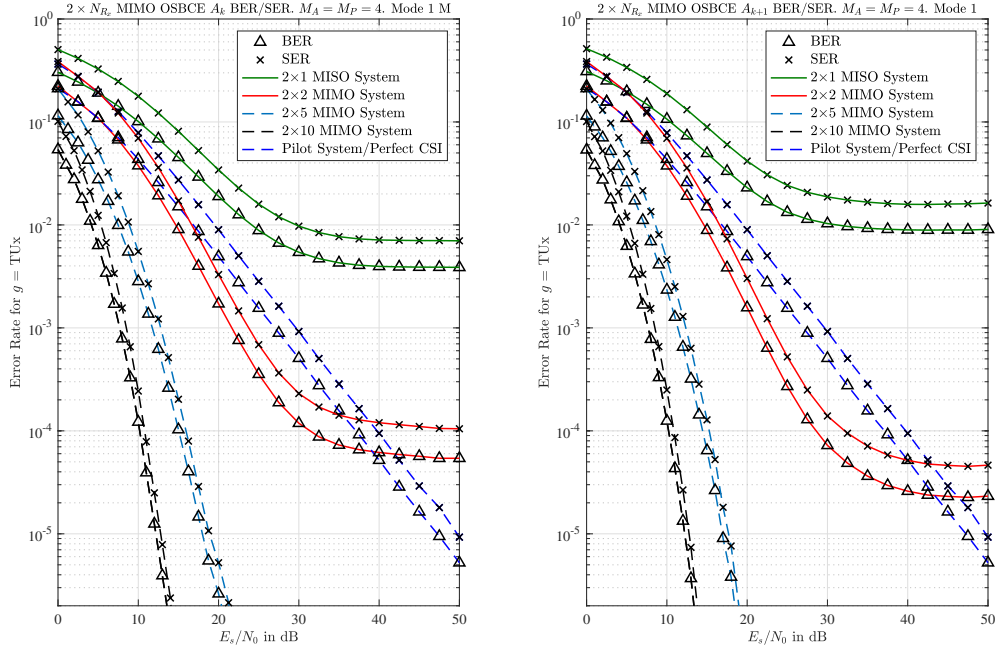
As mentioned previously, the MPSK symbol is detected using the phase of the combined equalized waveforms, hence, only the phase of $\sum_{n=1}^{N_{R_x}} \mathcal{S}_k^{(1,n)}$ is required for detection. $\vartheta_k^{(m,n)}$ and $\tilde{\eta}_k^{(n)}$ are the two sources of phase error that would effect the detection process. In this subsection, $\vartheta_k^{(1,n)}$ is redefined as $\vartheta_k^{(m,n)} = \theta_k^{(m,n)} - \hat{\theta}_{k+\kappa}^{(m,n)}$, where κ inherently affects $\vartheta_k^{(1,n)}$. Using MLD, the initial estimate, $\hat{A}_k^{(1)}$, is expressed as,

$$\hat{A}_k^{(1)} = \arg \min_{(A_k^{(1)})^{(i)}, i \in \mathbb{M}_P} \left| \sum_{n=1}^{N_{R_x}} \mathcal{S}_k^{(1,n)} - (A_k^{(1)})^{(i)} \right|^2. \tag{4.21}$$

Using $\hat{A}_k^{(1)}$, $\hat{H}_k^{(1,n)}$ at each n^{th} branch can be found using LSE as follows,

$$\hat{H}_k^{(1,n)} = \frac{r_k^{(n)}}{\hat{A}_k^{(1)}} = \frac{A_k^{(1)} H_k^{(1,n)} + \eta_k^{(n)}}{\hat{A}_k^{(1)}} \approx H_k^{(1,n)} + \ddot{\eta}_k^{(n)} \tag{4.22}$$

where $\ddot{\eta}_k^{(n)} = \left| \eta_k^{(n)} \right| e^{j(\arg\{\eta_k^{(n)}\} - \arg\{\hat{A}_k^{(1)}\})}$. Contrary to the OSBCE system in subsection


 Figure 4.4: $2 \times N_{R_x}$ F. OSBCE - \hat{A}_k & $\hat{A}_{k+\kappa}$ BER & SER vs. SNR - Modes 1 M & 1

4.2.1.1, no distortion terms are present and increasing the number of receive antennas is expected to drastically enhance the MSE. The first term of (4.22) corresponds to the CFR estimate. As the number of receiving antennas N_{R_x} increases, the SER for $\hat{A}_k^{(m)}$ hugely improves, to the point where $\hat{A}_k^{(m)} = A_k^{(m)}$ and the first term of (4.22) becomes the perfect CFR. Similarly, we can decode for $A_k^{(2)}$ using $\Lambda_{k+\kappa}^{(2,n)}$ and $r_{k+3\kappa}^{(n)}$ following the same approach outlined previously.

4.2.1.3 Results and Discussion - Mode 1 vs. Mode 1 M

SER and BER vs. SNR for $\hat{A}_k^{(m)}$ using Mode 1 M and Mode 1, respectively in a TUx channel environment are presented in Figure 4.4, in order to evaluate their performance with respect to each other. In general, Mode 1 is marginally better than Mode 1 M for $N_{R_x} \geq 2$ in terms of SER of the initial MPSK detection. This is due to the fact that in Mode 1, the imperfect phase estimate is received without any cross-talk from other transmit antennas. On the other hand, the phase of the imperfect CFR in Mode 1 M is a result of adding/subtracting two received symbols. In both modes, the SER of the blindly estimated MPSK at high SNRs hits an error floor produced by $\vartheta_k^{(m,n)}$. Moreover, the improvement rate gets lower as the number of receive antennas increases.

CHAPTER 4. OSBCE FOR MIMO-OFDM SYSTEMS

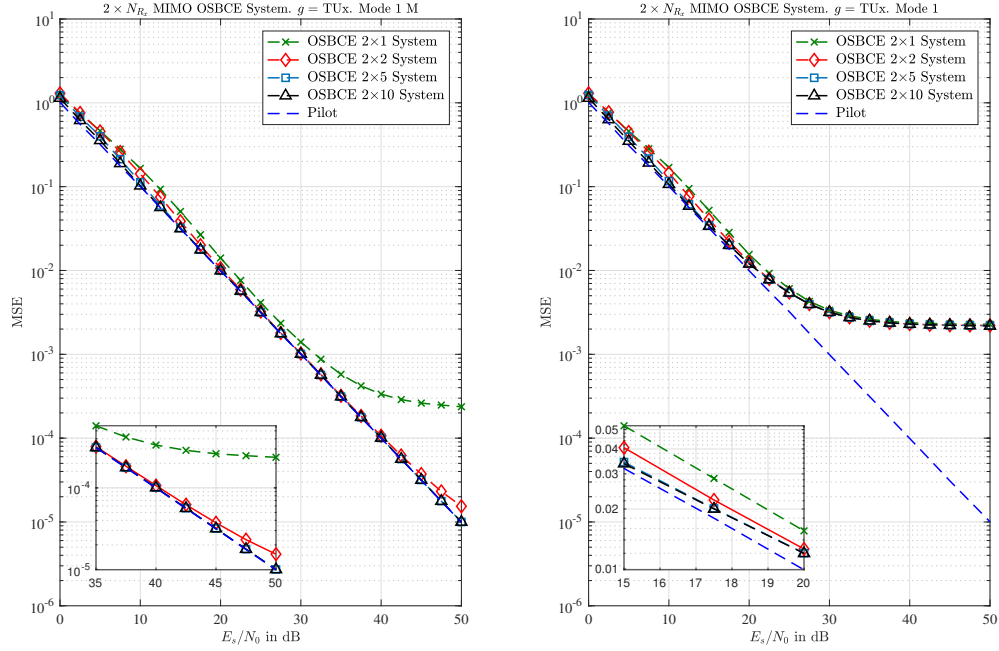


Figure 4.5: $2 \times N_{R_x}$ F. OSBCE - MSE vs. SNR for different N_{R_x} - Modes 1 M & 1

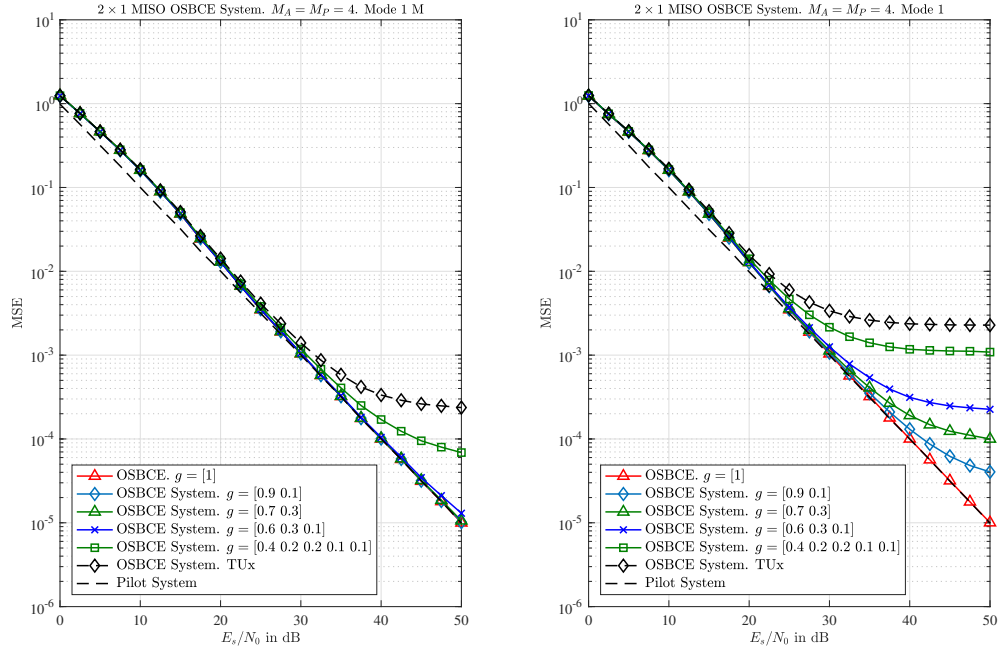


Figure 4.6: $2 \times N_{R_x}$ F. OSBCE - MSE vs. SNR for different channels - Modes 1 M & 1

Figure 4.5 compares the MSE of Mode 1 M to Mode 1 as the number of receive antennas

increases in a TUx channel environment. With Mode 1 M, simply using 2 receive antennas would improve the detection of $A_k^{(m)}$ to the point where the MSE of CFRs estimated using OSBCE almost matches that of the pilot-based system. As expected, OSBCE MSE using Mode 1 is not responsive to increasing the number of receive antennas, and the error floor is set by the channel-related terms in (4.11).

Figure 4.6 compares the MSE of Mode 1 M to Mode 1 for different channels. In a TUx channel environment, MSE using Mode 1 M is 2.5×10^{-4} at SNR = 50 dB, while for the same SNR, MSE using Mode 1 is 2.5×10^{-3} ; 10 times worse than Mode 1 M. Using Mode 1 M, the MSE performance of the OSBCE in a TUx channel environment starts deviating from the pilot-based system after SNR $\simeq 28$ dB. Generally speaking, simulation results show that Mode 1 M is more resilient to channel statistics than Mode 1.

Figure 4.7 shows the impact of increasing the modulation order across Mode 1 M and Mode 1 systems in a TUx channel environment. In Mode 1 M, as modulation order increases, the MSE performance gets worse, which is expected since increasing M_A will introduce more amplitudes with small values, which is similar to equalizing using less reliable channel estimates. Moreover, as M_P increases, smaller margins of phase noise can cause detection errors in \hat{A}_k . On the other hand, modulation order degrades the MSE using Mode 1 F.OSBCE until SNR $\simeq 24$ dB, then matches the MSE produced by lower modulation order systems.

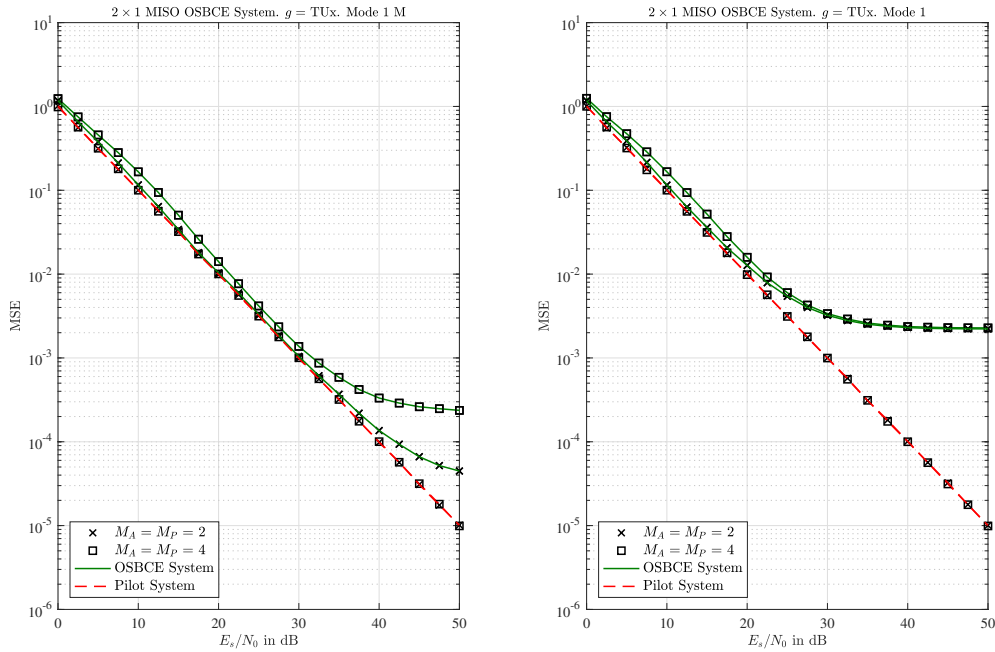


Figure 4.7: $2 \times N_{R_x}$ F. OSBCE - MSE vs. SNR for different M_A , M_P - Modes 1 M & 1

Therefore, even if higher modulation orders were to be used with Mode 1 F.OSBCE, it will eventually hit the same error floor produced by the Mode 1 F.OSBCE binary case.

It is worth mentioning that the pilot-based system performance neither benefits from increasing the number of transmit antennas nor receive antennas. Increasing the number of receive antennas would simply mean that there are more CFRs to estimate at the receiver side. In addition, in conventional LTE-A pilot-based systems, RE locations where the m^{th} transmit antenna transmits its pilots are nulled at all other transmitting antennas. Therefore, only the m^{th} antenna pilots are received at its designated locations in the RG.

Moreover, it is worth noting that MIMO F.OSBCE Mode 1 M achieves diversity gain by sending MASK over two different subcarriers, however, that nulls some of the spectral gain from replacing the pilot symbol by a data MPSK symbol.

4.2.1.4 Mode 2

In this MIMO F.OSBCE system, only original LTE-A pilot locations are used and no coding is needed, where MPSK and MASK are transmitted as shown in Figure 4.8. This system is introduced as an alternative to MIMO F.OSBCE Mode 1 M, in order to increase data rate by replacing pilots by MPSK and MASK data symbols.

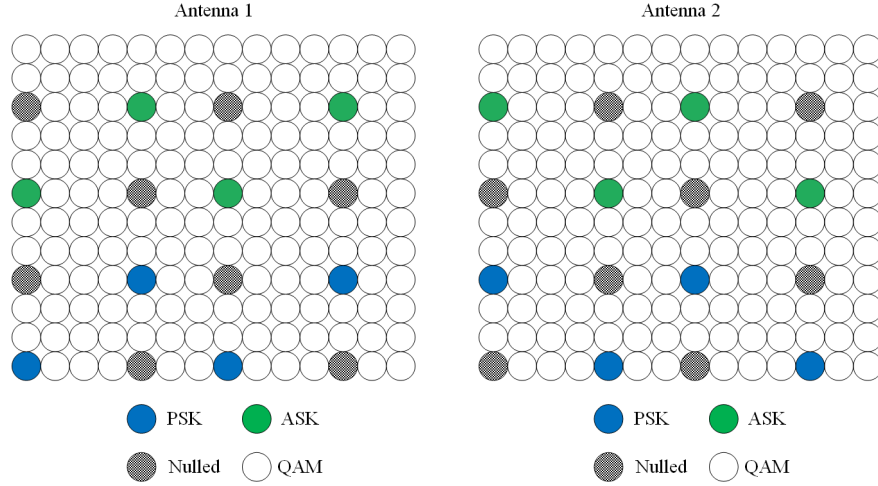


Figure 4.8: $2 \times N_{R_x}$ Frequency OSBCE system - Mode 2

The MPSK and MASK symbols are transmitted at subcarriers k , \hat{k} , and $k + \kappa$, $\hat{k} + \kappa$, respectively, where $\kappa = 6$. k and \hat{k} are the subcarriers indexing for transmitters 1 and 2, respectively, where $\hat{k} - k = 3$ for C-RS LTE-A [12]. Hence, the received post-FFT samples for receive antenna n are,

$$r_k^{(n)} = A_k^{(1)} H_k^{(1,n)} + \eta_k^{(n)} \quad (4.23)$$

$$r_{k+\kappa}^{(n)} = A_{k+\kappa}^{(1)} H_{k+\kappa}^{(1,n)} + \eta_{k+\kappa}^{(n)} \quad (4.24)$$

$$r_{\hat{k}}^{(n)} = A_{\hat{k}}^{(2)} H_{\hat{k}}^{(2,n)} + \eta_{\hat{k}}^{(n)} \quad (4.25)$$

$$r_{k+\kappa}^{(n)} = A_{k+\kappa}^{(2)} H_{k+\kappa}^{(2,n)} + \eta_{k+\kappa}^{(n)}. \quad (4.26)$$

Due to the employment of nulling in LTE-A RGs, every $1 \times N_{R_x}$ can be processed on its own. Meaning that the $2 \times N_{R_x}$ MIMO F.OSBCE Mode 2 system at hand is equivalent to two $1 \times N_{R_x}$ SIMO F.OSBCE systems with $\kappa = 6$. Therefore, the same analysis as in subsection 3.3.2 applies here for each transmit antenna on its own.

4.2.1.5 Results and Discussion - Mode 1 M vs. Mode 2

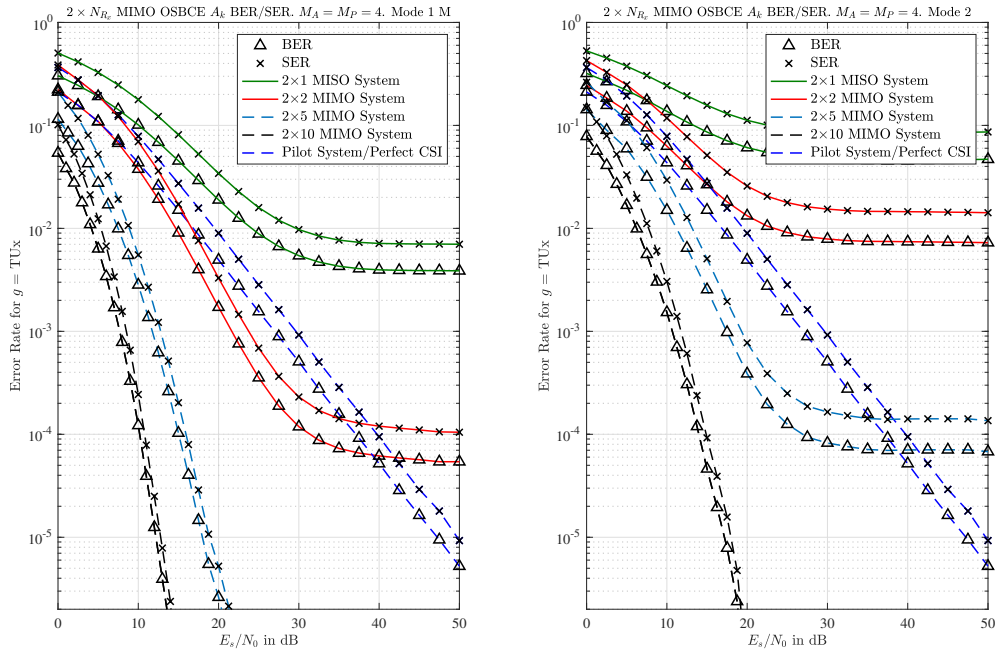
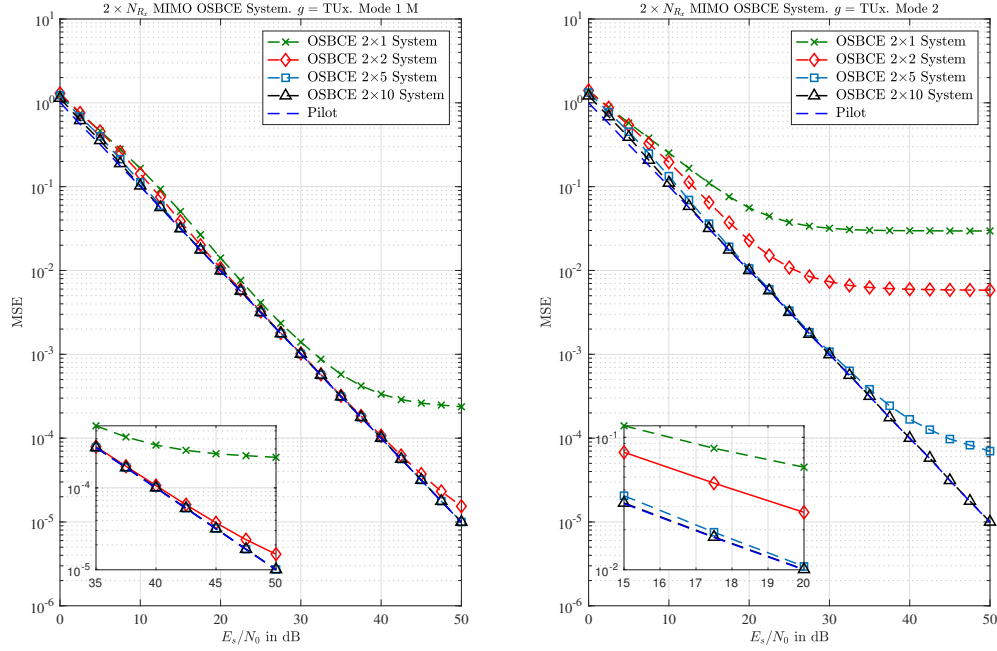


Figure 4.9: $2 \times N_{R_x}$ F. OSBCE - \hat{A}_k BER & SER vs. SNR - Modes 1 M & 2

SER and BER vs. SNR for $\hat{A}_k^{(m)}$ using Mode 1 M and Mode 2 in a TUx channel environment are shown in Figure 4.9, to compare their performances. As expected, MIMO F.OSBCE Mode 1 M outperforms Mode 2, due to a lower κ value. The SER at high SNR using Mode 1 M with 2 receive antennas outperforms the SER using Mode 2 with 5 antennas. Although $\kappa = 1$ for both MIMO F.OSBCE Mode 1 M and SIMO F.OSBCE, their performances do not match because of the noise associated with obtaining the MASK symbols in MIMO F.OSBCE Mode 1 M. Moreover, using Mode 1 M with $N_{R_x} = 5$, the $\hat{A}_k^{(m)}$ SER becomes


 Figure 4.10: $2 \times N_{R_x}$ F. OSBCE - MSE vs. SNR for different N_{R_x} - Modes 1 M & 2

lower than the $\hat{A}_k^{(m)}$ SER using perfect CSI. Moreover, $\hat{A}_k^{(m)}$ SER decreases as N_{R_x} increases, and hits an error floor as SNR increases. Also, improvement rate gets lower as N_{R_x} increases.

Figure 4.10 compares the MSE of Mode 1 M to Mode 2 as N_{R_x} increases in a TUx channel environment. While it is enough to use 2 receive antennas for Mode 1 M to match the pilot-based system, Mode 2 requires 10 receive antennas to achieve the same feat. Moreover, MSE using Mode 2 with $N_{R_x} = 5$ starts deviating from pilot-based MSE after $\text{SNR} \simeq 35$ dB.

Figure 4.11 compares the MSE of Mode 1 M to Mode 2 for channels with different number of taps and gains. In a TUx channel environment, MSE using Mode 2 is significantly worse than MSE using Mode 1M with 1 receive antenna, which achieves 2.5×10^{-4} at $\text{SNR} = 50$ dB, while for the same SNR, MSE using Mode 2 is 3×10^{-2} ; 120 times worse than Mode 1 M, and 10 times worse than Mode 1. Generally speaking, simulation results show that Mode 1 M is more resilient to channel statistics than Mode 2.

Figure 4.12 shows the effect of the modulation order across Mode 1 M and Mode 2 systems in a TUx channel environment. As noticed from previous simulations, as modulation order increases, the MSE performance gets worse. Contrary to Mode 1, Mode 2 is responsive to changing the modulation order of the system. Using Mode 2 for $\text{SNR} \simeq 50$ dB, MSE with 2-ary modulation is almost 6 times better than the MSE with 4-ary modulation. Generally, Mode 1 M is still the best among the three variation of MIMO F.OSBCE.

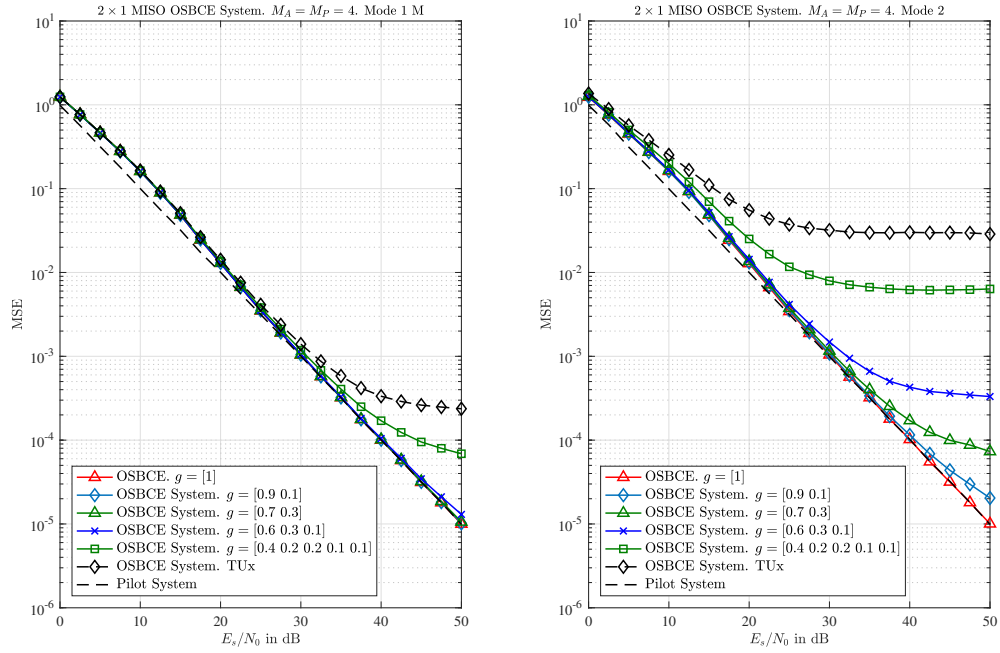


Figure 4.11: $2 \times N_{R_x}$ F. OSBCE - MSE vs. SNR for different channels - Modes 1 M & 2

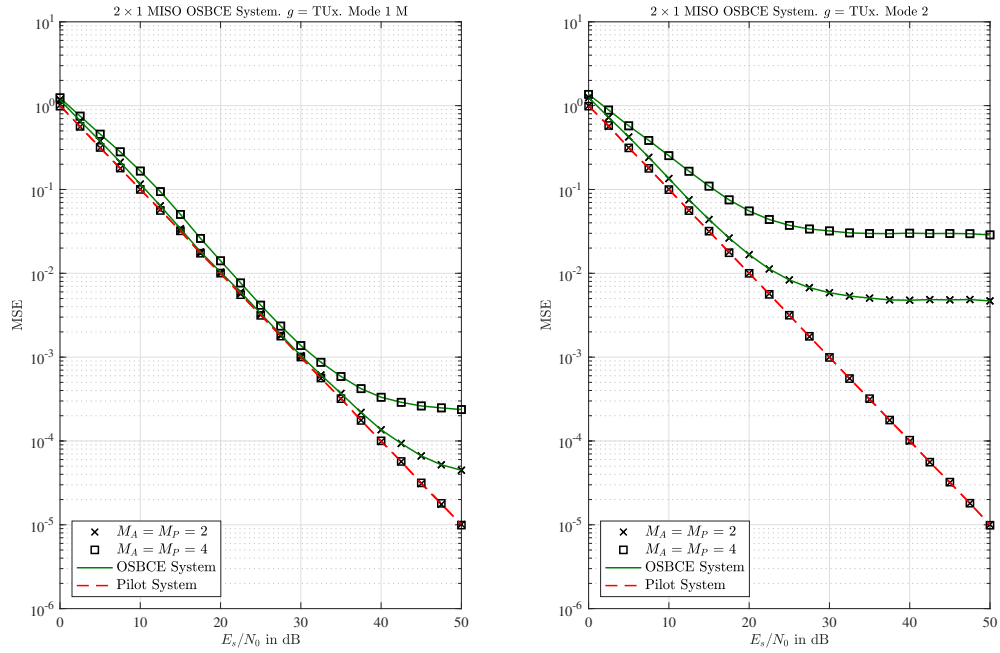


Figure 4.12: $2 \times N_{R_x}$ F. OSBCE - MSE vs. SNR for different M_A, M_P - Modes 1 M & 2

Although MIMO F.OSBCE Mode 2 performs worse than MIMO F.OSBCE Mode 1 M,

	Transmit Antenna 1	Transmit Antenna 2
Nullled	$A_{\ell+4\iota}^{(1)}$	$A_{\ell}^{(2)}$
MPSK	$A_{\ell}^{(1)}$	$A_{\ell+4\iota}^{(2)}$
MASK	$A_{\ell+\iota}^{(1)}$	$A_{\ell+\iota}^{(2)}$
Coded MASK	$A_{\ell+3\iota}^{(1)} = -A_{\ell+\iota}^{(1)}$	$A_{\ell+3\iota}^{(2)} = A_{\ell+\iota}^{(2)}$

Table 4.3: MIMO 1-D T.OSBCE Mode 1 coding scheme

Mode 2 can achieve higher data rates, given the channel is relatively flat with enough receiving antennas. Usually, choosing one of three variations over the others depend on the system requirements and constraints. Mode 1 M is an ideal candidate for ill-behaved channel, while achieving providing some diversity gain in transmitting MASK symbols. Since Mode 1 did not benefit from increasing N_{R_x} , this configuration is dropped, and only coding schemes similar to Table 4.2 will be used in all other variations of OSBCE labeled as “Mode 1”.

4.2.2 MIMO 1-D T.OSBCE - Across Time

4.2.2.1 Mode 1

This MIMO T.OSBCE system is similar to MIMO F.OSBCE Mode 1 M system, however, the pilots are distributed across the time dimension within one subcarrier frequency. Using the coding scheme presented in Table 4.3, the MPSK and MASK symbols are distributed for this OSBCE system based on the LTE-A configuration as shown in Figure 4.13. Moreover, it is assumed that ICI is eliminated before the CE step using ICI estimation or guard bands, and ϵ does not change within ι symbols duration. Subcarrier index k is dropped in this subsection and only included if necessary.

By using the coding scheme in Table 4.3, and following the procedure in subsection 4.2.1.2, the received post-FFT symbols at the k^{th} subcarrier and symbol indices ℓ , $\ell + \iota$, $\ell + 3\iota$, $\ell + 4\iota$, where $\iota = 1$, for receive antenna n are,

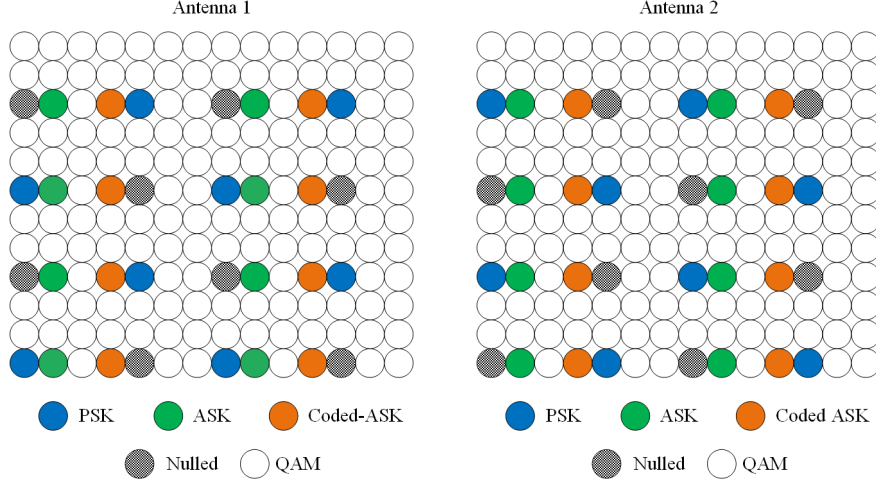
$$r_{\ell}^{(n)} = \varphi_{\ell}^{(1,n)} A_{\ell}^{(1)} H_{\ell}^{(1,n)} + \eta_{\ell}^{(n)} \quad (4.27)$$

$$r_{\ell+\iota}^{(n)} = \frac{1}{2} \left(\varphi_{\ell+\iota}^{(1,n)} A_{\ell+\iota}^{(1)} H_{\ell}^{(1,n)} + \varphi_{\ell+\iota}^{(2,n)} A_{\ell+\iota}^{(2)} H_{\ell}^{(2,n)} \right) + \eta_{\ell+\iota}^{(n)} \quad (4.28)$$

$$r_{\ell+3\iota}^{(n)} = \frac{1}{2} \left(-\varphi_{\ell+3\iota}^{(1,n)} A_{\ell+\iota}^{(1)} H_{\ell}^{(1,n)} + \varphi_{\ell+3\iota}^{(2,n)} A_{\ell+\iota}^{(2)} H_{\ell}^{(2,n)} \right) + \eta_{\ell+3\iota}^{(n)} \quad (4.29)$$

$$r_{\ell+4\iota}^{(n)} = \varphi_{\ell+4\iota}^{(1,n)} A_{\ell+4\iota}^{(2)} H_{\ell}^{(2,n)} + \eta_{\ell+4\iota}^{(n)} \quad (4.30)$$

where $\varphi_{\ell}^{(m,n)}$ between m^{th} transmit antenna and n^{th} receive antenna is defined in subsection 3.3.3. In time OSBCE, it is assumed that $E \left\{ \left(\varphi_{\ell}^{(m,n)} H_{\ell}^{(m,n)} \right) \left(\varphi_{\ell+\iota}^{(m,n)} H_{\ell}^{(m,n)} \right)^* \right\} = e^{j \times 0}$,


 Figure 4.13: $2 \times N_{R_x}$ Time OSBCE system - Mode 1

where $\iota = 1$. Thus, $\varphi_{\ell+\iota}^{(m,n)} H_{\ell}^{(m,n)} = \left(\varphi_{\ell}^{(m,n)} H_{\ell}^{(m,n)} + \Delta_{\iota}^{(m,n)} \right) \approx \varphi_{\ell}^{(m,n)} H_{\ell}^{(m,n)}$, where

$$\begin{aligned} \Delta_{\iota}^{(m,n)} &= \sum_{v=0}^{L_h} h_v e^{-j2\pi vk/N} \left[\varphi_{\ell+\iota}^{(m,n)} - \varphi_{\ell}^{(m,n)} \right] \\ &= \sum_{v=0}^{L_h} h_v e^{-j2\pi vk/N} \left[\varphi_{\ell}^{(m,n)} \left(e^{j\pi \epsilon \left(\frac{2\iota(N+N_{CP})}{N} \right)} - 1 \right) \right]. \end{aligned} \quad (4.31)$$

$\Delta_{\iota}^{(m,n)}$ is a RV describing the complex difference between OFDM symbols separated by ι . If $\iota = 0$, then the variance of $\Delta_{\iota}^{(m,n)} = 0$. It can be deduced from (4.31) that the variance of $\Delta_{\iota}^{(m,n)}$ is a function of channel's time auto-correlation. Now the MASK symbols from each antenna need to be separated, which is performed as follows,

$$\begin{aligned} A_{\ell+\iota}^{(1,n)} &= r_{\ell+\iota}^{(n)} - r_{\ell+3\iota}^{(n)} \\ &= A_{\ell+\iota}^{(1)} \left(\varphi_{\ell+\iota}^{(1,n)} H_{\ell}^{(1,n)} + \Delta_{\iota}^{(1,n)} \right) - A_{\ell+\iota}^{(2)} \Delta_{\iota}^{(2,n)} + \check{\eta}_{\ell+\iota}^{(n)} \end{aligned} \quad (4.32)$$

$$\begin{aligned} A_{\ell+\iota}^{(2,n)} &= r_{\ell+\iota}^{(n)} + r_{\ell+3\iota}^{(n)} \\ &= A_{\ell+\iota}^{(2)} \left(\varphi_{\ell+3\iota}^{(2,n)} H_{\ell}^{(2,n)} - \Delta_{\iota}^{(2,n)} \right) - A_{\ell+\iota}^{(1)} \Delta_{\iota}^{(1,n)} + \hat{\eta}_{\ell+\iota}^{(n)}. \end{aligned} \quad (4.33)$$

Now, $A_{\ell}^{(1)}$ is detected as follows,

$$\begin{aligned} \mathcal{S}_{\ell}^{(1,n)} &= r_{\ell}^{(n)} / A_{\ell+\iota}^{(1,n)} \\ &= \frac{\varphi_{\ell}^{(1,n)} A_{\ell}^{(1)} H_{\ell}^{(1,n)} + \eta_{\ell}^{(n)}}{A_{\ell+\iota}^{(1)} \left(\varphi_{\ell+\iota}^{(1,n)} H_{\ell}^{(1,n)} + \Delta_{\iota}^{(1,n)} \right) - A_{\ell+\iota}^{(2)} \Delta_{\iota}^{(2,n)} + \check{\eta}_{\ell+\iota}^{(n)}} \end{aligned}$$

$$\begin{aligned}
 &= \frac{\varphi_\ell^{(1,n)} A_\ell^{(1)} H_\ell^{(1,n)} + \eta_\ell^{(n)}}{\left| A_{\ell+\iota}^{(1)} \left(\varphi_{\ell+\iota}^{(1,n)} H_\ell^{(1,n)} + \Delta_\ell^{(1,n)} \right) - A_{\ell+\iota}^{(2)} \Delta_\ell^{(2,n)} + \tilde{\eta}_{\ell+\iota}^{(n)} \right| e^{j\hat{\theta}_{\ell+\iota}^{(1,n)}}} \\
 &= \frac{A_\ell^{(1)} \left| \varphi_\ell^{(1,n)} H_\ell^{(1,n)} \right| e^{j(\theta_\ell^{(1,n)} - \hat{\theta}_{\ell+\iota}^{(1,n)})} + \left| \eta_\ell^{(n)} \right| e^{j(\arg(\eta_\ell^{(n)}) - \hat{\theta}_{\ell+\iota}^{(1,n)})}}{\left| A_{\ell+\iota}^{(1)} \left(\varphi_{\ell+\iota}^{(1,n)} H_\ell^{(1,n)} + \Delta_\ell^{(1,n)} \right) - A_{\ell+\iota}^{(2)} \Delta_\ell^{(2,n)} + \tilde{\eta}_{\ell+\iota}^{(n)} \right|} \\
 &= \frac{1}{\left| A_{\ell+\iota}^{(1,n)} \right|} \left(\left| \varphi_\ell^{(1,n)} H_\ell^{(1,n)} \right| e^{j\vartheta_\ell^{(1,n)}} A_\ell^{(1)} + \tilde{\eta}_\ell^{(n)} \right) \tag{4.34}
 \end{aligned}$$

where $\vartheta_\ell^{(m,n)} = \theta_\ell^{(m,n)} - \hat{\theta}_{\ell+\iota}^{(m,n)}$, $\tilde{\eta}_\ell^{(n)} = \left| \eta_\ell^{(n)} \right| e^{j(\arg(\eta_\ell^{(n)}) - \hat{\theta}_{\ell+\iota}^{(1,n)})}$. Next, EGC is employed combine all the co-phased $\mathcal{S}_\ell^{(1,n)}$, $n \in \{1, 2, \dots, N_{R_x}\}$, from the different receive antennas as follows,

$$\sum_{n=1}^{N_{R_x}} \mathcal{S}_\ell^{(1,n)} = A_\ell^{(1)} \sum_{n=1}^{N_{R_x}} \frac{\left| \varphi_\ell^{(1,n)} H_\ell^{(1,n)} \right| e^{j\vartheta_\ell^{(1,n)}}}{\left| A_{\ell+\iota}^{(1,n)} \right|} + \sum_{n=1}^{N_{R_x}} \frac{\tilde{\eta}_\ell^{(n)}}{\left| A_{\ell+\iota}^{(1,n)} \right|}. \tag{4.35}$$

Using the phase of the combined equalized waveforms, the MPSK symbol can be detected with only the phase of $\sum_{n=1}^{N_{R_x}} \mathcal{S}_\ell^{(1,n)}$, where $\vartheta_\ell^{(m,n)}$ and $\tilde{\eta}_\ell^{(n)}$ are the two sources of phase distortion. In this subsection, $\vartheta_\ell^{(m,n)}$ is redefined as $\theta_\ell^{(m,n)} - \hat{\theta}_{\ell+\iota}^{(m,n)}$, where ι and ϵ inherently affects $\vartheta_\ell^{(m,n)}$. Using MLD, the initial estimate, $\hat{A}_\ell^{(1)}$, is expressed as,

$$\hat{A}_\ell^{(1)} = \arg \min_{\left(A_\ell^{(1)} \right)^{(i)}, i \in \mathbb{M}_P} \left| \sum_{n=1}^{N_{R_x}} \mathcal{S}_\ell^{(1,n)} - \left(A_\ell^{(1)} \right)^{(i)} \right|^2. \tag{4.36}$$

Using $\hat{A}_\ell^{(1)}$, $\hat{H}_\ell^{(1,n)}$ at each n^{th} branch can be found using LSE as follows,

$$\begin{aligned}
 \hat{H}_\ell^{(1,n)} &= \frac{r_\ell^{(n)}}{\hat{A}_\ell^{(1)}} = \frac{\varphi_\ell^{(1,n)} A_\ell^{(1)} H_\ell^{(1,n)} + \eta_\ell^{(n)}}{\hat{A}_\ell^{(1)}} \\
 &\approx \varphi_\ell^{(1,n)} H_\ell^{(1,n)} + \ddot{\eta}_\ell^{(n)} \tag{4.37}
 \end{aligned}$$

where $\ddot{\eta}_\ell^{(n)} = \left| \eta_\ell^{(n)} \right| e^{j(\arg\{\eta_\ell^{(n)}\} - \arg\{\hat{A}_\ell^{(1)}\})}$. As the number of receiving antennas N_{R_x} increases, $\hat{A}_\ell^{(m)}$ SER hugely improves, to the point where $\hat{A}_\ell^{(m)} = A_\ell^{(m)}$ and the first term of (4.37) becomes the perfect CFR. Using $A_{\ell+\iota}^{(2,n)}$ and $r_{\ell+4\iota}^{(n)}$ and following the same approach described in this section, $A_{\ell+4\iota}^{(2)}$ can be obtained. MIMO T.OSBCE Mode 1 works with a small ι , thus, the MSE is expected to be comparable to the pilot-based system. Moreover, MIMO T.OSBCE Mode 1 essentially sends the MASK symbol twice over two different OFDM symbols, which is regarded as temporal diversity gain. Nevertheless, that nulls the benefit

from replacing the pilot symbol by a data MPSK symbol. Therefore, similar to the MIMO F.OSBCE Mode 2, MIMO T.OSBCE Mode 2 is introduced in the next subsection.

4.2.2.2 Mode 2

In this MIMO T.OSBCE system, original LTE-A pilot locations are replaced with MPSK and MASK symbols without coding are transmitted as shown in Figure 4.14. This system is an alternative to MIMO T.OSBCE Mode 2, in order to increase data rate by replacing pilots by MPSK and MASK data symbols while sacrificing performance by using higher ι . The performance degradation is treated by increasing the number of receive antennas.

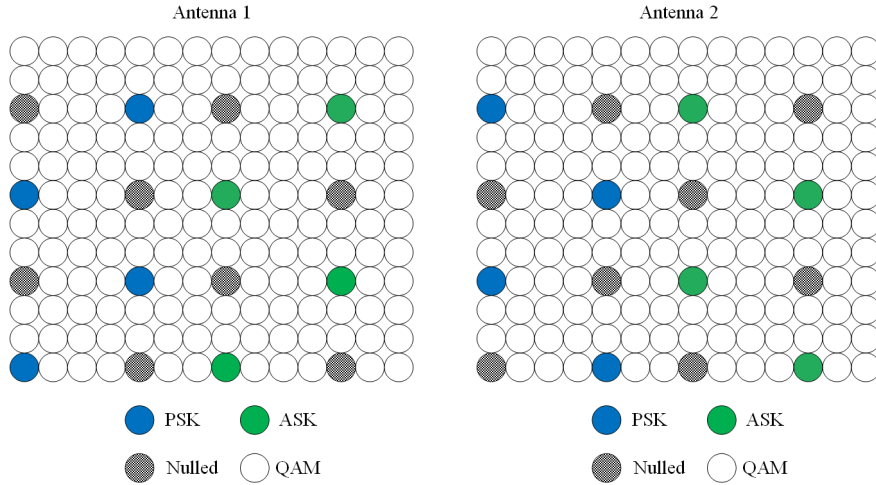


Figure 4.14: $2 \times N_{R_x}$ Time OSBCE system - Mode 2

The MPSK and MASK symbols are transmitted at OFDM blocks ℓ , $\hat{\ell}$, and $\ell + \iota$, $\hat{\ell} + \iota$, respectively, where $\iota = 7$. ℓ and $\hat{\ell}$ are the OFDM symbols indexing for transmitters 1 and 2, respectively, where $\hat{\ell} - \ell = 4$ in C-RS LTE-A [12]. Hence, the received post-FFT samples at the k^{th} subcarrier for receive antenna n are,

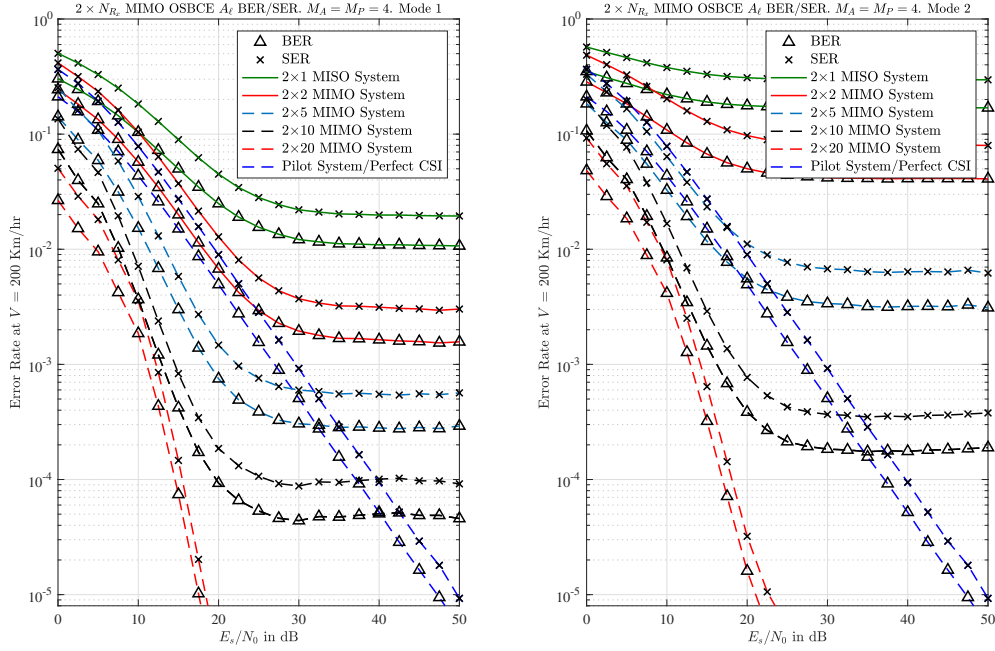
$$r_{\ell}^{(n)} = \varphi_{\ell}^{(1,n)} A_{\ell}^{(1)} H_{\ell}^{(1,n)} + \eta_{\ell}^{(n)} \quad (4.38)$$

$$r_{\ell+\iota}^{(n)} = \varphi_{\ell+\iota}^{(1,n)} A_{\ell+\iota}^{(1)} H_{\ell+\iota}^{(1,n)} + \eta_{\ell+\iota}^{(n)} \quad (4.39)$$

$$r_{\hat{\ell}}^{(n)} = \varphi_{\hat{\ell}}^{(2,n)} A_{\hat{\ell}}^{(2)} H_{\hat{\ell}}^{(2,n)} + \eta_{\hat{\ell}}^{(n)} \quad (4.40)$$

$$r_{\hat{\ell}+\iota}^{(n)} = \varphi_{\hat{\ell}+\iota}^{(2,n)} A_{\hat{\ell}+\iota}^{(2)} H_{\hat{\ell}+\iota}^{(2,n)} + \eta_{\hat{\ell}+\iota}^{(n)}. \quad (4.41)$$

Since there is no cross-talk at MPSK and MASK locations, every $1 \times N_{R_x}$ can be processed on its own. Hence, the $2 \times N_{R_x}$ MIMO T.OSBCE Mode 2 system processing is similar to two $1 \times N_{R_x}$ SIMO T.OSBCE systems with $\iota = 7$. Therefore, the same analysis as in subsection 3.3.3 applies here for each single transmit antenna.


 Figure 4.15: $2 \times N_{R_x}$ T. OSBCE - \hat{A}_ℓ BER & SER vs. SNR - Modes 1 & 2

4.2.2.3 Results and Discussion - Mode 1 vs. Mode 2

The impact of increasing the number of receive antennas on the initial estimate $\hat{A}_\ell^{(m)}$ in terms of SER and BER is shown in Figure 4.15 using Mode 1 and Mode 2. The speed of the moving object in Figure 4.15 is 200 Km/hr, which results in a maximum Doppler frequency of 351.9 Hz for $f_c = 1.9$ GHz.

The SER using Mode 1 and 2 receive antennas outperforms the SER using Mode 2 and 5 antennas, due to the higher ι in Mode 2 than Mode 1. Mathematically, it means that the phase error, $\vartheta_\ell^{(m,n)} = \theta_\ell^{(m,n)} - \hat{\theta}_{\ell+\iota}^{(m,n)}$, would be higher and cause more detection errors for $\hat{A}_\ell^{(m)}$, which is later used to estimate $\varphi_\ell^{(m,n)} H_\ell^{(m,n)}$. Moreover, Mode 1 with 10 receive antennas provides better SER than a system with perfect CSI till SNR $\simeq 40$ dB. For higher SNR, Mode 1 can further improve the SER by increasing the number of receive antenna. Again, blindly estimated $\hat{A}_\ell^{(m)}$ SER decreases as SNR increases until it hits an error floor produced by $\vartheta_\ell^{(m,n)}$. As N_{R_x} increases, Mode 2 approaches the performance of Mode 1 and matches it for $N_{R_x} = 20$, where the rate of enhancement by increasing N_{R_x} becomes marginal.

Figure 4.16 shows the impact of increasing N_{R_x} using Mode 1 and Mode 2. While $\iota = 1$ in Mode 1, it still requires 5 receive antennas to match the performance of 1×2 SIMO T.OSBCE with $\iota = 1$, as demonstrated by Figure 3.15. Moreover, it is noticed that for Mode 1 to achieve significant improvement from increasing the number of receive antennas, N_{R_x}

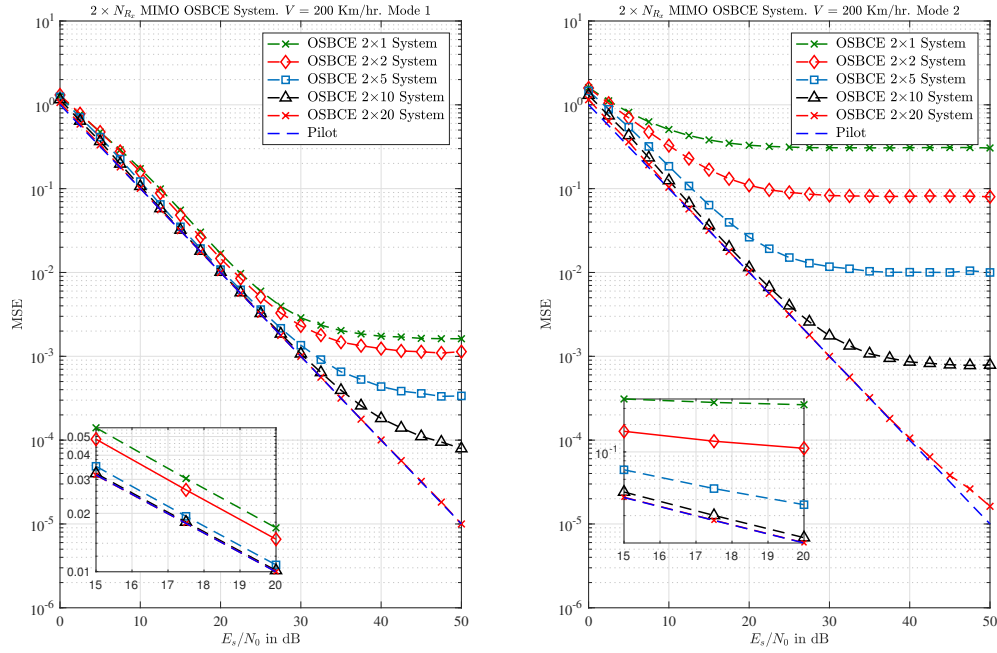


Figure 4.16: $2 \times N_{R_x}$ T. OSBCE - MSE vs. SNR for different N_{R_x} - Modes 1 & 2

increments must be relatively big. On the other hand, Mode 2 achieves greater improvements by increasing N_{R_x} . Moreover, while Mode 1 matches the performance of pilot-based system with 20 receive antennas, Mode 2 performance deviates from the performance of pilot-based system at $\text{SNR} \simeq 45$ dB, hence, a higher number of receive antennas is required with Mode 2.

Figure 4.17 shows how the receiver's relative speed affects the MIMO T.OSBCE MSE for Modes 1 and 2. With Mode 1, the MSE performance of the OSBCE for a relative speed of 100 Km/hr starts deviating from the pilot-based system performance after $\text{SNR} \simeq 33$ dB. The Doppler frequency in this case is 176 Hz for $f_c = 1.9$ GHz. Thus, as the speed increases, N_{R_x} must be increased accordingly to match the performance of pilot-based system. On the other hand, Mode 2 performance gets significantly worse as the relative speed increases. Since the performance degradation with Mode 2 is more severe than Mode 1 as the speed increases, a higher N_{R_x} is required with Mode 2.

Figure 4.18 shows how modulation order affects the OSBCE system with MIMO T.OSBCE Modes 1 and 2, at a relative motion speed of 200 Km/hr. Similar to previous simulations, as the modulation order increases, the MSE performance gets worse, which is a result of a worse SER performance of $A_\ell^{(m)}$.

CHAPTER 4. OSBCE FOR MIMO-OFDM SYSTEMS

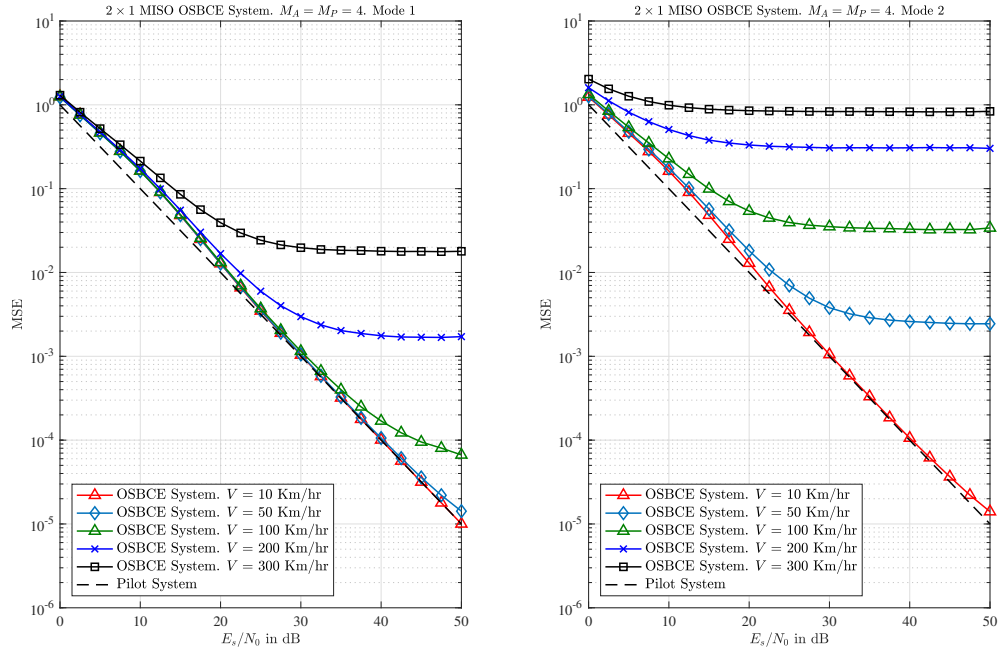


Figure 4.17: $2 \times N_{R_x}$ T. OSBCE - MSE vs. SNR for different speeds - Modes 1 & 2

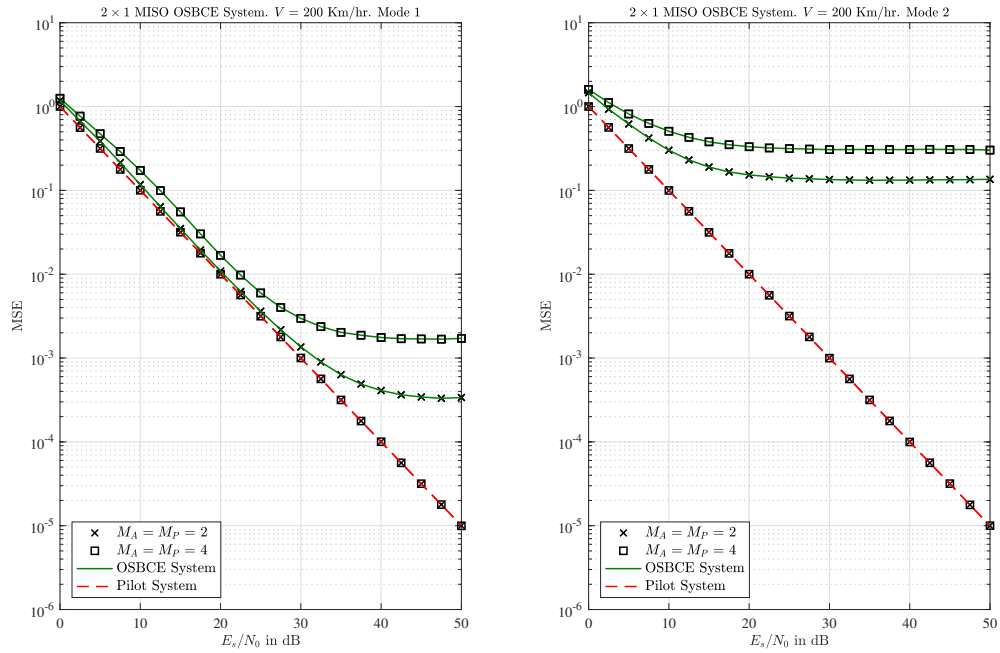
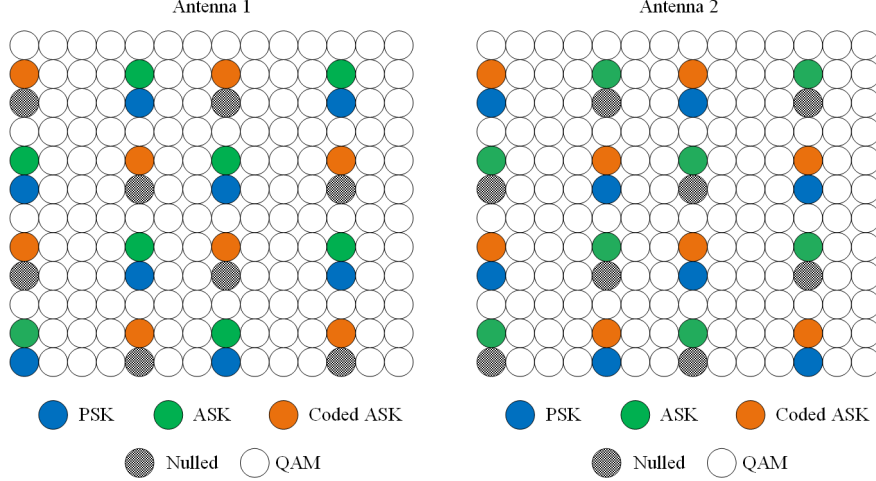


Figure 4.18: $2 \times N_{R_x}$ T. OSBCE - MSE vs. SNR for different M_A , M_P - Modes 1 & 2

Again, depending on the system's requirements and constraints, one MIMO T.OSBCE

	Transmit Antenna 1	Transmit Antenna 2
Nullled	$A_{k,\ell+\iota}^{(1)}$	$A_{k,\ell}^{(2)}$
MPSK	$A_{k,\ell}^{(1)}$	$A_{k,\ell+\iota}^{(2)}$
MASK	$A_{k+\kappa,\ell}^{(1)}$	$A_{k+\kappa,\ell}^{(2)}$
Coded MASK	$A_{k+\kappa,\ell+\iota}^{(1)} = -A_{k+\kappa,\ell}^{(1)}$	$A_{k+\kappa,\ell+\iota}^{(2)} = A_{k+\kappa,\ell}^{(2)}$

Table 4.4: MIMO 2-D T/F.OSBCE Mode 1 coding scheme


 Figure 4.19: $2 \times N_{R_x}$ Time-Frequency OSBCE system - Mode 1

Mode would be selected over the other. MIMO T.OSBCE Mode 2 can achieve higher data rates, given the channel is relatively slow changing with enough receiving antennas. Mode 1 would be the ideal choice of the two Modes for fast changing channels, while achieving providing some temporal diversity gain in transmitting MASK symbols.

4.2.3 MIMO 2-D T/F.OSBCE - Across Time & Frequency

4.2.3.1 Mode 1

This MIMO T/F.OSBCE is similar to SIMO T/F.OSBCE in the sense that it works across two dimensions, time and frequency. The objective is to investigate how OSBCE performs when distortions are introduced in both time and frequency. Similar notations as in subsection 3.3.4 are used. In addition, it is assumed that ISI and ICI are eliminated before the CE step. Enough N_{CP} CP samples are used for ISI mitigation and ICI estimation or guard bands are used for ICI mitigation. Using the coding scheme presented in Table 4.4, the MPSK and MASK symbols are distributed for this OSBCE system based on the LTE-A configuration as shown in Figure 4.13, where $(\kappa, \iota) = (1, 4)$.

By using the coding scheme in Table 4.4, and following the procedure in subsection 4.2.2.1, the received post-FFT symbols at the locations (k, ℓ) , $(k + \kappa, \ell)$, $(k + \kappa, \ell + \iota)$ and $(k, \ell + \iota)$ for receive antenna n are

$$r_{k,\ell}^{(n)} = \varphi_\ell^{(1,n)} A_{k,\ell}^{(1)} H_{k,\ell}^{(1,n)} + \eta_{k,\ell}^{(n)} \quad (4.42)$$

$$r_{k+\kappa,\ell}^{(n)} = \frac{1}{2} \left(\varphi_\ell^{(1,n)} A_{k+\kappa,\ell}^{(1)} H_{k+\kappa,\ell}^{(1,n)} + \varphi_\ell^{(2,n)} A_{k+\kappa,\ell}^{(2)} H_{k+\kappa,\ell}^{(2,n)} \right) + \eta_{k+\kappa,\ell}^{(n)} \quad (4.43)$$

$$r_{k+\kappa,\ell+\iota}^{(n)} = \frac{1}{2} \left(-\varphi_{\ell+\iota}^{(1,n)} A_{k+\kappa,\ell}^{(1)} H_{k+\kappa,\ell}^{(1,n)} + \varphi_{\ell+\iota}^{(2,n)} A_{k+\kappa,\ell}^{(2)} H_{k+\kappa,\ell}^{(2,n)} \right) + \eta_{k+\kappa,\ell+\iota}^{(n)} \quad (4.44)$$

$$r_{k,\ell+\iota}^{(n)} = \varphi_{\ell+\iota}^{(2,n)} A_{k,\ell+\iota}^{(2)} H_{k,\ell}^{(2,n)} + \eta_{k,\ell+\iota}^{(n)} \quad (4.45)$$

where $\varphi_\ell^{(m,n)}$ between m^{th} transmit antenna and n^{th} receive antenna is defined in subsection 3.3.3. In T/F.OSBCE, it is assumed that $E \left\{ \left(\varphi_\ell^{(m,n)} H_{k,\ell}^{(m,n)} \right) \left(\varphi_{\ell+\iota}^{(m,n)} H_{k+\kappa,\ell}^{(m,n)} \right)^* \right\} = e^{j \times 0}$, where $\kappa = \iota = 1$. Thus, $\varphi_{\ell+\iota}^{(m,n)} H_{k+\kappa,\ell}^{(m,n)} = \left(\varphi_\ell^{(m,n)} H_{k,\ell}^{(m,n)} + \Delta_{\kappa,\iota}^{(m,n)} \right) \approx \varphi_{k,\ell}^{(m,n)} H_{k,\ell}^{(m,n)}$, and using $\varphi_{\ell+\iota}^{(m,n)} = \varphi_\ell^{(m,n)} e^{j\pi\epsilon \left(\frac{2\iota(N+N_{CP})}{N} \right)}$, $\Delta_{\kappa,\iota}^{(m,n)}$ can be expressed as,

$$\begin{aligned} \Delta_{\kappa,\iota}^{(m,n)} &= \varphi_{\ell+\iota}^{(m,n)} H_{k+\kappa,\ell}^{(m,n)} - \varphi_\ell^{(m,n)} H_{k,\ell}^{(m,n)} \\ &= \varphi_\ell^{(m,n)} \left(e^{j\pi\epsilon \left(\frac{2\iota(N+N_{CP})}{N} \right)} H_{k+\kappa,\ell}^{(m,n)} - H_{k,\ell}^{(m,n)} \right) \\ &= \varphi_\ell^{(m,n)} \left(\left[e^{j\pi\epsilon \left(\frac{2\iota(N+N_{CP})}{N} \right)} \left(\sum_{v=0}^{L_h} h_v e^{-j \frac{2\pi v k}{N}} \left(e^{-j \frac{2\pi v \kappa}{N}} - 1 \right) \right) \right] \right). \end{aligned} \quad (4.46)$$

$\Delta_{\kappa,\iota}^{(m,n)}$ is a RV describing the complex difference between RE locations separated by ι OFDM symbols and κ subcarriers. If $\kappa = \iota = 0$, then the variance of $\Delta_{\kappa,\iota}^{(m,n)} = 0$. It is noticed that if $\epsilon = 0$ and $\kappa \neq 0$, then (4.46) is reduced to (4.5), and if $\kappa = 0$, $\epsilon \neq 0$, and $\iota \neq 0$, then (4.46) is reduced to (4.31). Moreover, it can be noticed from (4.46) that the variance of $\Delta_{\kappa,\iota}^{(m,n)}$ is a function of the channel's time and frequency auto-correlation. Now the MASK symbols from each antenna need to be separated, which is performed as follows,

$$\begin{aligned} A_{k+\kappa,\ell}^{(1,n)} &= r_{k+\kappa,\ell}^{(n)} - r_{k+\kappa,\ell+\iota}^{(n)} \\ &= A_{k+\kappa,\ell}^{(1)} \left(\varphi_\ell^{(1,n)} H_{k+\kappa,\ell}^{(1,n)} + \frac{\Delta_{\kappa,\iota}^{(1,n)}}{2} \right) - \frac{A_{k+\kappa,\ell}^{(2)} \Delta_{\kappa,\iota}^{(2,n)}}{2} + \tilde{\eta}_{k+\kappa,\ell+\iota}^{(n)} \end{aligned} \quad (4.47)$$

$$\begin{aligned} A_{k+\kappa,\ell}^{(2,n)} &= r_{k+\kappa,\ell}^{(n)} + r_{k+\kappa,\ell+\iota}^{(n)} \\ &= A_{k+\kappa,\ell}^{(2)} \left(\varphi_{\ell+\iota}^{(2,n)} H_{k+\kappa,\ell}^{(2,n)} - \frac{\Delta_{\kappa,\iota}^{(2,n)}}{2} \right) - \frac{A_{k+\kappa,\ell}^{(1)} \Delta_{\kappa,\iota}^{(1,n)}}{2} + \hat{\eta}_{k+\kappa,\ell+\iota}^{(n)}. \end{aligned} \quad (4.48)$$

Now, $A_{k,\ell}^{(1)}$ is detected as follows,

$$\begin{aligned}
 \mathcal{S}_{k,\ell}^{(1,n)} &= r_{k,\ell}^{(n)} / A_{k+\kappa,\ell}^{(1,n)} \\
 &= \frac{\varphi_\ell^{(1,n)} A_{k,\ell}^{(1)} H_{k,\ell}^{(1,n)} + \eta_{k,\ell}^{(n)}}{A_{k+\kappa,\ell}^{(1)} \left(\varphi_\ell^{(1,n)} H_{k+\kappa,\ell}^{(1,n)} + \frac{\Delta_{\kappa,\ell}^{(1,n)}}{2} \right) - \frac{A_{k+\kappa,\ell}^{(2)} \Delta_{\kappa,\ell}^{(2,n)}}{2} + \tilde{\eta}_{k+\kappa,\ell+\iota}^{(n)}} \\
 &= \frac{\varphi_\ell^{(1,n)} A_{k,\ell}^{(1)} H_{k,\ell}^{(1,n)} + \eta_{k,\ell}^{(n)}}{\left| A_{k+\kappa,\ell}^{(1)} \left(\varphi_\ell^{(1,n)} H_{k+\kappa,\ell}^{(1,n)} + \frac{\Delta_{\kappa,\ell}^{(1,n)}}{2} \right) - \frac{A_{k+\kappa,\ell}^{(2)} \Delta_{\kappa,\ell}^{(2,n)}}{2} + \tilde{\eta}_{k+\kappa,\ell+\iota}^{(n)} \right| e^{j\hat{\theta}_{k+\kappa,\ell+\iota}^{(1,n)}}} \\
 &= \frac{A_{k,\ell}^{(1)} \left| \varphi_\ell^{(1,n)} H_{k,\ell}^{(1,n)} \right| e^{j(\theta_{k,\ell}^{(1,n)} - \hat{\theta}_{k+\kappa,\ell+\iota}^{(1,n)})} + \left| \eta_{k,\ell}^{(n)} \right| e^{j(\arg(\eta_{k,\ell}^{(n)}) - \hat{\theta}_{k+\kappa,\ell+\iota}^{(1,n)})}}{\left| A_{k+\kappa,\ell}^{(1)} \left(\varphi_\ell^{(1,n)} H_{k+\kappa,\ell}^{(1,n)} + \frac{\Delta_{\kappa,\ell}^{(1,n)}}{2} \right) - \frac{A_{k+\kappa,\ell}^{(2)} \Delta_{\kappa,\ell}^{(2,n)}}{2} + \tilde{\eta}_{k+\kappa,\ell+\iota}^{(n)} \right|} \\
 &= \frac{1}{\left| A_{k+\kappa,\ell}^{(1,n)} \right|} \left(\left| \varphi_\ell^{(1,n)} H_{k,\ell}^{(1,n)} \right| e^{j\vartheta_{k,\ell}^{(1,n)}} A_{k,\ell}^{(1)} + \tilde{\eta}_{k,\ell}^{(n)} \right) \tag{4.49}
 \end{aligned}$$

where $\vartheta_{k,\ell}^{(m,n)} = \theta_{k,\ell}^{(1,n)} - \hat{\theta}_{k+\kappa,\ell+\iota}^{(1,n)}$, $\tilde{\eta}_{k,\ell}^{(n)} = \left| \eta_{k,\ell}^{(n)} \right| e^{j(\arg(\eta_{k,\ell}^{(n)}) - \hat{\theta}_{k+\kappa,\ell+\iota}^{(1,n)})}$. The co-phased $\mathcal{S}_{k,\ell}^{(1,n)}$, $n \in \{1, 2, \dots, N_{R_x}\}$, from the different receive antennas are combined using EGC as follows,

$$\sum_{n=1}^{N_{R_x}} \mathcal{S}_{k,\ell}^{(1,n)} = A_{k,\ell}^{(1)} \sum_{n=1}^{N_{R_x}} \frac{\left| \varphi_\ell^{(1,n)} H_{k,\ell}^{(1,n)} \right| e^{j\vartheta_{k,\ell}^{(1,n)}}}{\left| A_{k+\kappa,\ell}^{(1,n)} \right|} + \sum_{n=1}^{N_{R_x}} \frac{\tilde{\eta}_{k,\ell}^{(n)}}{\left| A_{k+\kappa,\ell}^{(1,n)} \right|}. \tag{4.50}$$

The MPSK symbol can now be detected with only the phase of $\sum_{n=1}^{N_{R_x}} \mathcal{S}_{k,\ell}^{(1,n)}$, where $\vartheta_{k,\ell}^{(m,n)}$ and $\tilde{\eta}_{k,\ell}^{(n)}$ are the two sources of phase distortion. In this subsection, $\vartheta_{k,\ell}^{(m,n)}$ is redefined as $\theta_{k,\ell}^{(1,n)} - \hat{\theta}_{k+\kappa,\ell+\iota}^{(1,n)}$, where ι and ϵ inherently affects $\vartheta_{k,\ell}^{(m,n)}$. Using MLD, the initial estimate, $\hat{A}_{k,\ell}^{(1)}$, is expressed as,

$$\hat{A}_{k,\ell}^{(1)} = \arg \min_{(A_{k,\ell}^{(1)})^{(i)}, i \in \mathbb{M}_P} \left| \sum_{n=1}^{N_{R_x}} \mathcal{S}_{k,\ell}^{(1,n)} - (A_{k,\ell}^{(1)})^{(i)} \right|^2. \tag{4.51}$$

Using $\hat{A}_{k,\ell}^{(1)}$, $\hat{H}_{k,\ell}^{(1,n)}$ at each n^{th} branch can be found using LSE as follows,

$$\hat{H}_{k,\ell}^{(1,n)} = \frac{r_{k,\ell}^{(n)}}{\hat{A}_{k,\ell}^{(1)}} = \frac{\varphi_\ell^{(1,n)} A_{k,\ell}^{(1)} H_{k,\ell}^{(1,n)} + \eta_{k,\ell}^{(n)}}{\hat{A}_{k,\ell}^{(1)}} \approx \varphi_\ell^{(1,n)} H_{k,\ell}^{(1,n)} + \ddot{\eta}_{k,\ell}^{(n)} \tag{4.52}$$

where $\ddot{\eta}_{k,\ell}^{(n)} = \left| \eta_{k,\ell}^{(n)} \right| e^{j(\arg\{\eta_{k,\ell}^{(n)}\} - \arg\{\hat{A}_{k,\ell}^{(1)}\})}$. As N_{R_x} increases, $\hat{A}_{k,\ell}^{(1)}$ SER significantly improves,

to the point where $\hat{A}_{k,\ell}^{(m)} = A_{k,\ell}^{(m)}$, and the first term of (4.52) becomes the perfect CFR. Using $A_{k+\kappa,\ell}^{(2,n)}$ and $r_{k,\ell+\iota}^{(n)}$ and following the same method outlines in this subsection, an initial estimate for $A_{k,\ell+\iota}^{(2)}$ can be obtained. MIMO T/F.OSBCE Mode 1 works with small κ and ι , hence, the MSE is expected to be similar to the pilot-based system. In addition, MIMO F/T.OSBCE Mode 1 design sends the MASK symbol twice over different REs, which is a form of diversity. However, the benefit from replacing the pilot symbol by a data MPSK symbol is nulled, and data rate is still almost the same. Thus, similar to the MIMO F.OSBCE Mode 2 and MIMO T.OSBCE Mode 2, MIMO T/F.OSBCE Mode 2 is introduced in the next subsection.

4.2.3.2 Mode 2

As an alternative to MIMO T/F.OSBCE Mode 1, MPSK and MASK symbols without coding are transmitted as shown in Figure 4.14, where $(\kappa, \iota) = (3, 4)$. This system aims at increasing data rate at the expense of performance degradation by using higher κ and ι . The performance degradation is remedied by increasing N_{R_x} .

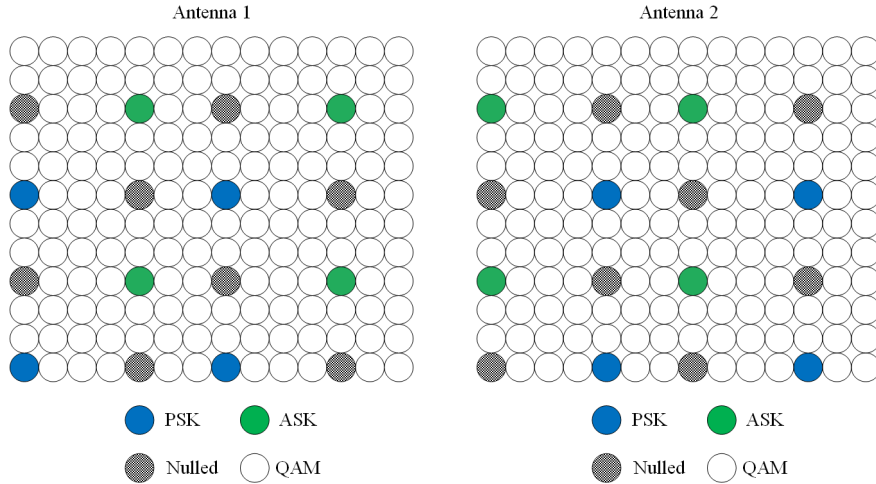


Figure 4.20: $2 \times N_{R_x}$ Time-Frequency OSBCE system - Mode 2

The MPSK and MASK symbols are transmitted as shown in Figure 4.20. Hence, the received post-FFT samples for receive antenna n are,

$$r_{k,\ell}^{(n)} = \varphi_{\ell}^{(1,n)} A_{k,\ell}^{(1)} H_{k,\ell}^{(1,n)} + \eta_{k,\ell}^{(n)} \quad (4.53)$$

$$r_{k+\kappa,\ell+\iota}^{(n)} = \varphi_{\ell+\iota}^{(1,n)} A_{k+\kappa,\ell+\iota}^{(1)} H_{k+\kappa,\ell+\iota}^{(1,n)} + \eta_{k+\kappa,\ell+\iota}^{(n)} \quad (4.54)$$

$$r_{k,\ell+\iota}^{(n)} = \varphi_{\ell+\iota}^{(2,n)} A_{k,\ell+\iota}^{(2)} H_{k,\ell+\iota}^{(2,n)} + \eta_{k,\ell+\iota}^{(n)} \quad (4.55)$$

$$r_{k+\kappa,\ell}^{(n)} = \varphi_{\ell}^{(2,n)} A_{k+\kappa,\ell}^{(2)} H_{k+\kappa,\ell}^{(2,n)} + \eta_{k+\kappa,\ell}^{(n)} \quad (4.56)$$

Every $1 \times N_{R_x}$ can be processed on its own, because there is no cross-talk between transmitters at MPSK and MASK locations. Thus, the $2 \times N_{R_x}$ MIMO T/F.OSBCE Mode 2 system processing is similar to two $1 \times N_{R_x}$ SIMO T/F.OSBCE systems with $(\kappa, \iota) = (3, 4)$. Therefore, similar analysis to subsection 3.3.4 can be applied to the system at hand for each single transmit antenna.

4.2.3.3 Results and Discussion - Mode 1 vs. Mode 2

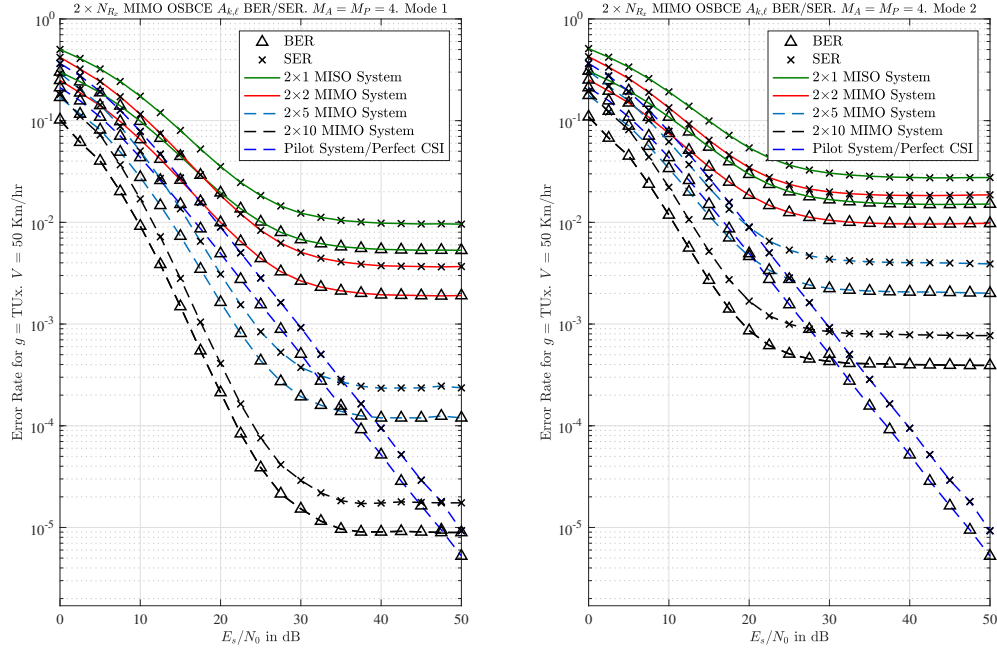


Figure 4.21: $2 \times N_{R_x}$ T/F. OSBCE - $\hat{A}_{k,\ell}$ BER & SER vs. SNR - Modes 1 & 2

Figure 4.15 shows the impact of increasing the number of receive antennas on the initial estimate $\hat{A}_{k,\ell}^{(m)}$ using Mode 1 and Mode 2. The speed of the moving object in Figure 4.15 is 50 Km/hr, which is a result of a maximum Doppler frequency of 88 Hz for $f_c = 1.9$ GHz. The SER using Mode 1 with $N_{R_x} = 2$ matches the SER performance of Mode 2 with $N_{R_x} = 5$. This is a result of a greater Euclidian distance between the MPSK and MASK symbols in Mode 2 compared to Mode 1. Mathematically, it means that the phase error, $\vartheta_{k,\ell}^{(m,n)} = \theta_{k,\ell}^{(m,n)} - \hat{\theta}_{k+\kappa,\ell+\iota}^{(m,n)}$, would be higher resulting in more detection errors for $\hat{A}_{k,\ell}^{(m)}$, which is later used to estimate $\varphi_{k,\ell}^{(m,n)} H_{k,\ell}^{(m,n)}$. Moreover, T/F.OSBCE Mode 1 with $N_{R_x} = 10$ achieves better SER than a system with perfect CSI up till SNR $\simeq 48$ dB, and for higher values, increasing N_{R_x} is required to further improve the SER using Mode 1. SER of $\hat{A}_{k,\ell}^{(m)}$ with a certain N_{R_x} at high SNR values hits an error floor courtesy of $\vartheta_{k,\ell}^{(m,n)}$. Also, the rate

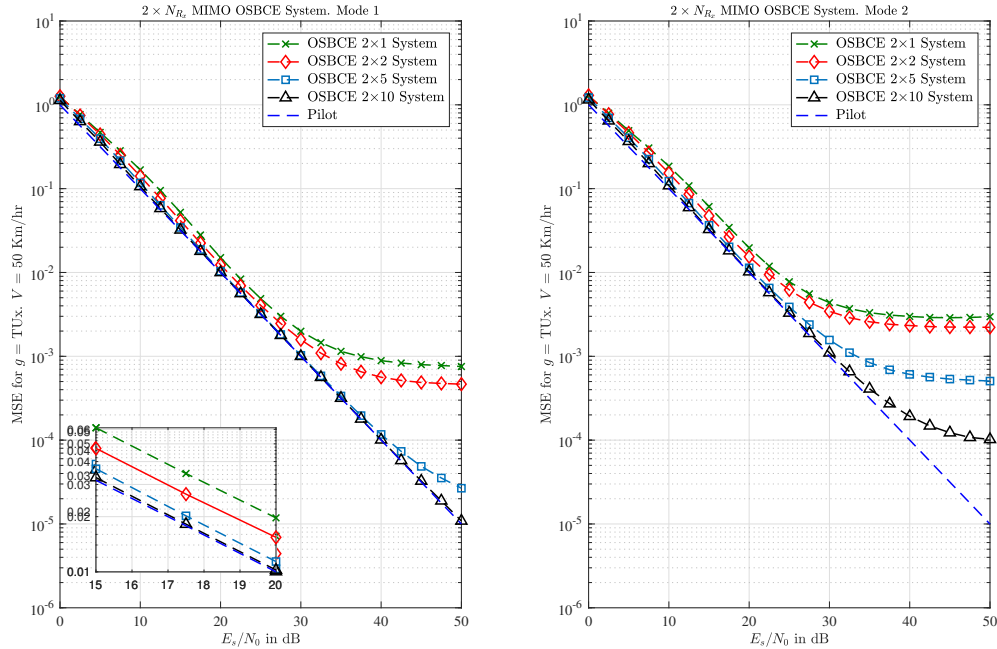


Figure 4.22: $2 \times N_{R_x}$ T/F. OSBCE - MSE vs. SNR for different N_{R_x} - Modes 1 & 2

of enhancement of Mode 1 is greater than the that of Mode 2 as N_{R_x} increases.

Figure 4.22 shows the impact of N_{R_x} on the MSE performance using Mode 1 and Mode 2. With Mode 1 and $N_{R_x} = 5$, the MSE of OSBCE estimated CFRs almost matches that of the pilot-based system up till SNR $\simeq 42$ dB. As for Mode 2, higher N_{R_x} are required to match the pilot-based system performance. With Mode 2 and $N_{R_x} = 10$, MSR still deviates from the pilot-based MSE at SNR $\simeq 27$ dB, which means higher N_{R_x} are needed.

Figures 4.10, 4.16, and 4.22 indicates that the enhancement rate due to higher N_{R_x} is slower with MIMO 2-D OSBCE than the MIMO 1-D OSBCE. This is a result of 2-D phase distortions, in frequency and time, in the case of 2-D OSBCE systems. In general, for 2-D OSBCE to match the MSE of either one of the two 1-D OSBCE systems in a frequency selective fast fading channel, a higher number of receive antennas is required.

Similar to the SIMO systems, 2-D OSBCE is preferable to 1-D OSBCE, since it provides information about the channel behavior over both dimensions. When 2-D OSBCE performs as well as one of the two 1-D OSBCEs, it means that no phase distortion is being introduced along the other dimension. Moreover, there would be no need to interpolate across the static dimension. Simply repeating the CFR coefficients along that static dimension would be sufficient, as long as the 2-D OSBCE performs as well as the 1-D OSBCE. For example, assume 2 MPSKs and 1 MASK were sent at (k, ℓ) , $(k + \kappa, \ell)$, and $(k + \kappa, \ell + \iota)$, respectively. If

$E \left\{ H_{k,\ell}^{(m,n)} \left(H_{k+\kappa,\ell}^{(m,n)} \right)^* \right\} \simeq E \left\{ H_{k,\ell}^{(m,n)} \left(\varphi_{\ell+\iota}^{(m,n)} H_{k+\kappa,\ell}^{(m,n)} \right)^* \right\}$, then the channel can be considered static across the different OFDM symbols. Hence, MIMO F.OSBCE is used to obtain the CFRs, perform interpolation along the frequency axis, and then repeat the CFRs for the other OFDM symbols as long as $E \left\{ H_{k,\ell}^{(m,n)} \left(H_{k+\kappa,\ell}^{(m,n)} \right)^* \right\} \simeq E \left\{ H_{k,\ell}^{(m,n)} \left(\varphi_{\ell+\iota}^{(m,n)} H_{k+\kappa,\ell}^{(m,n)} \right)^* \right\}$, resulting in less interpolation-related computations.

4.3 Conclusion

In this Chapter, different implementation schemes for the blind CE technique from Chapter 3 is developed for MIMO-OFDM systems using LTE-A pilots configuration. Two distinctive schemes are introduced, namely Mode 1 and Mode 2. In Mode 1, MASK symbols are coded and transmitted at different locations in the RG, where the coding facilitates the extraction of the associated MASK symbol per transmit antenna. The RE locations at one transmit antenna, where MPSK symbols are transmitted, are nulled at all other transmitting antennas. In Mode 2, no coding is required and the system depends heavily on the nulling used by LTE-A RG configuration. The RE locations where MPSK and MASK symbols are transmitted from one antenna, are nulled at all other transmitting antennas. In general, Mode 2 achieves better spectral efficiency than Mode 1, with relatively poorer performance. Mode 1 outperforms Mode 2, while achieving less spectral efficiency since MASK symbols are transmitted multiple times, while still using the same total energy.

Assuming channel variations are minimal within $\kappa\Delta_f$ Hz and $\iota\Delta_t$ seconds, then the MASK symbol is equivalent to an imperfect CFR with respect to the MPSK symbol. Therefore, the MPSK symbol can be immediately decoded, and then used in obtaining the CFR at the MPSK location. The OSBCE was presented in an LTE-A RG configuration, to show that the system can be effectively incorporated to current practical systems. It was shown that with enough receive antennas, the performance of the OSBCE-estimated CFRs, in terms of MSE, matches that of the pilot-based system. Due to the nature of pilot-based systems, the MSE of its CFRs does not improve by using multiple receive antennas.

Chapter 5

New Pilot Distributions for One-Shot Blind Channel Estimation for MIMO-OFDM Systems¹

5.1 Introduction

The MSE performance of OSBCE Mode 2 variations for MIMO-OFDM in Chapter 4 suffered because of the relatively huge distance between MPSK and MASK symbols, thus, their associated CFRs are not highly correlated. The design of the different variations of Mode 2 in Chapter 4 assumed an LTE-A RG configuration, which restricted the MPSK and MASK placement, and resulted in performance degradation in terms of MSE. Hence, in this Chapter, new RG configurations that serves the OSBCE in MIMO-OFDM DWCS are presented. The proposed configurations aims at placing the MPSK and MASK symbols adjacent to each other, to improve the MSE performance. Different configurations of OSBCE are presented, namely across frequency, time and time/frequency. The same system model setup and defined variables for the MIMO Mode 2 cases from Chapter 4 are carried over to the proposed MIMO configurations in this Chapter. Numerical results and discussions are presented throughout the Chapter after introducing each new RG configuration, and their MSE performances are compared to their counterparts from Chapter 4. Finally, the Chapter is summarized in the conclusion with some key insights about the proposed RG configurations.

¹Related Publications:

1. M. Zourob, A. Al-Dweik and R. Rao, "New Pilot Distributions Serving One-Shot Blind Channel Estimation for LTE DL Systems," IET in Communications, to be submitted.

5.2 Proposed Pilot Distributions

The proposed distribution aims at minimizing the distance across subcarriers, κ , between the MPSK and MASK symbols, since it was demonstrated in Chapter 3 that the accuracy of the estimated CFRs is critically affected by κ and ι .

5.2.1 Proposed Distribution for MIMO 1-D F.OSBCE

Assume a RG of 12 subcarriers and 14 OFDM symbols where the MPSK and MASK symbols are placed at adjacent subcarriers within one OFDM symbol as shown in Figure 5.1, and similar system model setup and variables as in Chapter 4. The percentage of nulled REs within the RG of the proposed configuration is the same as that of the LTE configuration. It is assumed that enough N_{CP} samples were used and there is no ISI. Since this work deals with an observation window of size 1, the block index notation ℓ is dropped in the remaining parts unless it is necessary to include it.

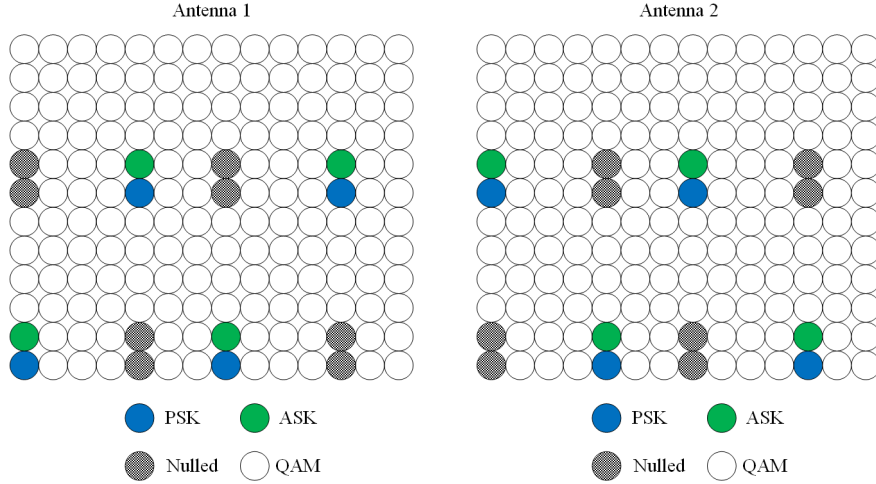


Figure 5.1: $2 \times N_{R_x}$ Frequency OSBCE system - proposed

The MPSK and MASK symbols are transmitted at subcarriers k , \hat{k} , and $k + \kappa$, $\hat{k} + \kappa$, respectively, where $\kappa = 1$. k and \hat{k} are the subcarriers indexing for transmitters 1 and 2, respectively, where $\hat{k} - k = 6$ for C-RS LTE-A [60]. Hence, the received post-FFT samples for receive antenna n are,

$$r_k^{(n)} = A_k^{(1)} H_k^{(1,n)} + \eta_k^{(n)} \quad (5.1)$$

$$r_{k+\kappa}^{(n)} = A_{k+\kappa}^{(1)} H_{k+\kappa}^{(1,n)} + \eta_{k+\kappa}^{(n)} \quad (5.2)$$

$$r_{\hat{k}}^{(n)} = A_{\hat{k}}^{(2)} H_{\hat{k}}^{(2,n)} + \eta_{\hat{k}}^{(n)} \quad (5.3)$$

$$r_{k+\kappa}^{(n)} = A_{k+\kappa}^{(2)} H_{k+\kappa}^{(2,n)} + \eta_{k+\kappa}^{(n)}. \quad (5.4)$$

Due to the usage of nulling in the RG, every $1 \times N_{R_x}$ can be processed on its own. Meaning that the proposed $2 \times N_{R_x}$ configuration is equivalent to two $1 \times N_{R_x}$ SIMO F.OSBCE systems with $\kappa = 1$. Since no coding is used, the proposed MIMO 1-D F.OSBCE will be compared with MIMO 1-D F.OSBCE Mode 2 from Chapter 4, which will be labeled in this Chapter as LTE MIMO 1-D F.OSBCE.

5.2.1.1 Results and Discussion - Proposed vs. Mode 2

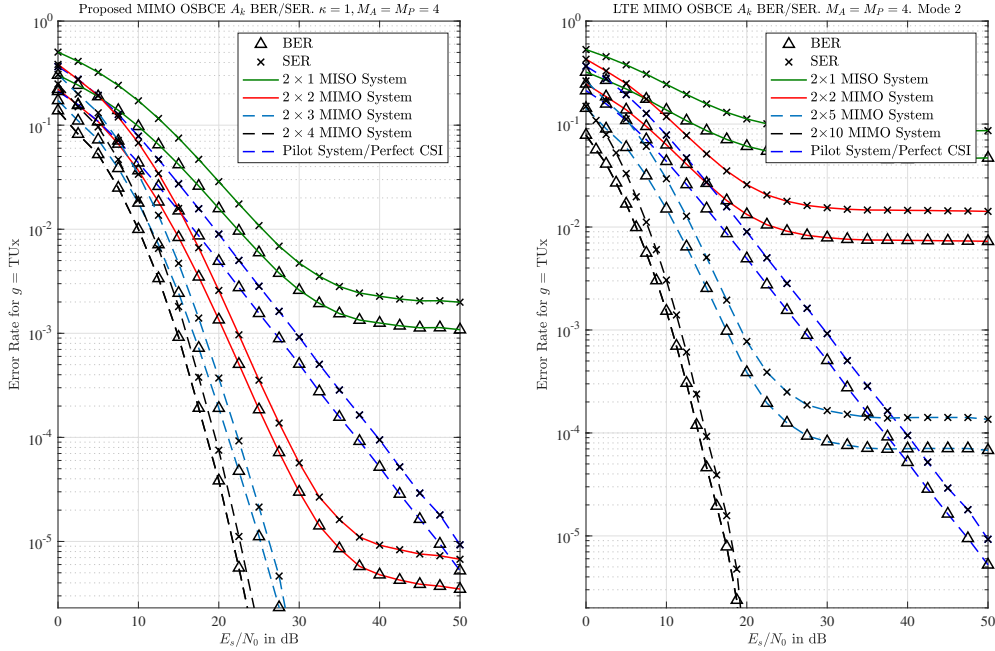


Figure 5.2: $2 \times N_{R_x}$ F. OSBCE - $\hat{A}_k^{(m)}$ BER & SER vs. SNR - Proposed & Mode 2

SER and BER vs. SNR for $\hat{A}_k^{(m)}$ using the proposed and LTE configurations in a TUx channel environment are shown in Figure 5.2. As expected, the proposed MIMO F.OSBCE outperforms its LTE counterpart, due to a lower κ value. The SER of the proposed configuration with 2 receive antennas outperforms the SER of the LTE configuration with 5 antennas. Moreover, using the proposed configuration with $N_{R_x} = 2$, the $\hat{A}_k^{(m)}$ SER becomes lower than the $\hat{A}_k^{(m)}$ SER using perfect CSI till SNR $\simeq 50$ dB. Moreover, the SER improvement rate gets lower as N_{R_x} increases. At any SNR point, $\hat{A}_k^{(m)}$ SER decreases as N_{R_x} increases, and hits an error floor at high SNRs.

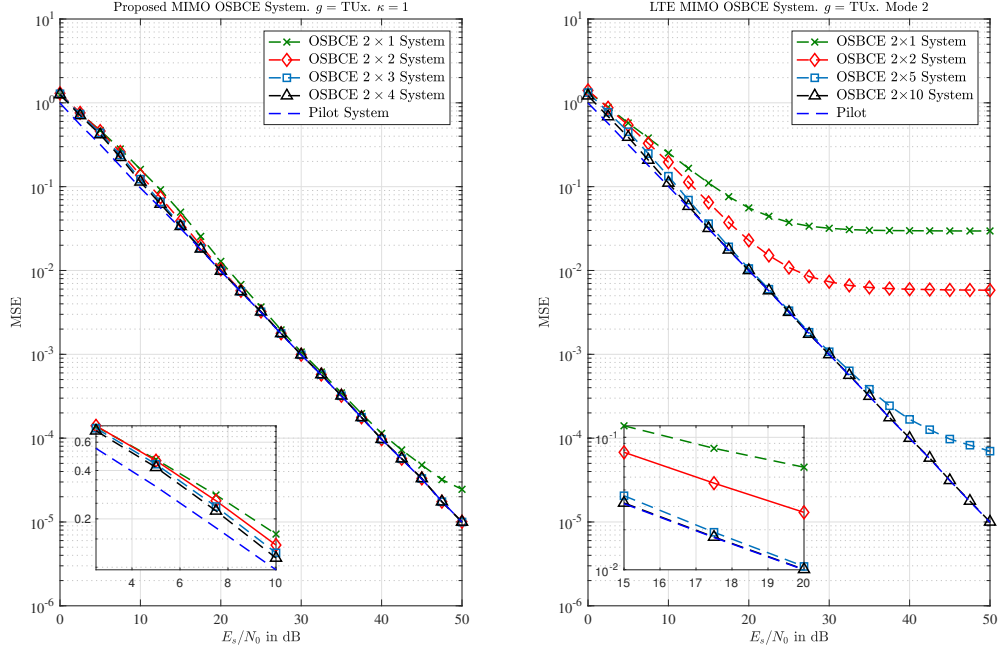


Figure 5.3: $2 \times N_{R_x}$ F. OSBCE - MSE vs. SNR for different N_{R_x} - Proposed & Mode 2

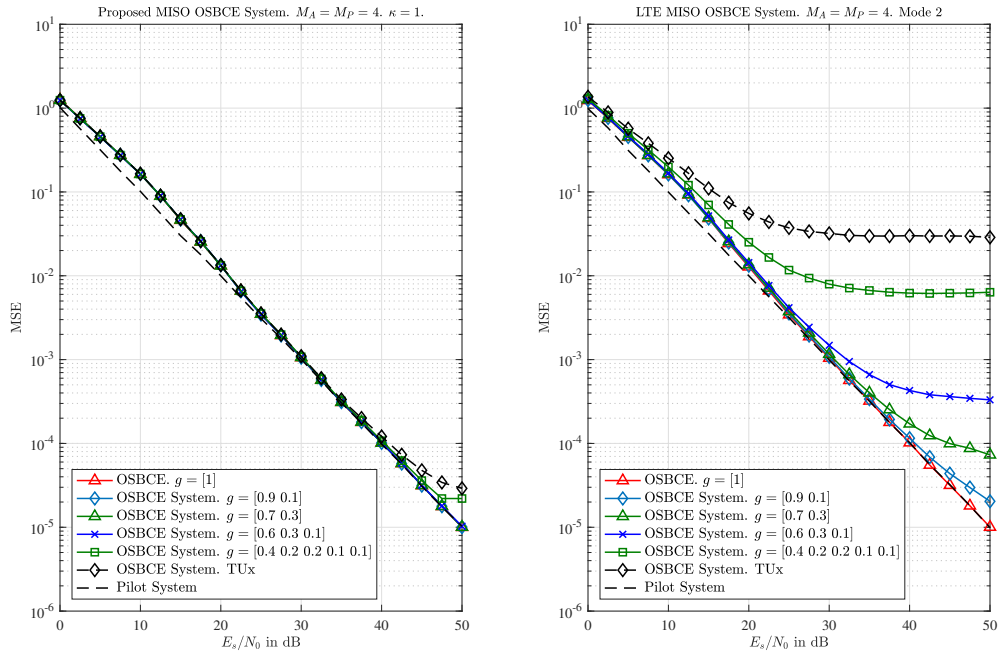


Figure 5.4: $2 \times N_{R_x}$ F. OSBCE - MSE vs. SNR for different channels - Proposed & Modes 2

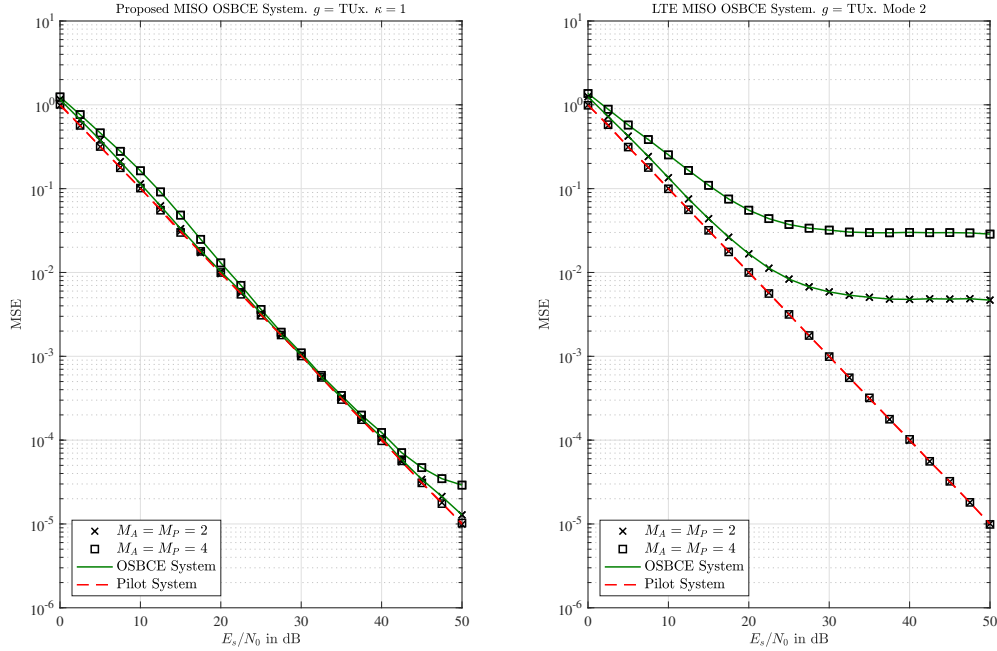

 Figure 5.5: $2 \times N_{R_x}$ F. OSBCE - MSE vs. SNR for different M_A , M_P - Proposed & Mode 2

Figure 5.3 shows the MSE of the proposed and LTE configurations as N_{R_x} increases in a TUx channel environment. While 2 receive antennas with the proposed configuration is enough to match the pilot-based system, the LTE configuration requires 10 receive antennas to achieve the same feat. Moreover, MSE using the proposed configuration with $N_{R_x} = 1$ starts deviating from pilot-based MSE after SNR $\simeq 40$ dB.

Figure 5.4 compares the MSE of the proposed system to the LTE system for different channels. In a TUx channel environment, MSE using the proposed configuration is significantly better than MSE using LTE configuration with 2 receive antennas, which achieves 6×10^{-3} at SNR = 50 dB, while for the same SNR, MSE using the proposed system is 1×10^{-5} ; 600 times better than the LTE configuration. Generally speaking, simulation results show that the proposed configuration OSBCE is more resilient to channel statistics than the LTE configuration OSBCE.

Figure 5.5 compares the effect of the modulation order across the proposed OSBCE and the LTE systems in a TUx channel environment. As noticed from Chapters 3 and 4, as modulation order increases, the MSE performance gets worse. Using the LTE configuration at SNR $\simeq 50$ dB, MSE with 4-ary modulation is almost 6 times worse than the MSE with 2-ary modulation.

Generally speaking, the proposed OSBCE system outperforms the LTE OSBCE system and the MIMO F.OSBCE Mode 1 from Chapter 4. However, the disadvantage of the pro-

posed system is the fact that it produces less CFR estimates than the pilot-based system and MIMO F.OSBCE Mode 1 M. In the pilot-based system, 8 CFRs are produced per RG, and they are well separated from each other. However, in the proposed system, 4 CFRs are produced per RG. This means that less number of interpolation points are available, thus, the accuracy of the interpolated CFRs using the proposed configuration would be degraded, especially with highly frequency selective channels. Therefore, the proposed system in this subsection is best suited to be used with near flat fading channels, to achieve better spectral efficiency by transmitting data symbols instead of pilots. It is worth mentioning that although $\kappa = 1$ for both MIMO F.OSBCE Mode 1 M and the proposed system, their performances are not the same because of the noise associated with obtaining the MASK symbols in MIMO F.OSBCE Mode 1 M.

5.2.2 Proposed Distribution for MIMO 1-D T.OSBCE

The proposed RG configuration for MIMO T.OSBCE is similar in concept to the proposed RG configuration in subsection 5.2.1. The MPSK and MASK are distributed across two adjacent OFDM symbols within one subcarrier, $\iota = 1$, as shown in Figure 5.6. Moreover, it is assumed that ICI is eliminated before the CE, and ϵ does not change within ι symbols duration. Subcarrier index k is dropped in this subsection and only included if necessary. Similar system model setup and variables as in subsection 4.2.2.2 are used. Again, the percentage of nulled REs within the RG of the proposed configuration is the same as that of the LTE configuration.

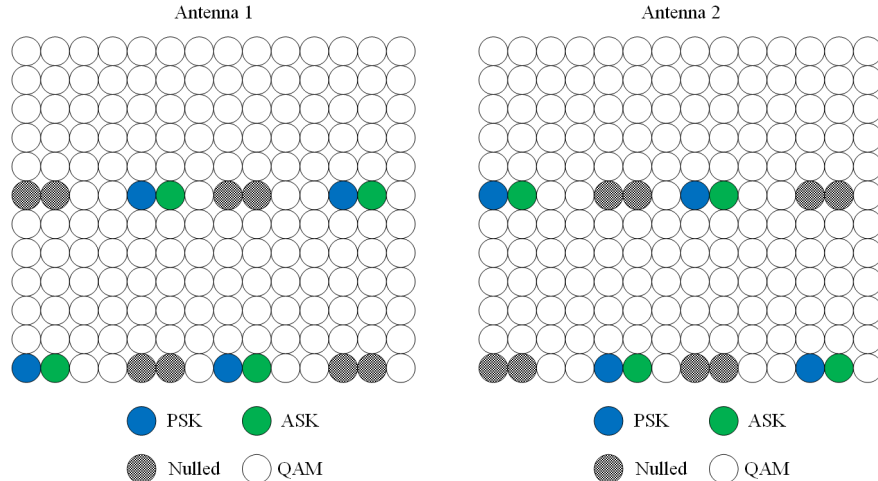


Figure 5.6: $2 \times N_{R_x}$ Time OSBCE system - proposed

The MPSK and MASK symbols are transmitted at OFDM blocks ℓ , $\hat{\ell}$, and $\ell + \iota$, $\hat{\ell} + \iota$, respectively, where $\iota = 1$. ℓ and $\hat{\ell}$ are the OFDM symbols indexing for transmitters 1 and 2,

respectively, where $\hat{\ell} - \ell = 7$ in C-RS LTE-A [12]. Hence, the received post-FFT samples at the k^{th} subcarrier for receive antenna n are,

$$r_{\ell}^{(n)} = \varphi_{\ell}^{(1,n)} A_{\ell}^{(1)} H_{\ell}^{(1,n)} + \eta_{\ell}^{(n)} \quad (5.5)$$

$$r_{\ell+\iota}^{(n)} = \varphi_{\ell+\iota}^{(1,n)} A_{\ell+\iota}^{(1)} H_{\ell+\iota}^{(1,n)} + \eta_{\ell+\iota}^{(n)} \quad (5.6)$$

$$r_{\hat{\ell}}^{(n)} = \varphi_{\hat{\ell}}^{(2,n)} A_{\hat{\ell}}^{(2)} H_{\hat{\ell}}^{(2,n)} + \eta_{\hat{\ell}}^{(n)} \quad (5.7)$$

$$r_{\hat{\ell}+\iota}^{(n)} = \varphi_{\hat{\ell}+\iota}^{(2,n)} A_{\hat{\ell}+\iota}^{(2)} H_{\hat{\ell}+\iota}^{(2,n)} + \eta_{\hat{\ell}+\iota}^{(n)}. \quad (5.8)$$

Because there is no cross-talk at MPSK and MASK locations, the proposed $2 \times N_{R_x}$ MIMO T.OSBCE system processing is similar to two $1 \times N_{R_x}$ SIMO T.OSBCE systems with $\iota = 1$. The proposed MIMO 1-D T.OSBCE is similar to MIMO 1-D T.OSBCE Mode 2 from Chapter 4, but with different ι . MIMO 1-D T.OSBCE Mode 2 will be labeled in this Chapter as LTE MIMO 1-D T.OSBCE.

5.2.2.1 Results and Discussion - Proposed vs. Mode 2

Figure 5.7 shows the effect of increasing N_{R_x} on the initial estimate $\hat{A}_{\ell}^{(m)}$ in terms of SER and BER using proposed and LTE configurations. The speed of the moving UE in Figure 5.7 is 200 Km/hr, which results in a maximum Doppler frequency of 351.9 Hz for $f_c = 1.9$ GHz.

Due to a lower distance between MPSK and MASK in terms of ι , SER using the proposed configuration with $N_{R_x} = 2$ outperforms the SER using the LTE configuration with $N_{R_x} = 5$. Moreover, the proposed configuration with $N_{R_x} = 2$ provides better SER than a system with perfect CSI after SNR $\simeq 36$ dB. For higher SNR, the proposed configuration can further improve the SER by using higher N_{R_x} . In addition, the SER of blindly estimated $\hat{A}_{\ell}^{(m)}$ decreases as SNR increases until it hits an error floor attributed to the UE relative motion to the BS and the number of receive antennas in use. As N_{R_x} increases, the rate of SER enhancement becomes marginal.

The impact of increasing N_{R_x} using the proposed and LTE configurations is shown in Figure 5.8. With $\iota = 1$ in the proposed system, it only requires 2 receive antennas to match the performance of the pilot-based system. Moreover, while the proposed configuration matches the performance of the pilot-based system with 2 receive antennas, MSE performance using LTE configuration deviates from the performance of pilot-based system at SNR $\simeq 45$ dB, hence, a higher number of receive antennas is required using the LTE RG.

The effect of the receiver's relative speed on the MSE performance is shown in Figure 5.9. With the proposed RG, the MSE performance of the OSBCE for a relative speed of

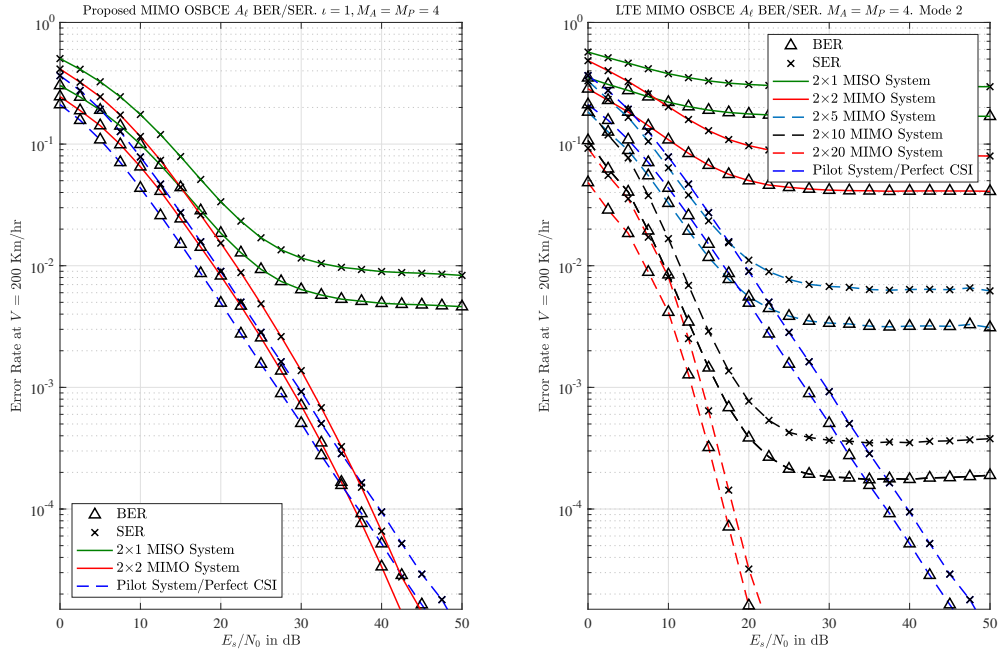


Figure 5.7: $2 \times N_{R_x}$ T. OSBCE - \hat{A}_ℓ BER & SER vs. SNR - Proposed & Mode 2

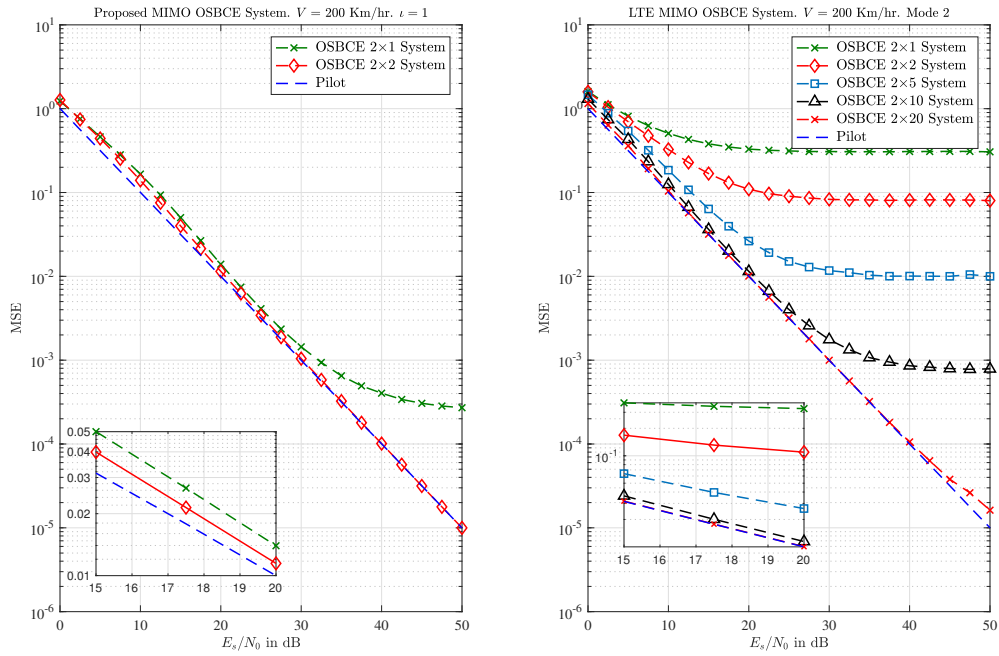


Figure 5.8: $2 \times N_{R_x}$ T. OSBCE - MSE vs. SNR for different N_{R_x} - Proposed & Mode 2

100 Km/hr starts deviating from the pilot-based system performance after $\text{SNR} \simeq 38$ dB. The Doppler frequency in this case is 176 Hz for $f_c = 1.9$ GHz. Hence, as the relative speed increases, N_{R_x} must be increased accordingly to match the performance of pilot-based system. On the other hand, MSE performance gets significantly worse as the relative speed increases when LTE RG is used. Since the performance degradation is higher when LTE RG is used compared to the proposed RG, a higher N_{R_x} is required with the LTE RG.

The effect of modulation order on OSBCE system MSE performance with proposed RG and LTE RG is shown in Figure 5.10 at a relative speed of 200 Km/hr. Similar to previous simulations, as the modulation order increases, the MSE performance gets worse, which would be a result of worse SER performance of $A_\ell^{(m)}$.

In general, the proposed OSBCE system outperforms the LTE OSBCE system and the MIMO T.OSBCE Mode 1 from Chapter 4. However, similar to the proposed MIMO F.OSBCE in subsection 5.2.1, the proposed system results in less CFR estimates than the pilot-based system and MIMO T.OSBCE Mode 1. This results in worse interpolation, especially with high mobility channels, where higher number of pilots are required. Therefore, the proposed system can achieve better spectral efficiency with the MSE performance of pilot-based system in slow fading channels. Although $\iota = 1$ for both MIMO T.OSBCE Mode 1 and the proposed system, their performances are similar due to the noise associated with obtaining the MASK symbols in MIMO T.OSBCE Mode 1.

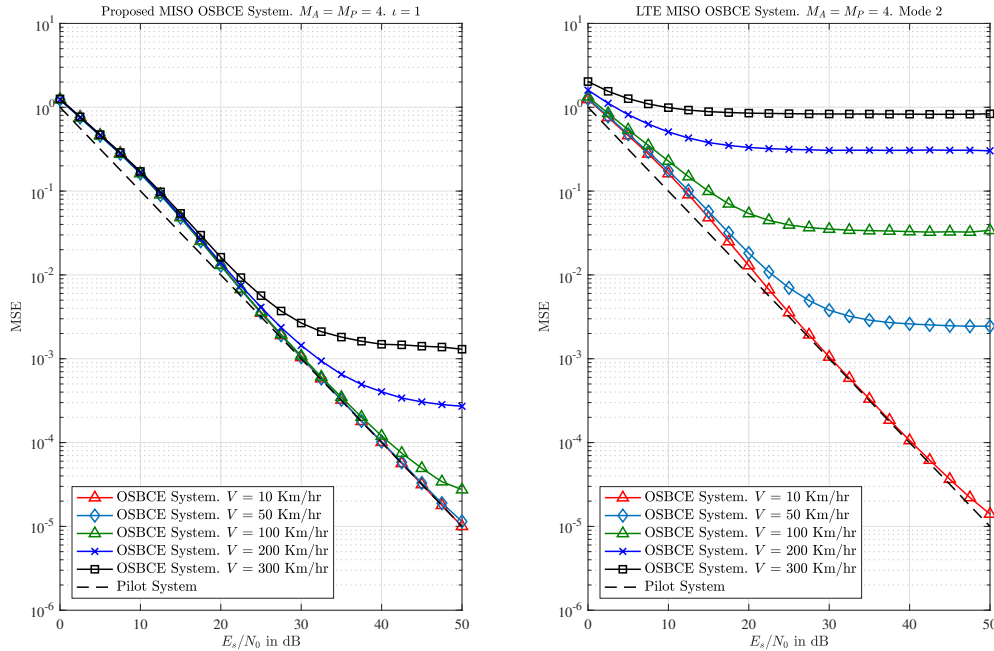
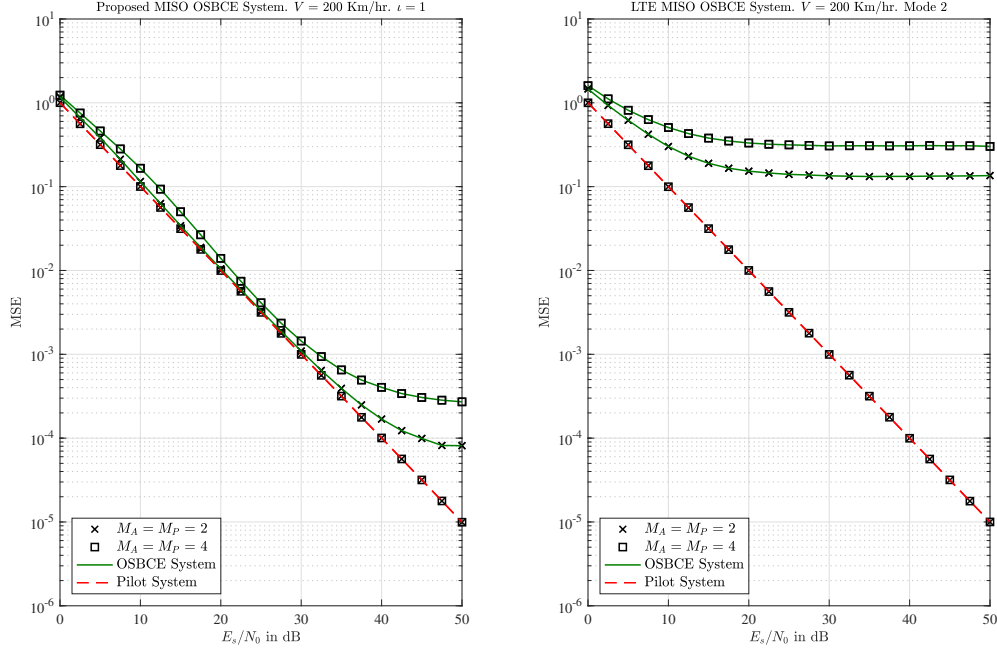


Figure 5.9: $2 \times N_{R_x}$ T. OSBCE - MSE vs. SNR for different speeds - Proposed & Mode 2


 Figure 5.10: $2 \times N_{R_x}$ T. OSBCE - MSE vs. SNR for different M_A , M_P - Proposed & Mode 2

5.2.3 Proposed Distribution for MIMO 2-D T/F.OSBCE

In this subsection, the proposed RG for the OSBCE system is designed to work across two dimensions, similar to MIMO T/F OSBCE Mode 2 from Chapter 4. The proposed RG distribution for this OSBCE system is shown in Figure 5.11. Again, the aim of the proposed configuration is to minimize the distance between the MPSK and MASK symbols. It is assumed that ISI and ICI are eliminated before the CE step, and the same system model and variables are carried over from Chapter 4. The MPSK and MASK symbols are transmitted as shown in Figure 5.11, and the received post-FFT samples at receive antenna n are,

$$r_{k,\ell}^{(n)} = \varphi_{\ell}^{(1,n)} A_{k,\ell}^{(1)} H_{k,\ell}^{(1,n)} + \eta_{k,\ell}^{(n)} \quad (5.9)$$

$$r_{k+\kappa,\ell+\iota}^{(n)} = \varphi_{\ell+\iota}^{(1,n)} A_{k+\kappa,\ell+\iota}^{(1)} H_{k+\kappa,\ell+\iota}^{(1,n)} + \eta_{k+\kappa,\ell+\iota}^{(n)} \quad (5.10)$$

$$r_{k,\ell+\iota}^{(n)} = \varphi_{\ell+\iota}^{(2,n)} A_{k,\ell+\iota}^{(2)} H_{k,\ell+\iota}^{(2,n)} + \eta_{k,\ell+\iota}^{(n)} \quad (5.11)$$

$$r_{k+\kappa,\ell}^{(n)} = \varphi_{\ell}^{(2,n)} A_{k+\kappa,\ell}^{(2)} H_{k+\kappa,\ell}^{(2,n)} + \eta_{k+\kappa,\ell}^{(n)}. \quad (5.12)$$

Every $1 \times N_{R_x}$ can be processed on its own, since transmitters do not cross-talk at MPSK and MASK locations. Thus, the proposed $2 \times N_{R_x}$ MIMO T/F.OSBCE system processing is similar to two $1 \times N_{R_x}$ SIMO T/F.OSBCE systems with $(\kappa, \iota) = (1, 1)$. The proposed MIMO

T/F.OSBCE is similar to MIMO T/F.OSBCE Mode 2 from Chapter 4, but with different ι . MIMO 1-D T.OSBCE Mode 2 will be labeled in this Chapter as LTE MIMO T/F.OSBCE.

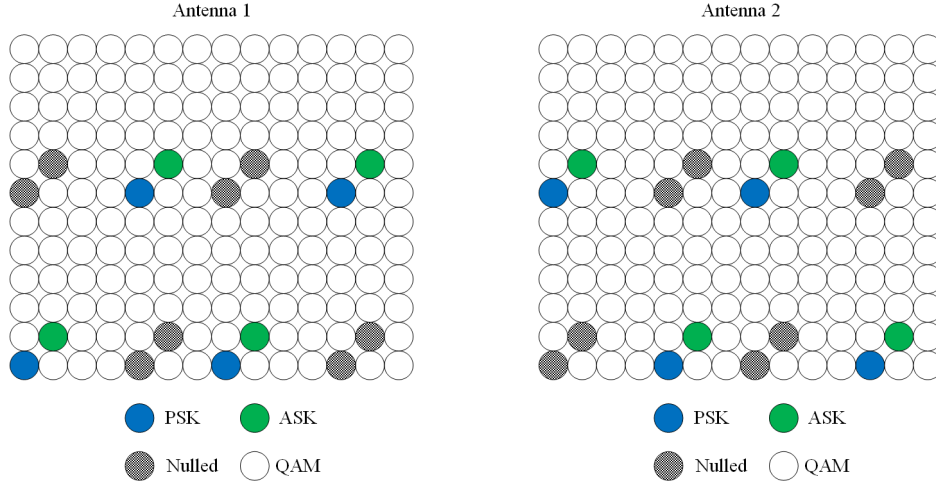


Figure 5.11: $2 \times N_{R_x}$ Time/Frequency OSBCE system - proposed

5.2.3.1 Results and Discussion - Proposed vs. Mode 2

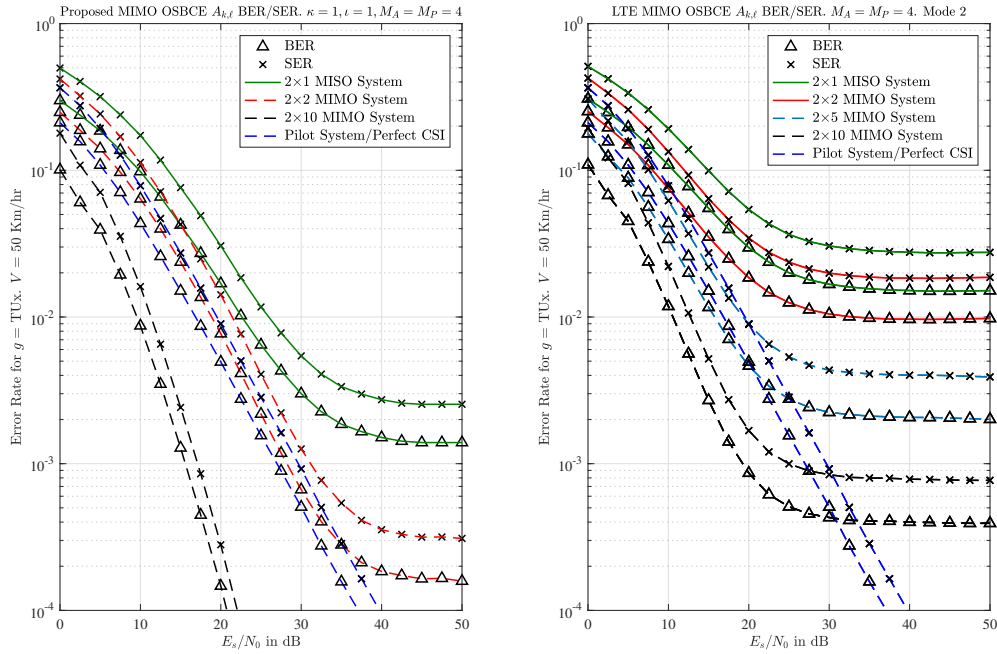
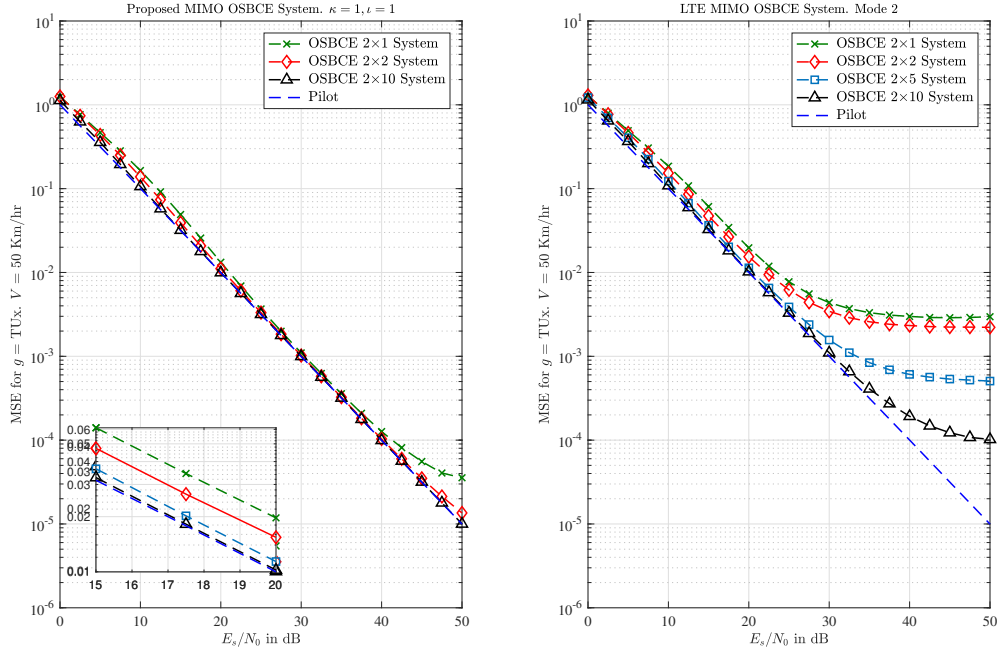


Figure 5.12: $2 \times N_{R_x}$ T/F. OSBCE - $\hat{A}_{k,\ell}$ BER & SER vs. SNR - Proposed & Mode 2

Figure 5.12 shows the impact of increasing N_{R_x} on the initial estimate $\hat{A}_{k,\ell}^{(m)}$ using proposed RD and LTE RG. The speed of the moving object in Figure 5.12 is 50 Km/hr, which results


 Figure 5.13: $2 \times N_{R_x}$ T/F. OSBCE - MSE vs. SNR for different N_{R_x} - Proposed & Mode 2

in maximum Doppler frequency of 88 Hz at $f_c = 1.9$ GHz. The SER using the proposed RG with $N_{R_x} = 2$ outperforms the SER performance using LTE RG with $N_{R_x} = 5$. This is a result of a greater Euclidian distance between the MPSK and MASK symbols in the proposed RG compared to the LTE RG. Moreover, the proposed RG T/F.OSBCE with $N_{R_x} = 10$ achieves better SER than a system with perfect CSI across the whole SNR region. SER of $\hat{A}_{k,\ell}^{(m)}$ with a certain N_{R_x} at high SNR values hits an error floor courtesy of the channel statistics. Also, the rate of enhancement by increasing N_{R_x} using the proposed RG is greater than the that of LTE RG.

Figure 5.13 shows the impact of N_{R_x} on the MSE performance using the proposed RG and LTE RG. Using the proposed RG and $N_{R_x} = 2$, the MSE of estimated CFRs almost matches that of the pilot-based system up till SNR $\simeq 45$ dB. Using LTE RG, higher N_{R_x} are required to match the pilot-based system performance. With LTE RG and $N_{R_x} = 10$, MSR still deviates from the pilot-based MSE at SNR $\simeq 27$ dB, which means higher N_{R_x} are needed.

Similar to the previously proposed configurations in subsections 5.2.1 and 5.2.2, the proposed RG in this subsection results in less CFR estimates than the pilot-based system and MIMO T/F.OSBCE Mode 1. Therefore, less interpolation points are available.

The proposed 2-D OSBCE is preferable to the proposed 1-D OSBCE, since information

is provided about the channel behavior over both dimensions. If the proposed 2-D OSBCE performs as well as one of the two 1-D OSBCEs, then no phase distortion is being introduced along the other dimension. Also, there would be no need to interpolate across the static dimension. Simply repeating the CFR coefficients along that static dimension would be sufficient in that case.

5.3 Conclusion

In this Chapter, new RG configurations that serves the OSBCE system in MIMO-OFDM are presented. The criteria for distribution is to minimize the separation distance, $d_{\kappa,\iota} = \sqrt{\kappa^2 + \iota^2}$, between the MPSK and MASK symbols of the OSBCE system. The proposed configurations places the MPSK and MASK symbols next to each other across frequency, time, or time and frequency, in order to improve the MSE performance. The minimum number of subcarriers spacing and OFDM symbols spacing between the MPSK and MASK symbols are $\kappa = 1$ and $\iota = 1$, respectively. Assuming channel variations are minimal within Δ_f Hz and Δ_t seconds, then the MASK symbol represents an imperfect CFR with respect to the MPSK symbol, and the MPSK symbol can be decoded for and then used to obtain the CFR at the MPSK location. Numerical results showed that the proposed RG configurations for OSBCE provide superior MSE performance compared to the LTE RG configuration with OSBCE, namely MIMO Mode 2 cases from Chapter 4. By increasing the number of receive antennas, MSE performance improves till it matches the pilot-based system. In general, the proposed RG requires less number of receive antennas than MIMO Mode 2, to match the pilot-based performance. However, compared to the pilot-based system, the proposed RG configuration results in half the number of interpolation points produced by the pilot-based system. Therefore, the interpolation step after the estimating the CFRs using the proposed RG with OSBCE is expected to result in worse overall performance, given that the channel is a frequency selective fast fading channel.

Chapter 6

Conclusion

6.1 Introduction

In this thesis, new pilot-based and blind-based CE techniques are proposed, developed, investigate, and analyzed for SIMO and MIMO-OFDM systems in the context of LTE-A. In addition, new RG configurations are introduced to enhance the OSBCE system compared to the LTE RG configurations. This Chapter summarizes the contributions made in this thesis and the conclusions from the results obtained. Moreover, some important future research areas are highlighted with respect to the finding in this thesis and the projected demands of DWCS.

6.2 Summary of Contributions

In Chapter 2, the main objective was to investigate the first of two major CE schemes, which is pilot-based CE. First, mathematical equations that describe pilot distribution and extraction for C-RS in LTE-A DL were presented. The provided equations were found through deep analysis of pilot locations in C-RS RG. The equations give flexibility in system design, where storage resources are limited and it is not possible to store lookup tables. Next, a hybrid pilot-based lower complexity CE scheme for C-RS and UE-RS in LTE-A DL system was introduced. The proposed scheme uses 2×1 -D Wiener filter to filter the noisy CFR LS estimates at pilot locations only instead of 2-D Wiener filter, and then uses cubic spline interpolation for data symbol locations instead of 2-D Wiener interpolation. Mathematical descriptions for the performance of LS equalization, EWA and Wiener filtering were derived, and used to confirm the computer simulations.

Performance of the proposed scheme was evaluated in terms of MSE under various channel

conditions, where numerical results showed that the proposed scheme is a sub-optimum version of the optimum 2-D Wiener filter and interpolation. The proposed scheme matches the optimum system up till certain channel conditions and noise levels, at a much reduced computational complexity. Results showed that the optimal method for noise reduction is lower bounded by a combination of both EWA and Wiener as a function of both SNR and channel statistics. Complexity analysis showed that the proposed scheme requires 8.8% of the number of computations needed by 2-D Wiener filtering with Wiener interpolation. Even if spline interpolation replaced Wiener, the proposed scheme still requires 74.5% the number of computations required by 2-D Wiener/Spline. Although the proposed 2×1 -D FFT/IFFT filtering and interpolation has less complexity than 2-D DFT/IDFT, its MSE performance is still worse than 2×1 -D Wiener/Spline in different channel conditions. Results indicate that one need to select the appropriate filtering and interpolation combination based on the acceptable MSE threshold for successful detection provided by the system detector in use, SNR value and channel delay profile. Thus, the optimal method for noise reduction after equalization. Finally, simulations in real-life LTE-A confirmed the practicality of the proposed hybrid Wiener CE system by achieving the throughput threshold for numerous test cases set by 3GPP.

The objective in Chapter 3 was to study the other major CE technique which is blind-based CE. A newly introduced blind CE technique for SISO systems [56] has been developed for SIMO-OFDM systems using a hybrid OFDM symbol structure. MPSK symbols are transmitted at conventional OFDM pilot REs, and REs that are generally separated from MPSK locations by $d_{\kappa,\iota} = \sqrt{\kappa^2 + \iota^2}$ are modulated using MASK. The MASK symbol acts as an imperfect CFR with respect to the MPSK and is used to detect the MPSK symbol, given that channel variations are minimal within $\kappa\Delta_f$ Hz and $\iota\Delta_t$ seconds. Afterwards, the estimated MPSK symbol is used to obtain the CFR at the MPSK location. The proposed OSBCE was presented in an LTE-A configuration, in order to prove that the system is practical and can be easily utilized in current systems.

The developed estimator with its different variations requires minimum observations windows; $d_{\kappa,\iota} = 1$ for the F.OSBCE and T.OSBCE, and $d_{\kappa,\iota} = \sqrt{2}$ for the T/F.OSBCE to estimate the CFR. Therefore, the developed OSBCE for SIMO-OFDM is appropriate for channels with fast variations in frequency, time or both directions. Numerical results were used to confirm the analytical results wherever possible, and verify that OSBCE can achieve reliable CFRs as compared to the benchmark pilot-based system, with improved spectral efficiency based on the OSBCE variation, and with similar complexity. Discussions of numerical results were given with focus on the impact of increasing N_{R_x} on the performance of OSBCE.

In Chapter 4, the OSBCE from Chapter 3 is developed for MIMO-OFDM systems using LTE-A pilots configuration, with different implementation schemes. Two distinctive schemes are proposed, namely Mode 1 and Mode 2. In Mode 1, MASK symbols are coded and transmitted at different RE locations next to the MPSK symbol. The RE locations at one transmit antenna, where MPSK symbols are transmitted, are nulled at all other transmitting antennas. The coding allows the extraction of the associated MASK symbol per transmit antenna, hence, OSBCE can be employed. In Mode 2, instead of coding the MASK symbols, the RE locations where MPSK and MASK symbols are transmitted from one antenna, are nulled at all other transmitting antennas. In general, Mode 2 achieves better spectral efficiency than Mode 1, with relatively poorer performance, thus, requiring higher number of receive antennas to match the MSE performance of pilot-based systems. Mode 1 outperforms Mode 2, while achieving less spectral efficiency since MASK symbols are transmitted multiple times, while still using the same total energy.

If channel is almost static within an observation window of $\kappa\Delta_f$ Hz and $\iota\Delta_t$ seconds, then the MASK symbol is equivalent to an imperfect CFR with respect to the MPSK symbol, which can then be detected and used to acquire the CFR at the MPSK RE. It was shown that MSE performance of OSBCE-estimated CFRs matches that of the pilot-based system, given that enough receive antennas are used.

In Chapter 5, new RG configurations that aims at enhancing the MSE performance of the OSBCE system in MIMO-OFDM are presented. The design criteria is to minimize the separation distance, $d_{\kappa,\iota} = \sqrt{\kappa^2 + \iota^2}$, between the MPSK and MASK symbols of the OSBCE system. In the proposed RGs, MPSK and MASK symbols are placed next to each other across frequency, time, or time and frequency. It was shown that the proposed RG configurations for OSBCE provides superior MSE performance compared to the LTE RG configuration with OSBCE, namely MIMO Mode 2 cases from Chapter 4. MSE performance improves by increasing N_{R_x} , till it matches the pilot-based system. The proposed RG requires less number of receive antennas than MIMO Mode 2 variations, to match the pilot-based performance. However, the proposed RG configuration results in half the number of interpolation points produced by the pilot-based system. Therefore, the interpolation step after the estimating the CFRs using the proposed RG with OSBCE is expected to result in worse overall performance, given that the channel is a frequency selective fast fading channel.

6.3 Recommendations for Future Work

In light of the work presented in this thesis, there exists a number of areas for further research and examination. They are as follows:

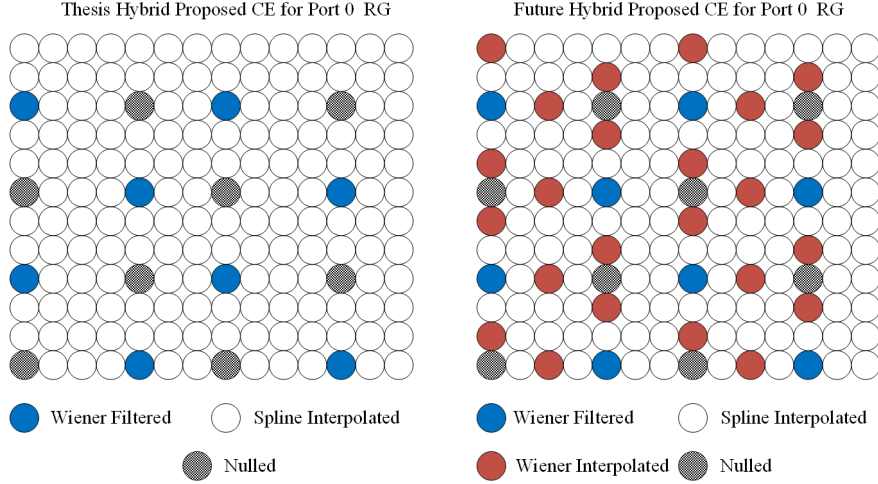


Figure 6.1: Suggested future pilot-based hybrid system

- The hybrid system in Chapter 2 can be enhanced at the cost of extra computations by using a combination of spline and Wiener interpolation, where intermediate points in the RG are estimated using the optimal Wiener interpolator, and then spline is used for the rest of the RG. An example comparing the proposed hybrid system in Chapter 2 to the suggested future system is shown in Figure 6.1.
- The proposed system in Chapter 2 was tested with pilot-based system after LS equalization. It would be interesting to see the effect of the hybrid pilot-based system of Chapter 2 when it is employed after using OSBCE instead of LS for the initial CFR estimation.
- All the proposed systems in Chapters 4 and 5 still use nulling to receive either the MASK, or the MPSK or both from one transmitter without interference from other transmitters. To increase the spectral efficiency of the OSBCE system, new coding schemes are needed that can accurately separate the symbols from different transmitters without the need for nulling. This means that a RG can use all of its REs to transmit data.
- One alternative method to enhance the OSBCE system performance without increasing N_{R_x} , would be to use iterations. For example, assume the estimates of the MPSK symbol and the associated CFR are $i\hat{A}_{k,\ell}$ and $i\hat{H}_{k,\ell}$, where i is the iteration number. At $i = 1$, the initial estimate ${}_1\hat{A}_{k,\ell}$ is used to find ${}_1\hat{H}_{k,\ell}$ using the received symbol, $r_{k,\ell}$ as was demonstrated in Chapter 3. Next, ${}_1\hat{H}_{k,\ell}$ is used as an imperfect CFR instead of the MASK symbol to detect the MPSK symbol again as ${}_2\hat{A}_{k,\ell}$. Then, using $r_{k,\ell}$ and ${}_2\hat{A}_{k,\ell}$, the second CFR estimate, ${}_2\hat{H}_{k,\ell}$, can be computed. The process is repeated until

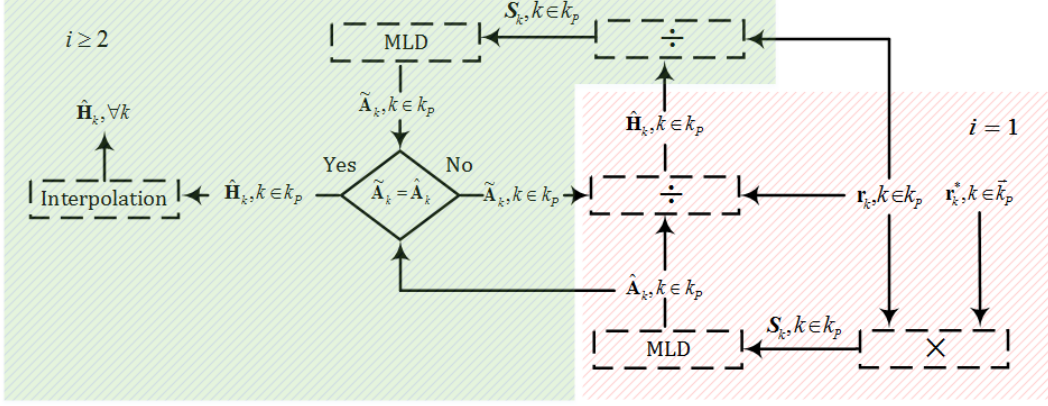


Figure 6.2: Suggested iterative OSBCE system

$\sum_{k,\ell} \left({}_{i+1}\hat{A}_{k,\ell} - {}_i\hat{A}_{k,\ell} \right) = 0$. The drawback of this method is increased computational complexity. However, it is an important alternative for users' terminals, which in most cases cannot accommodate N_{R_x} antennas and are required to be small in size. Figure 6.2 shows the flow diagram for the suggested iterative OSBCE system.

- The OSBCE design is based on the MPSK and MASK symbols, and any distortion to the pair would decrease their associated CFR's correlation. One major source of impairment is generated by the I/Q imbalance from using non-linear amplifiers. It would be interesting to investigate the effect of such impairment on the performance of the OSBCE system.
- Develop closed-form mathematical expressions and derive equations that describe the SER of the initial estimates for the MPSK symbols and the associated MSE of the initial estimates of the CFRs for the SIMO OSBCE and MIMO OSBCE.

Bibliography

- [1] J. G. Proakis and M. Salehi, *Digital Communications*, 2008.
- [2] B. Sklar, “Rayleigh fading channels in mobile digital communication systems part I: characterization,” *IEEE Communications Magazine*, vol. 35, no. 9, pp. 136–146, 1997.
- [3] Y. Li, L. J. Cimini, and N. R. Sollenberger, “Robust channel estimation for OFDM systems with rapid dispersive fading channels,” *IEEE Transactions on Communications*, vol. 46, no. 7, pp. 902–915, 1998.
- [4] H. Lin, “Flexible configured OFDM for 5G air interface,” *IEEE Access*, vol. 3, pp. 1861–1870, 2015.
- [5] E. Dahlman, S. Parkvall, and J. Skold, *4G: LTE/LTE-Advanced for Mobile Broadband*, 2013.
- [6] A. Al-Dweik, B. Sharif, and C. Tsimenidis, “Accurate BER analysis of OFDM systems over static frequency-selective multipath fading channels,” *IEEE Transactions on Broadcasting*, vol. 57, no. 4, pp. 895–901, 2011.
- [7] E. Al-Dalakta, A. Al-Dweik, A. Hazmi, C. Tsimenidis, and B. Sharif, “PAPR reduction scheme using maximum cross correlation,” *IEEE Communications Letters*, vol. 16, no. 12, pp. 2032–2035, 2012.
- [8] A. Al-Dweik, S. Younis, A. Hazmi, C. Tsimenidis, and B. Sharif, “Efficient OFDM symbol timing estimator using power difference measurements,” *IEEE Transactions on Vehicular Technology*, vol. 61, no. 2, pp. 509–520, 2012.
- [9] A. Al-Dweik, A. Hazmi, S. Younis, B. Sharif, and C. Tsimenidis, “Carrier frequency offset estimation for OFDM systems over mobile radio channels,” *IEEE Transactions on Vehicular Technology*, vol. 59, no. 2, pp. 974–979, 2010.
- [10] —, “Blind iterative frequency offset estimator for orthogonal frequency division multiplexing systems,” *IET Communications*, vol. 4, no. 16, pp. 2008–2019, nov 2010.

- [11] A. S. Khrwat, B. S. Sharif, C. C. Tsimenidis, S. Boussakta, and A. J. Al-Dweik, "Channel prediction for limited feedback precoded MIMO-OFDM systems," in *IEEE International Symposium on Signal Processing and Information Technology, ISSPIT 2009*, 2009, pp. 195–200.
- [12] ETSI, "LTE; Evolved Universal Terrestrial Radio Access (E-UTRA); Radio Resource Control (RRC); Protocol specification," Tech. Rep. Release 12, 2015.
- [13] I. Eizmendi, M. Velez, D. Gomez-Barquero, J. Morgade, V. Baena-Lecuyer, M. Slimani, and J. Zoellner, "DVB-T2: The second generation of terrestrial digital video broadcasting system," *IEEE Transactions on Broadcasting*, vol. 60, no. 2, pp. 258–271, 2014.
- [14] R. Marks, "IEEE Standard 802.16: A Technical Overview of the WirelessMAN Air Interface for Broadband Wireless Access," *IEEE Communications Magazine*, no. June, p. 12, 2002.
- [15] L. a. N. Man, *IEEE Standard for Information technology - Telecommunications and information Local and metropolitan area networks - Part 11 : Wireless LAN Medium Access Control (MAC)*, 2007, vol. 2007, no. June.
- [16] Cisco Mobile, *Cisco Visual Networking Index: Global Mobile Data Traffic Forecast Update, 2016-2021 White Paper*, 2017.
- [17] D. Gesbert, M. Kountouris, R. W. Heath, C. B. Chae, and T. Sälzer, "Shifting the MIMO Paradigm," *IEEE Signal Processing Magazine*, vol. 24, no. 5, pp. 36–46, 2007.
- [18] M. Kobayashi, N. Jindal, and G. Caire, "Training and feedback optimization for multiuser MIMO downlink," *IEEE Transactions on Communications*, vol. 59, no. 8, pp. 2228–2240, 2011.
- [19] V. Stankovic and M. Haardt, "Generalized design of multi-user MIMO precoding matrices," *IEEE Transactions on Wireless Communications*, vol. 7, no. 3, pp. 953–961, 2008.
- [20] G. Caire and S. Shamai, "On the achievable throughput of a multiantenna Gaussian broadcast channel," *IEEE Transactions on Information Theory*, vol. 49, no. 7, pp. 1691–1706, 2003.
- [21] P. Viswanath and D. N. Tse, "Sum capacity of the vector Gaussian broadcast channel and uplink-downlink duality," *IEEE Transactions on Information Theory*, vol. 49, no. 8, pp. 1912–1921, 2003.

- [22] T. Yoo and A. Goldsmith, “On the optimality of multiantenna broadcast scheduling using zero-forcing beamforming,” *IEEE Journal on Selected Areas in Communications*, vol. 24, no. 3, pp. 528–541, 2006.
- [23] T. L. Marzetta, “Noncooperative cellular wireless with unlimited numbers of base station antennas,” *IEEE Transactions on Wireless Communications*, vol. 9, no. 11, pp. 3590–3600, 2010.
- [24] X. Gao, O. Edfors, F. Rusek, and F. Tufvesson, “Linear pre-coding performance in measured very-large MIMO channels,” in *IEEE Vehicular Technology Conference*, 2011.
- [25] H. Q. Ngo, E. G. Larsson, and T. L. Marzetta, “Energy and spectral efficiency of very large multiuser MIMO systems,” *IEEE Transactions on Communications*, vol. 61, no. 4, pp. 1436–1449, 2013.
- [26] E. G. Larsson, O. Edfors, F. Tufvesson, and T. L. Marzetta, “Massive MIMO for next generation wireless systems,” *IEEE Communications Magazine*, vol. 52, no. 2, pp. 186–195, 2014.
- [27] M. Morelli and U. Mengali, “A comparison of pilot-aided channel estimation methods for OFDM systems,” *IEEE Transactions on Signal Processing*, vol. 49, no. 12, pp. 3065–3073, 2001.
- [28] Y. Li, “Pilot-symbol-aided channel estimation for OFDM in wireless systems,” *IEEE Transactions on Vehicular Technology*, vol. 49, no. 4, pp. 1207–1215, 2000.
- [29] W. C. Chen and C. D. Chung, “Spectrally Efficient OFDM Pilot Waveform for Channel Estimation,” *IEEE Transactions on Communications*, vol. 65, no. 1, pp. 387–402, 2017.
- [30] X. He, R. Song, and W.-P. Zhu, “Pilot Allocation for Distributed Compressed Sensing Based Sparse Channel Estimation in MIMO-OFDM Systems,” *IEEE Transactions on Vehicular Technology*, vol. 65, no. 5, pp. 2990–3004, 2016.
- [31] R. Mohammadian, A. Amini, and B. H. Khalaj, “Compressive sensing-based pilot design for sparse channel estimation in OFDM systems,” *IEEE Communications Letters*, vol. 21, no. 1, pp. 4–7, 2017.
- [32] X. Dong, W. S. Lu, and A. C. Soong, “Linear interpolation in pilot symbol assisted channel estimation for OFDM,” *IEEE Transactions on Wireless Communications*, vol. 6, no. 5, pp. 1910–1920, 2007.

- [33] M. X. Chang and T. D. Hsieh, "Detection of OFDM signals in fast-varying channels with low-density pilot symbols," *IEEE Transactions on Vehicular Technology*, vol. 57, no. 2, pp. 859–872, 2008.
- [34] C. Qi, G. Yue, L. Wu, Y. Huang, and A. Nallanathan, "Pilot Design Schemes for Sparse Channel Estimation in OFDM Systems," pp. 1493–1505, 2015.
- [35] S. Coleri, M. Ergen, A. Puri, and A. Bahai, "Channel estimation techniques based on pilot arrangement in OFDM systems," *IEEE Transactions on Broadcasting*, vol. 48, no. 3, pp. 223–229, 2002.
- [36] M. K. Ozdemir and H. Arslan, "Channel estimation for wireless ofdm systems," *IEEE Communications Surveys & Tutorials*, vol. 9, no. 2, pp. 18–48, 2007.
- [37] P. Hoeher, S. Kaiser, and P. Robertson, "Two-Dimensional Pilot-Symbol-Aided Channel Estimation By Wiener Filtering," *IEEE International Conference on Acoustics, Speech, and Signal Processing*, vol. 3, no. 3, pp. 1845 – 1848, 1997.
- [38] A. Zaib and S. Khattak, "Structure-Based Low Complexity MMSE Channel Estimator for OFDM Wireless Systems," *Wireless Personal Communications*, vol. 97, no. 4, pp. 5657–5674, 2017.
- [39] A. Khelifi and R. Bouallegue, "A Very Low Complexity LMMSE Channel Estimation Technique for OFDM Systems," pp. 1–5, 2015.
- [40] B. Ozbek and D. L. Ruyet, "Pilot-symbol-aided iterative channel estimation for OFDM-based systems," *Electronics and Communications*, 2005.
- [41] S. Liu, F. Wang, R. Zhang, and Y. Liu, "A simplified parametric channel estimation scheme for OFDM systems," *IEEE Transactions on Wireless Communications*, vol. 7, no. 12, pp. 5082–5090, 2008.
- [42] M. X. Chang, "A new derivation of least-squares-fitting principle for OFDM channel estimation," *IEEE Transactions on Wireless Communications*, vol. 5, no. 4, pp. 726–731, 2006.
- [43] Y. Liu, Z. Tan, H. Hu, L. J. Cimini, and G. Y. Li, "Channel Estimation for OFDM," *IEEE Communications Surveys & Tutorials*, vol. 16, no. 4, pp. 1891–1908, 2014.
- [44] A. Al-Dweik and Y. Iraqi, "Error Probability Analysis and Applications of Amplitude-Coherent Detection in Flat Rayleigh Fading Channels," *IEEE Transactions on Communications*, vol. 64, no. 5, pp. 2235–2244, 2016.

- [45] C. C. Tu and B. Champagne, "Subspace-based blind channel estimation for MIMO-OFDM systems with reduced time averaging," *IEEE Transactions on Vehicular Technology*, vol. 59, no. 3, pp. 1539–1544, 2010.
- [46] F. Gao, Y. Zeng, A. Nallanathan, and T. S. Ng, "Robust subspace blind channel estimation for cyclic prefixed MIMO OFDM systems: Algorithm, identifiability and performance analysis," *IEEE Journal on Selected Areas in Communications*, vol. 26, no. 2, pp. 378–388, 2008.
- [47] M. Necker and G. Stuber, "Totally Blind Channel Estimation for OFDM on Fast Varying Mobile Radio Channels," *IEEE Transactions on Wireless Communications*, vol. 3, no. 5, pp. 1514–1525, 2004.
- [48] F. Gao and A. Nallanathan, "Blind channel estimation for MIMO OFDM systems via nonredundant linear precoding," *IEEE Transactions on Signal Processing*, vol. 55, no. 2, pp. 784–789, 2007.
- [49] T. Y. Al-Naffouri, A. A. Dahman, M. S. Sohail, W. Xu, and B. Hassibi, "Low-complexity blind equalization for OFDM systems with general constellations," *IEEE Transactions on Signal Processing*, vol. 60, no. 12, pp. 6395–6407, 2012.
- [50] S. A. Banani and R. G. Vaughan, "OFDM with iterative blind channel estimation," *IEEE Transactions on Vehicular Technology*, vol. 59, no. 9, pp. 4298–4308, 2010.
- [51] S. Park, B. Shim, and J. W. Choi, "Iterative channel estimation using virtual pilot signals for MIMO-OFDM systems," *IEEE Transactions on Signal Processing*, vol. 63, no. 12, pp. 3032–3045, 2015.
- [52] M. G. Song, D. Kim, and G. H. Im, "Recursive channel estimation method for OFDM-based cooperative systems," *IEEE Communications Letters*, vol. 14, no. 11, pp. 1029–1031, 2010.
- [53] T. C. T. Cui and C. Tellambura, "Joint data detection and channel estimation for OFDM systems," *IEEE Transactions on Communications*, vol. 54, no. 4, pp. 670–679, 2006.
- [54] M. Muck, M. de Courville, and P. Duhamel, "A pseudorandom postfix OFDM modulator - Semi-blind channel estimation and equalization," *IEEE Transactions on Signal Processing*, vol. 54, no. 3, pp. 1005–1017, 2006.

BIBLIOGRAPHY

- [55] S. Abdallah and I. N. Psaromiligkos, "Semi-blind channel estimation with superimposed training for OFDM-based AF two-way relaying," *IEEE Transactions on Wireless Communications*, vol. 13, no. 5, pp. 2468–2477, 2014.
- [56] A. Saci, A. Al-Dweik, A. Shami, and Y. Iraqi, "One-Shot Blind Channel Estimation for OFDM Systems Over Frequency-Selective Fading Channels," *IEEE Transactions on Communications*, vol. 65, no. 12, pp. 5445–5458, dec 2017.
- [57] C. H. Tseng, Y. C. Cheng, and C. D. Chung, "Subspace-Based Blind Channel Estimation for OFDM by Exploiting Cyclic Prefix," *IEEE Wireless Communications Letters*, vol. 2, no. 6, pp. 691–694, dec 2013.
- [58] M. X. Chang and Y. T. Su, "Performance analysis of equalized OFDM systems in rayleigh fading," *IEEE Transactions on Wireless Communications*, vol. 1, no. 4, pp. 721–732, 2002.
- [59] Y. G. Li, "Simplified Channel Estimation for OFDM Systems With Multiple Transmit Antennas," *IEEE Transactions on Wireless Communications*, vol. 1, no. 1, pp. 67–75, 2002.
- [60] 3GPP, "TS 36.211 version 10.0.0 Release 10; Evolved Universal Terrestrial Radio Access (E-UTRA); Physical channels and modulation," *Technical Specification*, p. 9, 2011.
- [61] A. Van Zelst and T. C. Schenk, "Implementation of a MIMO OFDM-based wireless LAN system," *IEEE Transactions on Signal Processing*, vol. 52, no. 2, pp. 483–494, 2004.
- [62] W. G. Jeon, K. H. Paik, and Y. S. Cho, "An efficient channel estimation technique for OFDM systems with transmitter diversity," *IEICE Transactions on Communications*, vol. E84-B, no. 4, pp. 967–974, 2001.
- [63] J. Siew, R. Piechocki, A. Nix, and S. Armour, "A channel estimation method for MIMO-OFDM systems," *Proc. London Communications*, pp. 2–5, 2002.
- [64] I. Barhumi, G. Leus, and M. Moonen, "Optimal training design for MIMO OFDM systems in mobile wireless channels," *IEEE Transactions on Signal Processing*, vol. 51, no. 6, pp. 1615–1624, 2003.
- [65] T.-L. Tung, K. Yao, and R. E. Hudson, "Channel estimation and adaptive power allocation for performance and capacity improvement of multiple-antenna OFDM systems," in

- Wireless Communications, 2001. (SPAWC 01). 2001 IEEE Third Workshop on Signal Processing Advances in*, 2001, pp. 82–85.
- [66] Taewon Hwang, Chenyang Yang, Gang Wu, Shaoqian Li, and G. Ye Li, “OFDM and Its Wireless Applications: A Survey,” *IEEE Transactions on Vehicular Technology*, vol. 58, no. 4, pp. 1673–1694, 2009.
- [67] Y. Li, N. Seshadri, and S. Ariyavisitakul, “Channel estimation for OFDM systems with transmitter diversity in mobile wireless channels,” *IEEE Journal on Selected Areas in Communications*, vol. 17, no. 3, pp. 461–471, 1999.
- [68] Y. Gong and K. B. Letaief, “Low rank channel estimation for space-time coded wide-band OFDM systems,” in *IEEE 54th Vehicular Technology Conference. VTC Fall 2001. Proceedings (Cat. No.01CH37211)*, vol. 2, 2001, pp. 772–776 vol.2.
- [69] —, “Low complexity channel estimation for space-time coded wideband OFDM systems,” *IEEE Transactions on Wireless Communications*, vol. 2, no. 5, pp. 876–882, 2003.
- [70] S. M. Alamouti, “A simple transmit diversity technique for wireless communications,” *IEEE Journal on Selected Areas in Communications*, vol. 16, no. 8, pp. 1451–1458, 1998.
- [71] C. Suh, C.-s. Hwang, and H. Choi, “Preamble Design for Channel Estimation in MIMO-OFDM Systems,” *GLOBECOM '03. IEEE Global Telecommunications Conference (IEEE Cat. No.03CH37489)*, vol. 1, no. 1, pp. 317–321, 2003.
- [72] B. Popovic, “Efficient DFT of Zadoff-Chu sequences,” *Electronics Letters*, vol. 46, no. 7, p. 502, 2010.
- [73] J. Hou and J. Liu, “A novel channel estimation algorithm for 3GPP LTE downlink system using joint time-frequency two-dimensional iterative Wiener filter,” in *International Conference on Communication Technology Proceedings, ICCT*, 2010, pp. 289–292.
- [74] Y. Zheng, X. Gu, and Q. Guo, “A novel Doppler shift estimation algorithm for OFDM-based transform domain communication systems,” in *International Conference on Signal Processing Proceedings, ICSP*, vol. 2, 2012, pp. 1449–1453.
- [75] Q. Guo, M. Wu, Q. Zhang, X. Hao, and Y. Sun, “Channel Estimation for OFDM Systems over Time-Varying and Sparse Dispersive Channels,” in *Vehicular Technology Conference (VTC Spring), 2012 IEEE 75th*, 2012, pp. 1–5.

BIBLIOGRAPHY

- [76] A. M. Al-Samman, T. A. Rahman, U. A. Chude-Okonkwo, and R. Ngah, "Hybrid channel estimation for LTE downlink," in *Proceedings - 2013 IEEE 9th International Colloquium on Signal Processing and its Applications, CSPA 2013*, 2013, pp. 44–48.
- [77] K. Y. B. R. W. Tang Haiyun; Lau, "Interpolation-based maximum likelihood channel estimation using OFDM pilot symbols," *Global Telecommunications Conference, 2002. GLOBECOM '02. IEEE*, vol. 2, pp. 1860—1864 vol.2, 2002.
- [78] H. Schulze and C. Luders, *Theory and Applications of OFDM and CDMA*, 2005.
- [79] M. Mirahmadi, A. Al-Dweik, and A. Shami, "BER reduction of OFDM based broadband communication systems over multipath channels with impulsive noise," *IEEE Transactions on Communications*, vol. 61, no. 11, pp. 4602–4615, 2013.
- [80] M. S. Ahmed, S. Boussakta, B. S. Sharif, and C. C. Tsimenidis, "OFDM based on low complexity transform to increase multipath resilience and reduce PAPR," *IEEE Transactions on Signal Processing*, vol. 59, no. 12, pp. 5994–6007, 2011.
- [81] Q. T. Zhang, "Probability of error for equal-gain combiners over rayleigh channels: some closed-form solutions," *IEEE Transactions on Communications*, vol. 45, no. 3, pp. 270–273, 1997.

Curriculum Vitae

Name: Mohammed O. M. Zourob

Post-Secondary Education and Degrees: University of Western Ontario
London, ON, Canada
2018 Doctor of Philosophy (Ph.D.)
Electrical and Computer Engineering

University of Western Ontario
London, ON, Canada
2013 Masters of Engineering Science (M.E.Sc.)
Electrical and Computer Engineering

American University of Sharjah (AUS)
Sharjah, United Arab Emirates
2011 Bachelor of Engineering Science (B.E.Sc) with
Minor in Applied Mathematics
Electrical and Electronics Engineering

Honours and Awards: Alexander Graham Bell Canada Graduate Scholarship
NSERC-CGSD
University of Western Ontario
2013-2016

Queen Elizabeth II Graduate Scholarship in Science and Technology
QEII-GSST
University of Western Ontario
2012-2013

Western University Graduate Research Scholarship
WGRS
University of Western Ontario
2011-2017

Honours and Awards (continued):

Ranked 1st among 610 Graduates - Summa Cum Laude
American University of Sharjah
2011

AUS Dean's and Chancellor's List
American University of Sharjah
2007-2011

Shikha Salama Scholarship for Academic Excellence
American University of Sharjah
2007-2011

AUS Merit Scholarship
American University of Sharjah
2007-2011

Related Work Experience:

Wireless Communication Engineer
Sieco-Tech/Sagacity
2018-Present

Programming Fundamentals for Engineers Lecturer
University of Western Ontario
2017

Graduate Teaching and Research Assistant
University of Western Ontario
2011-2018

Teaching & Research Assistant
American University of Sharjah
2008-2010

Journal Publications During Doctoral Studies:

1. M. Zourob, A. Al-Dweik and R. Rao, "New Pilot Distributions Serving One-Shot Blind Channel Estimation for LTE DL Systems," IET in Communications, to be submitted.
2. M. Zourob, A. Al-Dweik and R. Rao, "One-Shot Blind Channel Estimation for MIMO-OFDM Systems Over Fast and Frequency-Selective Fading Channels," IEEE Transactions on Vehicular Technology (TVT by IEEE), under preparation.
3. M. Zourob and R. Rao, "Hybrid Lower-Complexity Wiener Filter for Pilot-Based Channel Estimation for C-RS in LTE-A DL System," Mobile Networks and Applications Journal (MONET by Springer), 2017, pp. 1-19.

Conference Publications During Doctoral Studies:

1. M. Zourob, A. Al-Dweik and R. Rao, "Different Implementation Schemes for One-Shot Blind Channel Estimation in SIMO-OFDM Systems," 2018 IEEE Conference on Standards for Communications and Networking (IEEE CSCN), to be submitted.
2. M. Zourob and R. Rao, " 2×1 -D Fast Fourier Transform Interpolation for LTE-A OFDM Pilot-Based Channel Estimation," 2017 International Conference on Electrical and Computing Technologies and Applications (ICECTA), Nov. 21-23, 2017, pp. 1-5. **(Best Student Paper Award - Second Place)**
3. M. Zourob and R. Rao, "On Linear Detector's Spectral Capacity for Massive MIMO Systems," 2017 International Conference on Electrical and Computing Technologies and Applications (ICECTA), Nov. 21-23, 2017, pp. 1-5.
4. M. Zourob and R. Rao, "Lower-Complexity Wiener Filtering for UE-RS Channel Estimation in LTE DL System," 2017 International Symposium on Wireless Systems and Networks (ISWSN), Nov. 19-22, 2017, pp. 1-5.
5. M. Zourob and R. Rao, "A Low-Complexity C-RS-Aided Channel Estimation Scheme for LTE Downlink System," 2017 International Conference on Smart Grid and Internet of Things (SGIoT), Jul. 11-13, 2017, pp. 1-10.
6. M. Zourob and R. Rao, "Reduced-Complexity Implementation Scheme for OFDM Channel Estimation," 2017 IEEE 30th Canadian Conference on Electrical and Computer Engineering (CCECE), May. 1-3, 2017, pp. 1-4.
7. M. Zourob and R. K. Rao, "Decision Aided Detection and Performance of Continuous Phase Chirp Keying," 2013 International Symposium on Performance Evaluation of Computer and Telecommunication Systems (SPECTS), Jul. 7-10, 2013, pp. 182-187.